CRANFIELD UNIVERSITY

Matt Stock

An investigation of the photocatalytic properties of lithium niobate and barium titanate

School of Applied Sciences

PhD thesis

Academic Year: 2008 - 2012

Supervisors: Dr Steve Dunn & Professor Robert Dorey

CRANFIELD UNIVERSITY

School of Applied Sciences

PhD thesis

2012

Matt Stock

An investigation of the photocatalytic properties of lithium niobate and barium titanate

Supervisors: Dr Steve Dunn & Professor Robert Dorey

Academic Year 2008- 2012

This thesis is submitted in partial fulfilment of the requirements for the degree of PhD

ABSTRACT

Efficiency of particulate semiconductors for driving photocatalytic reactions is impractically low due to the recombination of excited carriers and intermediate species at the interface. In the literature it has been demonstrated internal depolarisation fields in ferroelectric materials separate electron and hole carriers, this gives rise to spatially distinct reduction and oxidation processes. It is hypothesised this property can supress the rate of back reactions and carrier recombination to improve photocatalytic efficiency. In this thesis the properties of ferroelectric particulates for driving photocatalytic reactions are investigated.

Lithium niobate and barium titanate powders were suspended in aqueous solutions of acid black 1 or rhodamine b dye. Adsorption studies compared retention of dye in the double layer by the different powders. Under UV or simulated solar illumination barium titanate or lithium niobate powders photocatalytically decolourised the dye solutions. Powders of lithium niobate powder doped with magnesium or iron showed altered reaction rates and structural selectivity of decolourisation reactions. Photochemical deposition of silver nanoparticles at the surface of the barium titanate or lithium niobate powders increased the rate of photocatalytic decolourisation of rhodamine b solutions under UV or simulated solar illumination.

Photochemical reduction of carbon dioxide to form formic acid and formaldehyde over lithium niobate powder was studied under UV illumination. Solid-liquid phase reactions were carried out using aqueous suspensions of powder bubbled with carbon dioxide gas. Solid-gas phase reactions were investigated using a purpose built reaction vessels loaded with carbon dioxide gas and water vapour. Under solid-gas phase conditions the rate of formation of products over lithium niobate powder was greater than over titanium dioxide powder.

Keywords:

Photocatalysis, ferroelectric, carbon dioxide, dye decolourisation

ACKNOWLEDGEMENTS

I would like to thank Dr Steve Dunn and Professor Robert Dorey for their supervision and support during this work.

I would also like to extend my thanks to Dr Paul Jones, Dr Chris Shaw, Mrs Enza Giaracuni, Mr Andrew Stallard, Mr Matthew Taunt, Dr Keith Richards and Ms Jane Hubble for their helping hand.

Special thanks also go to my family for their support.

TABLE OF CONTENTS

LIST OF FIGURES

LIST OF TABLES

1 Introduction

1.1 Background

Photocatalysis reactions take place when a semiconductor is illuminated by light with energy equalling or exceeding that of the materials band gap. In this case absorption of photons by the semiconductor excites electron-hole pairs (Equation 1.1). A proportion of the electron and hole carriers recombine either at the surface or in the bulk releasing the absorbed light energy as unutilised heat. However, carriers that do not undergo recombination can migrate to the interface and drive chemical reduction or oxidation reactions of adsorbed species[1].

$$\mathbf{Photocatalyst} \xrightarrow{\mathbf{hv}} \mathbf{e^-_{CB}} + \mathbf{h^+_{vb}} \qquad (1.1)$$

Over the past four decades investigation of semiconductor photocatalysis has become a popular topic. The discovery by Honda and Fujishima in the 1970's that a titanium dioxide electrode could photo-electrochemically decompose water to form hydrogen when illuminated with super band gap light[2] sparked investigation of a range of semiconductor materials and reaction conditions for photocatalytic production of fuel stock[3-7]. The growing threat of climate change from release of greenhouse gases and the dwindling reserves of fossil fuels has maintained strong interest in this field. More recently photocatalysis has also been demonstrated as a method for generating reactive species from water and atmospheric oxygen[8] e.g. the hydroxyl radical ($OH^{\cdot}$), the neutral form of the hydroxyl ion (OH^-), and superoxide anion radical ($O_2^{\cdot -}$). These species are sufficiently oxidising to degrade a wide range of pollutants[9-11] which has led to investigation of photocatalytic reactions as a solution to the issues posed by treatment of hazardous wastes, polluted ground waters, and toxic air contaminants in industrialised nations[12]. However, despite the potential applications of photocatalytic reactions their use remains rare on an industrial scale. The efficiency of reactions over a photocatalyst are, generally speaking, dependent upon the rate of photogenerated carrier formation; the rate at which electron and hole carriers recombine; the rate of transfer of carriers to adsorbed

species; and the rate at which intermediate species undergo backward reactions at the photocatalyst's surface. In the case of semiconductor materials it is known that photogenerated carriers recombine at high rates[13] and that oxidation and reduction reactions occur at spatially similar locations allowing backward reactions to take place readily[4]. Semiconductor materials suitable for driving typical photocatalytic reactions also have intrinsic band gaps greater than 3 eV. This means that their sensitivity to solar light is low and so a UV light source is required to excite carriers. These factors limit the efficiency of reactions and mean that continued development of photocatalysis for real world applications requires new approaches.

Ferroelectrics are materials first discovered in 1920[14] that develop a spontaneous electrical polarisation. Their properties have been shown to have application in memory devices, waveguides[15] and the fabrication of micro electromechanical systems[16]. More recently ferroelectrics have been shown to display the properties of wide band gap semiconductors[17]. This characteristic makes ferroelectrics suitable for driving photocatalytic reactions[18;19]. It has been reported that the internal depolarisation fields in ferroelectric materials drive separation of photo excited electron and hole carriers[20]. This may improve the efficiency of photocatalytic reactions by reducing the rate at which recombination of excited carriers occurs. Separation of carriers in ferroelectric materials also causes photochemical reduction and oxidation reactions to take place at spatially distinct locations[21; 22]. Separating the locations of reduction and oxidation reactions is hypothesised to decrease the rate at which intermediates take part in backward reactions. Another property of ferroelectric materials is that molecule-surface interactions are reported to be polarisation dependent[23]. This means the orientation of the polarisation enables the location of adsorption of molecules at the surface to be influenced[24]. As a result this may allow the pathway of photochemical reactions to be controlled.

1.2 Aims and objectives

This thesis investigates ferroelectric barium titanate and lithium niobate particulates in order to contribute to understanding of these materials photocatalytic properties. This work also aims to demonstrate the application of ferroelectric materials in driving photocatalytic reactions in which a semiconductor would traditionally be used. The main objectives are:

1. Investigate the effect of the ferroelectric surface charge upon the electrical double layer, the structure formed at the interface of a solid when placed in a liquid that is discussed in detail in section 2.3 of the literature review, by monitoring the change in concentration of ionic dye molecules in aqueous solution after powders of barium titanate or lithium niobate are added
2. Study the properties of lithium niobate and barium titanate as photocatalysts for driving degradation of dye pollutants in aqueous solution under UV and simulated solar illumination
3. Determine the changes in the photocatalytic properties of lithium niobate and barium titanate powders for driving dye degradation reactions after silver nanoparticles have been photochemically deposited at the surface
4. Study the solid-liquid phase and solid-gas phase photochemical reduction of carbon dioxide to form hydrocarbon products using lithium niobate powder under UV illumination

1.3 Overview of thesis

The thesis comprises 9 Chapters with respective summaries below:

Chapter 2 is a literature review covering the properties of ferroelectric materials; the properties of semiconductor materials and semiconductor properties of ferroelectric materials; photocatalytic reactions, photocatalytic properties of ferroelectric materials and the properties of barium titanate and lithium niobate.

Chapter 3 details the methods used in the experimental work.

Chapter 4 is a discussion of the barium titanate, lithium niobate and iron or magnesium doped lithium niobate powders selected for use in this research.

Chapter 5 investigates the effect of surface charge of barium titanate and lithium niobate powders upon adsorption of dye molecules from aqueous solution (Objective 1).

Chapter 6 describes photocatalytic decolourisation of dye solutions under UV illumination over barium titanate, lithium niobate and magnesium or iron doped lithium niobate powders (Objective 2).

Chapter 7 discusses the photochemical deposition of metal nanoparticles at the surface of barium titanate or lithium niobate powders. The photocatalytic activity of lithium niobate and barium titanate powders for driving dye decolourisation reactions under UV or simulated solar illumination is compared before and after modification through addition of metal nanoparticles (Objectives 2 & 3).

Chapter 8 studies the properties of lithium niobate powder to drive solid-liquid phase and solid-gas phase photochemical reduction of carbon dioxide to form formic acid and formaldehyde under UV illumination (Objective 4).

Chapter 9 is a summary of the conclusions drawn from this work and possible future avenues of research indicated by this thesis.

2 Literature review

2.1 Ferroelectric materials

Ferroelectrics are materials that exhibit a spontaneous electric polarisation. A crystal is said to be ferroelectric when the polarisation has two or more orientational states in the absence of an electric field and can be shifted from one state to another by application of an electric field[25]. The reversibility of the polarisation was first discovered in Rochelle's salt by Valasek in 1920[14]. Valasek recognised the crystals ferroelectric character through investigations showing its dielectric properties to be similar in nature to the ferromagnetic properties of iron e.g. it displays a Curie temperature and large dielectric and piezoelectric response in and surrounding the ferroelectric region. This led to use of the term ferroelectric to describe these materials on the basis that they are the electrical equivalent of ferromagnetic materials. However, the two phenomena have distinct origins. Ferromagnetism stems from electron spin and angular momentum altering the magnetic moment of atoms[26]. The spontaneous polarisation in ferroelectric materials forms as a result of phase transitions at the Curie point.

2.1.1 The spontaneous polarisation

In a ferroelectric crystal the spontaneous polarisation is the magnitude of the polarisation in a single domain. The spontaneous polarisation in ferroelectric materials has been reported to range from the order of hundredths of μC cm^{-2} (e.g. Rochelle's salt 2.5 $x10^{-2}$ μC cm^{-2}) to tens of μC cm^{-2} (e.g. lithium niobate 78 μC cm^{-2})[27]. Above a specific transition temperature termed the Curie point (T_c) the spontaneous polarisation disappears and ferroelectric crystals are said to be in the paraelectric phase. The phase transitions occurring at the Curie point responsible for formation of the spontaneous polarisation in ferroelectric crystals are characterised as order-disorder or displacive. In displacive phase transitions atomic displacements in the paraelectric phase are oscillations

around a non-polar site while below the Curie point they are about a polar site. The class of displacive ferroelectrics include ABO_3-based perovskite structures e.g. lead titanate. The perovskite structure exists in two crystallographic forms. Above the Curie point the crystal class is body centred cubic. In this case the unit cell is centrosymmetric i.e. the positive and negative charges coincide. The unit cell comprises lead ions located at corner sites and a body centred titanium cation residing within a coordination polyhedron of oxygen anions. At the Curie point a displacive phase transition takes place altering the crystal class from body centred cubic to tetragonal. In the case of lead oxide this is a result of oxygen anions and lead cations being shifted in the same direction relative to the location of the titanium cation, without distortion of the oxygen octahedra occurring (Figure 2.1). The phase transition causes the titanium cation to no longer be body centred, generating a dipole in the unit cell.

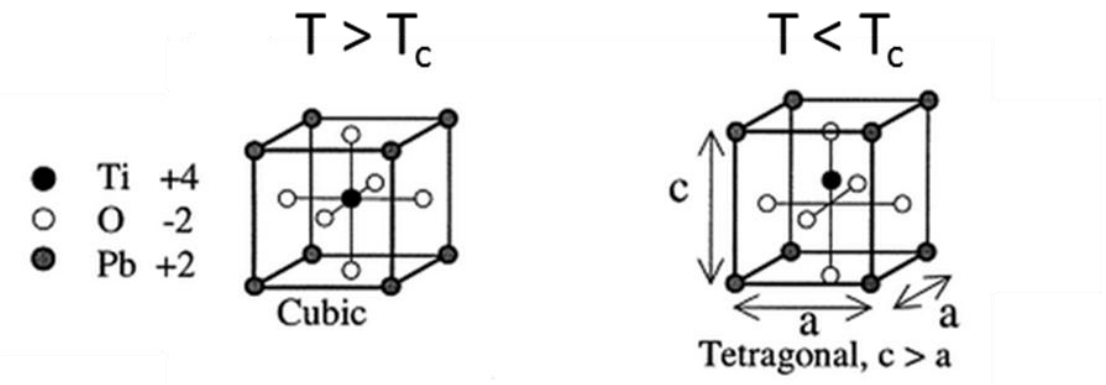

Figure 2.1 A scheme showing the unit cell of lead titanate undergoing a cubic to tetragonal phase transition when cooled below the Curie point as a result of displacement of both lead and oxygen ions in the same direction relative to the location of the titanium cation (Source ref. 28)

In order-disorder transitions atomic displacements in the paraelectric phase are about a double well or multi well configuration of sites while below the Curie point in the ferroelectric phase they are about an ordered subset of these wells. As a result, long range ordering takes place in the crystal at temperatures below the Curie point creating a spontaneous polarisation. The class of order-disorder ferroelectrics include hydrogen bonded crystals in which the hydrogen bonding

is related to the ferroelectric character. Potassium dihydrogen phosphate (KH_2PO_4) is an example of a hydrogen bonded ferroelectric crystal. The structure consists of phosphate groups (PO_4) bound via hydrogen bonds that are close to being perpendicular to the c-axis, and potassium ions. Above the Curie point the distribution of hydrogen atoms is disordered with each atom occupying one of two different crystallographic sites near phosphate groups with equal probability. Below the Curie point hydrogen atoms take on an ordered arrangement occupying specific crystallographic sites. The location of the hydrogen atoms in the structure does not directly contribute to formation of the spontaneous polarisation in potassium dihydrogen phosphate as their movement is perpendicular to the ferroelectric axis. The movement of hydrogen atoms, however, exerts coulomb forces on potassium, phosphorus and oxygen atoms in the structure causing them to shift parallel to the c-axis, creating long range ordering of dipoles in the crystal and a spontaneous polarisation.

2.1.2 Domains and domains walls

The spontaneous polarisation in ferroelectric materials can develop in opposing directions in at least one axis. This gives rise to regions of consistent polarisation in the crystal that only differ in their orientation referred to as ferroelectric domains. Domains orientated in the Z axis are termed C domains, C+ when in the Z+ direction and C- when in the Z- direction. Domains that are orientated in the plane of the surface are termed lateral domains. The regions separating two adjacent domains are termed domain walls, reported to be between 0.5 nm to several nm thick[29; 30]. Domain walls that separate C+ and C- domains are referred to as 180^o walls and the domain walls separating a C domain and lateral domains are termed 90^o walls (Figure 2.2).

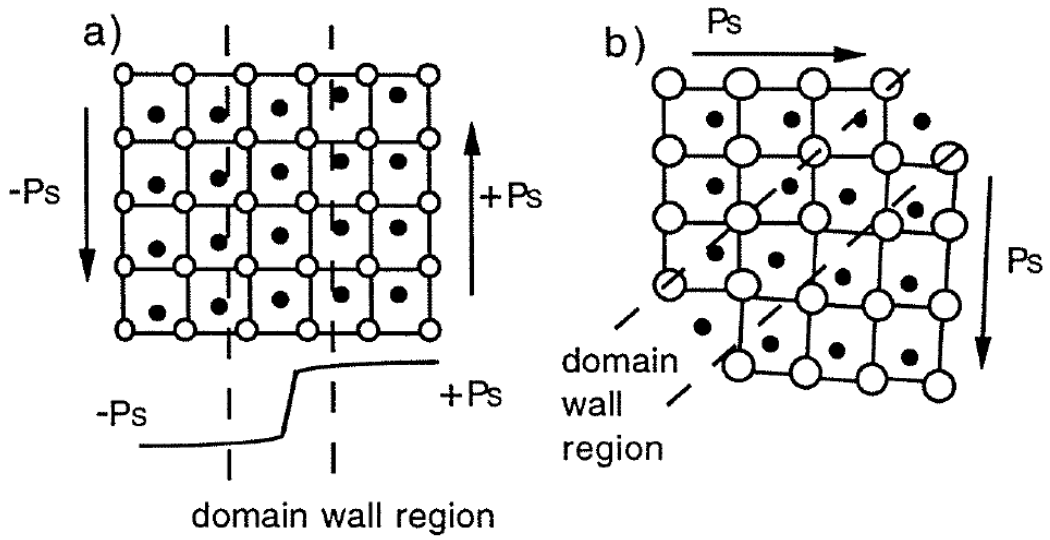

Figure 2.2 a) 180^{o} domain walls formed separating C+ and C- domains b) 90^{o} domain walls separating C- and lateral domains (Source ref. 31)

2.1.3 Depolarisation fields

The spontaneous polarisation is not homogeneous throughout ferroelectric crystals. At the crystals surface the polarisation decreases to zero i.e. the polarisation is zero outside the ferroelectric crystal and non-zero inside of it, producing a charge bound at the crystals surface. In the vicinity of defects in the crystals structure the polarisation also differs from that of the perfect crystal. As the divergence of the spontaneous polarisation is non-zero in ferroelectric crystals this gives rise to depolarisation fields i.e. electrical fields opposing the spontaneous polarisation. Depolarisation fields have a significant impact on the physical properties of ferroelectric materials as they act to supress or fully destroy the ferroelectric state[32]. Formation of a single domain creates a large depolarisation field[33]. As a result, in unpolarised ferroelectric materials multiple oppositely orientated domains spontaneously form at temperatures below the Curie point in order to minimise the total free energy of the crystal (Figure 2.3). The total free energy is a combination of the energies of the depolarisation fields, surface energy, energy of domain walls etc. The remaining depolarisation energy of a polydomain ferroelectric material is compensated through the

movement of mobile charge carriers inside domains or externally to the ferroelectric[34].

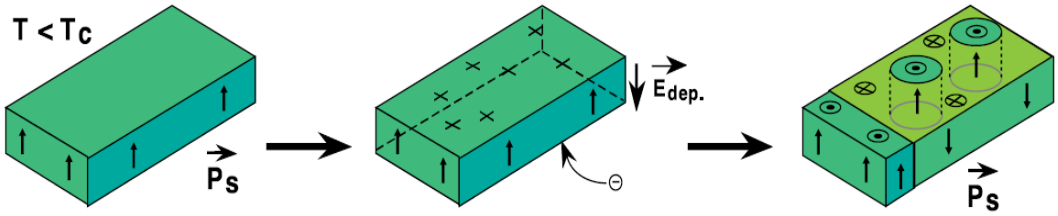

Figure 2.3 The formation of domains in a ferroelectric crystal. Below the Curie point an energetically unfavourable single crystal state is produced inducing a large depolarisation field. A multiple domain structure spontaneously forms to minimise the crystals electrostatic energy (Source ref. 33)

2.1.4 Ferroelectric hysteresis

The relationship between polarisation of a ferroelectric material and an external electric field is shown by a hysteresis loop[35]. Figure 2.4 shows an example of a hysteresis loop produced by a ferroelectric material. When a low AC electric field is applied the domains in the ferroelectric align in the direction of the field causing polarisation to initially increase linearly. When the field strength is increased, unfavourably orientated domains also switch to align with the field causing further increase in polarisation. After the external field is removed the proportion of domains that remain orientated in the direction of the field determines the strength of the remnant polarisation (Pr). If the applied field is sufficient to fully align all domains in the ferroelectric material the remnant polarisation is equal to that of the spontaneous polarisation and is termed the saturation remnant polarisation. Through reversal of the external field the polarisation in the crystal can be removed. The strength of field required to fully reduce the polarisation to zero is termed the coercive field (Ec). By increasing the electric field above that of the coercive field the crystal can be polarised in the opposite direction.

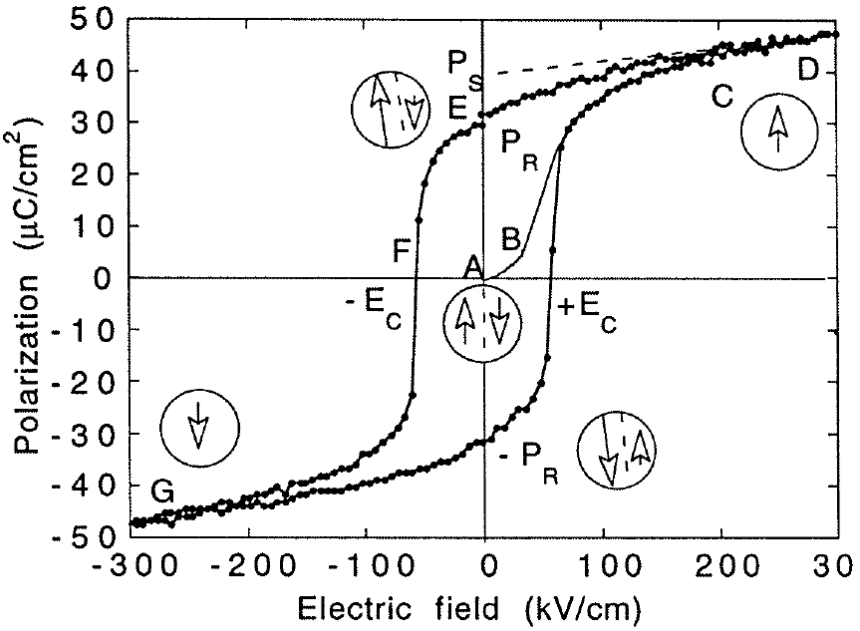

Figure 2.4 A hysteresis loop produced by a ferroelectric. Ps is the spontaneous polarisation, Pr is the remnant polarisation and Ec denotes the coercive electric field (Source ref. 31)

2.1.5 Size effects of ferroelectric materials

Through theoretical[36; 37] and experimental investigations[38; 39; 40] it has been shown that ferroelectric particulates display deviations from the physical properties of bulk materials. These departures are referred to as size effects[41]. The dielectric constant, spontaneous polarisation and Curie temperature of a ferroelectric typically decrease when the size is reduced below the order of micrometres in one or more dimensions (Figure 2.5). Particulates of ferroelectrics have also been shown to undergo a size driven transition to the paraelectric phase below a specific dimension, termed the ferroelectric critical size[42].

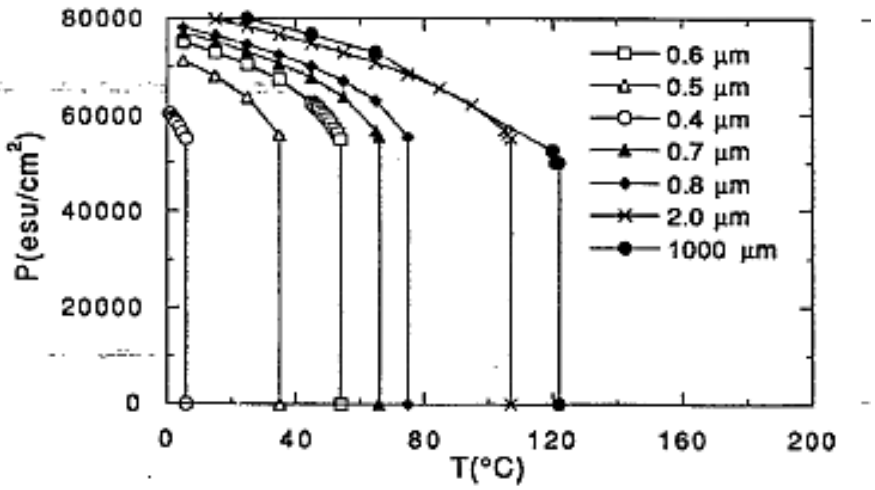

Figure 2.5 Decrease in the Curie point and polarisation of barium titanate particulates as the size is reduced (Source ref. 40)

The origins of size effects in ferroelectric materials are not fully understood; however, it has been suggested they are largely a result of two factors[43]. The first is the effect of size upon the domain wall energy, the energy associated with formation of the domain wall. As the volume of a ferroelectric material decreases the domain wall energy increases. This property causes polydomain ferroelectrics to form a single domain below a certain size e.g. barium titanate particulates have been shown to change from being polydomain to single domain when the size is reduced below 100 nm[44]. Formation of a single domain increases the depolarisation field energy of the ferroelectric. If particulates are unable to compensate the increased depolarisation field energy through internal or external mobile charge carriers the ferroelectric state can be fully destroyed[45]. The second factor proposed to drive size effects is the impact of reduced particle size upon long range dipole interactions supporting formation of the ferroelectric phase. Ginzburg-Landau mean field theory has been used to express the free energy for inhomogeneous ferroelectric particulates of a finite size using the polarisation as an order parameter[43]. According to the theory the polarisation can be expressed by two factors. The first is correlation length, the average distance over which the fluctuations of polarisation are coordinated. When the correlation length is large dipoles in the unit cell can interact over long distances. The second is the extrapolation length, the difference in the coupling

strength between the bulk of the material and the materials surface. If the coupling strength of the surface is less than that of the bulk material the surface becomes disordered in comparison to the bulk material. Surface disorder produces disorder in the bulk material over a distance defined by the correlation length. The range over which disorder in the surface layer affects the order of the bulk material is dictated by the material's correlation length. As a particle's size is decreased a relatively greater amount of bulk material becomes disordered by the surface layer (Figure 2.6). Eventually the disorder in the bulk will become sufficient to destroy the polar state.

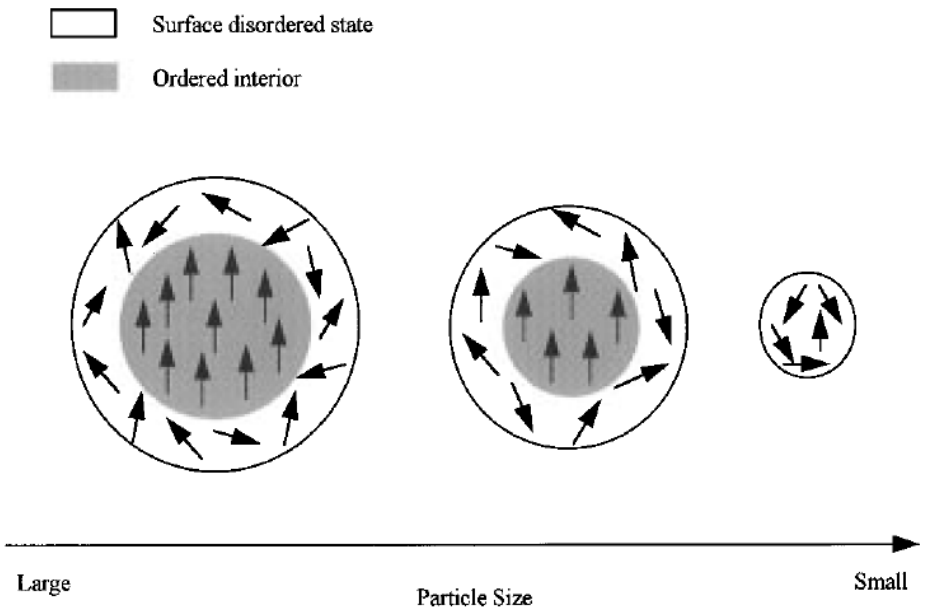

Figure 2.6 Scheme showing the increasing disorder in ferroelectric particulates as size is decreased (Source ref. 43)

2.1.6 Ferroelastic depolarisation of ferroelectrics

Strain is defined as the relative deformation of particles in a body in comparison to their original positions. Ferroelasticity describes a spontaneous strain that develops in the stress-strain behaviour of ferroic materials below the Curie point[46]. A crystal is said to be ferroelastic when it has two or more orientation states in the absence of mechanical stress and can be shifted between these

states by the application of mechanical stress[25]. Ferroelasticity is an almost universal property of ferroelectric ABO_3 perovskites in which there is a change in the crystal class at the Curie point. As discussed in Section 2.1.1 the change in crystal class is a result of a displacive phase transition in which oxygen anions and B sites cations are displaced in relation to the location of the A site cations. The displacement of atoms in the unit cell produces a dipole and creates both a spontaneous polarisation and a spontaneous strain in the crystal. In the absence of an electric field application of mechanical stress causes ferroelastic switching in ferroelectric perovskites (Figure 2.7). The orientation of the dipole in the unit cell can be switched in its original axis or changed to a new axis[47]. This action is driven by the motion of domain walls, favourably orientated domains are able to adsorb space that was occupied by unfavourably orientated domains[48].

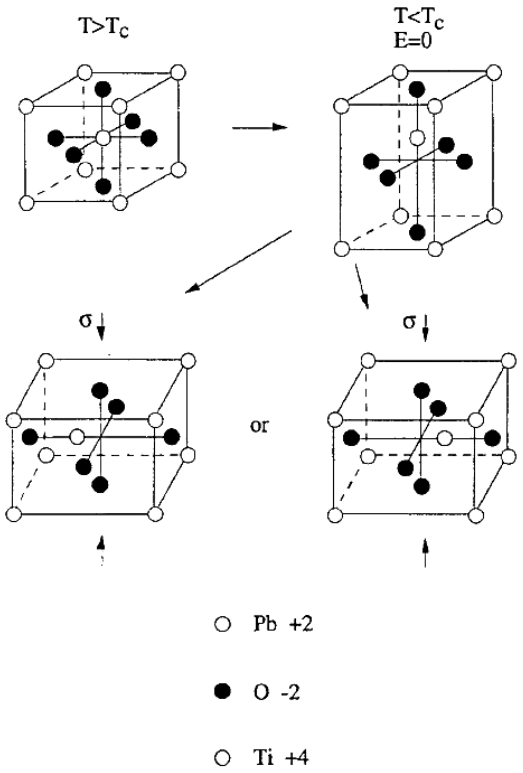

Figure 2.2.7 The cubic unit cell of lead titanate is shown above the Curie point (T>Tc). A displacive phase transition occurs when the crystal is cooled below the Curie point (T<Tc). The unit cell class changes from symmetric cubic to asymmetric tetragonal as a result of lead and oxygen atoms being displaced in relation to the location of titanium cations. The displacement of atoms produces a dipole in the unit cell and both a spontaneous polarisation and spontaneous strain. Below the Curie point ferroelastic switching can be induced in the crystal through motion of domain walls as a result of mechanical application of external stress (σ). External stress causes realignment of the unit cells tetragonality, changing the orientation of the unit cell dipole in its current axis or changing its orientation to a new axis. Switching of the orientation of the dipole of the unit cell alters the orientation of the spontaneous strain and polarisation in the lead titanate crystal (Source ref. 46)

In an unpoled ferroelectric an approximately equal number of domains form in each axis that the polarisation can arise. Application of mechanical stress causes an equal amount of switching in all axes producing a net increase in strain but no change in the materials net polarisation. However, if a ferroelectric material has been polarised to produce a single domain or a specific domain

structure then application of mechanical stress to produce ferroelastic domain switching causes the material to be depolarised, forming a poly domain structure. Depolarisation as a result of applied stress has been demonstrated to occur in thin film samples of lead zirconate titanate[49; 50] and lead lanthanum titanate[51].

2.2 Semiconducting materials

2.2.1 Electronic band structure of solids

The electronic band structure of solids describes the energy states electrons are 'allowed' and 'forbidden' to possess. Both the optical and electronic properties of a solid are determined by its electronic band structure. In a single unbound atom the electrons occupy atomic orbitals with discrete energy levels. Each energy level can be occupied by a maximum of two electrons with opposite spin according to the Pauli Exclusion Principal. If more atoms become chemically bonded to the isolated atom the individual atomic orbitals are combined to form molecular orbitals comprising two states, bonding and anti-bonding orbitals. If the atomic orbitals interact with each other constructively i.e. in phase, they create a bonding orbital with a lower energy state than the atomic orbitals. If the atomic orbitals interact destructively i.e. out of phase, an anti-bonding orbital with higher energy than the atomic orbitals is formed. The number of molecular orbitals produced is proportional to the total number of bound atoms in a solid. If a large quantity of atoms (more than x 10^{20}) bond together to produce a bulk solid then a correspondingly large number of molecular orbitals are formed. This causes the discrete energy levels to converge and become indistinguishable resulting in formation of continuous energy bands (Figure 2.8). Bonding molecular orbitals combine to form an energy band related to the valence band (Ev) while anti-bonding orbitals converge to form an energy band related to the conduction band (Ec).

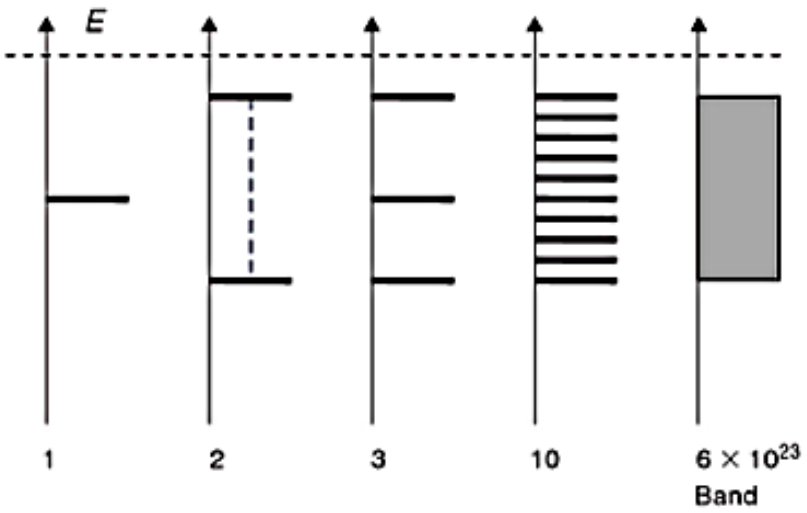

Figure 2.8 Scheme showing the convergence of atomic orbitals to form a continuous band as the number of bound atoms increases (Source ref. 52)

2.2.2 Metals, semiconductors and insulators

When a solid produces a current upon application of an external electric field it is termed a conductor. This property arises from the conduction band being partially filled with mobile electrons. In metals such as lithium the conduction band becomes partially filled due to overlap between the top of the valence band and bottom of the conduction band (Figure 2.9). Materials in which application of an electric field does not produce a current are termed insulators. In insulating materials a gap of forbidden energy states exists between the valence band and conduction band termed the band gap (Eg) (Figure 2.9). In insulating materials the conduction band can only be partially filled if valence band electrons are excited to the conduction band by adsorbing energy equal to or exceeding the band gap. As insulators typically have wide band gaps e.g. diamond has a band gap of 7eV, this means under ambient conditions excitation of electrons does not occur. If an insulator has a small band gap below 2 eV e.g. silicon has a band gap of 1 eV, electrons can be promoted to the conduction band through adsorption of photons or thermal excitation to

produce conducting character. These materials can be considered as room temperature semiconductors rather than as insulators (Figure 2.9).

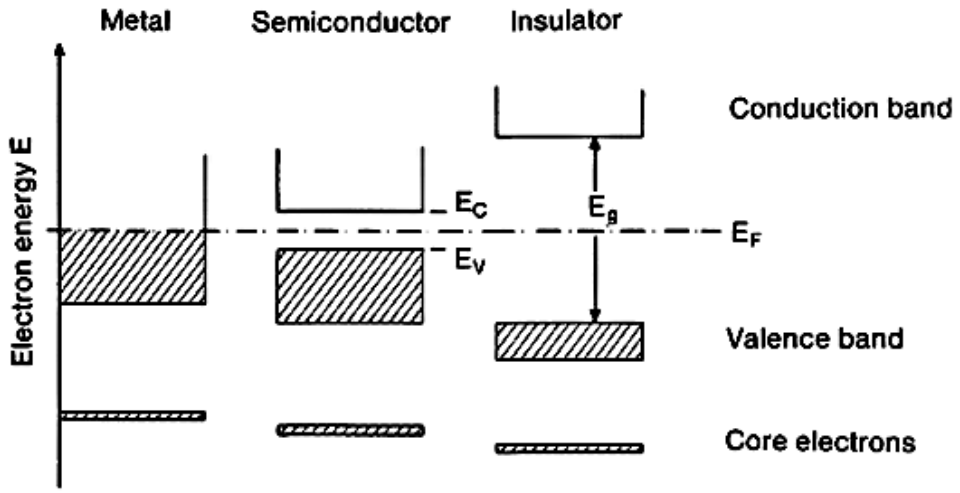

Figure 2.9 The energy levels of a metal, semiconductor and insulator. Ec is the conduction band, Ev is the valence band and Eg is the band gap (Source ref. 53)

2.2.3 Semiconductor doping

When the crystal structure of a semiconductor contains an insignificant number of impurities or no impurities at all then the semiconductor is described as intrinsic. The number of charge carriers produced in the material and the majority carrier type is, therefore, determined by the materials properties alone[54]. Impurities can be intentionally introduced into a semiconductors structure in a process termed doping. Semiconductors altered in this fashion are described as being extrinsic. Dopants are elements other than those that usually comprise the semiconductors structure. These atoms create impurities by replacing atoms in the structure or occupying interstitial sites. Doping in a semiconductor structure can alter the concentration of charge carriers at thermal equilibrium and the majority carrier type. If the dopant atoms introduced to the structure has a higher number of valence electrons than the atom replaced then the additional electrons can be donated into the materials conduction band (Figure 2.10). These dopants are referred to as donors and

increase the concentration of electron carriers in the material to produce an n-type semiconductor. Donor doping causes the position of the Fermi level to move toward the conduction band. When dopant atoms have fewer valence electrons than the atoms they replace they are termed as acceptors (Figure 2.10). These dopants are able to remove electrons from the materials valence band in order to fill their outer shell. This increases the number of hole carriers and produces a p-type material. Doping with acceptor atoms shifts the Fermi level down toward the valence band.

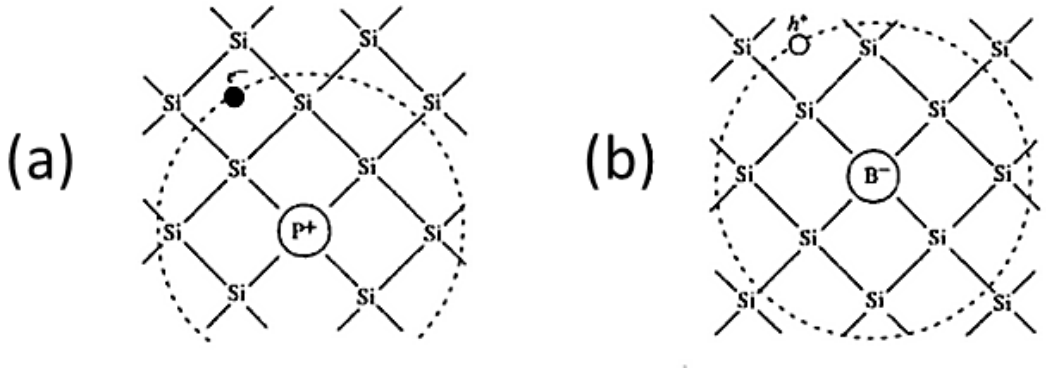

Figure 2.10 (a) a phosphorus atom introduced into the structure of silicon to form a donor centre P+ with a weakly bound additional electron (b) a boron atom forming an acceptor centre B- with a weakly bound additional hole carrier (Source ref. 55)

2.2.4 Semiconductor surfaces

Work by Shockley[56] has shown that where the crystal structure of a semiconductor is interrupted new localised energy levels are created, termed surface states. Surface states are energy states effectively removed from the conduction band meaning their formation does not affect the total number of energy states within the semiconductor. The most significant impact of surface states is that they can remove and trap free carriers from the bulk crystal until the Fermi level at the surface and in the bulk have reached equilibrium. The location of surface states in relation to the Fermi level of the bulk material determines whether they trap electron or hole carriers. Surface states with

energy exceeding that of the Fermi level trap hole carriers while surface states with energy below that of the Fermi level trap electron carriers. Trapping of free carriers at the surface produces a bound electrostatic charge. After the formation of a surface state the semiconductor as a whole is known to remain electrically neutral. This is explained by the action of depolarisation fields inside the semiconductor compensating the potential by drawing free carriers of opposite charge to the interface. As a result regions of increased carrier density are formed termed space charge regions (SCR). When a positive surface potential draws electrons to the interface the SCR is termed an accumulation region. The increase in electron density causes a conceptual downward bending of the band potentials of the semiconductor. When a negative surface potential draws hole carriers to the surface the SCR is termed a depletion region. The low electron density produces a conceptual upward bending of the bands potentials (Figure 2.11).

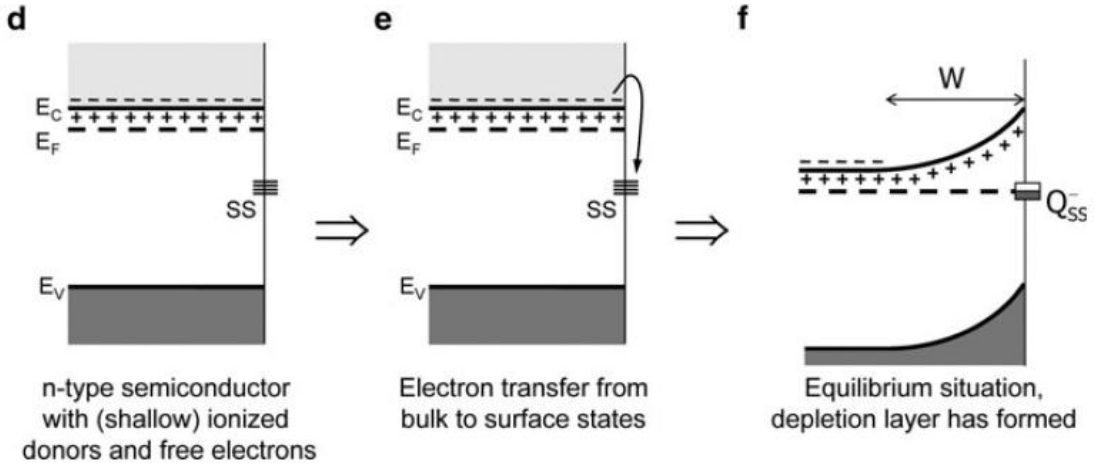

Figure 2.11 A simplified scheme showing the formation of a SCR at the surface of a metal oxide. Surface states form below the Fermi level causing the trapping of conduction band electrons and formation of a depletion region (Source ref. 57)

2.2.5 Semiconductor-metal interfaces

The work function is the minimum energy required to remove an electron to a point immediately outside a solid material with a band gap. The work function

can be calculated as the difference between the Fermi energy (Ef) and the vacuum energy level (Eo). If the work function of a metal (ϕm) and semiconductor (ϕs) are not equal then when they are placed in contact electrons flow from the solid with the lower work function until an equilibrium is reached[58]. The Schottky barrier height (ϕb) is the potential barrier that electrons must overcome in order to flow from one material to the other. For an n-type semiconductor the Schottky barrier height is calculated using Equation 2.1.

$$\boldsymbol{\phi b} = \boldsymbol{\phi m} - \boldsymbol{\chi} \qquad (2.1)$$

$\boldsymbol{\phi b}$ is the Schottky barrier height in eV, $\boldsymbol{\phi m}$ is the work function of the metal in eV and $\boldsymbol{\chi}$ is the electron affinity of the semiconductor in eV.

For a p-type semiconductor the Schottky barrier height is given by Equation 2.2.

$$\boldsymbol{\phi b} = \mathbf{E_g} - (\boldsymbol{\phi m} - \boldsymbol{\chi}) \qquad (2.2)$$

$\boldsymbol{\phi b}$ is the Schottky barrier height in eV, $\boldsymbol{\phi m}$ is the work function of the metal in eV, $\boldsymbol{\chi}$ is the electron affinity of the semiconductor in eV and $\mathbf{E_g}$ is the semiconductor band gap in eV.

When the Schottky barrier height is negative an Ohmic contact is formed causing electrons to flow from the metal to the semiconductor. If the Schottky barrier height is positive the contact is described as being rectifying and electrons are transferred from the semiconductor to the metal. Transfer of electrons from the semiconductor to the metal creates a depletion region and upward band bending in the semiconductor (Figure 2.12).

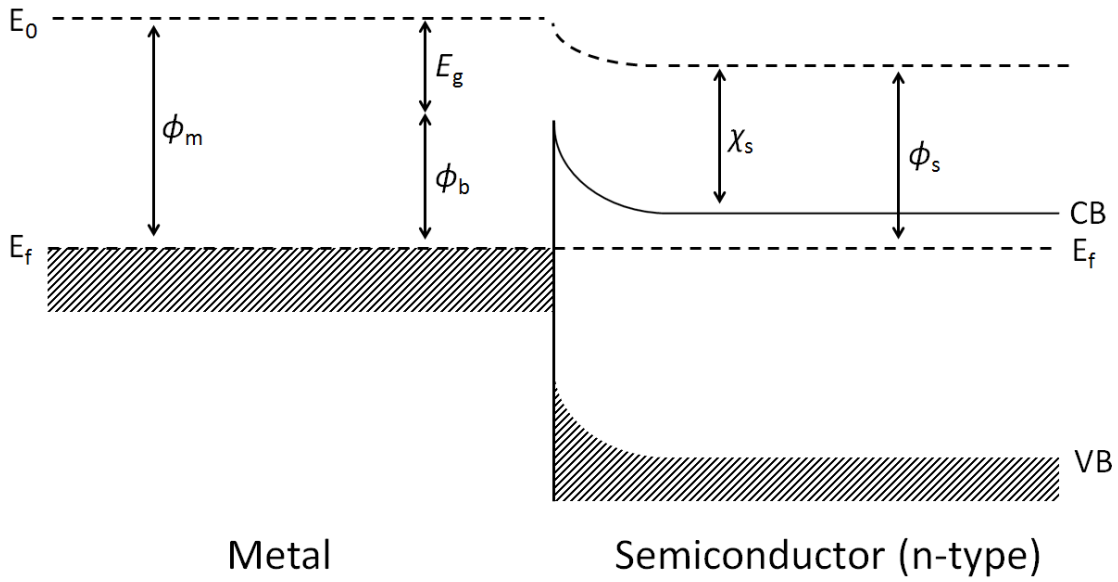

Figure 2.12 A Schottky barrier formed between an n-type semiconductor and metal (Reproduced from ref. 13)

2.2.6 Semiconductor properties of ferroelectrics

Traditionally ferroelectric materials have been regarded as insulators[25]. More recently investigations by various groups have shown the majority of perovskite and non-perovskite ferroelectrics can be considered as wide band gap semiconductors in which the spontaneous polarisation modifies the electronic properties[17]. Lead based ferroelectric such as lead zirconate titanate (PZT) have been shown to form rectifying Schottky contacts with electrode metals e.g. platinum, a property associated with semiconductor materials[59; 60]. The ferroelectric and semiconductor properties of PZT films have also been investigated through current-voltage and capacitance-voltage analysis[61; 62]. Application of a DC voltage across a PZT thin film contacted by metal electrodes is reported to cause the semiconductor properties of PZT to dominate over its ferroelectric properties[63]. The space charge region was calculated to widen from approximately half the thickness of the film to almost the entire thickness of the film, diminishing the films ferroelectric character e.g. the remnant polarisation. Under super band gap illumination ferroelectric materials have also been found to follow basic semiconductor theory, producing

a state of disequilibrium due to formation of photogenerated electron-hole pairs[64; 65]. It has been demonstrated that this allows ferroelectric materials to act as photocatalysts to drive reactions at the surface as will be discussed in detail in Section 2.4.6. Movement of excited charge carriers inside ferroelectric material to screen the surface charge also produces band bending that is analogous to that produced by surface states in semiconductor materials.

2.2.6.1 Band bending at ferroelectric surfaces

The charge at ferroelectric surfaces (σ) can be expressed as shown in Equation 2.3.

$$\boldsymbol{\sigma} = \vec{\mathbf{P}}.\hat{\mathbf{n}} \qquad (2.3)$$

σ is the surface charge in μC cm^{-2}, $\vec{P}$ is the polarisation vector in μC cm^{-2} and $\hat{n}$ is the unit vector normal to the surface.

The electrostatic properties of a ferroelectric surface can be described by the charge formed by the polarisation P and the screening of the charge by the depolarisation field –ρ. Four scenarios are possible[66]-

1. The surface charge is completely unscreened, -ρ = 0
2. The surface is partially screened, P > -ρ
3. The surface charge is completely screened, P = -ρ
4. The surface charge is over screened P < -ρ

The depolarising fields screen the surface potential through driving movement of mobile charged species. External screening occurs when ions or polar molecules are drawn to the ferroelectric surface and adsorbed into the double layer, a structure formed at the interface of a solid when placed in a liquid that is discussed in detail in section 2.3. Internal screening takes place when electron or hole charge carriers are driven to the interface. A totally unscreened surface charge is energetically unfavourable. This means that ferroelectrics only tend toward this scenario when under high vacuum as few species are available to

externally screen the surface charge. Over screening in which charged species more than compensate the surface potential is unusual under ambient conditions and only observed in specific circumstances e.g. when an external coercive field is applied to a ferroelectric. Typically ferroelectric surfaces are, therefore, either partially or completely screened. The ratio between external and internal screening of a surface is dependent upon the number of non-equilibrium carriers in the material produced by super band gap photons, thermal excitation or surface defects. In materials such as PZT reported to have a large numbers of surface defects the surface charge is largely internally screened by electrons or holes[17]. Materials such as lithium niobate contain a comparatively small number of defects near the interface[67] and so the surface potential is instead predominantly externally screened by charged molecules or ions. Internal screening of the surface charge causes an accumulation region to form at positively charged surfaces and a depletion region to form at negatively charged surfaces. This produces upward band bending at the surface of C- domains and downward band bending at C+ domains (Figure 2.13).

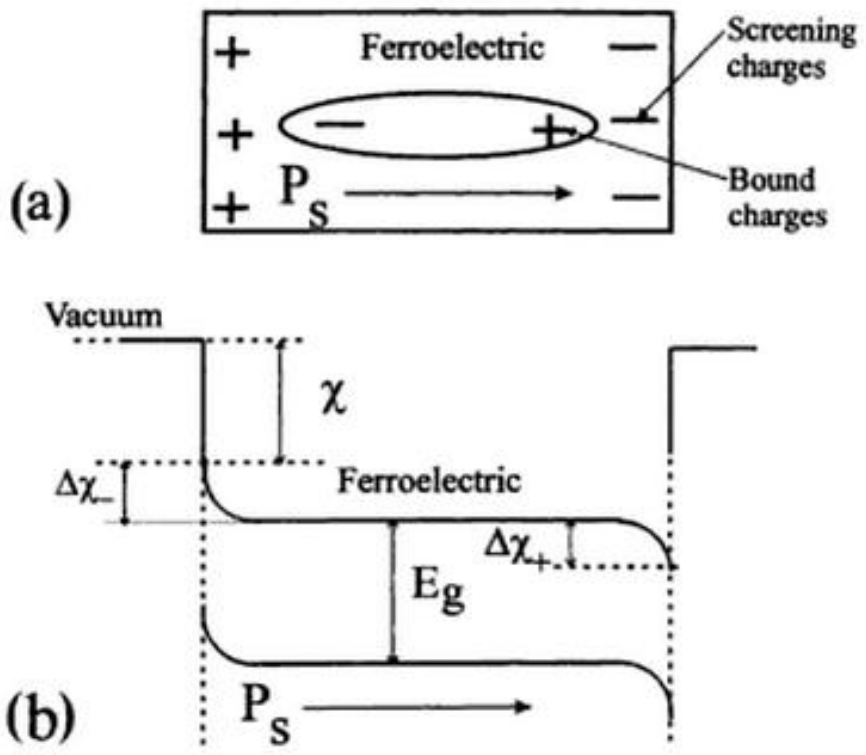

Figure 2.13 Asymmetric band bending in a ferroelectric material (a) the separation of charges by the internal depolarisation fields (b) band bending at C+ domains and C- domains(Source ref. 68)

2.3 The electrical double layer

2.3.1 The Gouy-Chapman-Stern model

The electrical double layer is a structure formed at the interface between a solid object and a surrounding solution or gas. A model of this phenomenon was first proposed by Helmholtz in 1879 that was derived mathematically by envisaging the solid surface as a capacitor[69]. It was suggested that when a solid is surrounded by a liquid or gas that locally charged sites at the surface are compensated by drawing a monoatomic layer of oppositely charged species to the interface. These species become chemically and rigidly bound at the solids surface. In this model the potential of the solid is completely screened by the

single atomic layer resulting in no electrostatic interactions between the surface and the bulk solution (Figure 2.14).

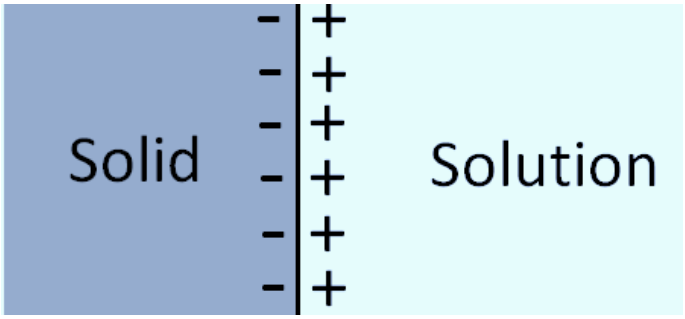

Figure 2.14 A scheme showing the Helmholtz model of the interface between a negatively charged solid and solution containing positive ions

The concept of the double layer was further developed by Gouy and Chapman through their theory put forward in 1917[69]. They proposed that rather than a single atomic layer compensating the surface charge that the thermal motion of ions in solution causes counter ions to form a diffuse layer that screens the surface, termed the Gouy-Chapman layer (Figure 2.15).

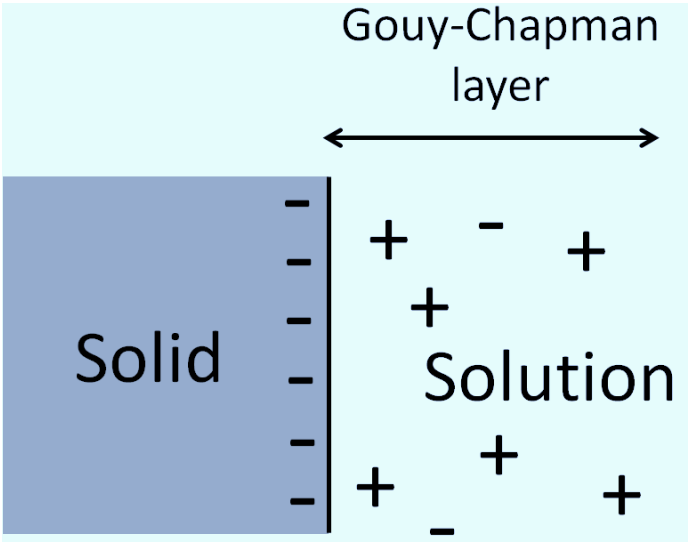

Figure 2.15 A scheme showing the Gouy-Chapman model of the interface between a negatively charged solid and solution containing positive ions

The mathematical basis for the Gouy-Chapman model is the Poisson-Boltzmann equation, a differential equation that describes the electrostatic interactions of molecules in an ionic solution (Equation 2.4). The Poisson-

Boltzmann equation can be used to produce an approximation of the potential change in the diffuse layer with respect to the distribution of charge. Solving the Poisson-Boltzmann equation for complex systems to give a numeric answer requires the use of computation.

$$\nabla^2\varphi = \frac{c_0 e}{\varepsilon\varepsilon_0}\left(e^{\frac{e\varphi(x,y,z)}{k_B T}} - e^{-\frac{e\omega(x,y,z)}{k_B T}}\right) \qquad (2.4)$$

φ is the potential, k_B is the Boltzmann constant, T is the temperature, c_0 is the concentration of ions in solution in Mol dm^{-3}, ε is the relative permittivity and ε_0 is the vacuum permittivity.

In the Gouy-Chapman layer the potential of the solids surface decreases exponentially with distance in to the solution. The Debye length describes the length over which the potential fully decays[70]. This property is reciprocally proportional to the square root of the concentration of ions in solution as shown in Equation 2.5.

$$\lambda_D = \sqrt{\frac{\varepsilon\varepsilon_0 k_B T}{2c_0 e^2}} \qquad (2.5)$$

Where λ_D is the Debye length in meters.

After the Gouy-Chapman model was proposed it was shown that when considering solid surfaces with a high potential this model breaks down. To resolve this issue a further adaption of the double layer model was proposed in 1924 by Stern[71] that combined concepts of both the Gouy-Chapman and Helmholtz models. The Gouy-Chapman-Stern model suggested an immobile compact monolayer of opposite charged atoms forms at the surface called the inner Helmholtz plane (Figure 2.16). Following this, a second immobile layer of solvated ions of opposite charge forms termed the outer Helmholtz layer. Together the inner and outer Helmholtz layers are referred to as the Stern layer or Helmholtz layer (Figure 2.16). Beyond the Stern layer it was proposed that a diffuse region formed as suggested by the Gouy-Chapman model (Figure 2.16).

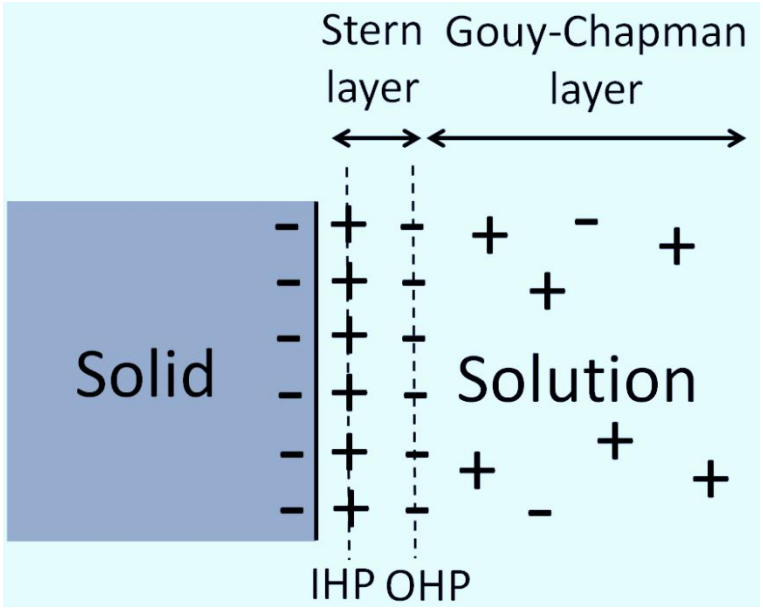

Figure 2.16 A scheme showing the Gouy-Chapman-Stern model of the interface between a negatively charged solid and a solution containing positive ions. The inner Helmholtz plane (IHP) is a line drawn through the middle of species adsorbed in the inner Helmholtz layer and the outer Helmholtz plane (OHP) is a line drawn through the middle of species adsorbed in the outer Helmholtz layer.

The potential at the point where the Stern layer ends and the diffuse layer begins is termed the zeta potential (ψδ). The slipping plane describes the boundary beyond which, when the solid moves, species in the double layer do not move with the surface and instead remain in the bulk solution.

2.3.2 The metal oxide-liquid interface

At the surface of a metal oxide in an aqueous solution (or in moist air) desorption and adsorption of water molecules takes place continuously. It is generally considered that the surface becomes covered by hydroxyl species at metal sites formed by chemisorption of water molecules[57; 72]. The hydroxyl groups (OH) can dissociatively form positive (H^+) or negative species (OH^-) as shown in Equations 2.6 and 2.7.

$$\mathbf{M-OH} \leftrightarrow \mathbf{M-O^-} + \mathbf{H^+(aq)} \qquad (2.6)$$

$$\mathbf{M-OH} + \mathbf{H^+(aq)} \leftrightarrow \mathbf{M-OH_2^+} \qquad (2.7)$$

A dynamic equilibrium of hydroxyl species at the metal oxide surface is reached which determines the net charge of the inner Helmholtz layer. The point of zero charge refers to the pH value of the surrounding solution at which the inner Helmholtz layer at the interface of the metal oxide has a net charge of zero. At pH values above the point of zero charge the inner Helmholtz layer is negatively charged and at pH values below the point of zero charge the inner Helmholtz layer is positively charged (Figure 2.17). The point of zero charge of a metal oxide depends upon the stoichiometry of the material at the interface and the electronic characteristics of the metal-oxygen bonds that are formed at its surface.

$$\underset{\text{decreasing pH}}{\longleftarrow} \quad \mathrm{M{-}OH_2^+ \rightleftharpoons M{-}OH \rightleftharpoons M{-}O^- + H^+} \quad \underset{\text{increasing pH}}{\longrightarrow}$$

Figure 2.17 The effect of pH upon formation of positive and negative hydroxyl species at a metal oxides surface (Source ref. 72)

The isoelectric point is a related property to the point of zero charge and describes the pH value at which particles of a metal oxide suspended in a solution do not move under application of an external electric field. When specific adsorption of charged species does not occur in the metal oxide double layer then the isoelectric point and point of zero charge are equal to each other. If cationic species are adsorbed in the inner Helmholtz layer then the isoelectric point is increased compared to the point of zero charge. If anionic species are adsorbed in the inner Helmholtz layer the isoelectric point is decreased compared the point of zero charge.

A scheme showing the interface between a metal oxide semiconductor and an electrolyte is shown in Figure 2.18. Hydroxide ions are specifically adsorbed in

the inner Helmholtz layer to screen the positive surface charge produced by electrons trapped by surface states. Ionic species outside the inner Helmholtz layer are solvated due to the high dipole moment of water molecules. In the outer Helmholtz layer solvated protons are adsorbed by the negative inner Helmholtz layer. Solvation of ions outside the inner Helmholtz layer are preventing them from approaching the surface closer that the diameter of that of a water molecule.

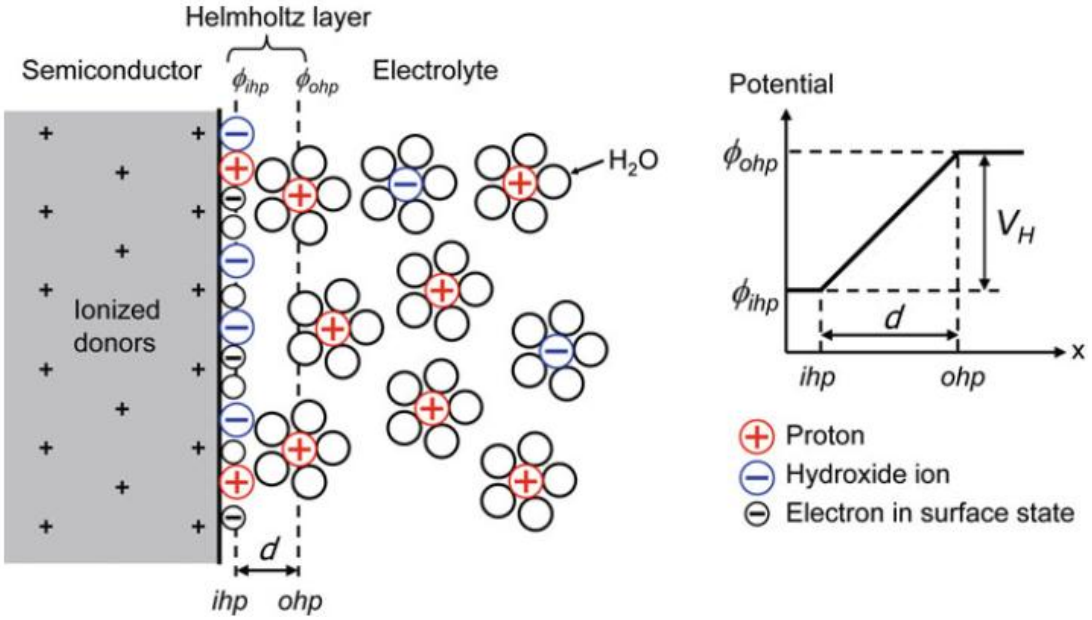

Figure 2.18 A scheme showing the interface between a metal oxide semiconductor and an aqueous solution (Source ref. 57)

2.3.3 Interactions between charged surfaces and adsorbed species

As discussed in Section 2.1.3 the polarisation in ferroelectric materials produces an opposite surface charge at C+ and C- domains. In the literature, investigations have demonstrated that the manner in which molecules are physically and chemically adsorbed at the surface of ferroelectric materials is dependent upon the orientation of the polarisation. Yun et al[73] used temperature programmed desorption analysis (TPD) to investigate adsorption of polar acetic acid, 2-propoanol and non-polar dodecane adsorbed at the surface of poled

lithium niobate. The quantity of polar molecules adsorbed at the C+ domain surface was found to be higher than non-polar dodecane molecules. It was also observed that the quantity of 2-propanol molecules adsorbed was different at C+ and C- domains (Figure 2.19).

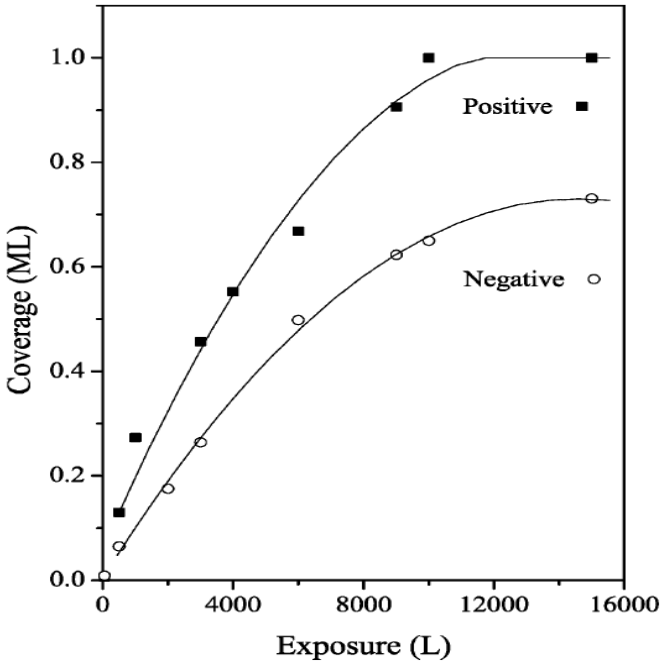

Figure 2.19 Uptake of 2-propanol at the C+ and C- domain of lithium niobate as a function of exposure (Source ref. 73)

The authors proposed this to be a result of the mode of physical adsorption of the molecules being affected by electrostatic interactions with the surface charge[73]. Building on this work Bonnell et al[74] carried out in situ TPD investigation of the adsorption of ethanol at the surface of barium titanate thin films. The change was monitored as the surface was polarised positively or negatively in the C axis or the film was depolarised by heating above the Curie point (Figure 2.20). The adsorption of ethanol was found to be higher when the surface was poled. It was also shown that adsorption was greater when the surface was poled to produce a C+ face rather than a C- face. The use of in situ analysis provided unequivocal evidence that the observed changes were a result of electrostatic interactions between the surface charge and the ethanol molecules.

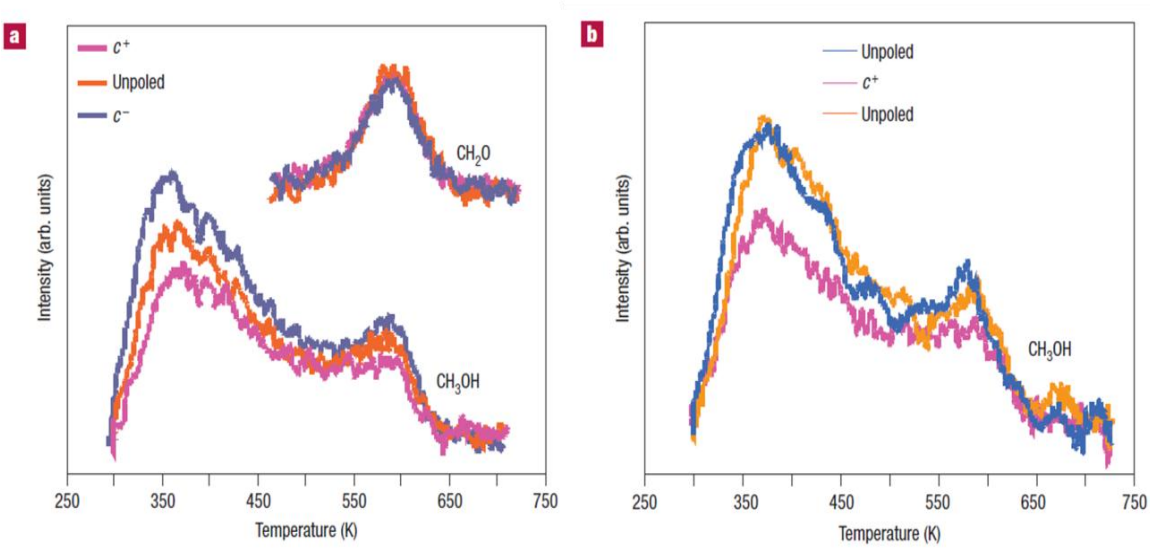

Figure 2.20 TPD spectra showing retention of ethanol at the surface of a barium titanate thin film as a function of the polarisation. a) shows runs in which the order of polarisation was C+, unpolarised, C-. b) shows runs where the order of polarisation was unpolarised, C+, unpolarised (Source ref. 74)

The effect of the surface charge upon chemisorption of ethanol molecules at the surface of barium titanate thin films has also been demonstrated using TPD analysis[75]. Ethanol molecules were shown to react to form ethylene and acetaldehyde when dissociatively chemisorbed at the surface. At doses of ethanol below those required to produce saturation surface coverage of the barium titanate film it was shown the yield of ethylene and acetaldehyde was impacted by the orientation of the polarisation (Figure 2.21). The quantity of products formed was greater at poled surfaces than the unpolarised surface. More products were formed when at the C+ domain than the C- domain.

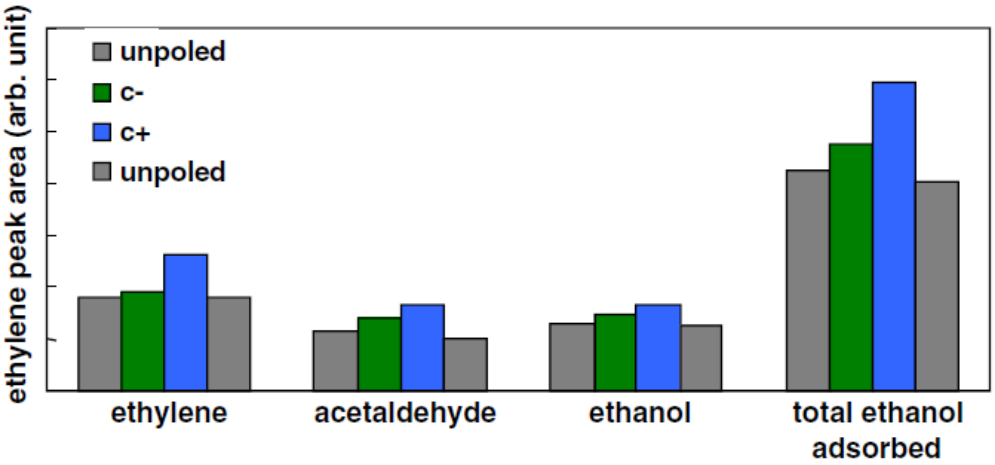

Figure 2.21 The peak areas of gas desorption from TPD spectra of ethanol adsorbed at the surface of barium titanate thin films as a function of the polarisation (Source ref. 75)

Ramos-Moore et al studied the effect of the adsorption of carbon dioxide gas upon the remnant polarisation of niobium doped lead zirconate titanate (PNZT) thin films (Figure 2.22). Hysteresis measurements were carried out before and after the samples were exposed to carbon dioxide gas at room temperature. Where no voltage was applied across the sample the polarisation was found to be unaffected by gas adsorption. Application of a positive or negative 9.9 V field to the back electrode was found to shift the remnant polarisation by -0.52 μC cm^{-2} or by +0.58 μC cm^{-2} respectively after adsorption of carbon dioxide gas (Figure 2.22).

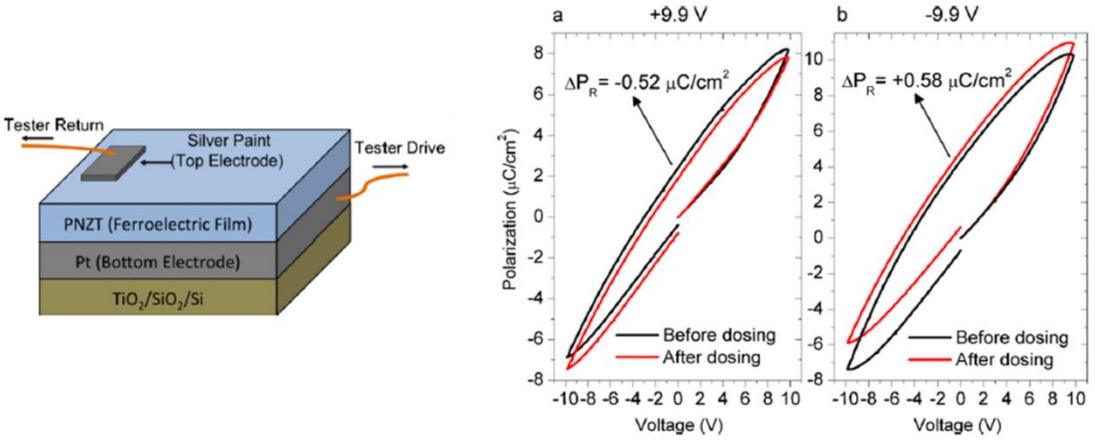

Figure 2.22 PNZT sample and the hysteresis loops before and after exposure to carbon dioxide gas (Source ref. 76)

The change in the remnant polarisation was explained by the presence of carbon dioxide molecules at the surface producing a depolarisation field. The morphology of carbon dioxide molecules is linear under ambient conditions. Investigation of the morphology of carbon dioxide molecules adsorbed at the surface of magnesium oxide has shown that molecules can be adsorbed weakly through end on interactions with oxygen atoms or the molecules can lay flat on the surface with oxygen atoms coordinated with adjacent metal sites[77; 78]. When molecules are adsorbed lying flat on the surface it has been predicted the symmetry decrease as a result of interactions with the surface charge resulting in bending in the molecules bond angles. It was proposed in the case of the PZNT samples that carbon dioxide molecules were adsorbed as polar molecules with the orientation determined by the charge at the surface (Figure 2.23). After the applied voltage had been removed from the samples of PZNT the change in the remnant polarisation was stable. This indicated that the carbon dioxide molecules responsible for producing the depolarising field had remained chemisorbed or physisorbed at the surface.

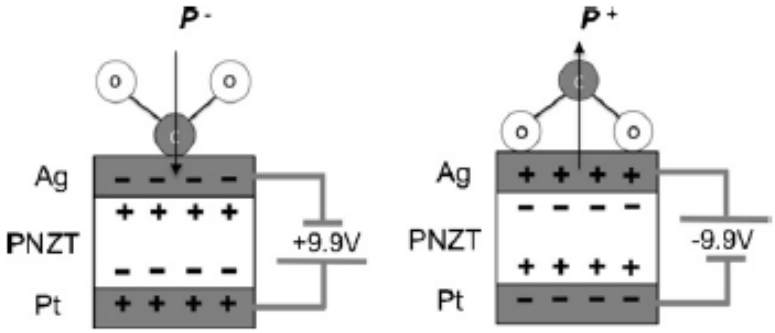

Figure 2.23 Orientation of carbon dioxide molecules adsorbed at the surface of the PZNT sample (Source ref. 76)

The preferential adsorption of polar or ionic species at the surface of ferroelectric materials has been demonstrated through immersion of samples in aqueous solutions or suspensions. Periodically poled lithium niobate was used to adsorb polystyrene particles with a diameter of 100 nm from an aqueous suspension[79]. The polystyrene particles were negatively charged due to their functionalization through addition of a carboxyl group at the surface. Atomic force microscopy revealed the polystyrene particles were preferentially adsorbed at the C+ domains of the lithium niobate samples. Deposition decreased sharply at the 180^{o} domain wall (Figure 2.24). The preferential adsorption was proposed to be explained by the surface charge driving electrostatic interactions between the polystyrene particles, attraction at positive domains and repulsion at C- domains.

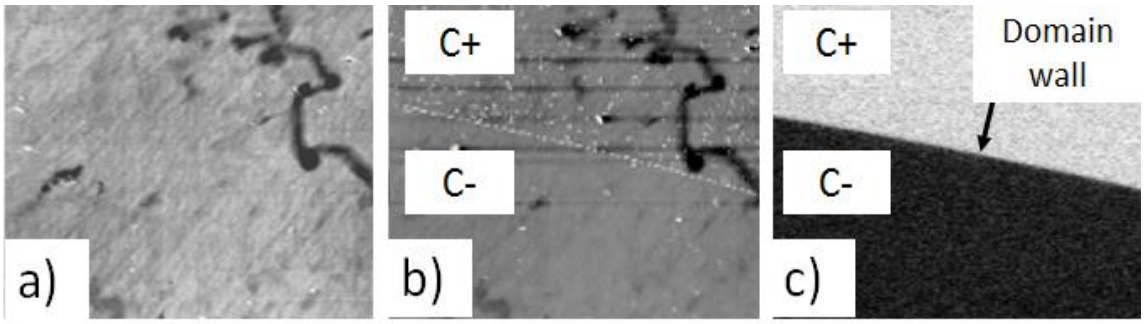

Figure 2.24 a) a non-contact atomic force microscopy (AFM) image showing the surface of a sample of periodically poled lithium niobate prior to use in experiments b) a non-contact AFM image showing the same area of the sample's surface after being dipped in an aqueous suspension of polystyrene microspheres. The polystyrene microspheres appear as white deposits on the samples surface located mainly on the C+ face. c) shows a corresponding piezo force microscopy phase image of the lithium niobate sample's surface showing the domain structure (Source ref. 79)

A similar study investigated adsorption of d-cysteine molecules in aqueous solution at the surface of periodically poled lithium niobate[80]. Analysis was carried out using infrared spectra microscopy (Figure 2.25). The d-cysteine molecules were shown to be preferentially adsorbed at C+ domains of the lithium niobate sample. The authors proposed this to be a result of a negative net charge of d-cysteine molecules resulting in increased electrostatic attraction at C+ domains and repulsion at C- domains.

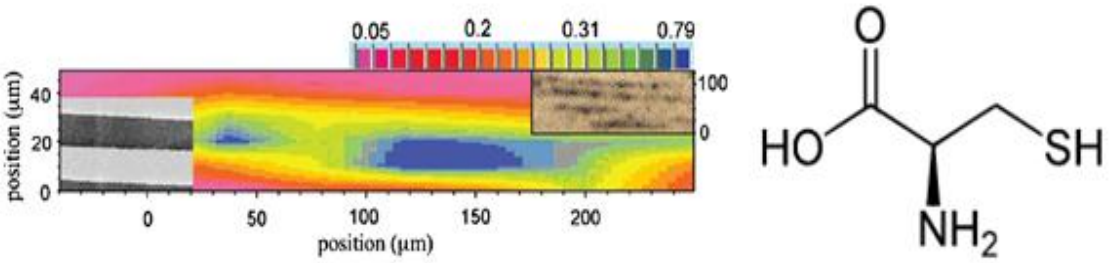

Figure 2.25 Spatial locations of molecules of d-cysteine (shown on the right) adsorbed at the surface of periodically poled lithium niobate. The dark areas on the left inset show C+ domains. Infrared microspectroscopy shows areas of high adsorption in blue and low adsorption in red (Source ref. 80)

Poled PZT thin films have also been used to adsorb tobacco mosaic virus particles dissolved in sodium chloride solution[81]. The pH of the solution caused the virus molecules to have a positive charge. In contrast to the studies using periodically poled lithium niobate the virus was found to be adsorbed preferentially at like charged C+ domains and repelled from the surface at oppositely charged C- domains (Figure 2.26). The authors proposed this observation to be a result of a Stern layer forming of sodium and chloride ions at the surface of PZT. The virus molecules were retained as solvated ions in the outer Helmholtz layer by the negative charged inner Helmholtz layer at C+ domains and repelled by the positively charged inner Helmholtz layer at C- domains.

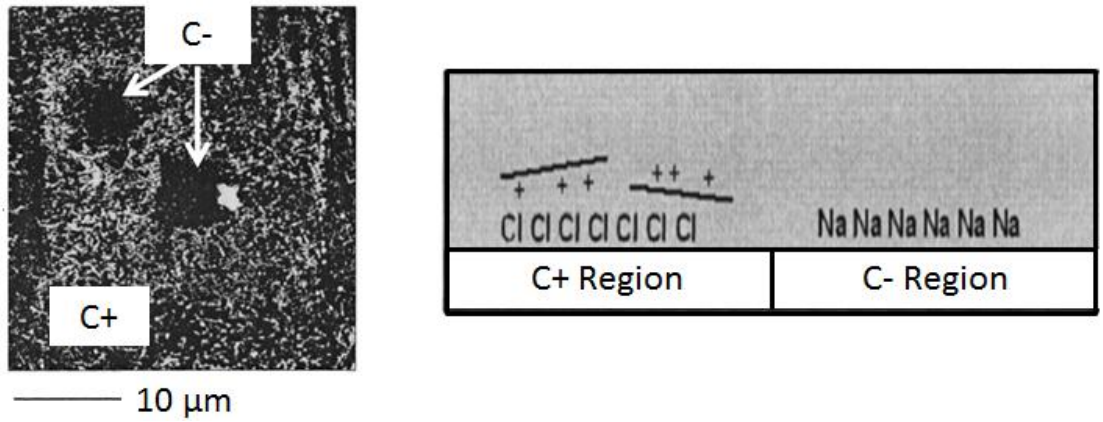

Figure 2.26 Shown on the left is a tapping mode scanning probe microscopy image of the surface of a PZT thin film sample after a solution of tobacco mosaic virus molecules dissolved in aqueous sodium chloride was placed on the films surface and allowed to dry. The white contrast in the image shows the distribution of virus molecules. Prior to use in experiments the PZT filmed was poled to produce square negatively charged (C-) regions with the rest of the surface charged positively (C+). A low concentration of viruses (1 particle per µm2) was found in the regions that had a negative spontaneous polarisation. On the positively poled areas of the film there is an almost a fully packed layer of virus particles. The image on the right shows a possible structure of the double layer formed at the C+ and C- faces of the PZT film. At the C+ face positively charged virus molecules are adsorbed through electrostatic interactions with negative chlorine ions adsorbed in the Stern layer. At the C- face positive sodium ions adsorbed in the Stern layer repel the positively charged virus molecules (Source ref. 81)

Monte-Carlo methods are a class of computational algorithms that use repeated random sampling to produce a result and are often used to simulate complex systems with many degrees of freedom such as fluids. The structure of the interfacial double formed at polar surfaces has been investigated through the use of Monte-Carlo simulations. In one study a modified Poisson–Boltzmann theory for 1:1 electrolytes was used imagining fictitious image charges within an electrode that mimic a surface polarisation charge[82]. The double layer was modelled as a Gouy-Chapman diffuse layer. The capacitance at the surface was calculated as a function of reduced density (p*), the dimensionless

parameter describing the density of ionic charges in an electrolyte (Equation 2.8).

$$p^* = \sum_i p_i d^3 \qquad (2.8)$$

p^* is the reduced density and p_i is the mean number density of ions of species i.

When an electrolyte with a low reduced density was simulated the capacitance of the double layer was shown to be lowest at the point of zero charge (Figure 2.27). As the surface charge increased the double layer capacitance also increased up to a maximum value. When an electrolyte with high reduced density was simulated the capacitance of the double layer was greatest at the point of zero charge. Increasing the surface charge was found to cause the double layer capacitance to decrease.

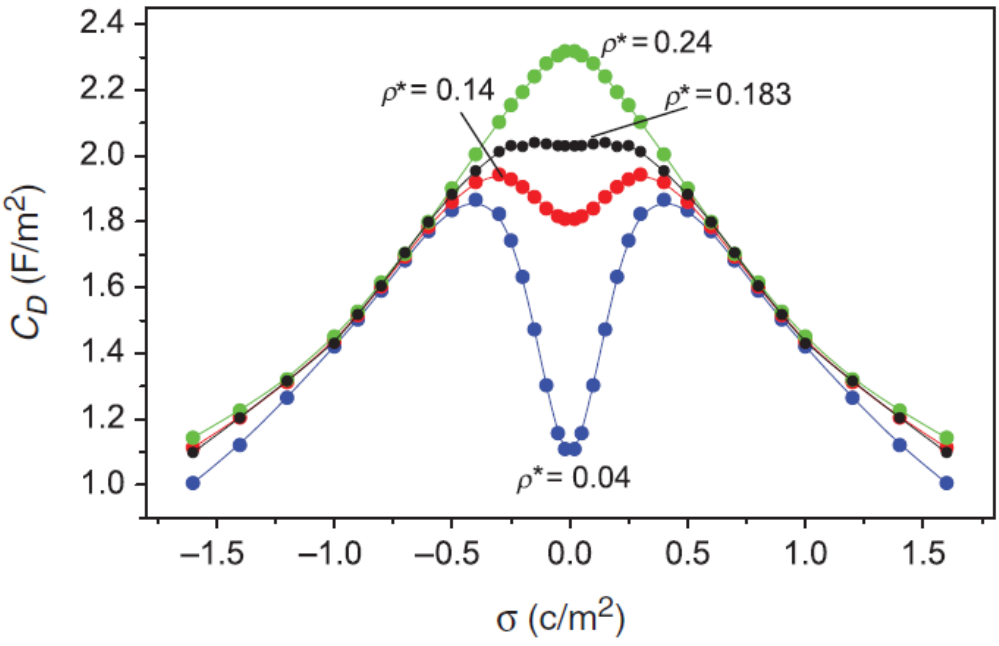

Figure 2.27 The Monte Carlo differential capacitance of a polar surface calculated using different values of reduced density (p^*) (Source ref. 82)

Another study used Monte-Carlo simulations of a 1:1 electrolyte to investigate the effect of altering the simulated surface charge upon the formation of the counter ion layer[83]. The simulations showed that as the surface charge

increases the number of species in the counter ion layer also increases (Figure 2.28).

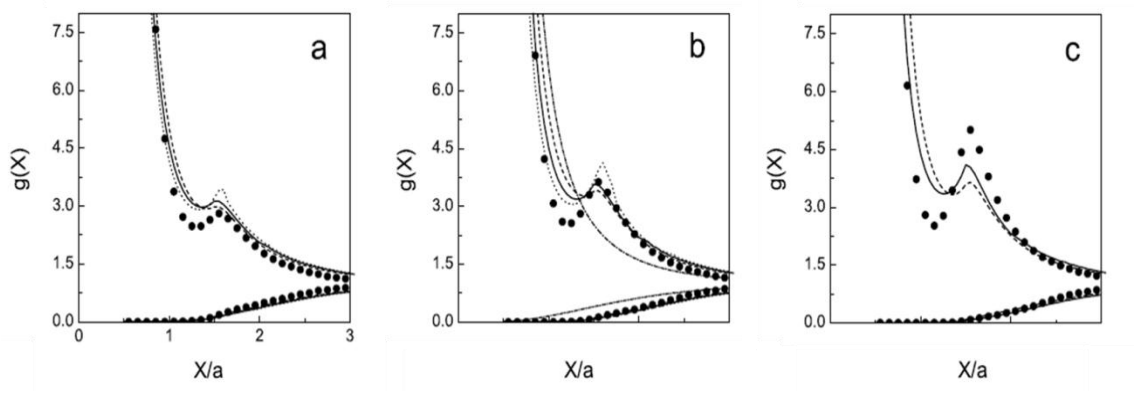

Figure 2.28 The wall-ion singlet distribution function for a planar double layer containing a 1:1 electrolyte at 298.15 K. The surface is simulated to have a charge of a) 60 μC cm-2 b) 70 μC cm-2 or c) 80 μC cm-2. The filled black circles show Monte Carlo simulations. The other lines correspond to modified Gouy-Chapman-Stern calculations (Source ref. 83)

2.4 Photocatalytic reactions

2.4.1 Background

Titanium dioxide has been used as a white pigment in paints, fabrics and dyes during the past century. It has been observed that products containing titanium dioxide will flake, crack and degrade after prolonged exposure to sunlight[84]. Early investigation of this phenomenon in 1938 by Goodeve and Kitchener showed this effect to be dependent upon the wavelength of light[85]. It was found that titanium dioxide containing products only became unstable when exposed to light in the ultra violet region. A series of reports in 1956 published by Kato and Mashio studied the effect of illuminating of suspensions of titanium dioxide powder in organic solvents with UV light[86]. In the presence of titanium dioxide the solvents were converted into chemical products. The authors suggested this to be a result of titanium dioxide adsorbing super band gap light to excite electron-hole pairs. The excited carriers were then transferred to adsorbed

molecules to drive chemical reduction or oxidation reactions. This process was termed photocatalysis. Since, numerous reviews have discussed titanium dioxides photocatalytic properties[87-89] and reactions over titanium dioxide have been demonstrated to have applications in a range of areas e.g. destruction of bacteria and viruses[90; 91], odour control[92] and removal of oil spills[93]. Over the past 40 years two uses of photocatalysis have emerged as the most popular. The first is the photocatalytic generation of fuel stock. Honda and Fujishima showed in 1972 that single crystal rutile can be used as an electrode to produce hydrogen by splitting water in the presence of super band gap irradiation[2]. The desire for environmentally sustainable routes to energy production has led to a wide range of semiconductor materials and conditions being investigated as methods of photocatalytically producing fuel stock e.g. water splitting to produce hydrogen[4; 94-96] or photochemical conversion of carbon dioxide to form hydrocarbon products[3; 6; 97; 98]. The second application is the photocatalytic remediation of organic waste. Under ambient conditions semiconductors such as titanium dioxide generate reactive species through reactions with water and atmospheric oxygen[8]. These species are sufficiently reactive to fully mineralise a variety of organic pollutants such as dyes, aliphatic alcohols, aromatic carboxylic acids and halogenated alkanes and alkenes[1; 12]. This has led to photocatalysis being studied as potential solution to the environmental problems caused by waste production in industrialised nations[12].

2.4.2 Mechanisms of photocatalytic reactions

2.4.2.1 Heterogeneous photocatalysis

Photocatalytic reactions can be divided in to two main categories depending upon where the initial excitation by absorption of photons occurs. The first group of reactions are referred to as heterogeneous photocatalysis. These reactions take place after absorption of super band gap light excites electron-hole pairs in a semiconductor (Equation 1.1). A proportion of the excited carriers recombine in the bulk or at the interface releasing the absorbed light energy as unutilised heat. However, when carriers are formed within the SCR they are separated by

depolarisation fields[99]. The excited carriers can then be transferred to adsorbed species or species that become adsorbed at the surface to drive chemical reduction or oxidation reactions (Figure 2.29).

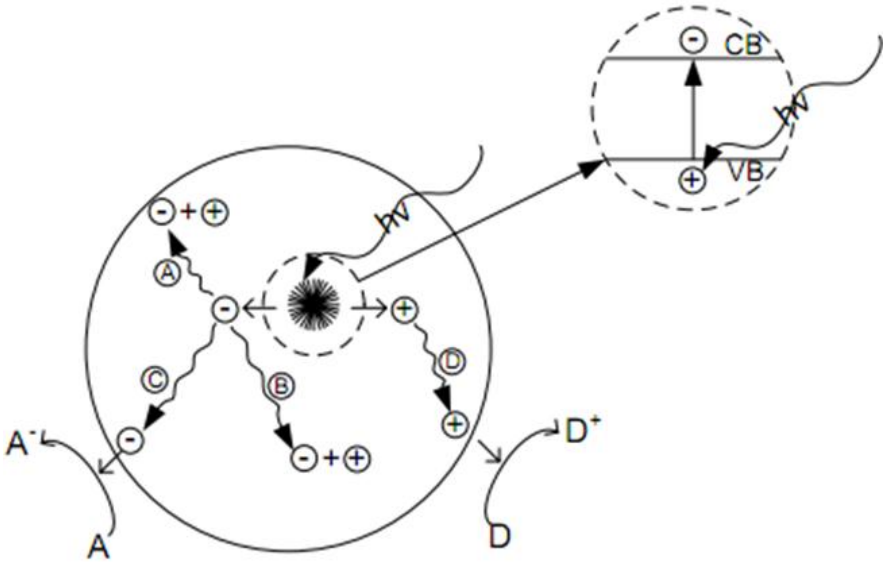

Figure 2.29 Scheme showing reactions at a photocatalysts surface, Ⓐ & Ⓑ shows recombination of excited carriers (electrons ⊖ & holes ⊕) at the interface or in the bulk material. Ⓒ shows transfer of electrons at the interface to drive reduction of adsorbed species (A to A^-) and Ⓓ shows transfer of holes at the interface to drive oxidation of adsorbed species (D to D+) (Source ref.13)

In heterogeneous photocatalysis reactants are mineralised by active oxygen species formed when ambient oxygen is reduced by excited electrons to form the superoxide anion radical ($O_2^{\cdot-}$) and water is oxidised by hole carriers to form the hydroxyl ion ($OH^{\cdot}$) (Figure 2.30). Adsorbed reactants can also be oxidised or reduced directly by the excited carriers.

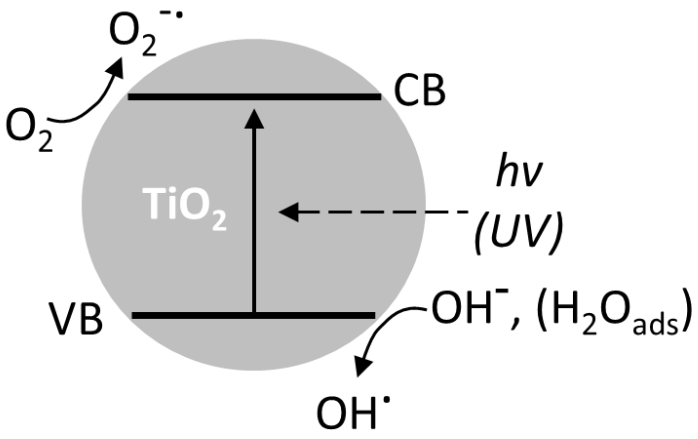

Figure 2.30 Photocatalytic reduction of oxygen and oxidation of water at the surface of titanium dioxide

A general scheme proposed for the mineralisation of organic pollutants by activated oxygen species over a titanium dioxide photocatalyst is shown in Figure 2.31.

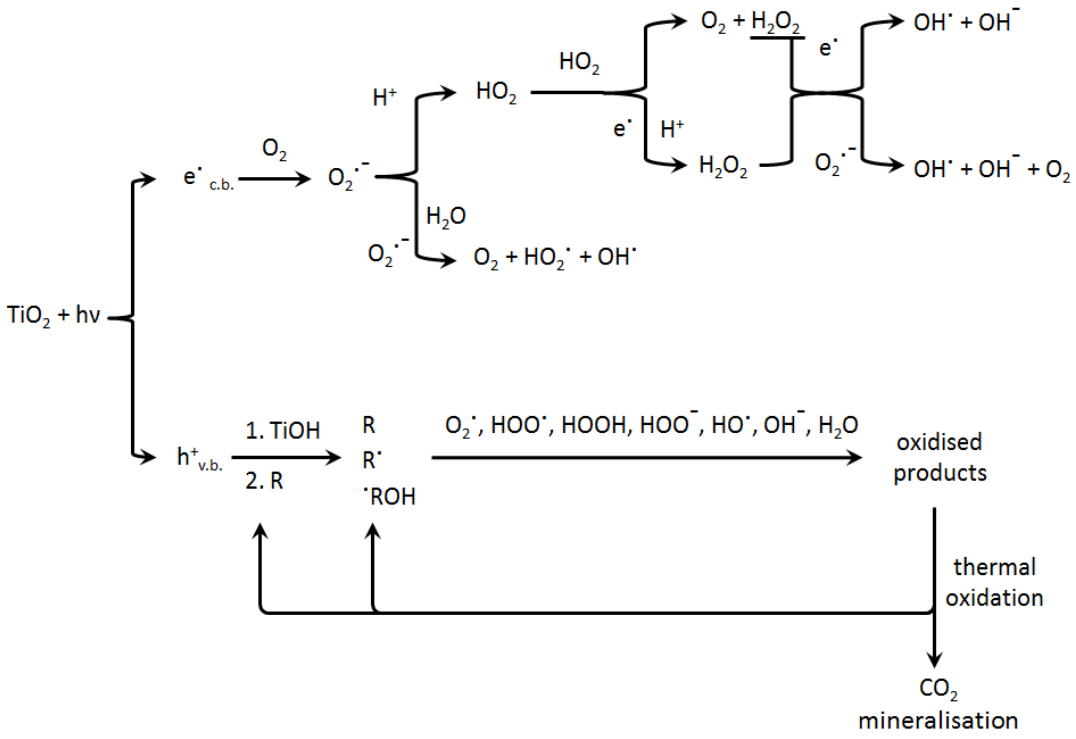

Figure 2.31 Secondary reactions of active oxygen species in photocatalytic reactions (Reproduced from ref.12)

2.4.2.2 Catalysed photoreactions

The second group of photocatalytic reactions are termed catalysed photoreactions[1]. In these processes the initial excitation by photons occurs in molecules adsorbed at the photocatalysts surface e.g. dye pollutants. The excited electrons in the adsorbate can be transferred to the conduction band of the photocatalyst. This oxidises the reactant and provides the photocatalyst with a source of conduction band electrons to drive reduction of oxygen to form the superoxide anion radical (Figure 2.32). Catalysed photoreactions can take place in addition to heterogeneous photocatalysis reactions or separately.

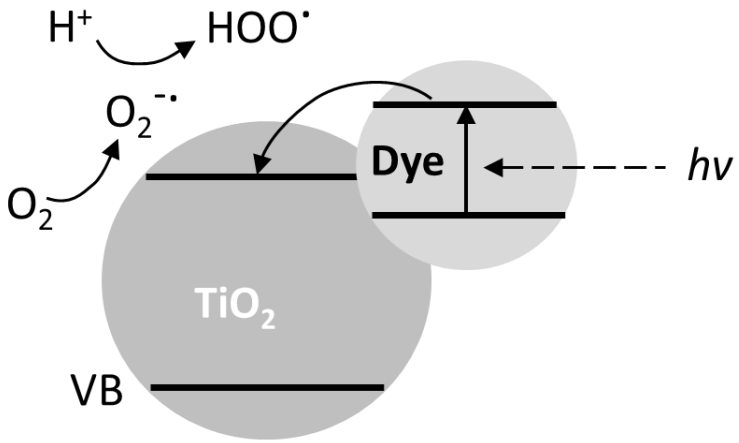

Figure 2.32 Excitation of electrons in a dye molecule adsorbed at the surface of a titanium dioxide photocatalyst. The excited electrons are transferred to the conduction band of titanium dioxide where they drive reduction of oxygen

2.4.3 Reactions over metal modified semiconductor systems

Semiconductor powders with noble metal nanoparticles e.g. silver or palladium, deposited at the surface are widely studied[100-103]. The resulting semiconductor-metal systems have been shown to drive many photocatalytic reactions e.g. degradation of organic pollutants, at increased rates[102; 104; 105]. The higher activity is proposed to be a result of two factors. Firstly, the metal forms a rectifying Schottky barrier with the semiconductor. Excited electron carriers can become trapped by the metal particles. This helps to supress the rate at which excited carriers undergo recombination at the interface of the photocatalyst (Figure 2.33).

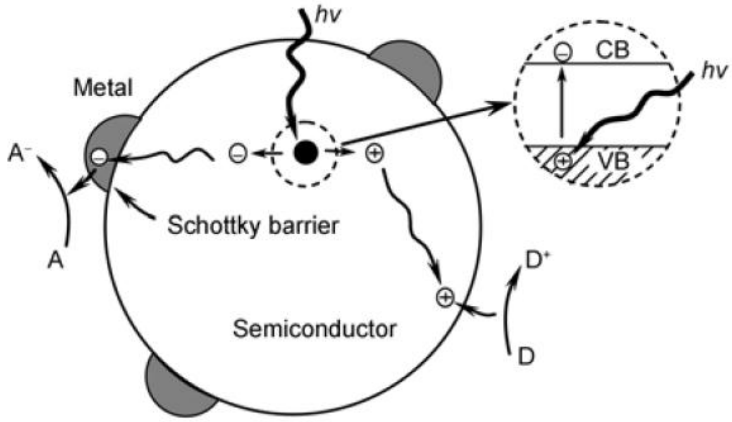

Figure 2.33 Heterogeneous photocatalysis at the surface of a metal modified semiconductor. A Schottky barrier is formed between the semiconductor and the metal particles. When carriers (electrons ⊖ & holes ⊕) are excited in the semiconductor by adsorption of super band gap light electrons are transferred from the semiconductor to the metal particles via the Schottky barrier. Trapping of electrons by the metal particles lowers the rate at which electron and hole carriers recombine in the semiconductor. Photo excited electrons trapped by the metal particles drive reduction of species adsorbed at the metal particles surface (A to A-). Hole carriers in the semiconductor migrate to interface and drive oxidation of adsorbed species (D to D+) (Source ref.106)

The second factor is the adsorption of visible light photons by metal nanoparticles. This excites a localised surface plasmon resonance (LSPR) i.e. photons interact with metal particles free conduction electrons causing collective excitation and oscillation inducing a strong enhancement of local electromagnetic fields[107]. Evidence has shown the enhanced field produced by the LSPR excites carriers in the semiconductor host material[108]. It is also suggested the greater oscillating electric field can increase the rate at which electrons are trapped by metal particles[103]. The loading of metal particles at the surface of semiconductors has been shown to have an optimal value beyond which increased loading reduces the activity of the semiconductor-metal system[102]. This is attributed to the negative potential of the metal particles attracting hole carriers toward them at high loadings (Figure 2.34). This causes the metal deposits to drive carrier recombination at the photocatalyst's surface[106].

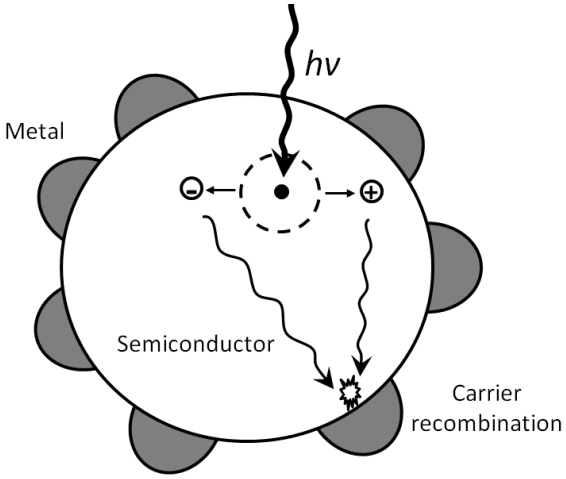

Figure 2.34 Scheme showing a semiconductor with a high density of metal particles deposited at the surface. The high loading of negatively charged metal particles causes the metal deposits to act as recombination centres, this increases the number of photo excited carriers which undergo recombination compared to in the unmodified semiconductor. Photo excited electrons (⊖) are transferred to the metal particles via the Schottky barrier and trapped. The metal particles act as recombination centres as positive hole carriers (⊕) are drawn toward the high loading of negatively charged metal particles at the surface and recombine with trapped electrons rather than migrating to the semiconductor interface to drive oxidation reactions (Reproduced from ref.106)

2.4.4 Interfacial carrier transfer

In order for a photocatalyst to transfer excited electron or hole carriers to an adsorbed species the reduction or oxidation potential must be inside of the photocatalysts band edges. Figure 2.35 shows the position of some of the redox couples typical of photocatalysis reactions in relation to the band edges of commonly used semiconductor photocatalysts. The energy levels of the valence and conduction bands of semiconductors are often given in relation to the vacuum level which describes a free and stationery electron with infinite energy. However, in electrochemistry redox couples potentials are quoted in relation to reference electrode scales such as the normal hydrogen electrode (NHE) which sets the reduction potential of hydrogen at 0 V[109]. Empirical models have shown

the vacuum level exists at approximately 4.5 eV above that of the reduction potential of hydrogen[84; 110]. This allows the vacuum level and the NHE to be related to each other (Figure 2.35).

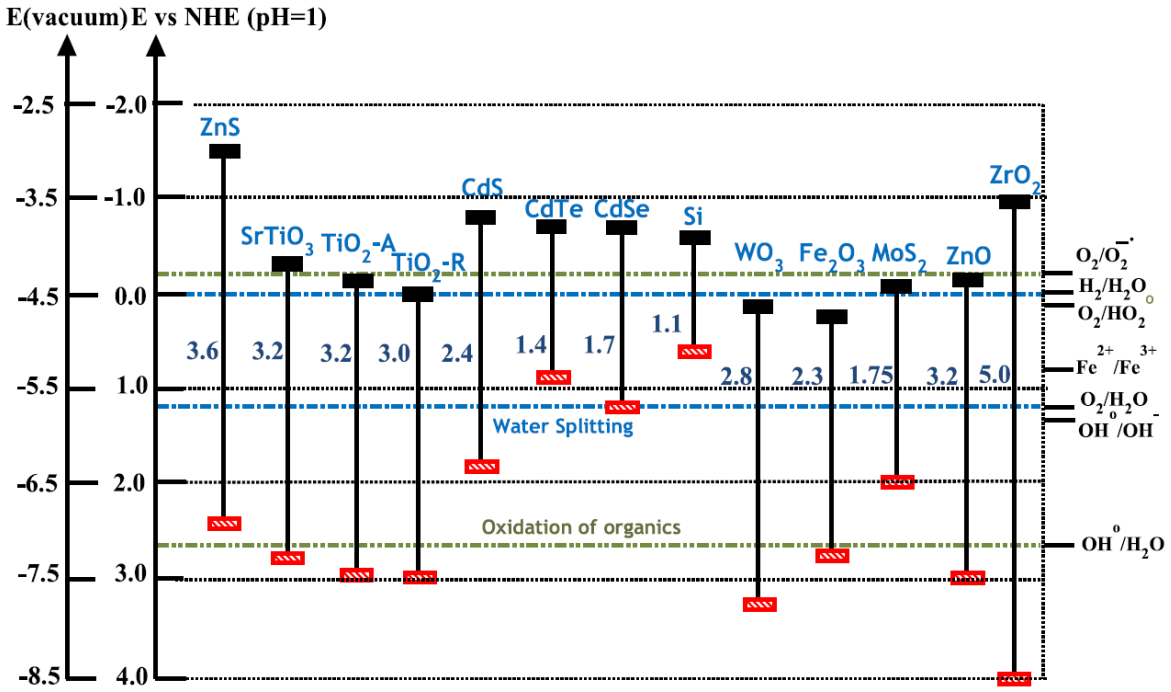

Figure 2.35 The conduction band edge (black), valence band edge (red) and band gap in eV of some typical semiconductors are shown. The positions are shown in relation to both the normal hydrogen electrode (NHE in V) and the vacuum level (vacuum in eV) as references. On the right hand side the standard potential of redox couples that form activated oxide species are shown. The scheme shows the ability of some typical semiconductors to photocatalytically produce activated oxide species. Photo excited carriers in a semiconductor can drive redox couples with a potential within the semiconductors band edges, couples with redox potentials outside the semiconductor band edges cannot be driven by photo excited carriers (Source ref.10)

2.4.5 Factors affecting photocatalytic reactions

The efficiency of the photocatalyst in converting adsorbed light energy into chemical energy is, generally speaking, dependent upon the number of

photogenerated species formed; the efficiency at which electron-hole pairs are separated; the rate of transfer of carriers to adsorbed species; and the rate of backward reactions occurring at the surface. Investigation of typical reaction conditions has shown that a variety of factors contribute to the rate of photocatalytic reactions. The intensity of light emitted with energy exceeding that of the photocatalysts band gap determines the rate of carrier formation. Reaction rates are typically proportional to the intensity of super band gap light[1]. The photocatalyst surface area plays an important role as it is proportional to the number of active sites at which reactants can be adsorbed for carrier transfer to occur. Investigation of titanium dioxide powders has shown a correlation between rate of reaction and the quantity of reactant adsorbed at active sites[12; 111]. The correlation between surface area and photocatalytic activity has been shown to only be relevant when comparing structurally related compounds[111]. High concentrations of reactant can increase adsorption at the surface of the photocatalyst. In some cases this can become detrimental to reaction rates. At high concentrations reactants sensitive to the UV spectrum can adsorb light that would otherwise excite carriers in the photocatalyst either in the bulk solution or in the double layer of the photocatalyst. A study of the degradation of dye acid orange 7 over titanium dioxide powder showed that reaction rate decreased as the initial concentration of the solution was increased. Adjusting the pH to decrease adsorption of dye ions in the double layer of the photocatalyst was found to cause the reaction rate to increase[112]. The pH of solutions has been found to not strongly affect the rate of photo catalytic reactions over semiconductor materials. Investigation of dye decolourisation reactions using range of pH 2-12 resulted in less than an order of magnitude difference in the rate over a titanium dioxide photocatalst[1]. Anions, cations or organics in solution can, by competing for excited carriers and active surface sites, alter the rate of reactions. If these species scavenge carriers driving the rate limiting step this can increase efficiency of reactions otherwise they can reduce the rate of reactions.

2.4.6 Photocatalytic reactions at ferroelectric surfaces

2.4.6.1 Spatially separated reduction and oxidation reactions

The polarisation in ferroelectrics produces an opposite charges at the surface of C+ and C- domains as discussed in section 2.1.3. Depolarisation fields acting to screen the charge at the surface cause photogenerated charge carriers to be separated and move in opposite directions. Electrons form an accumulation space charge region at C+ domains and hole carriers form a depletion space charge region at C- domains. As a result the location of photochemical oxidation and reduction sites are spatially distinct. This property has been demonstrated experimentally in work by Giocondi and Rohrer[21; 22; 113]. Photo reduction of silver ions (Equation 2.9) and the photo oxidation of lead ions (Equation 2.10) were used to characterise the surface reactivity of barium titanate thin films and bulk samples.

$$\mathbf{Ag^{+} + e^{-} \rightarrow Ag_{(S)}} \qquad (2.9)$$

$$\mathbf{Pb + 2H_2O + 2h^{+} \rightarrow PbO_2 + 4H^{+}} \qquad (2.10)$$

It was shown that silver and lead oxide deposits formed at complementary locations, silver deposits at C+ domains and lead oxide deposits at C- domains[21] (Figure 2.36).

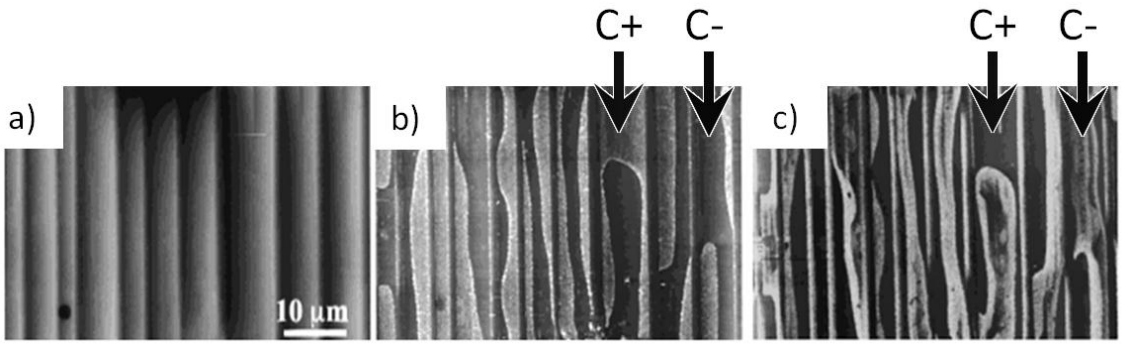

Figure 2.36 Topographic AFM images of the (001) surface of a barium titanate single crystal sample. (a) Shows the surface prior to reactions taking place. (b) Shows the surface after the sample was illuminated with UV light while submerged in aqueous silver nitrate solution. The white contrast corresponds to photocatalytically formed silver metal deposits on the surface of C+ domains. (c) Shows the same area of the sample after being cleaned and subsequently illuminated with UV light while submerged in aqueous lead acetate solution. The white contrast in the image corresponds to photocatalytically formed lead oxide deposits on the surface of C- domains (Source ref. 21)

It was also shown that the location of photochemically reduced silver deposits reflected the domain structure. Barium titanate's domain structure has been well characterised[114; 115]. The polarisation forms in one of three axes with domains that are perpendicular separated by 180^{o} domain walls and adjacent domains in the same axis separated by 90^{o} domain walls. 90^{o} domain walls form in the 110 habit plane and appear as regions with straight edges while 180^{o} domain walls do not have a distinct habit plane and form curved boundaries (Figure 2.37). Photochemically deposited silver particles have been shown to form a striping pattern marking domains separated by 90^{o} walls and areas of deposits with curved edges mark domains separated by 180^{o} walls (Figure 2.37).

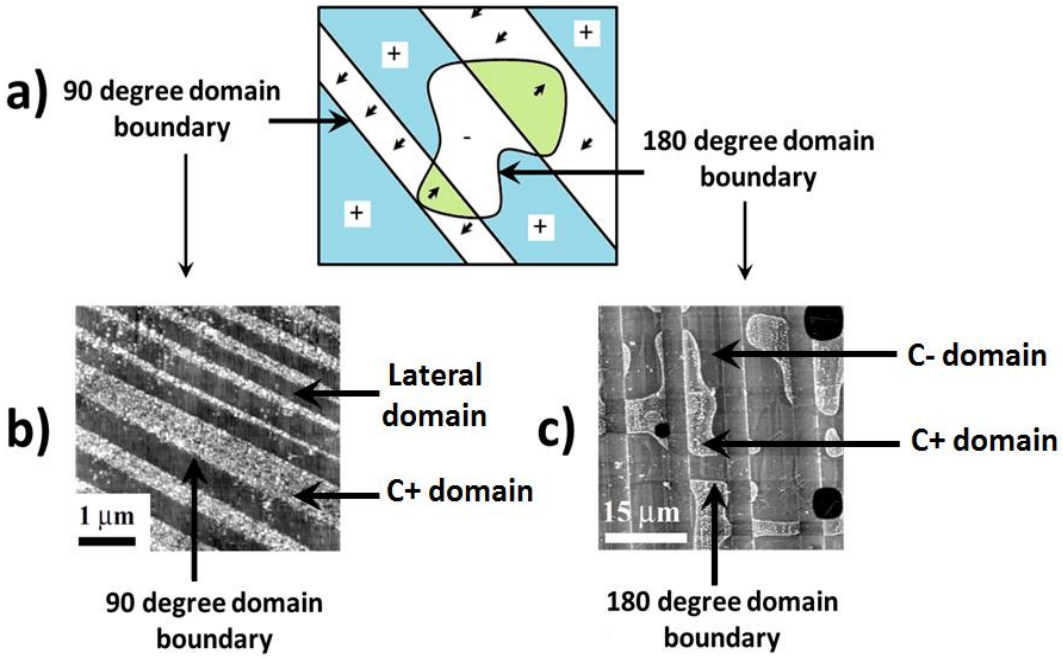

Figure 2.37 a) The domain structure at the surface of barium titanate. The picture shows C+ (+), C- (-) and lateral domains (➔). Straight edged 90 degree domain boundaries separate adjacent lateral domains and C axis domains. Curved 180 degree domain boundaries separate adjacent C+ and C- domains. b) Shows an SEM of the surface of a barium titanate sample after photochemical deposition of silver at the surface of C+ domains. The silver deposits are shown as a white contrast and mark the straight edged 90 degree domain boundaries separating lateral domains and C+ domains. c) An AFM image of the surface of a barium titanate sample after photochemical silver deposition at C+ domains. The silver deposits mark the 180 degree domain boundaries separating C+ and C- domains (Source ref. 113)

Investigation of photochemical deposition of silver at the surface of barium titanate particles with sizes between 4-6 µm produced similar results to reactions at the surface of bulk samples or thin films[116]. Striping patterns and regions of deposition with curved edges marked the location of 90^{o} and 180^{o} boundaries (Figure 2.38). It was observed that the different faces displayed different reactivity which, in order of reactivity, were shown to be (100)>(111)>(110) (Figure 2.38).

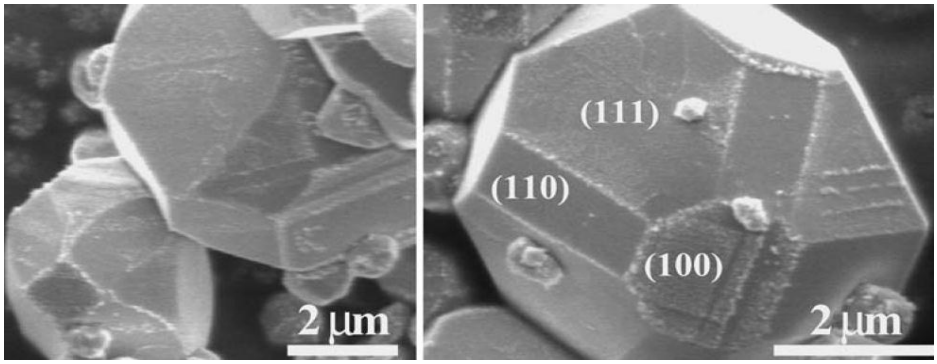

Figure 2.38 Photochemical reduction of silver particles at the surface of barium titanate particulates of between 4-6 μm (Source ref. 116)

Spatially distinct reduction and oxidation reactions have also been demonstrated to occur at the surface of other ferroelectric materials. Deposition of silver at the surface of PZT has been extensively investigated showing similar properties to studies using barium titanate[117-120]. PZT thin films have also been used to consider the use of domain patterning to constrain the location of photochemistry. Conducting tip atomic force microscopy was used to pattern domains of 50 nm at the surface of samples[121]. It was found that silver deposition occurred only at the poled C+ domains showing spatially distinct reactions occurred on the nanometre scale (Figure 2.39).

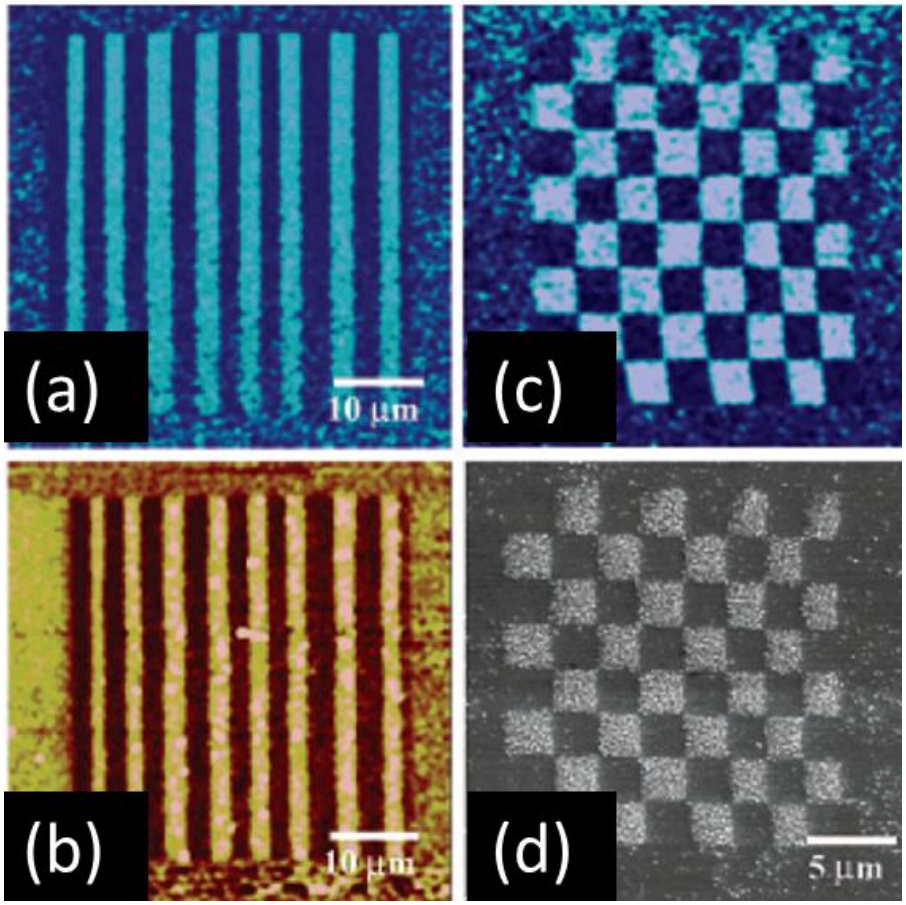

Figure 2.39 a) shows a PFM image of lines patterned on the surface of a PZT sample using ac +10 and -10 direct current voltage. Bright areas are C+ domains and dark areas are C- domains. b) shows a PFM image of the surface topography after the photocatalytic deposition of silver particles on the sample. Silver deposits only formed on the surface of C+ domains. c) shows a PFM image of a checkerboard domain structure patterned on the surface of a PZT sample. Bright areas are C+ domains and dark areas are C- domains. d) shows an SEM image of samples surface after photocatalytic deposition of silver particles. The silver deposits formed only on the surface of C+ domains (Source ref. 121)

Investigation by Sun et al has shown the location of photochemical growth of silver deposits can be controlled at the surface of periodically poled lithium niobate by altering the concentration of the silver salt solution and intensity of super band gap illumination[19]. Experiments using a high concentration of silver salt solution and a high intensity of super band gap light found that metal deposits formed preferentially at domain boundaries (Figure 2.40).

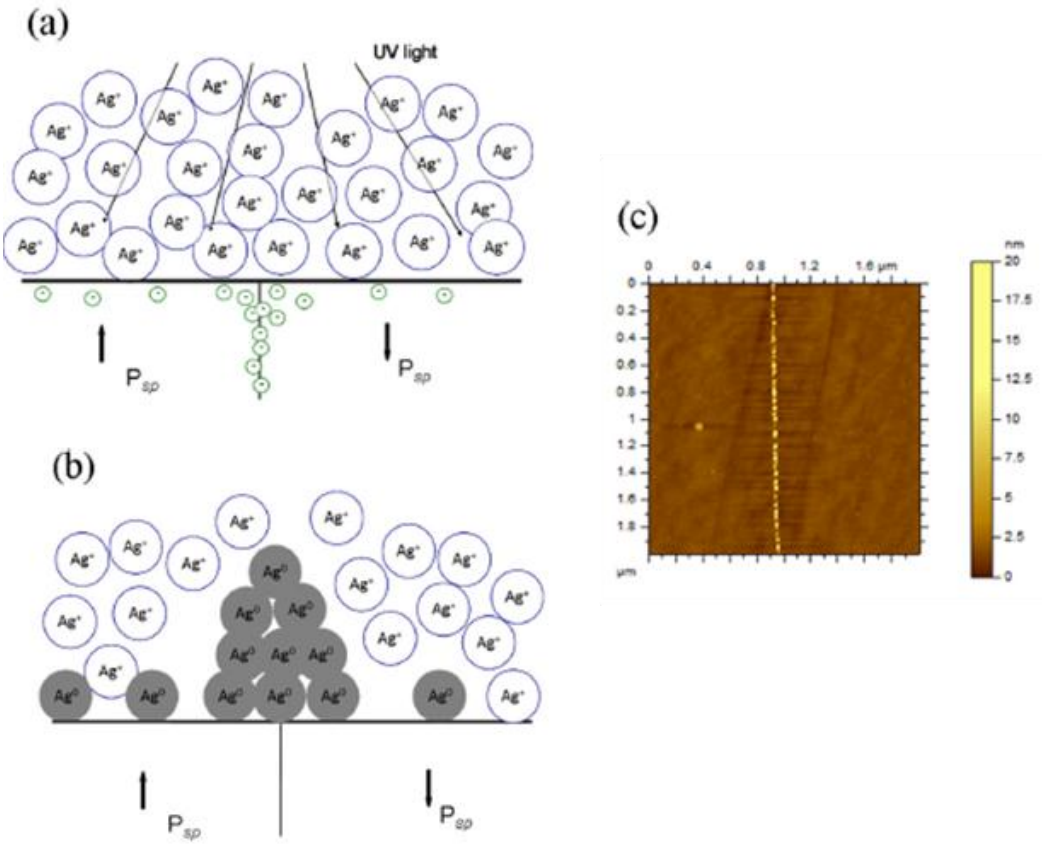

Figure 2.40 Preferential grain boundary photochemical deposition of silver particles at the surface of periodically poled lithium niobate using a high ratio of silver ions to super band gap light intensity (a) For each electron migrating to the surface, there is an Ag ion available to combine and produce an Ag^0 atom. (b) The resulting Ag(s) atom density and distribution reflects the electron distribution as determined by the electric field distribution. (c) The corresponding AFM image of the deposition pattern (Source ref.19)

This is explained by the high coverage of silver ions at the surface causing electrons to react immediately with silver ions after having migrated to the surface. As a result formations of silver deposits reflected the electron density in the lithium niobate sample. The electric field distribution toward the interface of periodically poled lithium niobate has been calculated showing that the field is unevenly distributed[67]. The field is strongest at the edge of 180^o boundaries and decreases rapidly travelling away from the boundary due to the effect of internal screening (Figure 2.41). This caused carrier density to be greater near the

domain walls producing preferential domain boundary deposition of silver deposits.

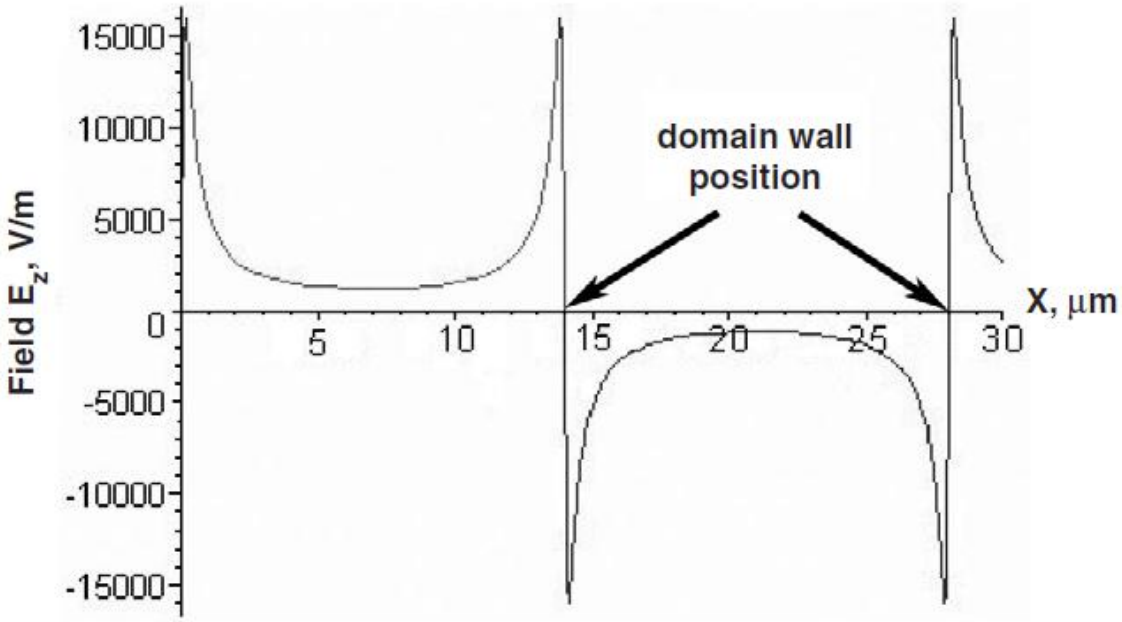

Figure 2.41 Calculated potential toward the surface of lithium niobate. The potential decreases toward the centre of the domain (Source ref. 67)

Using a low ratio of silver ions in solution to super band gap light intensity was shown to cause the location of silver deposits to reflect the coverage of silver ions in the double layer rather than the distribution of carriers in the lithium niobate sample (Figure 2.42). The lower concentration of silver ions in solution meant that when excited electrons migrated to the interface it was less likely they would readily drive reduction to form a silver deposit. However, for each silver ion impinging upon the surface an electron was available at the surface to form a silver deposit (Figure 2.42)

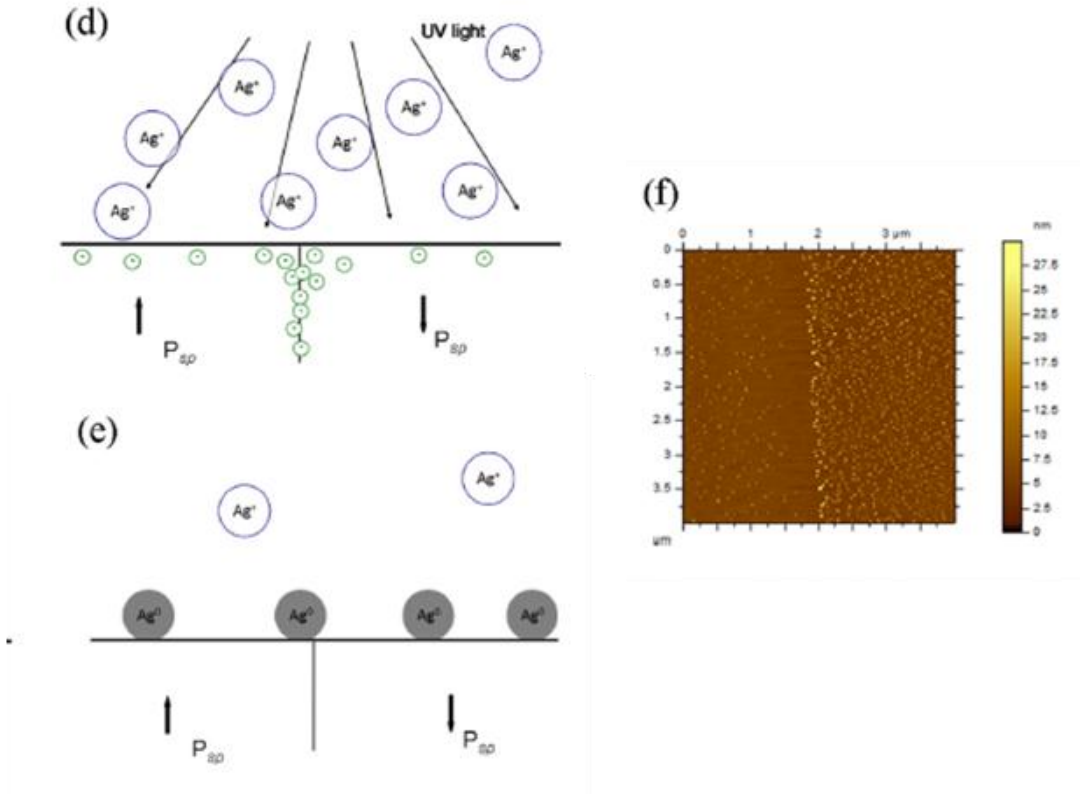

Figure 2.42 Distribution of photochemically deposited silver particles across the surface of periodically poled lithium niobate using a low ratio of silver ions to super band gap light intensity (d) For each Ag ion impinging on the surface, there is a supply of electrons available to produce an Ag(s) atom. Conversely, for each electron migrating to the surface, there may not be an Ag ion available. (e) The Ag(s) atom distribution is determined by the Ag ion flux, which is uniform over the lithium niobate surface. (f) The corresponding AFM image of the deposition pattern (Source ref. 19)

2.4.6.2 Ferroelectric photocatalysis

Several studies in the literature have considered the properties of ferroelectric materials upon their photocatalytic activity. Inoue investigated the rate of photocatalytic water decomposition over four different barium titanates ($BaTi_4O_9$, $Ba_2Ti_9O_{20}$, $Ba_4Ti_{13}O_{30}$ and $Ba_6Ti_{17}O_{40}$) impregnated with RuO_2 particles acting as a promoter[122]. Of the materials studied only $BaTi_4O_9$ produced distorted TiO_6 octahedra due to displacement of titanium ions in the

unit cell. The distortion induced internal dipolar fields. Under super band gap illumination photocatalytic reactions over $BaTi_4O_9$ formed a greater volume of hydrogen and oxygen than reactions over the other compositions of barium titanate (Figure 2.43). The author proposed this may be explained by the dipolar fields in $BaTi_4O_9$ separating excited carriers to suppress the rate of recombination and increase the materials photocatalytic activity compared to the other barium titanate samples.

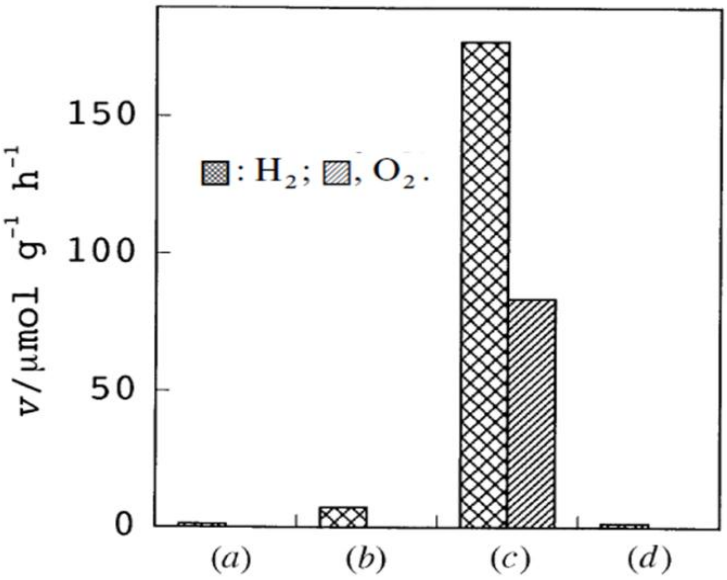

Figure 2.43 Photocatalytic production of hydrogen and oxygen over ruthenium oxide barium titanates a) $Ba_6Ti_{17}O_{40}$ b) $Ba_4Ti_{13}O_{30}$ c) $BaTi_4O_9$ d) $Ba_2Ti_9O_{20}$ (Source ref. 122)

Inoue also investigated alkali metal titanates of the formula $M_2Ti_nO_2n+1$ (M =Na, K, Rb or Cs) as a photocatalyst for decomposition of water[123]. The different compositions had distorted TiO_6 octahedra that produced internal dipolar fields with the exception of samples prepared using caesium[124]. Under super band gap illumination the samples all drove photocatalytic water splitting reactions to produce hydrogen gas except samples prepared using caesium. It was concluded that the greater photocatalytic activity of samples with distorted TiO_6 octahedra may be a result of carrier separation by the internal dipolar fields reducing the rate of recombination.

Ohara et al studied the change in photocatalytic activity at the ferroelectric to non-ferroelectric transition through comparing the amount of silver photochemically deposited at the surface of different $Sr_{1-x}Ba_xTiO_3$ ($0 < x < 1$) epitaxial films using X ray fluorescence[125]. The relationship between the composition and the quantity of silver deposition was found to show an abrupt change at $x = 0.6$. For this composition the Curie point is close to that of room temperature. The authors concluded that the change in activity was a result of ferroelectric and paraelectric domains co-existing in the film in compositions between $x = 0.5$ and $x = 0.7$, confirmed by x ray diffraction. A similar study investigated the change in photocatalytic activity at the ferroelectric phase transition of different compositions of barium strontium titanate. It was found that photocatalytic activity of ferroelectric samples for driving decomposition of aqueous dye solutions was greater than non-ferroelectric compositions and a local maximum in reactivity was observed at the phase transition[126] (Figure 2.44). The authors propose the greater reactivity of the ferroelectric compositions compared to the paraelectric compositions may be a result of internal depolarisation fields increasing separation of photo excited carriers, decreasing the rate at which recombination occurs and increasing the materials reactivity. The local maximum in reactivity at the transition from ferroelectric to paraelectric phase corresponds to a maximum in the dielectric constant of the compositions. The authors propose the dielectric constant may affect reactivity of the samples through its influence on the width of the space charge region. With increasing dielectric constant the width of the space charge region becomes larger. Widening the space charge region allows a greater proportion of photo excited carriers to be separated, supressing the rate of carrier recombination and increasing photocatalytic reactivity. This study shows evidence that both the spontaneous polarisation and dielectric constant of the barium strontium titanate compositions studied may be related to photocatalytic activity.

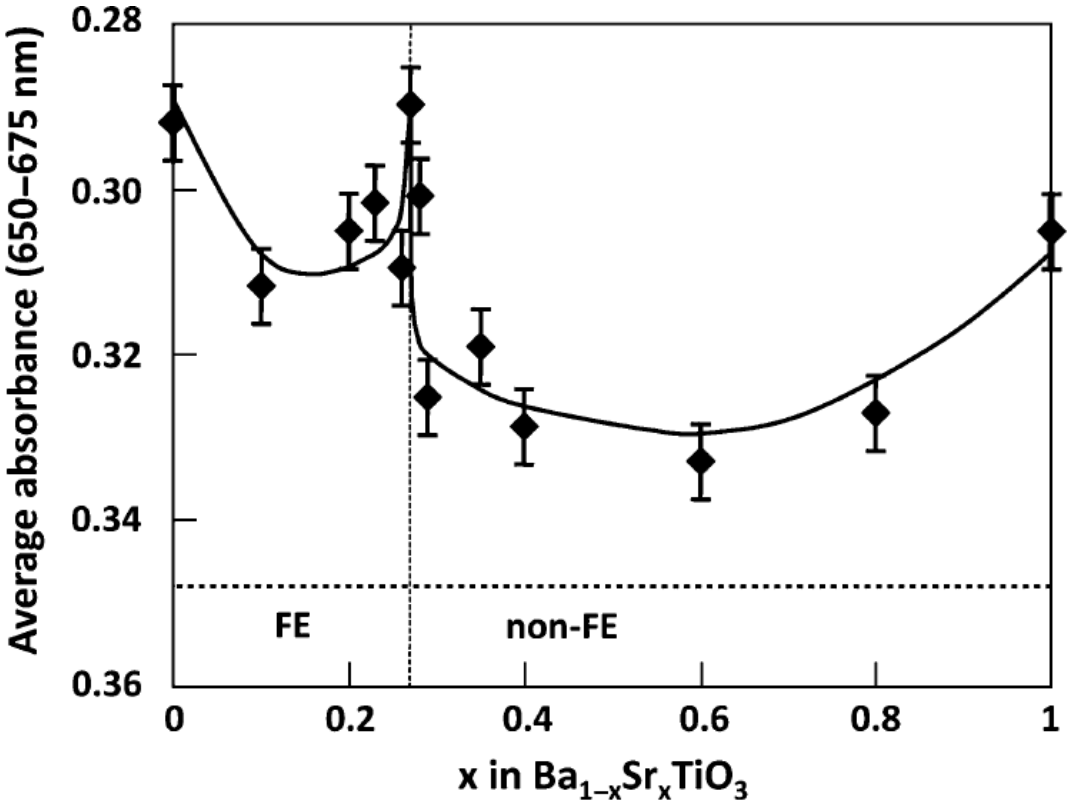

Figure 2.44 The decolourisation of methylene blue dye solution after 200 min UV illumination over ferroelectric and non-ferroelectric compositions of barium strontanate titanate. The dotted line marks the transition from the ferroelectric to non-ferroelectric phase. A larger Y axis value indicates greater photocatalytic reactivity. As x increases (shown on the X axis) the reactivity decreases. A local maximum in reactivity occurs at the transition from ferroelectric to paraelectric phase, coinciding with a maximum in the materials dielectric constant (Source ref. 126)

2.5 Ferroelectric materials used in this research

2.5.1 Barium titanate

The Curie point of barium titanate is reported to be 120 ^{o}C[127]. Above the Curie point barium titanates unit cell is a cubic perovskite structure and below the Curie point it is a tetragonal structure (Figure 2.45). The body centred cation can shift to an off centre position in three axis. This means there are a total of six orientations of the polarisation. At room temperature the band gap of barium

titanate is reported to be 3.2 eV[128] and the polarisation is reported to be 26 μC cm^{-2} [66; 129] .

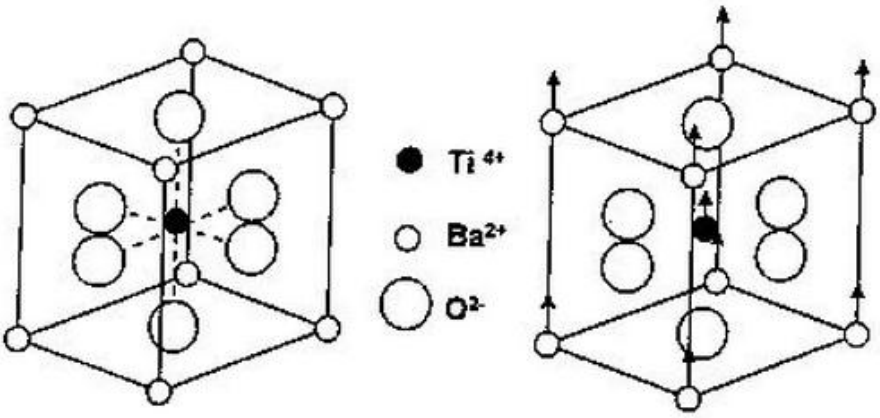

Figure 2.45 Phase transition from cubic to tetragonal unit cell in barium titanate below the Curie point (Source ref. 130)

As discussed in section 2.4.4, excited carriers in a ferroelectric material can only photocatalytically drive redox couples with a standard potential that is within its conduction and valence band edges. This means that to determine the ability of a ferroelectric material to drive photocatalytic reactions the position of its valence band edge and conduction band edge in relation to the NHE scale have to be determined. The energies of the valence and conduction band of barium titanate have not been reported in the literature; however, the conduction band energy can be estimated using Equation 2.11.

$$\chi = X - \frac{1}{2}E_g \qquad (2.11)$$

χ is the electron affinity in eV, X is the Sanderson electronegativity in eV and E_g is the materials band gap in eV.

Equation 2.11 shows the relationship between a materials electron affinity (χ), the materials band gap (E_g) and the materials Sanderson electronegativity (X). The Sanderson electronegativity of a semiconductor is a measure of its tendency to attract electrons that is calculated using the reciprocal of the volumes of its constituent atoms. The electron affinity of a semiconductor is the

energy difference in eV between the vacuum energy and the minimum energy of the conduction band. As the vacuum energy level is reported to exist at approximately 4.5 eV above that of the reduction potential of hydrogen (0.0 V vs. NHE), calculating the electron affinity of barium titanate using Equation 2.11 allows the minimum energy of its conduction band to be estimated in relation to the NHE scale. The Sanderson electronegativity of barium titanate is 5.8 eV and barium titanates band gap is 3.2 eV. Using equation 2.11 the electron affinity of barium titanate is calculated to be 4.2 eV. The conduction band minimum energy can, therefore, be estimated to be -0.3 V vs. NHE, close to that of titanium dioxide (Figure 2.46).

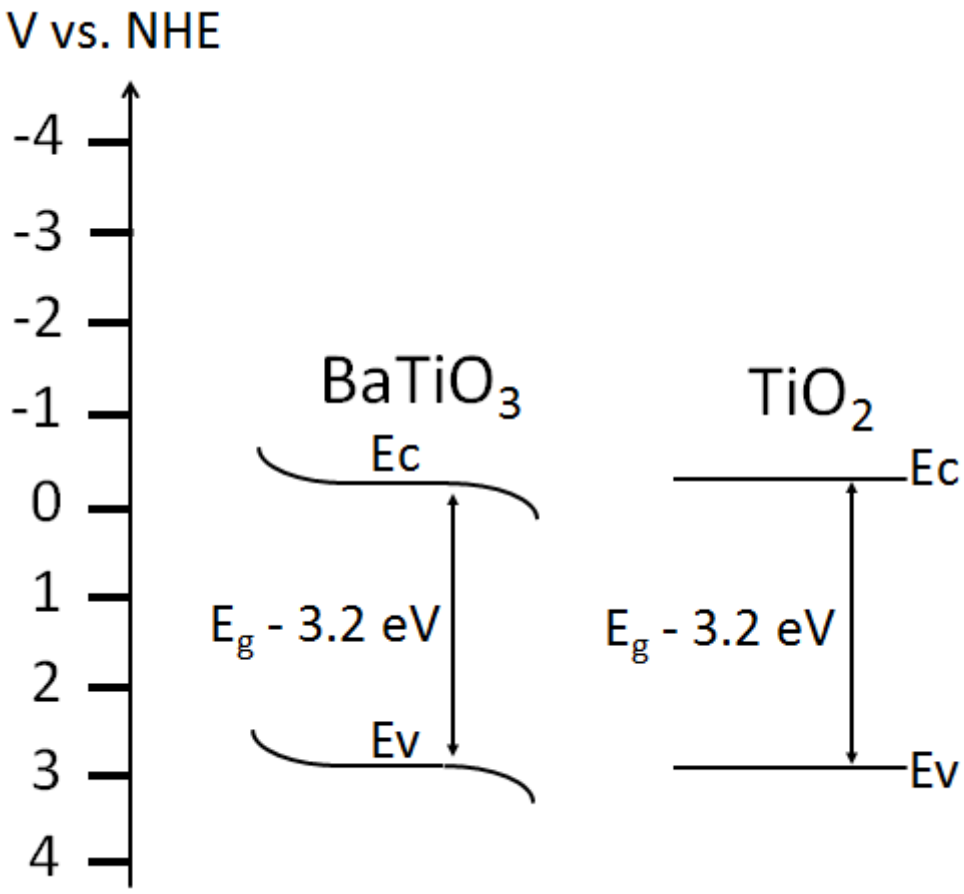

Figure 2.46 The band potentials of barium titanate and the flat band potential of titanium dioxide vs. NHE

2.5.2 Lithium niobate

Lithium niobate is reported to have a Curie point of 1210 ^{o}C[131] and a spontaneous polarisation of 78 µC cm^{-2} at room temperature[132]. Lithium niobate is classified as an oxygen octahedral ferroelectric and has the general formula ABO_3. Lithium niobate procures a trigonal crystal structure at room temperature[133] as shown in Figure 2.47. The movement of lithium and niobium cations is restricted to the C axis meaning that only antiparallel domains can form.

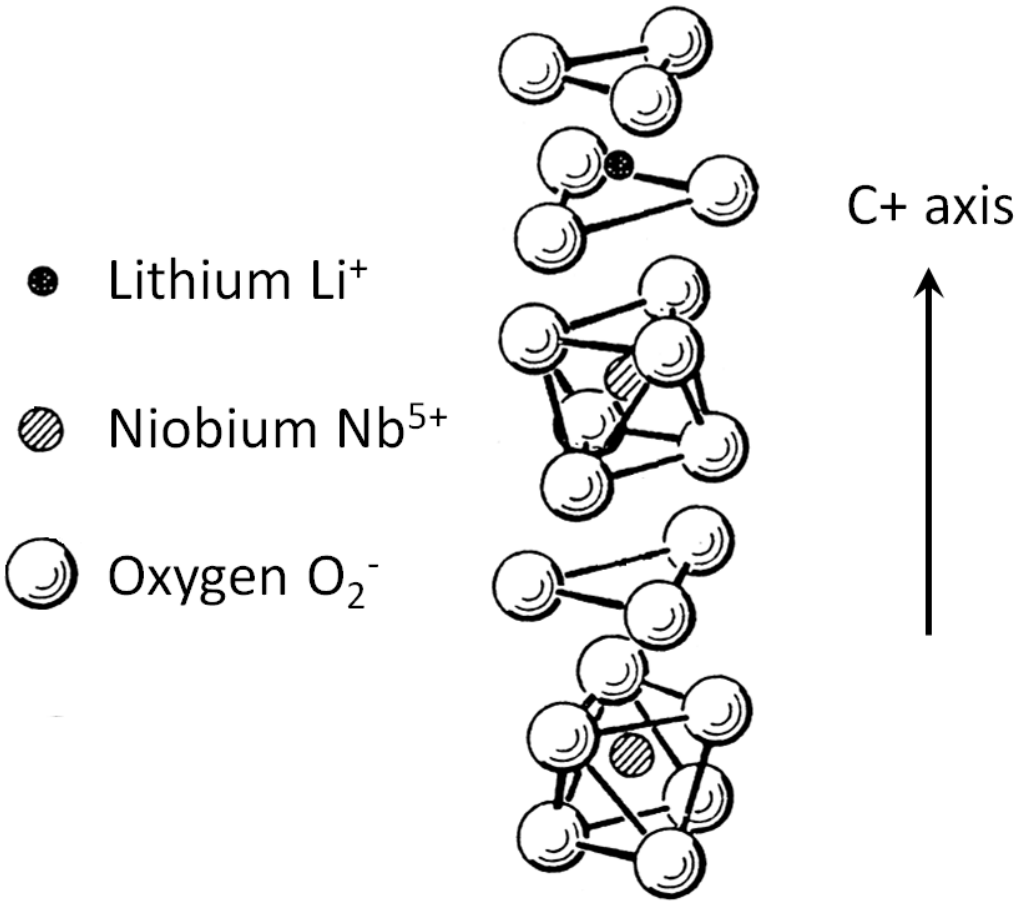

Figure 2.47 The trigonal unit cell of lithium niobate (Source ref.135)

The band gap of lithium niobate is reported to be 3.7 eV[136] and the electron affinity of lithium niobate has been reported to be 1.1 eV[137]. The band potentials of lithium niobate vs. NHE are shown in Figure 2.48. Lithium niobate is reported to be n-type by thermoelectric power measurements[138]. Doping lithium niobate with iron has been reported to increase the materials n-type character[139].

Doping of lithium niobate with magnesium has been found to increase the band gap to 4.0 eV[140]. High concentration magnesium doping e.g. 5 %, is also reported to produce material with increased p-type character[141;142].

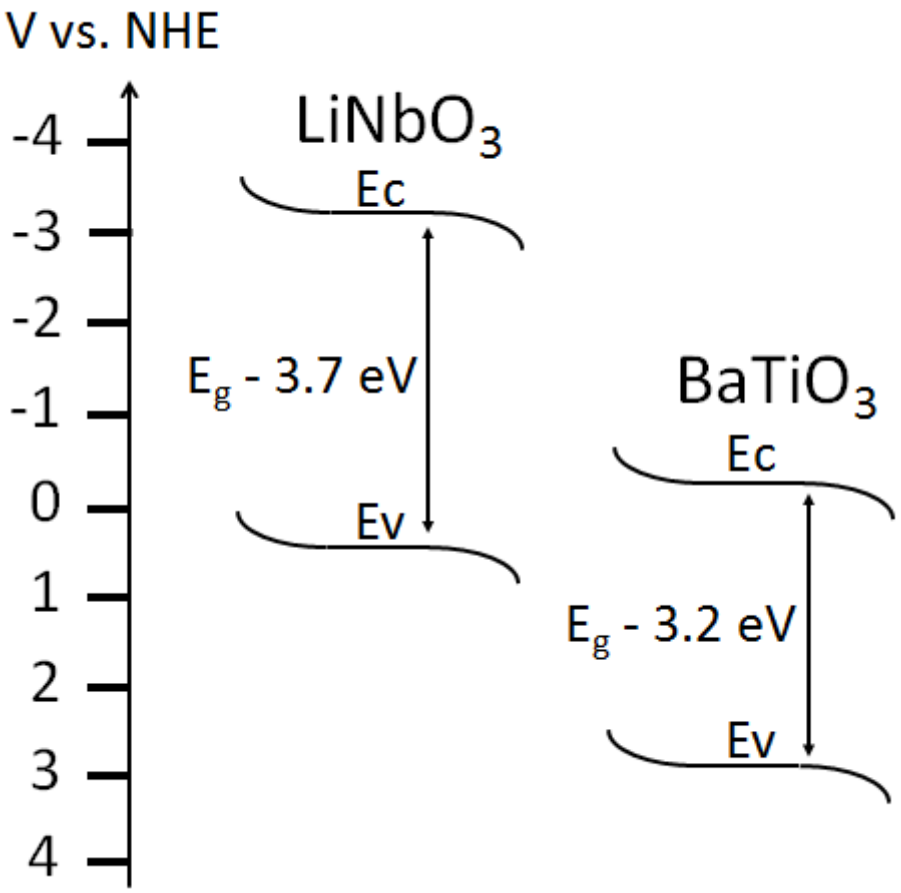

Figure 2.48 The band potentials of lithium niobate and barium titanate vs NHE

3 Methodology

3.1 Ferroelectric powders

Polycrystalline barium titanate powder (99.9 %), lithium niobate powder (99.9 %) and titanium dioxide powder (99.7 %) were purchased from Sigma Aldrich and used as provided. Optical grade single crystal slides of lithium niobate or 5% magnesium doped lithium niobate were purchased from MTI Corporation[143] and a bulk sample of polycrystalline 0.05% iron doped lithium niobate was purchased from Photox Optical Systems[144]. The polarisation of the optical lithium niobate slides and a sliver of the 0.05 % iron doped lithium niobate were measured using a Berlincourt d_{33} meter. The optical grade lithium niobate slides and the bulk 0.05 % iron doped lithium niobate were then ground for 10 minutes with a mortar and pestle to produce fine particle powders of lithium niobate, 5% magnesium doped lithium niobate or 0.05 % iron doped lithium niobate. To distinguish the different powders in the following Chapters abbreviations are used shown in Table 3.1. The lithium niobate and barium titanate powders were analysed using a scanning electron microscope (SEM) Phillips XL30 SFEG in secondary electron detector mode to determine the particle size distribution. Brunauer-Emmett-Teller isotherm (BET) analysis was carried out using nitrogen gas to determine the surface areas of the powders.

Table 3.1 The powders of lithium niobate, doped lithium niobate, barium titanate and titanium dioxide used in experiments. Powders of barium titanate, titanium dioxide and lithium niobate provided by Sigma Aldrich were used as supplied. Bulk samples of lithium niobate and magnesium or iron doped lithium niobate provided by MTI Corporation or Photox optical systems were ground to produce powders

Material	Supplier	Abbreviation for powder
Barium titanate powder	Sigma Aldrich	BT
Lithium niobate powder	Sigma Aldrich	LN
Lithium niobate single crystal optical slide	MTI Corporation	SLN
5 % magnesium doped lithium single crystal optical slide	MTI Corporation	MgLN
0.05% iron doped lithium niobate bulk sample	Photox optical systems	FeLN
Titanium dioxide powder	Sigma Aldrich	TiO_2

3.2 Light sources

3.2.1 UV lamp

Illumination of samples with ultra violet (UV) light was carried out using an exposure unit built for use in experiments. The unit consisted of a Honle UVASPOT® lamp housed inside an aluminium frame. The frame allowed the unit to be sealed preventing users being exposed to UV light. Samples were illuminated by opening a shutter fitted inside the exposure unit. A mercury gas bulb was fitted to the lamp. The emission spectrum was measured between

200-850 nm using a Red Tide UV-Vis spectrophotometer connected to a computer running Logger Pro software (Figure 3.1). Samples were illuminated at a distance of 10 cm from the bulb. Using a UV intensity meter the lamp was measured to emit an intensity of 28.6 mW cm^{-2} between wavelengths of 200-400 nm at a distance of 10 cm from the bulb.

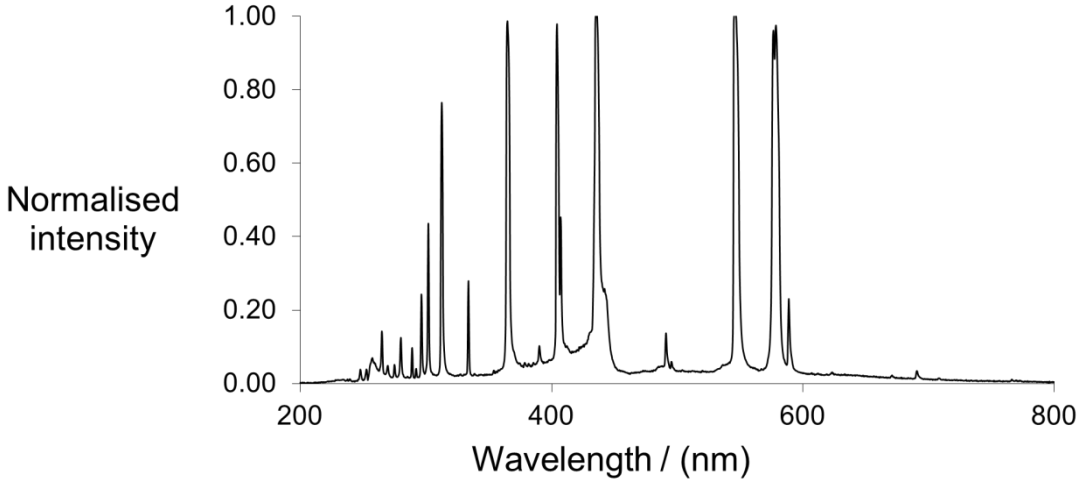

Figure 3.1 Normalised intensity of the wavelength output of the Honle mercury lamp measured using a Red Tide UV-Vis spectrophotometer

3.2.2 Solar simulator

Illumination of samples with simulated solar light was carried out using a 1000 W full spectrum Newport Solar Simulator with a 4 x 4 inch beam size. The emission spectrum of the solar simulator between 200-850 nm was collected using a Red Tide UV-Vis spectrophotometer connected to a computer running Logger Pro software (Figure. 3.2). The source emitted a spectrum equivalent to air mass 1.5. The intensity of light emitted by the solar simulators full spectrum (200-900 nm) was measured in suns at air mass 1.5 using a solar intensity meter. At air mass 1.5 1.0 sun is defined as 100 mW cm^{-2} of irradiance. The source was found to emit intensity equivalent to 1.0 sun at the base of a 500 mL Pyrex beaker used as a reaction vessel in experiments and 1.4 suns at the top.

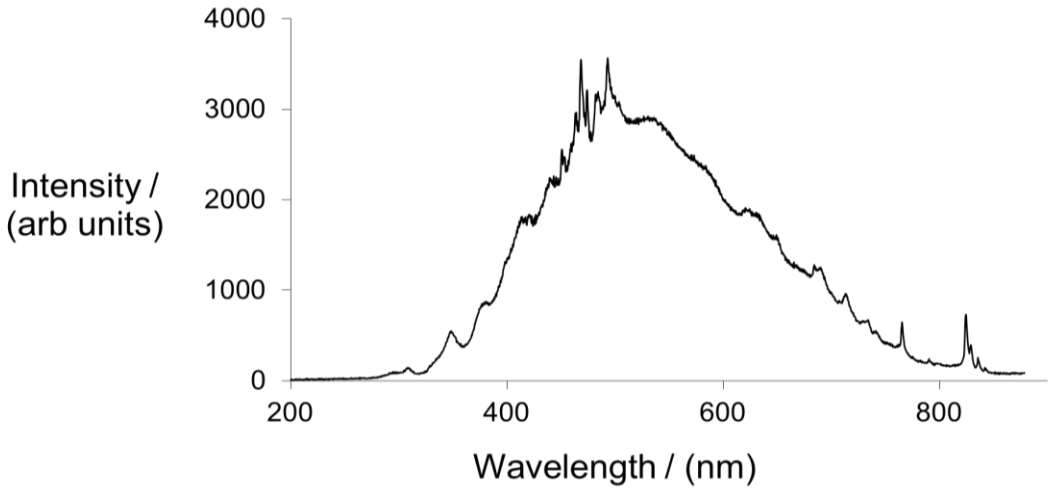

Figure 3.2 Emission spectrum of the wavelength output of the solar simulator measured using a Red Tide UV-Vis spectrophotometer

3.2.3 Estimation of light intensity emitted by UV lamp and solar

The intensity of light (mW cm^{-2}) emitted between specific wavelengths by the UV lamp or solar simulator was not able to be directly measured. These values were instead estimated for the light sources using the data collected by the spectrophotometer for the UV lamp or solar simulator and the intensity in mW cm^{-2} recorded by the UV intensity meter for the UV lamp (28.56 mW cm^{-2}) or solar intensity meter for the solar simulator (100-140 mW cm^{-2}). The method of estimation involved first producing a spread sheet for each light source. An example of the layout of the spread sheet is shown in Table 3.2. In the first column, A, all the wavelengths between 200-850nm measured by the spectrophotometer were listed. In the second column, B, the arbitrary intensity for each wavelength recorded by the spectrophotometer was listed. In the third column, C, the energy of photons at each wavelength in eV was listed. The fourth column, D, shows the values of column B (intensity in arb units) and C (photon energy in eV) multiplied together. The values in column D estimate the relative intensity in eV emitted at each wavelength by the light source.

Table 3.2 An example of the layout of the spread sheet used to estimate the intensity of light emitted by the UV lamp or solar simulator between specific wavelengths

A Wavelength (nm)	B Intensity measured by spectrophotometer (arb units)	C Photon energy (eV)	D Intensity (arb units) x photon energy (eV)
200.5	2.76	6.18	17.05
200.9	7.00	6.17	43.17
201.3	7.83	6.16	48.20
201.6	10.53	6.14	64.70
202.0	11.20	6.13	68.69
202.4	5.30	6.12	32.44

To estimate the intensity of light emitted in mW cm^{-2} between two wavelengths of interest e.g. 200nm to 380nm, the values in column D were summed between 200nm-380nm and divided by the sum of the values of column D over the wavelengths which the UV intensity meter measured (200nm-400nm) or the solar intensity meter measured (200nm-900nm). This gave a ratio of the sum of the relative intensities emitted by the light source between 200nm-380nm compared to the sum of the relative intensities emitted over the wavelengths measured by the UV or solar intensity meter. Multiplying this value by the value in mW cm^{-2} that was recorded by the UV or solar intensity meter gave an estimate of the intensity of light emitted between 200-380 nm in mW cm^{-2}. An example of a calculation estimating the intensity emitted by the UV lamp between two wavelengths, A nm to B nm, using the UV lamp spread sheet is shown in Equation 3.1. The values of column D are summed in the spread sheet between A nm and B nm. This figure is then divided by the sum of column

D for the wavelengths over which the intensity was measured in mW cm^{-2} by the UV meter, 200-400nm. This value is then multiplied by the intensity recorded by the UV meter for wavelengths between 200-400nm, 28.56 mW cm^{-2}, to give an estimated intensity in mW cm^{-2} emitted by the UV lamp between A nm to B nm.

$$Estimated\ intensity\ of\ the\ UV\ lamp\ between\ A\ nm - B\ nm\ (mW\,cm^{-2}) = \left[\frac{Sum\ of\ column\ D\ between\ A\ nm - B\ nm\ (eV)}{Sum\ of\ column\ D\ between\ 200\ nm - 400\ nm\ (eV)}\right] X\ Measured\ UV\ light\ intensity\ between\ 200\text{-}400\ nm\ (28.56\ mW\,cm^{-2}) \quad (3.1)$$

3.2.4 Fluorescent bulb

Illumination of samples with fluorescent light was carried out using a 1 meter long bulb. According to the manufactures specification the bulb emitted light between wavelengths of approximately 400-700 nm.

3.3 Photochemical deposition of metal nanoparticles

3.3.1 Selection of metal salts

For photochemical reduction of metal ions to take place the reduction potential must be within the band edges of the photocatalyst. Solutions of salts of silver, copper and iron were chosen as the reduction potential of these metal ions is within the band edges of barium titanate and lithium niobate (Figure. 3.3). The salts used are detailed in Table 3.3.

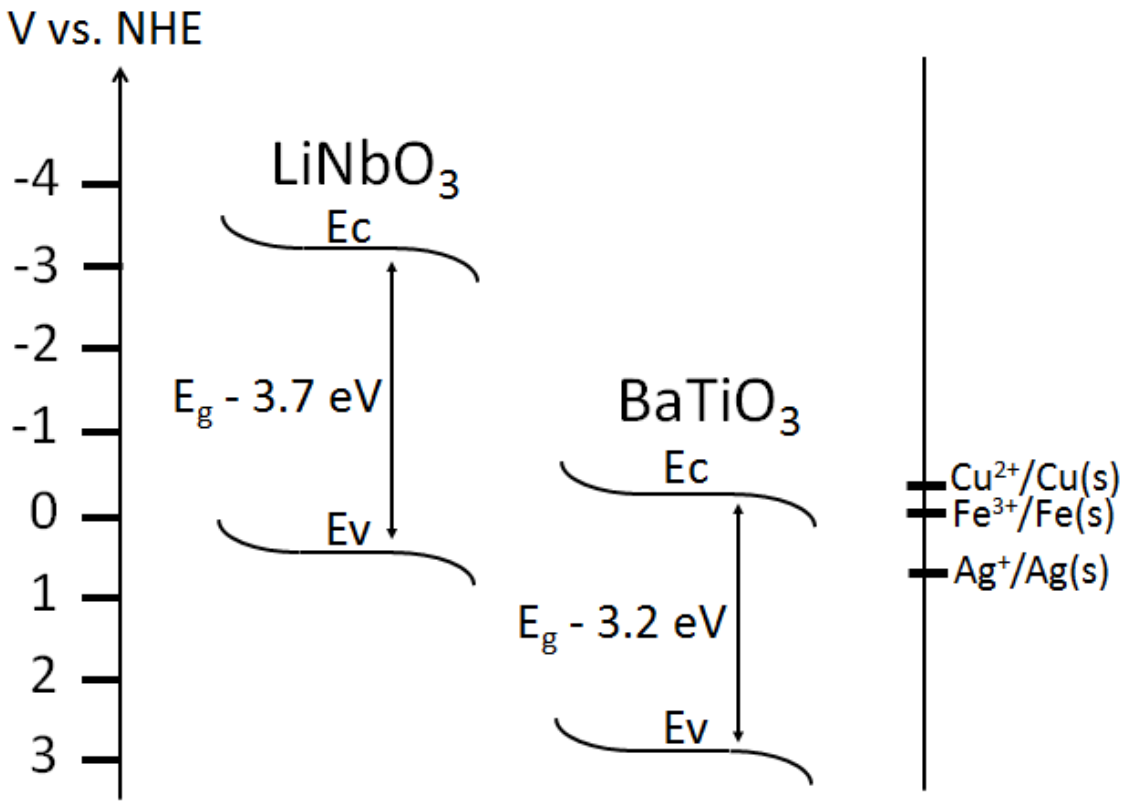

Figure 3.3 The Band edges of lithium niobate and barium titanate vs. NHE. The position of the reduction potentials of silver, copper or iron ions are shown on the right hand side

Table 3.3 Metal salt solutions used in photochemical deposition experiments

Metal salt	Formula	Supplier
Silver (I) nitrate	$AgNO_3$	Sigma Aldrich 99.99%
Copper (II) sulphate	$CuSO_4$	Sigma Aldrich 98.00%
Iron (III) nitrate	$Fe(NO_3)_3$	Sigma Aldrich 98.00%

3.3.2 Photochemical reduction of metal ions under UV illumination

0.01M solutions of the metal salts were prepared by dissolving them in deionized water. Photochemical metal deposition was carried out by suspending ferroelectric powder in the salt solutions (2.5 gL^{-1}, 100 mL) inside a 250 mL Pyrex beaker. The suspensions were agitated continuously using a stir bar and magnetic stirrer plate while being irradiated with UV light for either 20 or 30 minutes. After illumination the powders were recovered and washed three times with 250 mL of deionized water to remove any remaining metal salt. The powders were dried at room temperature. Analysis of the surface of the powders was carried out using SEM with an energy dispersive X-ray spectroscopy detector attached. Quantitative analysis was carried out using INCA^{TM} software.

3.4 Adsorption studies and photocatalytic dye decolourisation

3.4.1 Preparation of aqueous dye solutions

Acid black 1 (Sigma Aldrich 99.99%) or rhodamine b (Sigma Aldrich 99.99%) dye were dissolved in deionized water (0.01 gL^{-1}) to produce 10 ppm concentration stock solutions. The stock solutions were stored in a sealed container under dark conditions at ambient temperature. Fresh stock solution was prepared every 3-4 months. Using a digital pH meter the pH of acid black 1 stock solution was measured to be 5.9 and the pH of rhodamine b stock solution was measured to be 6.4.

3.4.2 Absorption measurements

Absorption measurements of dye samples were collected using a lambda 7 spectrophotometer. The peak absorption of the rhodamine b stock solution was found to be 554 nm and the peak absorption of acid black 1 stock solution was found to be 620 nm. Dilution of samples of stock solution showed that the peak

absorption of both acid black 1 and rhodamine b deceased linearly with concentration down to 1 ppm.

3.4.3 Adsorption studies

Dye adsorption studies were carried out by suspending ferroelectric powder, ferroelectric powder with metal nanoparticles deposited at the surface or TiO_2 powder in solutions of acid black 1 or rhodamine b. In experiments either suspensions of 1.5 g L^{-1} of powder in 40 mL of dye solution placed in a 250 mL Pyrex beaker or suspensions of 0.1 g L^{-1} of powder in 200 mL of dye solution placed in a 500 mL Pyrex beaker were used. The suspensions were stirred under dark conditions using a stir bar and magnetic stirrer plate. After addition of powders to dye solutions the changes in the absorbance due to adsorption/desorption of dye at the powders surface were found to have reached equilibrium after 15 min. The suspensions were stirred for a further 15 min to ensure equilibrium had been fully reached. Samples were collected from the suspensions (1.5 mL) and centrifuged using a Centurion scientific C2 centrifuge for 45 min at 200,000 rpm to remove the powder. The peak absorbance of the dye samples was measured. The percentage decrease in concentration (*X*) compared to the stock dye solution was calculated using Equation 3.2.

$$X\ (\%) = \left(1 - \left(\frac{C}{C_{Stock}}\right)\right) x\ 100 \qquad (3.2)$$

C is the peak absorbance of the sample and C_{Stock} is the peak absorbance of the stock dye solution.

3.4.4 Decolourisation reactions under UV, simulated solar or fluorescent illumination

Photocatalytic decolourisation of solutions of acid black 1 and rhodamine b solutions was investigated under UV, simulated solar or fluorescent light

illumination. Ferroelectric powders or ferroelectric powders modified by photochemical deposition of metal particles at the surface were suspended in rhodamine b or acid black 1 solution. In experiments either suspensions of 1.5 g L^{-1} of powder in 40 mL of dye solution placed in a 250 mL Pyrex beaker or a suspension of 0.1 g L^{-1} of powder in 200 mL of dye solution placed in a 500 mL Pyrex beaker were used. A quartz filter that adsorbs all light of wavelengths shorter than 295 nm was purchased from UQG optics[145] and used as a lid placed on top of the beaker. The suspensions were allowed to reach equilibrium by stirring under dark conditions for 30 min. Illumination was carried out while the suspensions were agitated continuously using a stir bar and magnetic stirrer plate. Samples (1.5 mL) were removed at predetermined intervals and centrifuged for 45 min to remove the powder. Using Equation 3.2 the change in the peak absorption of the dye solutions compared to the peak absorbance of the solution at equilibrium (C/C_o) was determined and plotted against time.

$$\frac{C}{C_0} = \frac{C}{C_{Equilibrium}} \qquad (3.3)$$

C is the peak absorbance of a collected sample and $C_{Equilibrium}$ is the peak absorbance of dye suspension at equilibrium prior to illumination.

3.5 Photochemical reduction of carbon dioxide over lithium niobate powder or titanium dioxide powder

3.5.1 Solid-liquid phase reactions

SLN powder was suspended in distilled water (2.0 gL^{-1}, 50 mL) in a 250 mL Pyrex beaker. The suspension was bubbled with carbon dioxide gas (99.95%) purchased from BOC for 5 min at an approximate rate of 0.1 L min^{-1} to saturate the distilled water with gas. The suspension was then illuminated with UV light for 45 min whilst bubbling with carbon dioxide gas continued. Liquid samples (2.5 mL) were collected after illumination was complete and analysed for the

concentration of formic acid and formaldehyde using gas chromatography mass spectroscopy (GC/MS).

3.5.2 Gas chromatography mass spectroscopy (GC/MS) analysis of liquid samples for formic acid and formaldehyde

Simultaneous GC/MS analysis of formic acid and formaldehyde was carried out using a modified version of the method reported by del Barrio et al[146]. 1 weight % of p-toluenesulfonic acid (99.99%, Sigma Aldrich) was dissolved in ethanol (200 proof, Sigma Aldrich). The ethanol solution was mixed in a 1:1 ratio with aqueous samples collected from reactions. This drove chemical mediation of formic acid and formaldehyde to ethyl formate and diethoxymethane respectively in a 1:1 ratio. The samples were then loaded in headspace vials and sealed. GC/MS analysis of the levels of ethyl formate and diethoxymethane was carried out using an Agilent Model 6890N fitted with a Model 5973N quadrapole mass selective detector, a Model 7694 headspace auto sampling unit and a Phenomenex ZB-Wax column (30 m long with a 0.32 mm i.d. and 0.5 μm film thickness). Helium was used as the carrier gas, set at a constant flow rate of 2.5 mL min^{-1} (57 cm^3 sec^{-1}) and a head pressure of 6.45 psi. The injector was maintained at a temperature of 150 ^oC with a split ratio of 10:1 and split flow of 25 mL min^{-1}. The headspace samples were equilibrated at 60 ^oC for 15 min. The vials were pressurized for 6 sec, the sample loop filled with the headspace gas for 30 sec and equilibrated for 3 sec before a 1 mL injection was taken. The column oven temperature program was initially set at 40 ^oC for 4.2 min with a ramp rate of 40 ^oC min^{-1} up to a temperature of 160 ^oC at which the temperature was held for 2 min. Mass selective detection was performed at 280 ^oC using either full scan for identification of ions or with selected ion monitoring (SIM) mode to quantitatively analyse the level of ions. The ions detected by SIM mode analysis were m/z 27 and 31 corresponding to ethyl formate and m/z 31, 59 and 103 corresponding to diethoxymethane. The response of the detector was calibrated using standard samples of ethyl formate and diethoxymethane. The standard samples were prepared by dissolving 0.1 g of formic acid (99.99%

Sigma Aldrich) or 0.1 g of formaldehyde (99.99% Sigma Aldrich) in 10 g of 1% p-toluenesulfonic acid ethanol solution. Through serial dilution standard samples with concentrations of 0.01, 0.1, 1.0, 10.0, 20.0, 30.0, 40.0 and 50.0 ppm were prepared.

3.5.3 Solid-gas phase reactions

A vessel was designed and constructed using materials that are stable under UV irradiation to house solid-gas phase reactions (Figure 3.4).

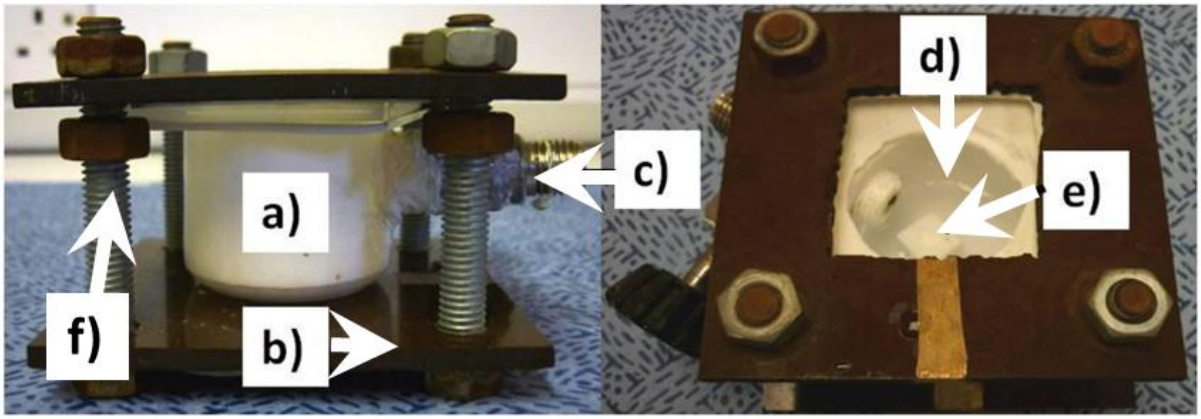

Figure 3.4 Vessel constructed for housing solid gas-phase reactions constructed from a) a PTFE beaker b) tunfol sheet c) a needle valve d) a quartz window e) a PTFE stand containing powder f) and threaded bar with bolts fitted for compressing the lid onto the reaction chamber

The vessel comprised a polytetrafluoroethylene (PTFE) beaker, silicone gaskets, a quartz slide, a metal needle valve covered in PTFE tape, 2 pieces of tufnol sheet, threaded metal bars and metal bolts. The PTFE beaker was used as the reaction chamber and fitted with the quartz slide and gaskets as a lid. The tufnol sheet, threaded bars and bolts were used to compress the lid onto the beaker to produce an air tight seal. A cut out was removed from the tufnol sheet to allow light to enter the vessel through the quartz slide. In experiments the PTFE beaker was loaded with deionized water (5 mL). A holder, also made from PTFE (1 cm^3), was filled with SLN or TiO_2 powder. The holder was used to raise the powder above the water line. The holder had been milled to have a

circular cut out 0.2 cm in diameter and 0.1 cm deep. Powder placed in the cut out was pressed flat to produce a circular surface with an area of 0.13 cm^2. The holder was placed in the reaction chamber. The vessel was then vented with carbon dioxide gas (99.95%, BOC) for 5 minutes at a flow rate of approximately 0.1 L min^{-1}. Once venting was complete the vessel was quickly sealed using the quartz window and compressed closed using the tufnol sheets and threaded bars. Gaseous samples were withdrawn through the needle valve and analysed for the concentration of carbon dioxide gas in the vessel using a gas chromatogram fitted with a thermal conductivity detector (GC/TCD). The vessel loaded with SLN or TiO_2 was illuminated with UV light for between 20-120 min. After illumination the vessel was allowed to cool to room temperature. The lid was removed and liquid samples (2.5 mL) were collected. The samples were analysed for the concentration of formic acid and formaldehyde using GC/MS as descried in Section 3.5.2.

3.5.3.1 Gas chromatography/ thermal conductivity (GC/TCD) analysis of gas samples

Gas samples collected from the reaction vessel were injected manually into a Agilent 6890 series gas chromatogram fitted with a thermal conductivity detector and Carboxen 1010 column (30 m long with a 0.32 mm i.d. and 15 µm film thickness). Helium was used as the carrier gas set at a flow rate of 8.6 ml min^{-1}. The detector was set at a temperature of 100^oC and the oven was set at a temperature of 150 ^oC. The carbon dioxide response peak produced by injected samples was integrated. The value was fitted to a calibration curve of the integrated peak area produced by carbon dioxide when samples of calibration gas were injected. The calibration gases were purchased from Greyhound gases and had a composition of 75 %, 50 % or 25 % by volume of carbon dioxide gas in nitrogen gas.

3.6 Summary

In this chapter experiments to photocatalytically deposit metal particles on the surface of ferroelectric powders, determine adsorption of dye molecules by ferroelectric powders, investigate the rate of photocatalytic decolourisation of dye solutions over ferroelectric powders and to study the products of photocatalytic solid-liquid phase or solid-gas phase reactions of carbon dioxide over lithium niobate powder were described. The designs of these experiments were based upon methods reported in similar studies in the literature. The parameters that were used e.g. the loading of powder, concentration of dye solution etc. when collecting data were set for each experiment by carrying out preliminary tests in which different conditions were trialled until analysis showed a measurable result. The most challenging experiment to design and carry out were the solid-gas phase reactions of carbon dioxide over lithium niobate powder as the purpose built air tight reaction vessel that was used in these experiments was difficult to manufacture. Calibrating the GC/MS to accurately detect concentrations of products of less than 1 ppm in aqueous samples removed from the vessel was also time consuming as a large number of calibration samples had to first be prepared and tested. The experimental setup measuring the rate of decolourisation of dyes over different ferroelectric powders proved the most useful of the experiments carried out. The duration of super band gap illumination, concentration of dye and loading of powder in these trials were able to be repeated with a high degree of accuracy between runs. The data collected from these experiments allow a clear comparison of the photocatalytic activities of the powders tested.

4 Selection of lithium niobate and barium titanate powders for use in experiments

4.1 Introduction

The photocatalytic properties of barium titanate, lithium niobate and lithium niobate doped with iron or magnesium were investigated in this thesis. Barium titanate and lithium niobate were chosen as these materials have previously been shown to be photoactive. It has also been shown that, due to their spontaneous polarisation, barium titanate and lithium niobate drive spatially separated reduction and oxidation reactions under super band gap illumination[19; 22; 67]. This characteristic is hypothesised to increase photocatalytic efficiency by decreasing the rate of both recombination of excited carriers and backward reactions of intermediates. Doped lithium niobate powders were studied as it is reported doping with iron increases lithium niobates n-type character[139] while magnesium doping has been shown to produce p-type lithium niobate[141;142].

Powders of lithium niobate and barium titanate were used in experiments as in comparison to bulk materials they have desirable properties for potential real world photocatalytic applications. The larger surface area increases the number of active sites at which reactions can take place. Powder photocatalysts also use practical operation conditions compared to immobilised photocatalysts or photochemical cells. In the generic case the powder is simply suspended in a solution of reactant and illuminated with super band gap light. The size of the powders had to be considered as this property influences the stability of the polarisation of ferroelectrics. Below a specific dimension termed the ferroelectric critical size particles undergo a size driven transition to the paraelectric phase[42]. It has also been shown that decreasing the dimensions of ferroelectrics below 1 µm in one or more axis produces size effects that reduce the polarisation and Curie point of particles compared to that of bulk material[40]. This means if the Curie point is decreased sufficiently then the powder will enter the paraelectric phase. In experiments ferroelectric powders were suspended in aqueous

solution under ambient conditions or when illuminated by a UV lamp or simulated solar light source. Illumination of the suspensions by the UV lamp was found to increase the temperature of reactants to between 50-55 ^{o}C and illumination by the solar simulator increased the temperature of reactants increased to 40-45 ^{o}C. Powders of barium titanate, lithium niobate and doped lithium niobate were, therefore, selected for use based upon their ability to maintain a stable ferroelectric phase under experimental conditions.

4.2 Barium titanate powder (BT)

The ferroelectric critical size of barium titanate is reported to be between 38-60 nm by experimental and theoretical investigations[41]. Particulates with a diameter larger than 60 nm exhibit a spontaneous polarisation and so can potentially be used in investigations of ferroelectric properties. However, Shih et al have reported that the Curie point of particles of barium titanate decreases toward room temperature as the size is reduced (Figure 4.1).

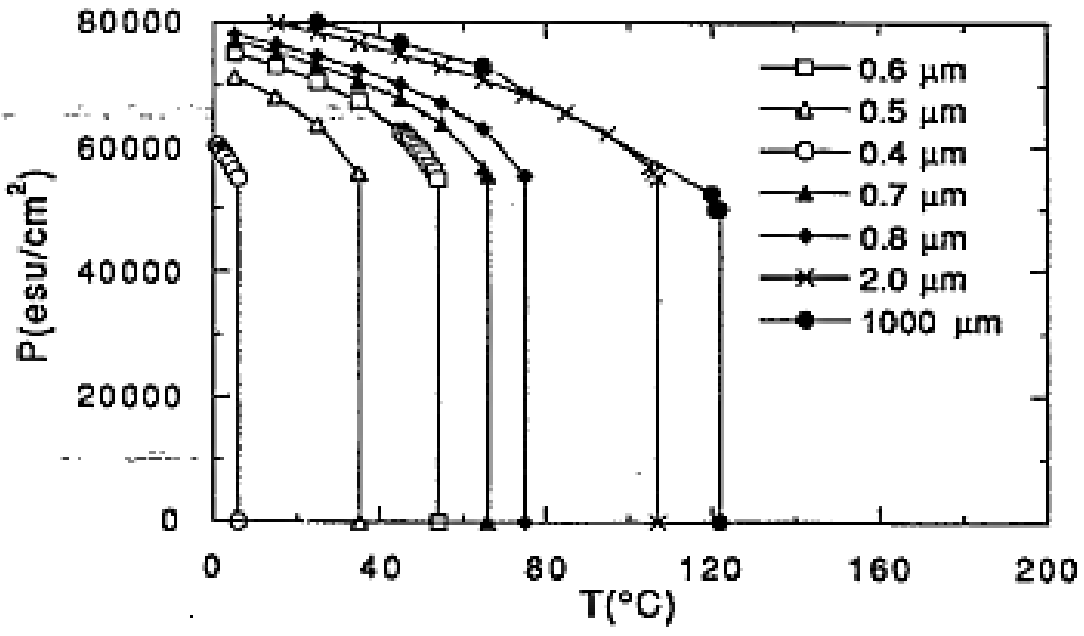

Figure 4.1 Plot showing the change in barium titanates polarisation and Curie point as the size is decreased (Source ref. 40)

The data reported in Figure 4.1 shows the Curie point of barium titanate particles with a diameter of 0.6 μm to be 48 ^{o}C. Particles of this size or smaller have a Curie point below the temperature reached by reactants when illuminated by the UV lamp in experiments (50-55 ^{o}C). To maintain a stable polarisation in the powder during UV illumination reactants would need to be cooled to maintain the temperature below the Curie point. Due to the impractical conditions this would require barium titanate powder with larger particle size and a higher Curie point was instead used. Polycrystalline barium titanate powder (BT) was purchased stated to have a particle size below 2 μm by the suppliers. The distribution of sizes was determined by collecting an SEM image of the powder (Figure 4.2) and measuring 50 particles. A histogram of the sizes is shown in Figure 4.3.

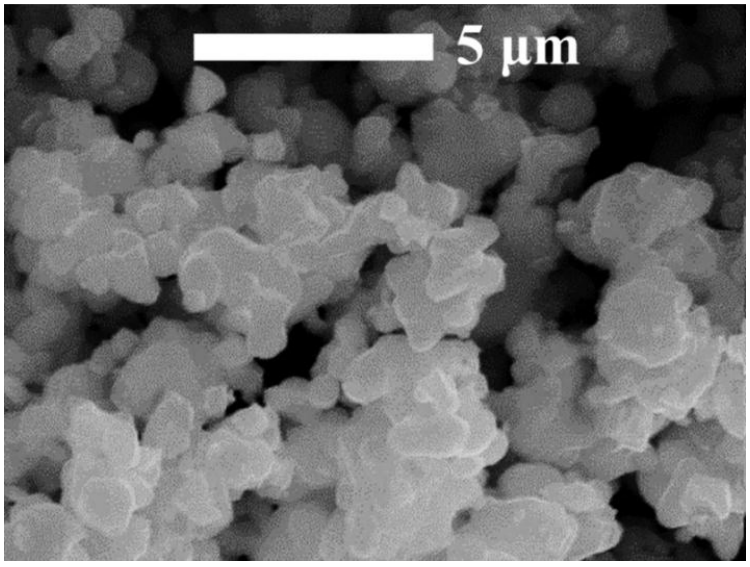

Figure 4.2 SEM image of barium titanate powder (BT)

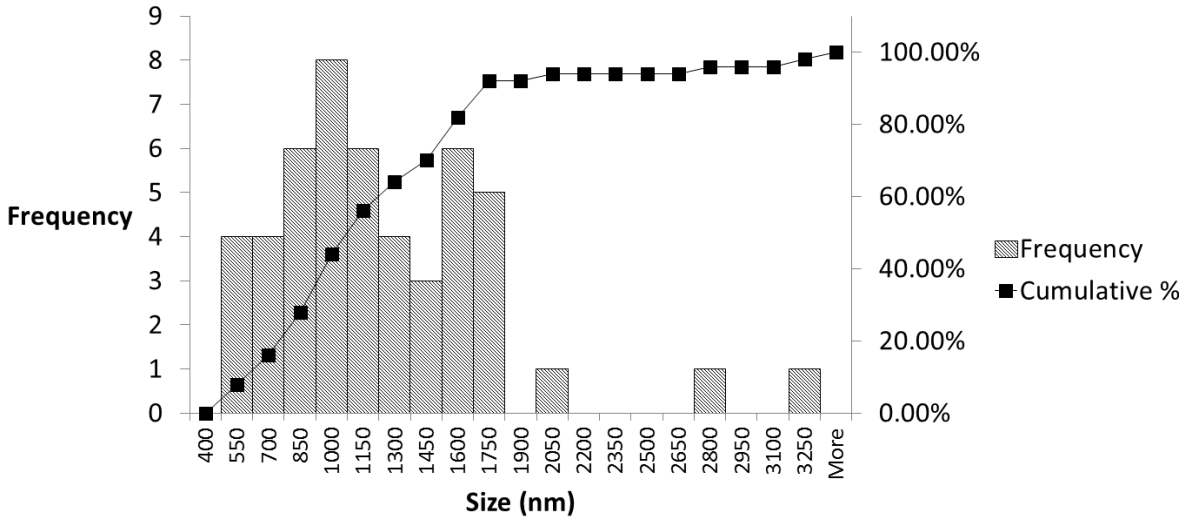

Figure 4.3 A histogram showing the size distribution of particles in barium titanate (BT) powder

All particles measured were found to be larger than barium titanates ferroelectric critical size of 60 nm (Figure 4.3). This meant that the particles produce a ferroelectric phase below the Curie point. The data reported in Figure 4.1 shows the Curie point of barium titanate particles with a size of 0.7 µm to be 64 ^{o}C. As this is above the temperature of suspensions in experiments when illuminated by UV (50-55 ^{o}C) or simulated solar light (40-45 ^{o}C) it was assumed that particles with a size of 0.7 µm or greater were able to maintain a stable polarisation. Particles smaller than 0.7 µm were assumed to undergo a thermally driven transition to the paraelectric phase during illumination experiments. The histogram in Figure 4.3 shows 42 of the particles of BT powder measured were larger than 0.7 µm. This meant it can be estimated that up to 84 % of the particles in the BT powder would remain in the ferroelectric phase during experiments. The size distribution of particles was also used to estimate the polarisation of the particulates. The majority of particles were measured to have a size greater than 0.4 µm and smaller than 1.9 µm (Figure 4.3). Using the values reported in Figure 4.1 under ambient conditions (23 ^{o}C) this meant the polarisation of particles ranged between 62,000-78,000 esu (20.7-26.4 µC cm^{-2}). Under illumination (50 ^{o}C) the polarisation of particles larger than 0.7 µm and smaller than 1.9 µm can be estimated to range between

64,000-72,000 esu (21.3-24.0 μC cm^{-2}). The surface area of BT powder was measured by BET analysis to be 0.7 m^2 g^{-1}.

4.3 Lithium niobate powder (LN)

The ferroelectric critical size of lithium niobate particulates has not been reported. Synthesised stoichiometric lithium niobate powder with an average particle size of 150 nm has, however, been reported to be in the ferroelectric phase with a Curie point shown to be 1122.5 ^oC[147]. Particles of lithium niobate equal or greater to 150 nm can be assumed to exhibit a polarisation and to not undergo a thermal phase transition under ambient or experimental conditions due to the Curie point greater than 1000 ^oC. Polycrystalline lithium niobate (LN) powder was purchased that had been sieved with a standard 200 mesh. An SEM image of the powder was collected (Figure 4.4) and the distribution determined by measuring the size of 50 particles (Figure 4.5). The particles measured were found to all be larger than 0.25 μm. This meant the polarisation of particles in the powder was stable under ambient or experimental conditions. 34 of the particles were measured to have a size larger than 1.25 μm. Size effects are only typically significant in ferroelectrics at dimensions below 1 μm and so the polarisation of majority of the particles can be estimated to be close to that of bulk material (78 μC cm^{-2}). The polarisation of the particles smaller than 1 μm may be decreased compared to that of bulk material due to size effects. BET analysis of the LN powder measured the surface area to be 0.6 m^2 g^{-1}.

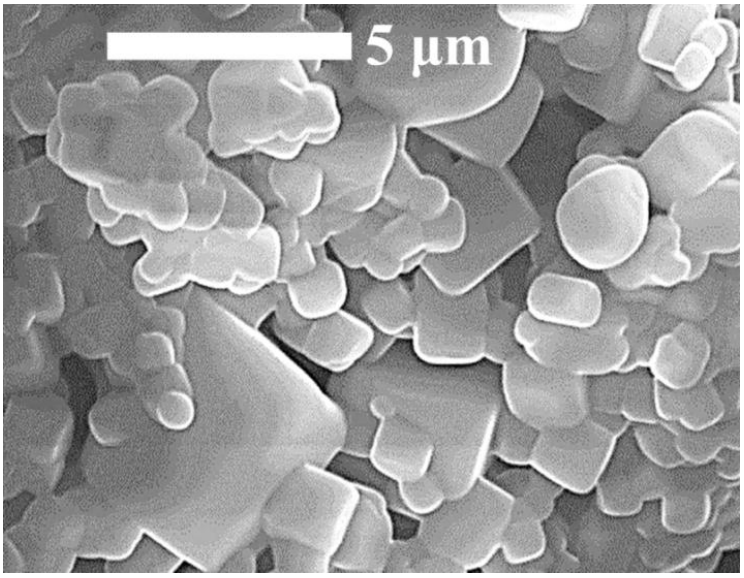

Figure 4.4 SEM images of lithium niobate powder (LN)

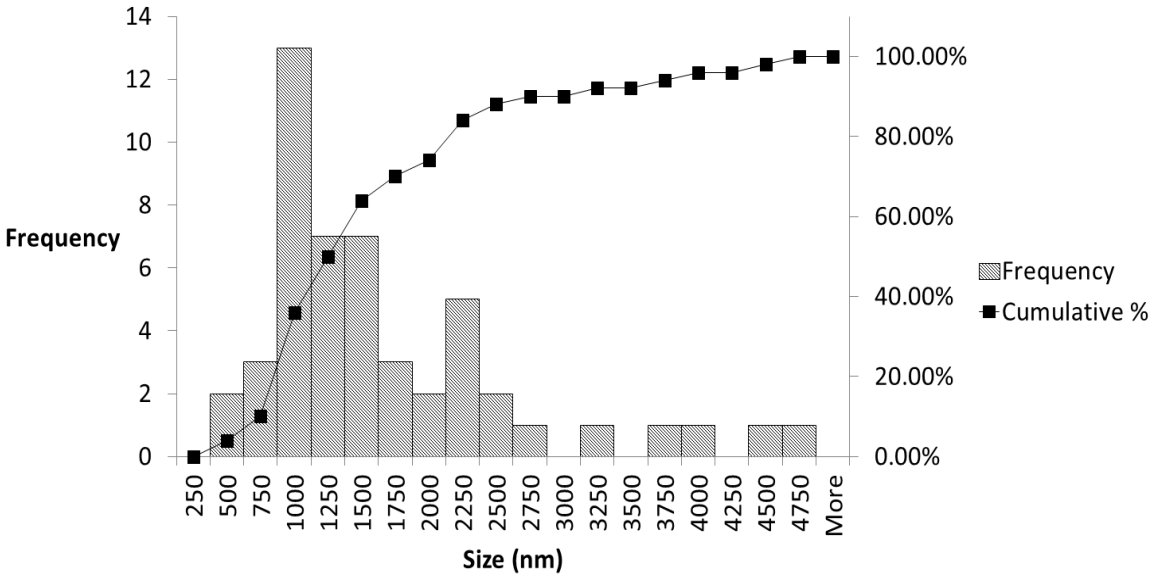

Figure 4.5 Histogram showing the size distribution of particles in the lithium niobate powder (LN)

4.4 Powders of lithium niobate (SLN), magnesium doped lithium niobate (MgLN) and iron doped lithium niobate (FeLN)

High purity optical grade slides of single crystal lithium niobate (SLN) or 5% magnesium doped single crystal lithium niobate (MgLN) and polycrystalline bulk samples of 0.05 % iron doped lithium niobate (FeLN) were purchased. Using a Radiant Technologies RT66 meter the polarisation of the bulk samples of SLN was measured to be 78 μC cm^{-2}, the polarisation of bulk samples of FeLN was measured to be 72 μC cm^{-2} and the polarisation of bulk samples of MgLN was measured to be 65 μC cm^{-2}. The bulk materials were ground using a mortar and pestle to produce fine particle powders. SLN was prepared by this method in addition to doped materials to allow comparison of the photocatalytic properties of doped and undoped material. For ferroelectric perovskite crystals in which there is a change in the crystal class at the ferroelectric phase transition, application of external stress can result in realignment of the unit cell orientation to drive ferroelastic depolarisation. The external stress of grinding a poled ferroelectric perovskite crystal, therefore, may produce a powder of which the particles have a polydomain structure. The crystal class of lithium niobate does not change at the ferroelectric phase transition. This means that application of external stress does not result in a realignment of the unit cell orientation or the dipole in lithium niobate crystals. Consequently the external stress exerted upon bulk lithium niobate samples when ground to produce powders did not result in ferroelastic depolarisation occurring. The powders particles instead retained the domain structure of the bulk samples. As SLN or MgLN powders were prepared from single crystal samples the powders particles also had a single domain structure. FeLN powder was prepared from a polydomain crystal and so the powders particles also had a polydomain structure. . The size distributions were determined by collecting SEM images of the powders (Figure 4.6) and measuring 50 of the particles. The histogram showing particle size distribution of SLN powder is shown in Figure 4.7, the histogram of particles of FeLN powder is shown in Figure 4.8 and the size distribution of particles in MgLN powder is shown in Figure 4.9. All three powders contained particles larger than 1 μm but in each case the majority of particles were below 1 μm. The

histograms show the percentage of particles larger than 150 nm was 68 % in SLN powder, 74 % in FeLN powder and 76 % in MgLN powder. The majority of particles in the three powders are, therefore, in a stable ferroelectric phase under experimental or ambient conditions. As the ferroelectric critical size of lithium niobate is not known some of the particles smaller than 150 nm may also be in the paraelectric phase. The polarisation of particles larger than 1 µm is again likely to be close to those of the respective bulk material as size effects are not significant. In particles below 1 µm the polarisation would be expected to be diminished compared to bulk material as a result of size effects. The comparable size distribution of SLN, MgLN and FeLN powders may mean that the extent to which size effects decrease the polarisation is similar in the powders. BET analysis of the powders measured the surface area to be 1.4, 0.8 and 1.3 $m^2 g^{-1}$ for SLN, FeLN and MgLN powders respectively.

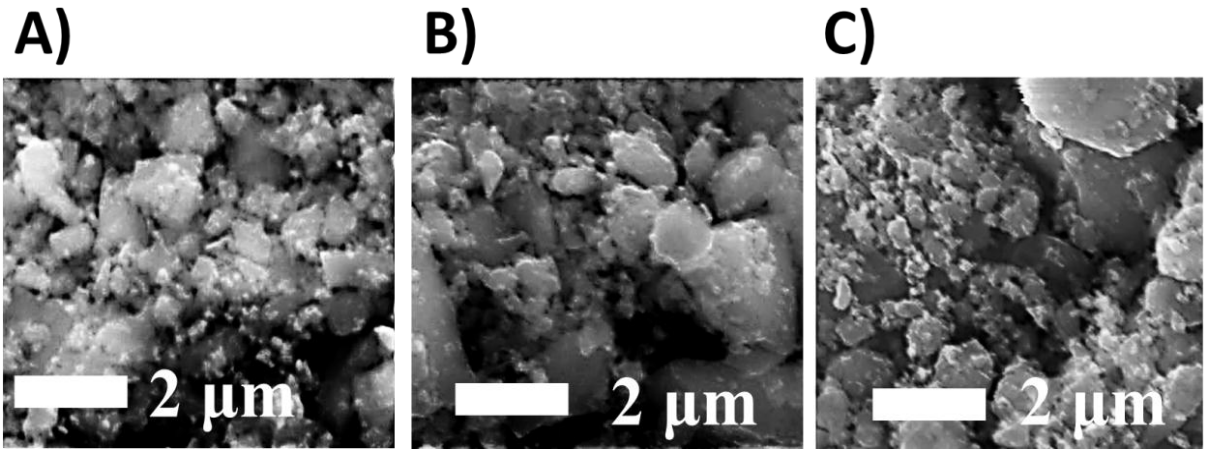

Figure 4.6 SEM images of a) lithium niobate powder (SLN), b) magnesium doped lithium niobate (MgLN) and c) iron doped lithium niobate (FeLN) prepared by grinding bulk samples

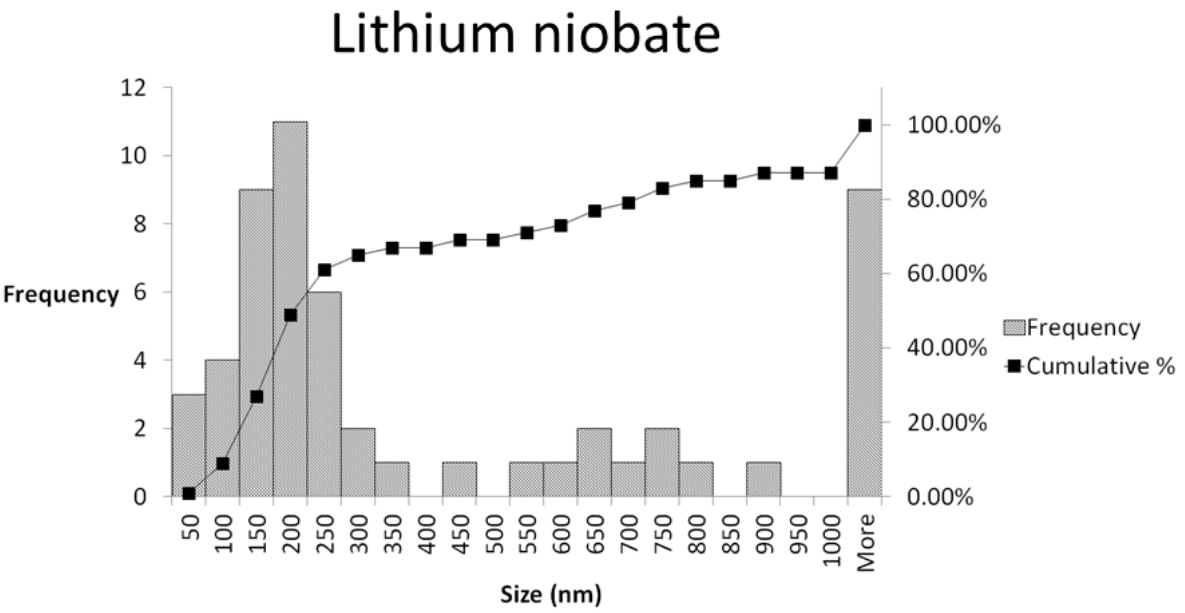

Figure 4.7 Histogram showing the size distribution of particles in the lithium niobate powder (SLN)

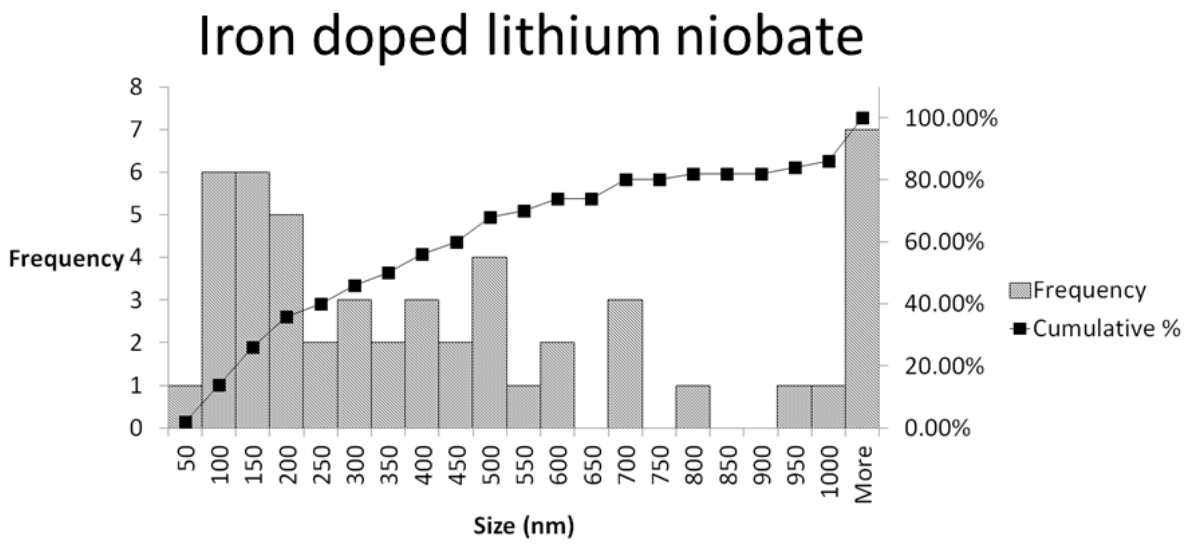

Figure 4.8 Histogram showing the size distribution of particles in the iron doped lithium niobate powder (FeLN)

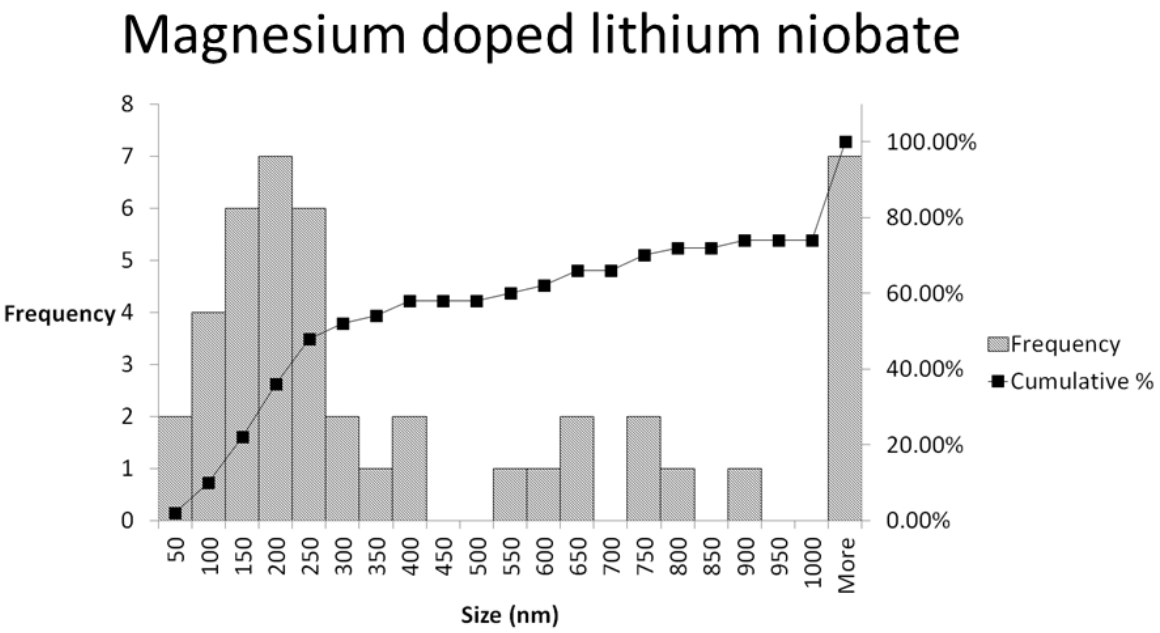

Figure 4.9 Histogram showing the size distribution of particles in the magnesium doped lithium niobate powder (MgLN)

4.5 Titanium dioxide powder (TiO_2)

Titanium dioxide powder is one of the most widely studied semiconductor materials for use in photocatalytic reactions[8; 148]. Titanium dioxide powder was purchased and used in experiments to draw comparison between the properties of ferroelectric materials and a non-polar semiconductor. An SEM image collected of the powder showed the average particle size to be 200nm (Figure 4.10). Nitrogen adsorption BET analysis has reported the surface area of the powder purchased to be between 8.9-10.0 $m^2 g^{-1}$ [149;150].

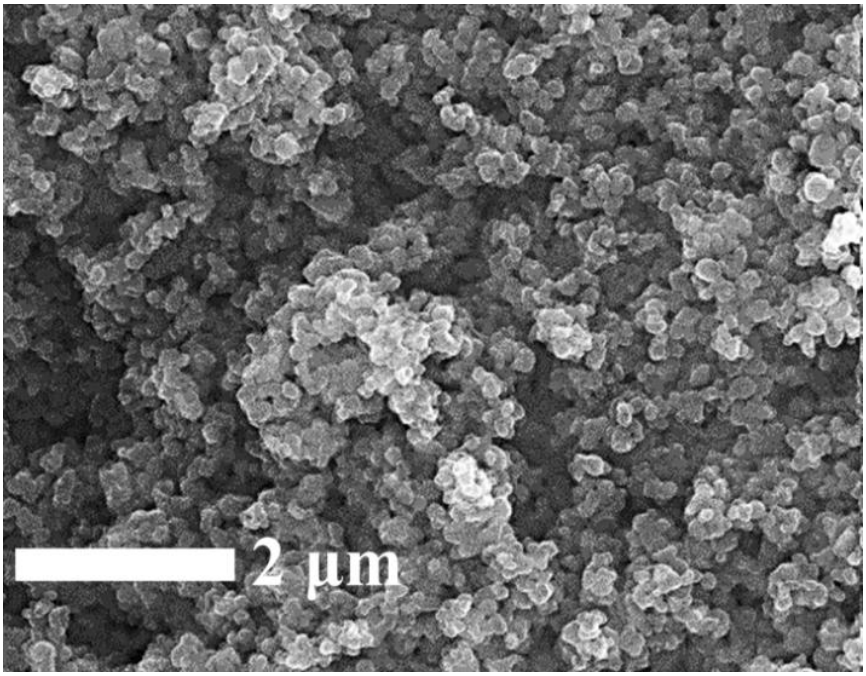

Figure 4.10 SEM image of titanium dioxide powder with a particle size of 200nm

4.6 Summary

Powders of barium titanate (BT), lithium niobate (LN, SLN) and magnesium or iron doped lithium niobate (MgLN, FeLN) were prepared for use in experiments. The sizes of particles of LN powder were sufficiently large to maintain a stable ferroelectric phase under experimental conditions and exhibit a polarisation close to that of bulk material. The size distributions of BT powder showed the particles were above the ferroelectric critical size but that up to 16 % of particles undergo a thermally driven transition to the paraelectric phase when illuminated by UV or simulated solar light. The size distribution of SLN, FeLN and MgLN powders showed that between 24-32 % of the particles may be smaller than the ferroelectric critical size, however, the majority of particles exhibit a stable polarisation under ambient or experimental conditions. The polarisation of particles of BT, SLN, FeLN and MgLN powders were proposed to be reduced compared to that of the respective bulk material as a result of size effects.

5 Adsorption of dye molecules in the double layer at ferroelectric surfaces

5.1 Introduction

Adsorption of polar species at the surface of ferroelectric materials has been reported to be polarisation dependent[74]. The orientation of the polarisation of barium titanate thin films has been shown to alter the quantity of polar molecules that are physisorbed or chemisorbed[75]. This property has potential applications in photocatalytic reactions. Reactions are typically initiated after adsorption takes place at the surface of the photocatalyst[151]. The quantity of dye adsorbed at the surface has been suggested to alter the rate of reactions over semiconductor photocatalysts[111; 112; 152-154]. As photochemical reduction occurs at C+ domains and photochemical oxidation reactions occur at C- domains over ferroelectric materials the preferential adsorption of species at either domain may allow the pathway of photocatalytic reactions to be controlled. In this chapter ferroelectric powders were suspended in aqueous solutions of acid black 1 or rhodamine b. Both of these dyes represent typical pollutants released in industrial effluents. The change in the concentration of dye solutions after addition of ferroelectric powders was used to investigate the influence of the surface charge upon adsorption of dye ions in the double layer.

5.2 Results

5.2.1 Comparison of adsorption of rhodamine b ions by BT, LN or TiO_2 powders

BT, LN or TiO_2 powders were placed in aqueous rhodamine b solution (0.5g L^{-1}, 200 mL). Addition of the powders was found to cause a decrease in the peak absorbance of the solutions. This was attributed to dye molecules being adsorbed into the double layer at the powders surfaces, decreasing the concentration of the solution. The relative quantity of dye molecules adsorbed by BT, LN and TiO_2 powders was compared after adsorption/desorption

processes had reached equilibrium. The experiment was performed twice using each powder. The percentage decrease in dye concentration after addition of powders was found to be repeatable to 2 significant figures. The concentration of the dye solution was found to decrease by 13 % after addition of BT powder; 13 % after addition of TiO_2 powder and by 8 % after addition of LN powder (Table 5.1).

Table 5.1 Decrease in concentration of rhodamine b solution after addition of powders of BT, LN or TiO_2

Powder	Surface area ($m^2 g^{-1}$)	Decrease in rhodamine b solution concentration (%)	Estimated experimental error (%)
LN	0.6	8	± 1
BT	0.7	13	± 1
TiO_2	8.9-10.0	13	± 1

5.2.2 Impact of photochemical deposition of silver particles at the surface of BT or LN powders upon adsorption of rhodamine b ions

The effect that photochemical deposition of silver particles at the surface of LN or BT powders had upon the adsorption of dye molecules was investigated. LN or BT powders were suspended in silver nitrate solution (2.5 g L^{-1}, 100 mL) and illuminated by UV light for 20 min. After illumination powders had changed from being white in colour to grey. The colour change showed indication of formation of a surface coating. X-ray photoelectron spectroscopy (XPS) is a spectroscopic technique that measures the elemental composition and the chemical state and electronic state of elements that comprise the surface of a material. XPS analysis is carried out by irradiating a material with an X-ray beam and measuring the number of electrons and their kinetic energy that escape from the top 1-10 nm of the materials surface. XPS analysis of the LN or BT powders detected binding energies at 368 eV and 376 eV which correspond to silver in

the metal state (Ag^0) (Figure 5.1). This confirmed the surface coating on the powders to be silver metal and showed that the photochemically deposited silver had not reacted to form silver oxide (Ag_2O).

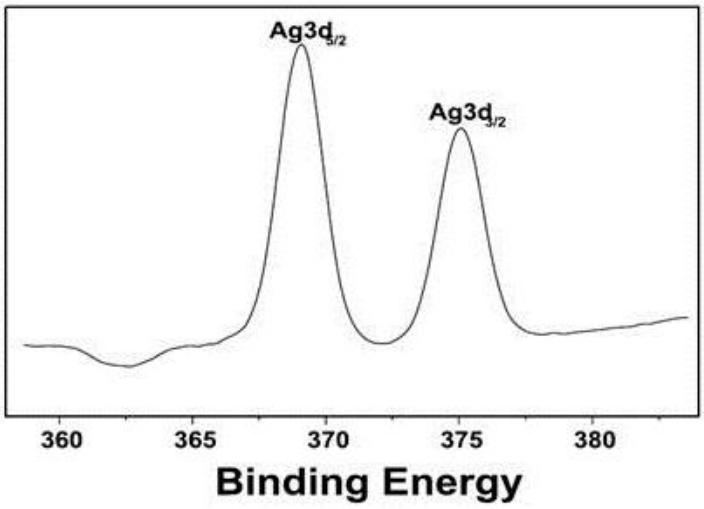

Figure 5.1 XPS scan showing peaks at binding energies corresponding to silver in the metal state at the surface of BT or LN powders

Silver modified LN or BT powders were added to rhodamine b solution (0.5 g L^{-1}, 200 mL) and the change in concentration measured. The experiment was performed twice for each powder. The percentage decrease in dye concentration was found to be repeatable to 2 significant figures. The silver modified BT or LN powders produced a smaller decrease in concentration of the dye solution compared to unmodified BT or LN powders. Addition of silver modified LN powder decreased the solutions concentration by 6 %. The total decrease in concentration of the dye solution was 75 % of that produced by addition of unmodified LN powder (8 %). Addition of silver modified BT powder decreased the concentration by 7 %. The total decrease in concentration was 54 % of that when unmodified BT powder was added to the dye solution (13 %).

5.2.3 Comparison of adsorption of rhodamine b or acid black 1 ions by SLN, MgLN or FeLN powders

The change in concentration of acid black 1 and rhodamine b solutions after addition of SLN, MgLN or FeLN powder (1.5 gL^{-1}, 40mL) was also compared (Table 5.2). The experiment was performed twice for each powder using rhodamine b or acid black 1 solution. The percentage decrease in the dye concentration was found to be repeatable within 2 significant figures when powders were added to solutions of either acid black 1 or rhodamine b. Decrease in concentration of rhodamine b solution was greater than the decrease in concentration of acid black 1 solution after SLN, MgLN or FeLN powders were added (Table 5.2). Comparison showed addition of MgLN or FeLN powders caused a larger decrease in concentration of rhodamine b or acid black 1 solution than addition of SLN powder (Table 5.2). Decrease in concentration of rhodamine b solution was greater after addition of FeLN powder (17 %) than MgLN powder (16 %). Addition of MgLN powder produced a larger decrease in concentration of acid black 1 solution (15 %) than FeLN powder (14 %).

Table 5.2 Decrease in absorbance of rhodamine b or acid black 1 solution after addition of SLN, FeLN or MgLN powder

Powder	Surface area ($m^2 g^{-1}$)	Decrease in acid black 1 solution absorbance (%)	Decrease in rhodamine b solution absorbance (%)	Estimated experimental error (%)
SLN	1.4	10	11	± 1
FeLN	0.8	14	17	± 1
MgLN	1.7	15	16	± 1

5.3 Discussion

5.3.1 Adsorption rhodamine b ions at semiconductor and ferroelectric surfaces

In aqueous solution rhodamine b dissolves to form a positive ion and a negative chlorine counter ion (Figure 5.2). The dimensions of rhodamine b ions are reported to be 1.44 x 1.09 x 0.64 nm by experimental investigation[155]. In comparison chlorine ions are reported to have a diameter of 0.4 nm and water molecules to have a diameter of 0.3 nm[156].

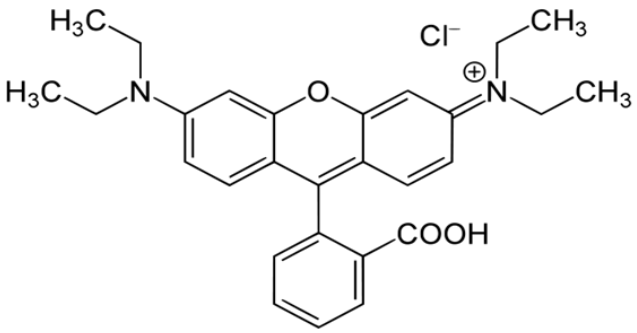

Figure 5.2 Structure of rhodamine b dye

A scheme showing the double layer formed at the interface between a metal oxide semiconductor and aqueous rhodamine b solution is shown in Figure 5.3. The semiconductor surface is non-polar and so electrostatic interaction between ionic species and the surface are weak. Few or no ions are specifically adsorbed in the inner Helmholtz layer (Figure 5.3). The inner Helmholtz layer is filled with hydroxyl species specifically adsorbed at metal sites (M-OH) (Figure 5.3). The hydroxyl species can dissociatively form positive ($M\text{-}OH_3^+$) or negatively charged species ($M\text{-}OH^-$). If the solutions pH is above the metal oxides isoelectric point the majority of the hydroxyl species are negative. If the pH is below the isoelectric point of the metal oxide the majority of hydroxyl species are positively charged. The charge of the hydroxyl species in the inner Helmholtz layer determines the structure of the outer Helmholtz layer. Negative hydroxyl species in the inner Helmholtz layer drive electrostatic attraction with solvated positive rhodamine b ions. The rhodamine b ions undergo conformational changes to allow the positive nitrogen ion to be bound in the

outer Helmholtz layer (Figure 5.3). Positive hydroxyl species in the inner Helmholtz layer attract solvated chlorine ions that become bound in the outer Helmholtz layer (Figure 5.3).

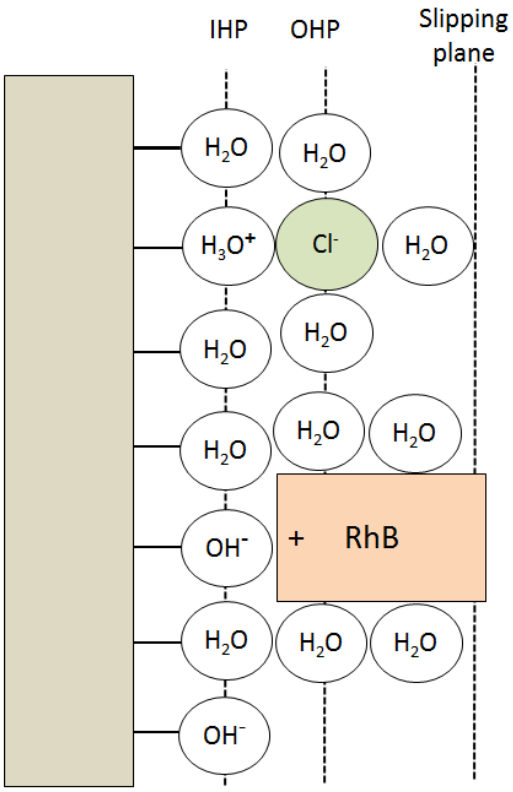

Figure 5.3 Scheme showing a possible structure of the double layer formed at the interface between a metal oxide semiconductor and aqueous rhodamine b solution. As the semiconductor surface is non-polar few or no ions are adsorbed in the inner Helmholtz layer (IHP) through electrostatic interactions. The IHP is populated by non-dissociatively adsorbed neutral water molecules and positive hydroxyl species (H_3O^+ hydronium ions) and negative hydroxyl species (OH^-, hydroxyl ions) formed by dissociative adsorption of water molecules. In the outer Helmholtz layer (OHP) solvated positive rhodamine b ions (RhB^+) are adsorbed through electrostatic interactions with negative hydroxyl ions (OH^-) in the inner Helmholtz plane. Solvated chlorine ions (Cl^-) are adsorbed in the OHP through electrostatic interactions with hydronium ions (H_3O^+) in the inner Helmholtz plane. The slipping plane marks the boundary beyond which, when the solid moves, species in the double layer do not move with the surface and instead remain in the bulk solution

In unpoled ferroelectric materials an approximately equal number of C+ and C- domains form below the Curie point. LN and BT powders were not polarised by the manufacturer and FeLN powder was prepared from unpolarised bulk material and so all three powders were assumed to have an approximately equal number of domains in each axis. SLN and MgLN powders were prepared from single crystal bulk samples and, as was discussed in Chapter 4, were not depolarised. These powders had a single domain. A scheme showing the double layer formed at the interface between the C+ or C- domains of a ferroelectric in contact with aqueous rhodamine b solution is shown in Figure 5.4. At the surface of ferroelectric metal oxides the inner Helmholtz layer is also largely filled by hydroxyl species bound at metal sites. However, oppositely charged ions or polar species are preferentially adsorbed in the inner Helmholtz layer to externally screen the surface charge (Figure 5.4). The structure of the outer Helmholtz layer is determined by the charge of hydroxyl species and the ionic species bound in the inner Helmholtz layer. At C+ domains chlorine ions become specifically bound in the inner Helmholtz layer (Figure 5.4). In the outer Helmholtz layer solvated chlorine ions are adsorbed at positive hydroxyl species in the inner Helmholtz layer. Solvated rhodamine b ions are adsorbed by negative hydroxyl species or chlorine ions bound in the inner Helmholtz layer (Figure 5.4). At C- domains rhodamine b ions undergo conformational changes to become adsorbed in the inner Helmholtz layer (Figure 5.4). In the outer Helmholtz layer solvated rhodamine b ions are bound by negative hydroxyl species in the inner Helmholtz layer. Solvated chlorine ions are adsorbed in the outer Helmholtz layer by rhodamine b ions or positive hydroxyl species in the inner Helmholtz layer (Figure 5.4).

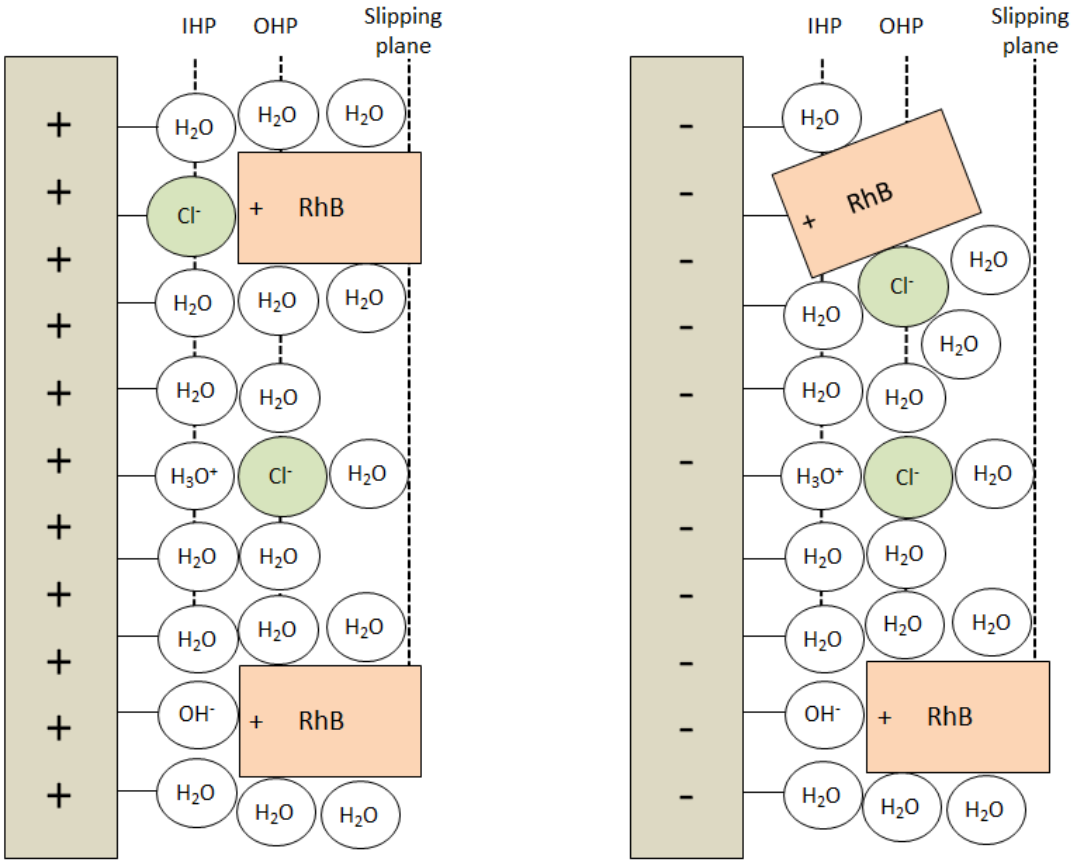

Figure 5.4 Scheme showing a possible structure of the double layer formed between a C+ (left) or C- (right) domain of a ferroelectric and aqueous rhodamine b solution. The ferroelectric surface charge causes oppositely charged ions to be preferentially adsorbed in the inner Helmholtz layer (IHP). As the surface charge is positive at C+ domains and negative at C- domains the structure of the double layer formed at these surfaces are different. At the C+ face the IHP is filled with chlorine ions (Cl^-), neutral undissociated water molecules and positive (H_3O^+) and negative (OH^-) hydroxyl species formed by dissociative adsorption of water. The outer Helmholtz layer (OHP) comprises solvated rhodamine b ions (RhB^+) adsorbed through interactions with chlorine ions (Cl-) or negative hydroxyl species in the IHP and solvated chlorine ions adsorbed through interactions with positive hydroxyl species in the IHP. At the C- face the IHP comprises rhodamine b ions, undissociated water molecules and positive and negative hydroxyl species formed by dissociative adsorption of water. In the OHP solvated chlorine ions are adsorbed through interactions with rhodamine b ions or positive hydroxyl species in the IHP and solvated

rhodamine b ions are adsorbed through interactions with negative hydroxyl species in the IHP.

5.3.2 Adsorption of rhodamine b ions at the surface of BT, LN or TiO_2 powders

The number of active sites at the surface of a metal oxide i.e. metal or oxygen atoms at the surface at which adsorbates can become bound, depends upon the materials morphology and composition. It is, however, generally true that as the surface area of a material increases more active sites are exposed. The surface area of BT powder was measured to be 0.7 m^2 g^{-1} while the surface area of TiO_2 powder is reported to be 8.9-10.0 m^2 g^{-1} (Table 5.1). The smaller specific surface area of BT powder means it can be assumed to have a lower number of active surface sites than TiO_2 powder. In experiments the decrease in concentration of rhodamine b solutions was found to be similar when BT powder was placed in the solution (13 %) to when TiO_2 powder was added (13 %) (Table 5.1). Adsorption of rhodamine b ions per active site at the surface of BT powder was, therefore, greater in comparison to TiO_2 powder. As TiO_2 powder has a non-polar surface the adsorption of rhodamine b ions was determined by the charge of the hydroxyl species in the inner Helmholtz layer. The isoelectric point of titanium dioxide powders has been reported to decrease with increasing particle size. The isoelectric point of particles with a size of 16 nm is reported to be 6 while the isoelectric point of particles with an average size of 104 nm is reported to be 4[157]. The powder used in this work had an average particle size of 200 nm, as discussed in Chapter 4, so the isoelectric point can be estimated to be 4 or lower. The pH of the rhodamine b solution was measured to be 6.4. As this is above the estimated isoelectric point of the TiO_2 powder the inner Helmholtz layer had a net negative charge. Electrostatic interactions between the negatively charge inner Helmholtz layer and solvated positive rhodamine b ions caused the dye to be adsorbed in the outer Helmholtz layer. In Chapter 4 a histogram of the distribution of measured particle sizes of BT powder showed the highest frequency was for particles with size between 0.85-1.15 µm. The isoelectric point of barium titanate powder with a particle size of 1 µm is reported to be 4.3[158] and so the isoelectric point of BT powder was

assumed to be similar. This meant the inner Helmholtz layer at the surface of BT powder also had a net negative charge that attracted solvated rhodamine b ions into the outer Helmholtz layer. The greater adsorption of dye ions per active site by BT powder compared to TiO_2 powder may partly be attributed to the relative isoelectric points of the materials. If the actual isoelectric point of BT was lower than that of TiO_2 powder then the negative charge produced in the inner Helmholtz layer may be comparatively higher. This would be expected to increase adsorption of solvated rhodamine b ions in the outer Helmholtz layer. The greater adsorption of rhodamine b ions by BT powder can also be explained by the surface charge that was estimated to be between 20.7-26.4 μC cm^{-2} at ambient conditions as discussed in Chapter 4. Compared to non-polar TiO_2 powder the surface charge increased specific adsorption of ions in the inner Helmholtz layer. At C- domains the surface charge increased the number of rhodamine b ions specifically bound in the inner Helmholtz layer. At C+ domains specific adsorption of chlorine ions in the inner Helmholtz layer increased the negative charge of the inner Helmholtz layer. As a result electrostatic attraction between solvated rhodamine b ions and the inner Helmholtz layer were increased to produce greater adsorption of dye ions (Figure 5.4).

As discussed in chapter 4 the surface charge of particles in LN powder were estimated to be close to that of bulk material (78 μC cm^{-2}) and greater than of particles in BT powder (20.7-26.4 μC cm^{-2}). If the surface charge of BT powder was the primary factor that increased adsorption of rhodamine b ions per surface site compared to TiO_2 powder it would be expected that the greater surface charge of particles of LN powder would adsorb more dye ions than BT powder. However, the decrease in concentration of the rhodamine b solution after addition of LN powder (8 %) was less than when BT powder was added (13 %) (Table 5.1). This may be the result of several factors. Firstly, the different composition and morphology of LN powder may produce fewer active sites compared to that of BT powder. This would mean that although LN powder was measured to have a similar surface area (0.6 m^2 g^{-1}) to BT powder (0.7 m^2 g^{-1}) adsorption in the double layer may be decreased. Secondly, the isoelectric point

of lithium niobate has not been reported and was not determined in experiments. If the isoelectric point of LN powder was greater than the pH of the solution the inner Helmholtz layer would have a net positive charge. This would cause electrostatic repulsion between positive solvated rhodamine b ions and the inner Helmholtz layer resulting in decreased adsorption in the outer Helmholtz layer. Lastly the greater surface charge of LN particles compared to particles of BT powder may have in fact decreased adsorption of ionic species in the double layer. Simulation of the capacitance in the double layer at charged surfaces has shown that at low ionic density the capacitance initially increases with surface charge before reaching a maximum[82]. Capacitance then decreases with further increase in surface charge. The solutions used had a concentration of 10 ppm. The low concentration may have meant that the surface charge had a similar effect to in simulations of charged surfaces with the greater surface charge of LN powder above the maximum causing decreased capacitance in the double layer whereas BT powders surface charge was below the maximum capacitance increasing the double layer capacitance compared to non-polar TiO_2 powder.

5.3.3 Comparison of adsorption of rhodamine b ions by LN and SLN powders

The decrease in concentration of rhodamine b solutions after addition of LN or SLN powders was investigated under different experimental conditions. 1.5 g L^{-1} of SLN powder was placed in 40 mL of rhodamine b solution and 0.5 g L^{-1} of LN powder was placed in 200 mL of rhodamine b solution. It was expected SLN powder would produce a significantly greater decrease in concentration of the rhodamine b solution than LN powder. SLN powder had a larger surface area (1.4 m^2 g^{-1}) than LN powder (0.6 m^2 g^{-1}). It can be assumed that there are a greater number of active sites at the surface of SLN powder than LN powder. In experiments the loading of SLN powder used (1.5 g L^{-1}) was three times the loading of LN powder used (0.5 g L^{-1}). The larger loading of SLN powder would be expected to cause greater adsorption of rhodamine b ions. The volume of

solution used in investigation of SLN powder (40 mL) was also lower than in investigation of LN powder (200 mL). This meant that each dye molecule adsorbed by SLN powder produced a larger decrease in concentration of rhodamine b solution in comparison to each molecule adsorbed by LN powder. Results showed the decrease in concentration after addition of SLN powder (11 %) was greater than after addition of LN powder (8 %). However, the difference was only 3 %. The small difference in the decrease in concentration suggested that, per active surface site, LN powder had adsorbed more rhodamine b ions than SLN powder. This may be explained by difference in the isoelectric point of the powders. The isoelectric point of a material is typically affected by particle size. In Chapter 4 histograms of the particle size distribution showed 70 % of the particles of SLN powder to be smaller than 0.4 μm. For LN powder the size distribution showed 64 % of particles to be larger than 1.0 μm. If the isoelectric point of LN powder was lower than that of SLN powder this would reduce the positive charge or increases the negative charge in the inner Helmholtz layer compared to SLN powder. As a result electrostatic attraction between in the inner Helmholtz layer would increase or electrostatic repulsion between positive rhodamine b ions and the inner Helmholtz layer would decrease to result in greater adsorption. Another factor may be size effects present in particles of SLN powder. The size distribution of LN powder in Chapter 4 showed that all particles were all above the ferroelectric critical size. The majority of particles were also larger than 1.0 μm. As size effects that decrease the polarisation of a ferroelectric are typically not significant above 1.0 μm the particles polarisation was assumed to be close to that of bulk material. For SLN powder the size distribution of particles in Chapter 4 showed up to 12 % of the particles may be below the ferroelectric critical size and so in the paraelectric phase. The majority of particles were also below 0.4 μm which meant size effects would be expected to decrease the particles polarisation in relation to bulk material. As SLN powder comprised particles with a decreased polarisation and particles in the paraelectric phase the electrostatic interactions with rhodamine b and chlorine ions in solution may be reduced compared to the interactions between

particles of LN powder and the ions in solution resulting in lower retention of ions in the double layer.

5.3.4 The effect of silver deposition at the surface of LN and BT powders upon rhodamine b ion adsorption

After photochemical deposition of silver nanoparticles at the surface of LN or BT powders the adsorption of rhodamine b ions was lower than compared to unmodified powder. The total adsorption of rhodamine b ions by silver modified BT powder was 56 % of that by unmodified BT powder. The total adsorption of rhodamine b ions by silver modified LN powder was 63 % that of unmodified LN powder. Spatial separation of redox reactions at ferroelectric surfaces meant that the silver nanoparticles formed at C+ domains of BT or LN powders with few or no deposits produced at C- domains. The decrease in dye adsorption can be attributed to the effect of silver deposition on the structure of the double layer at C+ domains. Silver nanoparticles are reported to have a negative zeta potential[159; 160; 161]. At C+ ferroelectric domains solvated rhodamine b ions are adsorbed in the outer Helmholtz layer by negatively charged species in the inner Helmholtz layer i.e. negative hydroxyl species, silver particles or chlorine ions (Figure 5.5).

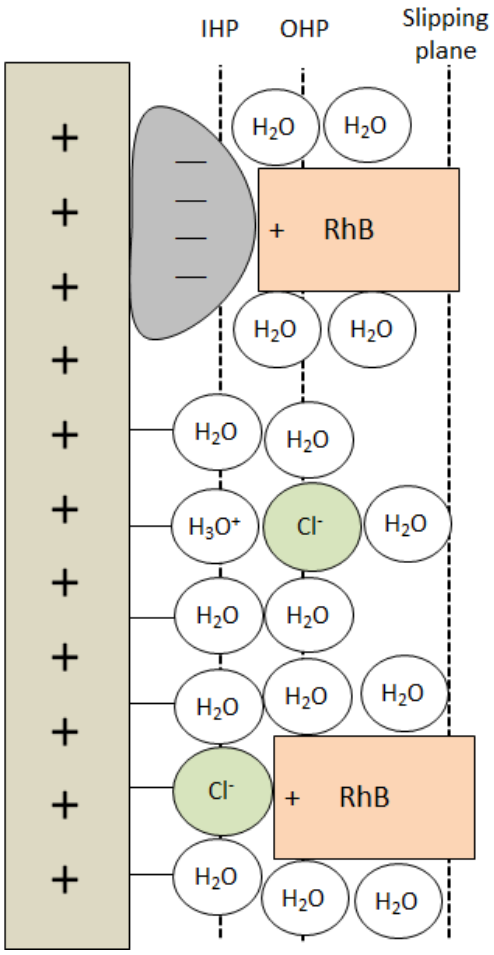

Figure 5.5 Scheme showing the possible structure of the double layer at the surface of a positive ferroelectric domain after deposition of silver particles. The negative silver particles adsorb positive solvated rhodamine b ions (RhB^+) in the outer Helmholtz layer.

Deposition of negative metal particles externally screens the C+ domains surface charge (Figure 5.5). This meant the number of chlorine ions specifically bound in the inner Helmholtz layer was decreased after silver deposition. The decrease in retention of rhodamine b ions after metal deposition can be explained by the surface charge of silver deposits producing a weaker electrostatic attraction with solvated rhodamine b ions than chlorine ions adsorbed in the inner Helmholtz layer of the unmodified powder.

5.3.5 Adsorption of acid black 1 and rhodamine b ions at the surface of SLN powder

When dissolved in aqueous solutions acid black 1 forms a negative ion and positive sodium counter ion (Figure 5.6). The diameter of a sodium ion is 0.3 nm[156]. The size of acid black 1 ions has not been reported. It would be expected the acid black 1 ions have dimensions of the same order of magnitude to rhodamine b ions as both molecules comprise a comparable number of conjugated rings and functional groups (Figure 5.6).

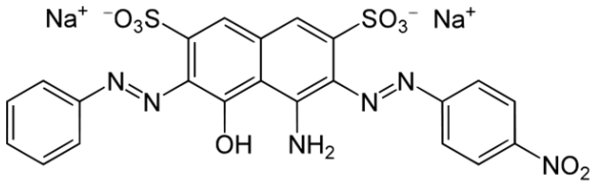

Figure 5.6 Acid black 1 molecule

A scheme showing adsorption of acid black 1 ions in the double layer at the interface of C+ and C- ferroelectric domains is shown in Figure 5.7. Acid black 1 ions are specifically adsorbed in the inner Helmholtz layer at C+ domains and as solvated ions in the outer Helmholtz layer at C- domains. Solvated acid black 1 ions are adsorbed in the outer Helmholtz layer by positive hydroxyl species or sodium ions in the inner Helmholtz layer (Figure 5.7).

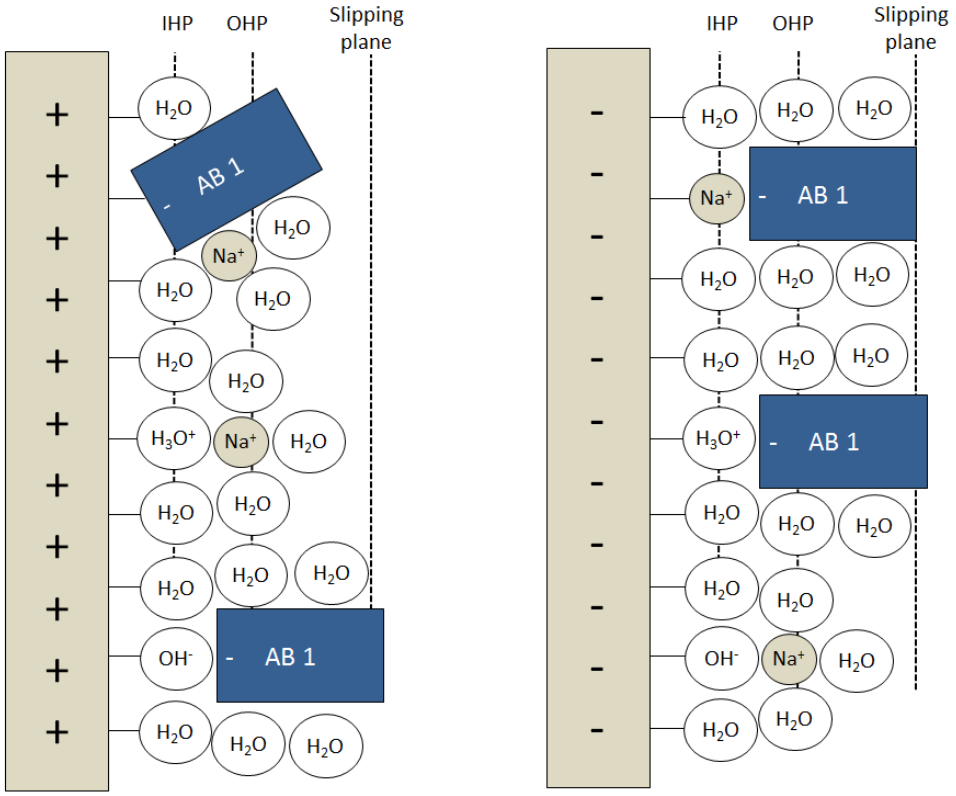

Figure 5.7 Scheme showing a possible structure of the double layer formed between a C+ (left) or C- (right) domain of a ferroelectric and aqueous acid black 1 solution. At the C+ face the inner Helmholtz layer (IHP) is filled with acid black 1 ions (AB 1^-), neutral undissociated water molecules and positive (H_3O^+) and negative (OH^-) hydroxyl species formed by dissociative adsorption of water. The outer Helmholtz layer (OHP) comprises solvated sodium ions (Na^+) adsorbed through interactions with acid black 1 ions or negative hydroxyl species in the IHP and solvated acid black 1 ions that are adsorbed through interactions with positive hydroxyl species in the IHP. At the C- face the IHP comprises sodium ions, undissociated water molecules and positive and negative hydroxyl species formed by dissociative adsorption of water. In the OHP solvated acid black 1 ions are adsorbed through interactions with sodium ions or positive hydroxyl species in the IHP and solvated sodium ions are adsorbed through interactions with negative hydroxyl species in the IHP.

SLN powder was prepared from single crystal bulk samples. As discussedin Chapter 4 ferroelastic depolarisation did not occur in the lithium niobate

samples as a result of the stress of grinding and so the particles of SLN powder also have a single domain structure with a single C+ and C- face. Ions of rhodamine b and acid black 1 have different structures, acid black 1 ions are negatively charged whereas rhodamine b ions are positively charged. As a result rhodamine b ions or acid black 1 ions experienced different electrostatic interactions with the surface charge at the C+ or C- face of SLN powder particles. The quantity of acid black 1 or rhodamine b ions specifically adsorbed in the inner Helmholtz layer at the surface of either a C+ or C- face would, therefore, be expected to be different. The quantity of the ions adsorbed in the outer Helmholtz layer would also be expected to differ. The pH of acid black 1 solution was measured to be 5.9, close to that of rhodamine b solution of 6.4. Compared to when suspended in acid black 1 solution the inner Helmholtz layer of SLN powder would had a smaller positive or greater negative charge in rhodamine b solution as a result. The inner Helmholtz layer charge would, however, be comparable to in Acid black 1 solution. As the molecules are of opposite charge if the inner Helmholtz layer had a net positive charge adsorption of negative acid black 1 ions would be greater in the outer Helmholtz layer than positive rhodamine b ions. If the inner Helmholtz layer had a net negative charge adsorption of rhodamine b ions would be expected to be greater than acid black 1 ions. When SLN powder was placed in acid black 1 solution the concentration decreased by 10 % and when placed in rhodamine b solution the concentration decreased by 11 %. This indicated a similar quantity of both dyes was adsorbed in the double layer at the surface of the SLN powder. As discussed the quantity of acid black 1 and rhodamine b ions would be expected to be different if electrostatic interactions were the main factor driving adsorption. The similar amount of dyes adsorbed suggests the structure of the dye ions are significant in determining the quantity adsorbed as well as the electrostatic interactions with the surface charge. For the charged atoms of the dye ions to be adsorbed in the inner or outer Helmholtz layer as a result of electrostatic interactions with the surface charge of the ferroelectric the ions had to undergo conformational changes. If the dye ion that experienced greater electrostatic attraction with the surface charge and inner Helmholtz layer

experienced greater steric hindrance preventing the charge atom from being adsorbed at the surface this would reduce the quantity retained in the double layer. The similar amount of acid black 1 and rhodamine b ions adsorbed by SLN powder suggests that steric hindrance was significant in determining retention of dye ions.

5.3.6 Adsorption of rhodamine b and acid black 1 ions by SLN, MgLN and FeLN powders

As discussed in Chapter 4 the polarisation of bulk MgLN and FeLN was measured to be 65 μC cm^{-2} and 72 μC cm^{-2} respectively. These materials polarisation is lower than that of undoped lithium niobate measured to be 78 μC cm^{-2}. This may be a result of doping increasing the total number of mobile carriers able to internally screen the surface potential. Changes in the unit cell may also have affected the formation of the spontaneous polarisation or the long range ordering of the polarisation in the doped materials. Doping with iron increases lithium niobates n-type character and doping with magnesium increases its p-type character. Due to the action of internal depolarisation fields in lithium niobate this meant doping in MgLN increased screening at C- domains and in FeLN screening increased at C+ domains. The powders of MgLN, FeLN or SLN all had comparable particle sizes as discussed in Chapter 4. Size effects reducing the polarisation in the powders would be expected to be similar in all three powders. The polarisation of the powders can be assumed to reflect that of the bulk materials with SLN powder exhibiting the greatest polarisation followed by FeLN powder and MgLN powder producing the lowest polarisation. In the case of both MgLN and FeLN powders the smaller polarisation compared to SLN powder would be expected to decrease adsorption of acid black 1 or rhodamine b ions. The decreased charge at C- domains of MgLN powder would be expected to reduce specific adsorption of rhodamine b ions in the inner Helmholtz layer. In acid black 1 solution the number of sodium ions adsorbed in the inner Helmholtz layer at C- domains would decrease. This would reduce the inner Helmholtz layer charge and so decrease adsorption of acid black 1 ions in

the outer Helmholtz layer. Analogously for FeLN powder greater internal screening of the C+ domains would decrease adsorption of chlorine ions in the inner Helmholtz layer and decrease adsorption of rhodamine b ions in the outer Helmholtz layer. In acid black 1 solution specific adsorption of acid black 1 ions in the inner Helmholtz layer would be reduced. The change in concentration of the dye solutions after FeLN, MgLN or SLN powders were added contradicted this expectation. In each case the doped powders produced a decrease in absorbance of the dye solutions 4-5 % greater than SLN powder. This may be explained by one of two reasons. As discussed in section 5.3.2 simulation of polar surfaces has suggested that at high surface charges reducing the polarisation through increased internal screening may increase double layer capacitance. Alternatively doping may have increased adsorption in MgLN or FeLN powders by affecting the surface morphology and the number of active sites of the powder. In this case this would mean the materials composition had a greater effect on increasing ion adsorption than the difference in the surface charge.

5.4 Summary and conclusions

The experiments in this chapter aimed to study the effect of the surface charge of ferroelectric powders upon the quantity of rhodamine b and acid black 1 ions adsorbed from aqueous solution into the double layer. Compared to non-polar TiO_2 powder BT powder was found to adsorb more rhodamine b ions per active surface site. This was attributed to the surface charge increasing electrostatic interactions with ions in solution. Photochemical deposition of silver at the surface of BT and LN powders was also found to decrease the adsorption of rhodamine b ions compared to unmodified BT or LN powders. This was explained by silver deposits externally screening the surface charge at C+ domains and decreasing the adsorption of chlorine ions in the inner Helmholtz layer. This indicated electrostatic interactions between positive rhodamine b ions and negative silver particles were weaker than between negative chlorine ions and rhodamine b ions. These results showed some evidence the

ferroelectrics surface charge increased retention of ionic species in the double layer. However, results also showed that other factors are important in influencing adsorption of dye ions e.g. the isoelectric point, surface area and morphology. The polarisation of LN powder was larger than that of BT powder but LN powder adsorbed fewer rhodamine b ions than BT powder. This suggested either the greater surface charge reduced adsorption of ionic species or that the materials other properties determined the number of ions adsorbed. Acid black 1 and rhodamine b ions of opposite charge were also found to be adsorbed in similar quantity at the surface of SLN powder. As acid black 1 forms a negative ion and rhodamine forms a positive ion the dyes would be expected to be adsorbed in different amounts if adsorption was driven primarily by electrostatic interactions with the powders surface charge. This result was attributed to the molecules different structures altering the degree of steric hindrance that prevented ions undergoing conformational changes to be adsorbed in the double layer. In conclusion although the results showed some evidence that the surface charge of the ferroelectric powders influenced the quantity of dye molecules adsorbed in the double layer no conclusive relationship between the surface charge and dye adsorption was demonstrated. The isoelectric point and surface area were different for the powders of BT, LN, SLN, MgLN, FeLN and TiO_2 tested and so the influence of these properties upon adsorption of dye could not be distinguished from that of the ferroelectric materials surface charge. The relationship between the surface charge of ferroelectric materials and the amount of dye retained in the double layer may be more systematically investigated through repeating these experiments using thin film or single crystal samples rather than powders. Using powders meant that dye molecules were adsorbed into the double layer at both the C+ and C- domains of the powders particles. The use of single domain thin films or single crystal samples would allow the C+ domain and the C- domain of each material to be exposed to solutions of dye separately. Comparing the dye adsorption by the same sized area of the C+ or C- domains of a sample individually would allow improved analysis of the influence of the surface charge upon retention of dye molecules. Single crystal or thin film samples were not tested in this work,

however, as the focus of this thesis was to investigate the properties of ferroelectric powders for application in photocatalytic reactions rather than bulk materials.

6 Lithium niobate and barium titanate powders as photocatalysts for remediation of dye pollutants

6.1 Introduction

Non-fixed dyes constitute one of the largest classes of organic compounds in industrial waste. It has been estimated that up to 20% of the world dye production is released into the environment[8]. Dyes, in addition to causing aesthetic pollution, are toxic[162], cause eutrophication, and originate dangerous by-products due to chemical reactions that take place in the waste water phase[8]. As most dyes are non-bio degradable and resistant to traditional physico-chemical methods[154] there has long been demand for a cost effective method of treating this waste. Heterogeneous photocatalysis reactions driven by illuminating suspensions of semiconductor with super band gap light have been demonstrated to be a suitable technique for degrading a wide range of dye pollutants[152; 153; 163; 164]. Decrease in the absorbance of dye solution is commonly used as an indication of the rate of degradation over a photocatalyst. The dye molecules are decolourised when bonds in the chromophore i.e. the conjugated pi bond system responsible for the molecules colour, are altered or broken after undergoing reactions. In this chapter the properties of ferroelectric powders as photocatalysts for driving decolourisation of aqueous dye solutions are investigated.

6.2 Results

6.2.1 Photocatalytic decolourisation of dye solutions under UV illumination

BT, LN, SLN, MgLN or FeLN powder was placed in rhodamine b or acid black 1 solution (1.5 g L^{-1}, 40 mL). The suspensions were illuminated with UV light for 60 min and the absorbance of samples collected from the dye solutions was measured using UV-Vis spectroscopy. When dye solutions contained no photocatalyst the absorbance was found to not detectably decrease. The

absorbance of suspensions containing ferroelectric powders decreased with time indicating photocatalytic decolourisation reactions to have taken place. The experiments were performed twice for each powder with the change in the absorption of solutions of acid black 1 or rhodamine b in the samples collected after 5, 10, 20, 30 or 60 min found to be repeatable to two significant figures. The rate of decolourisation of rhodamine b or acid black 1 solution over BT or LN powder is shown in Figure 6.1. The rate of decolourisation reactions of acid black 1 or rhodamine b solutions over SLN, MgLN or FeLN powder are shown in Figure 6.2. It was found the rate of reactions over the powders increased gradually for the first 10-20 min of UV illumination (Figure 6.1 & Figure 6.2). After this initial period reactions appear to follow pseudo-first order kinetics.

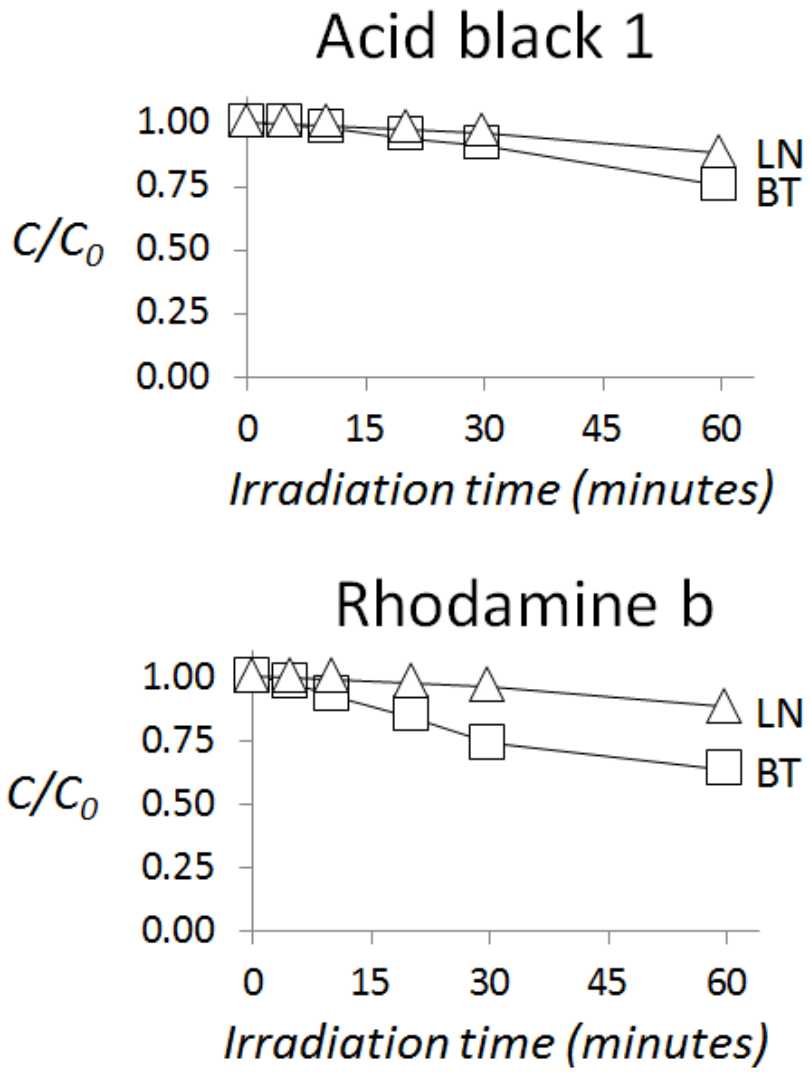

Figure 6.1 The rate of photocatalytic decolourisation of acid black 1 and rhodamine b solutions over powders of LN or BT under UV illumination

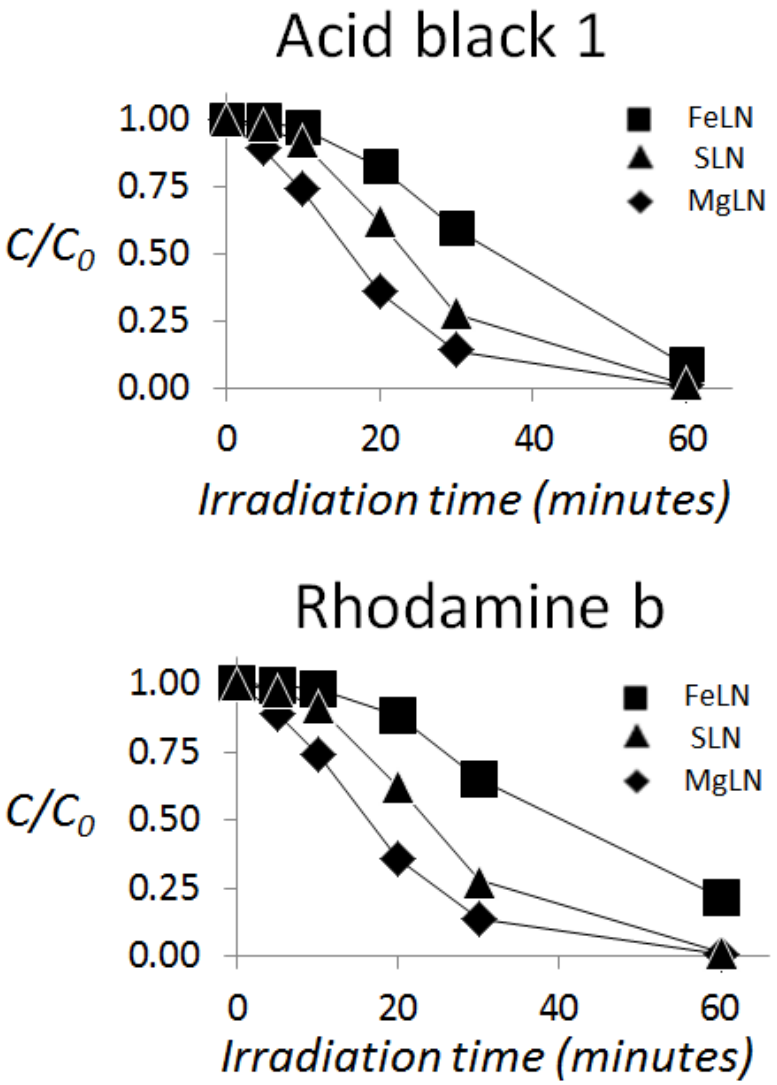

Figure 6.2 The rate of photocatalytic decolourisation of acid black 1 and rhodamine b solutions over powders of SLN, MgLN or FeLN under UV illumination

The total decrease in absorbance of the acid black 1 or rhodamine b solutions after 60 min UV illumination are shown in Table 6.1. The percentage amount by which the dye solutions were decolourised can be used to compare the rates of photocatalytic reactions over powders of SLN, LN, BT, MgLN or FeLN. Comparison of BT and LN powder found the rate of reactions to be greater over BT powder than LN powder, producing a larger decrease in the dye solutions absorbance after 60 minutes illumination. Reactions over SLN, MgLN or FeLN powders were found to proceed at a faster rate than reactions over LN or BT

powders. Comparison of reactions over SLN, MgLN and FeLN powders showed the rate of reactions was greater over MgLN powder and slower over FeLN powder in relation to the rate of reactions over SLN powder. The difference in the amount by which powders of LN, SLN, MgLN, FeLN or BT photocatalytically decolourised solutions of acid black 1 in comparison to solutions of rhodamine b are also shown in Table 6.1. BT powder produced a larger decrease in absorbance of rhodamine b solution (37 %) than acid black 1 solution (25 %). FeLN powder produced a greater decrease in absorbance of acid black 1 solution (91 %) than rhodamine b solution (79 %). Reactions over MgLN, SLN or LN powder decreased absorbance of both dye solutions by similar amounts (Table 6.1).

Table 6.1 Decrease in absorbance of acid black 1 or rhodamine b solutions as a result of photocatalytic reactions over LN, SLN, MgLN, FeLN or BT powders after 60 minutes UV illumination

Powder	Decrease in absorbance of acid black 1 solution (%)	Estimated experimental error (%)	Decrease in absorbance of rhodamine b solution (%)	Estimated experimental error (%)
BT	25	± 1	37	± 1
LN	12	± 1	12	± 1
SLN	99	± 1	99	± 1
MgLN	99	± 1	99	± 1
FeLN	91	± 1	79	± 1

6.2.2 Photocatalytic decolourisation of dye solutions under fluorescent illumination

BT or LN powder was placed in rhodamine b solution (0.5 g L^{-1}, 200 mL). The suspensions were illuminated with fluorescent light for 48 hrs. Solution

containing LN powder did not show a detectable change in absorbance after this period. The absorbance of solution containing BT powder was found to have decreased by 4 %.

6.3 Discussion

6.3.1 Heterogeneous photocatalysis under super band gap illumination

The mechanism by which photocatalytic degradation of dye molecules takes place over titanium dioxide has been widely discussed[153; 165; 166]. The principal reaction pathway is suggested to be a heterogeneous photocatalysis mechanism termed photocatalytic oxidation (PCO). Photocatalysts with similar band potentials to titanium dioxide e.g. zinc oxide, have been proposed to also photocatalytically degrade dye molecules via a PCO mechanism[167; 168]. The steps of PCO reactions are shown in Equations 6.1 to 6.6. When the photocatalyst is illuminated with super band gap light electron and hole carries are excited. Electrons reduce oxygen to form the superoxide anion radical ($O_2^{\cdot -}$) and hole carriers oxidise hydroxide ions, formed by dissociative adsorption of water at the photocatalyst surface, to produce the hydroxyl radical ($OH^{\cdot}$). Degradation of dye molecules occurs when the superoxide anion radicals or hydroxyl radicals react with the dye or if the dye is oxidised or reduced directly by excited carriers at the photocatalysts surface (Equations 6.4 to 6.6).

$$\mathbf{PC} + \mathbf{hv} \rightarrow \mathbf{e_{cb}^-} + \mathbf{h_{vb}^+} \quad (6.1)$$

$$\mathbf{h_{vb}^+} + (\mathbf{H_2O} \Leftrightarrow \mathbf{H^+} + \mathbf{OH^-})\,\mathbf{ads} \rightarrow \mathbf{H^+} + \mathbf{OH^{\cdot}} \quad (6.2)$$

$$\mathbf{e_{cb}^-} + \mathbf{O_2}\,\mathbf{ads} \rightarrow \mathbf{O_2^{\cdot -}} \quad (6.3)$$

$$\mathbf{Dye} + \mathbf{OH^{\cdot}}\ \mathbf{or}\ \mathbf{O_2^{\cdot -}} \rightarrow \mathbf{Degradation\ products} \quad (6.4)$$

$$\mathbf{Dye} + \mathbf{e_{cb}^-} \rightarrow \mathbf{Reduction\ products} \quad (6.5)$$

$$\mathbf{Dye} + \mathbf{h_{vb}^+} \rightarrow \mathbf{Oxidation\ product} \quad (6.6)$$

The band edges of titanium dioxide in relation to the half-cell equations of reduction of oxygen (-0.3 V vs. NHE) and oxidation of the hydroxide ion (-1.9 V vs. NHE) are shown in Figure 6.3. Typically a photocatalyst can only photostably transfer carriers to a reactant when the reduction or oxidation potential is within its band edges. Although it is accepted that titanium dioxide photostably produces the hydroxyl radical under super band gap light[8; 12] the oxidation potential of the hydroxide ion is reported to be outside of titanium dioxide's conduction band edge[169]. The pathway by which titanium dioxide oxidises the hydroxyl ions is, therefore, not fully understood. One explanation put forward is that thermal fluctuations alter the alignment of the energy levels of the hydroxide ion[169]. If energy levels of the hydroxide ion move below that of the conduction band edge of titanium dioxide then photocatalytic oxidation can take place.

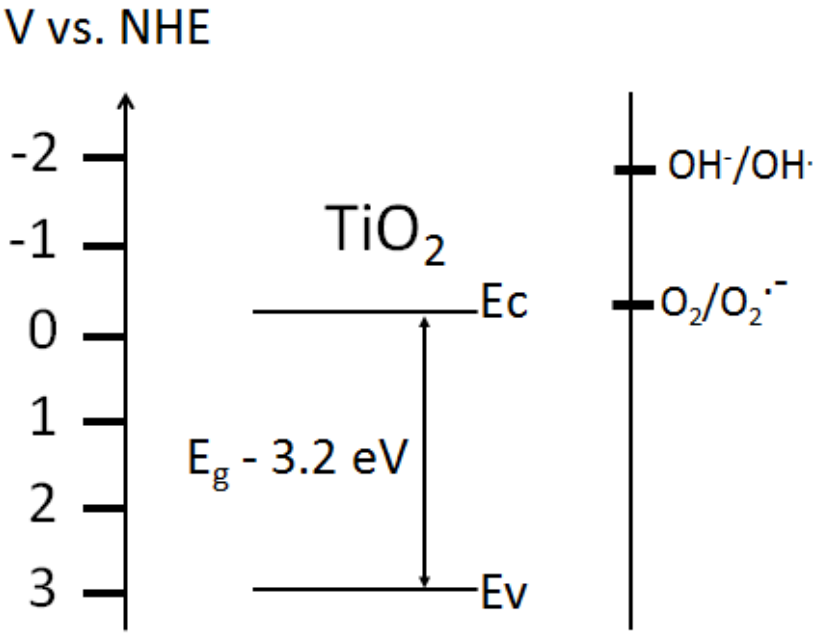

Figure 6.3 The flat band potentials of titanium dioxide in relation to the half equation for reduction of oxygen and the oxidation of the hydroxide ion

The reported room temperature band gaps of the ferroelectric materials used are 3.2 eV for barium titanate[170;171], 3.7 eV for lithium niobate[136], 3.7 eV for iron doped lithium niobate[172] and 4.0 eV for magnesium doped lithium niobate[140]. The UV lamp emitted photons with energy exceeding (or equalling) the band gaps of all four materials (Figure 6.4).

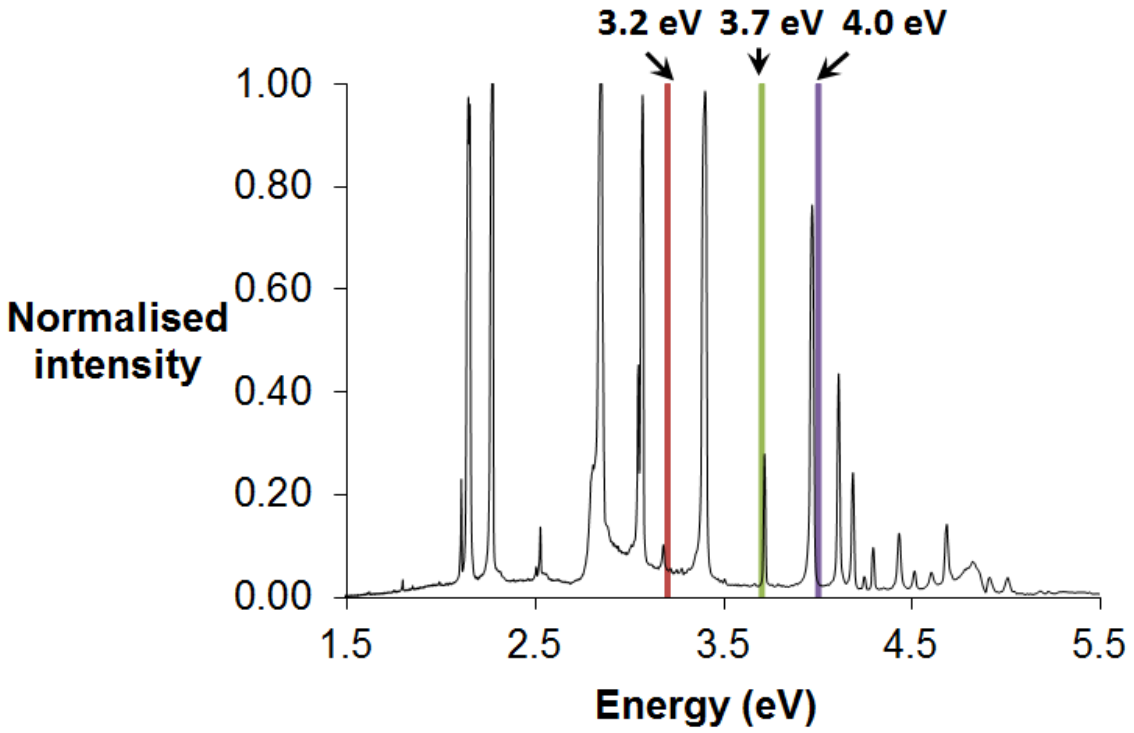

Figure 6.4 The emission spectrum of the UV lamp with the band gap energies of barium titanate (3.2 eV), lithium niobate (3.7 eV), magnesium doped lithium niobate (4.0 eV) and iron doped lithium niobate (3.7 eV) marked

The decrease in absorbance of the dye solutions when illuminated with UV light can be attributed to excited carriers in the ferroelectric powders formed by absorption of super band gap light driving heterogeneous photocatalytic degradation of dye molecules. Barium titanate's conduction band and valence band edges positions are comparable to those of titanium dioxide (Figure 6.5) the mechanism by which BT powder photocatalytically degraded dye molecules can be assumed to be similar to the PCO mechanism proposed in Equations 6.1 to 6.6. Lithium niobates band edges are significantly different from those of barium titanate or titanium dioxide (Figure 6.5). Degradation of dye molecules may have occurred via a modified PCO mechanism. Electrons in the conduction band of lithium niobate can reduce oxygen to form the superoxide anion radical (Figure 6.5). The valence band edge position allows the hydroxide radical to be formed either via oxidation of the hydroxide ion (without the need for thermal fluctuations to alter the energy levels) or oxidation of undissociated water molecules (Figure 6.5).

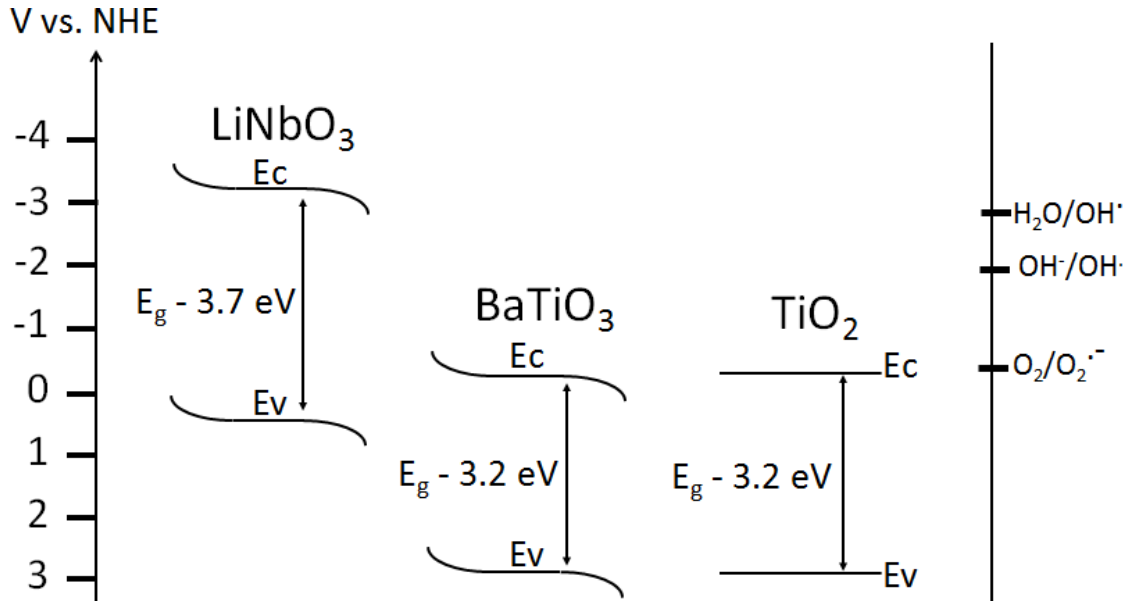

Figure 6.5 The band edges of lithium niobate and barium titanate in relation to the flat band potentials of titanium dioxide and the half equation for reduction of oxygen, the oxidation of the hydroxide ion and oxidation of water to form the hydroxyl ion

6.3.2 Catalysed photoreactions under sub band gap illumination over BT or LN powders

Under sub band gap illumination titanium dioxide is reported to degrade dye molecules via a catalysed photoreaction mechanism[8]. A proposed pathway for these reactions is shown in Equations 6.7 to 6.11. Photons adsorbed by dye molecules excite electrons from the highest occupied molecular orbital (HOMO) to the lowest occupied molecular orbital (LUMO). The electrons are transferred to the conduction band of the photocatalyst, partially oxidising the dye. The electrons transferred to the photocatalysts conduction band drive reduction of oxygen to form the superoxide anion radical that reacts with dye molecules or partially oxidised dye molecules.

$$\mathbf{Dye} + \mathbf{hv} \rightarrow \mathbf{Dye_1^*\ or\ Dye_3^*} \quad (6.7)$$

$$\mathbf{Dye_1^*\ or\ Dye_3^*} + \mathbf{PC} \rightarrow \mathbf{Dye^{+\cdot}} + \mathbf{PC}\,(\mathbf{e_{cb}^-}) \quad (6.8)$$

$$\mathbf{PC}\,(\mathbf{e_{cb}^-}) + \mathbf{O_2} \rightarrow \mathbf{O_2^{-}} + \mathbf{PC} \quad (6.9)$$

$$\mathbf{Dye} + \mathbf{O_2^{-\cdot}} \rightarrow \mathbf{Degradation\ products} \quad (6.10)$$

$$\mathbf{Dye^{+\cdot}} + \mathbf{O_2^{-\cdot}} \rightarrow \mathbf{Degradation\ products} \quad (6.11)$$

In experiments a fluorescent bulb was used to illuminate suspensions of BT or LN powder in rhodamine b solution. The bulb emitted light between wavelengths of 400-700 nm. The florescent light did not emit photons at wavelengths with energy equal to or exceeding the band gap of BT (photons of wavelength 388 nm or shorter) or LN (photons of wavelength 335 nm or shorter). This meant that PCO reactions could not take place. The bulb did, however, emit photons at the peak adsorption of rhodamine b dye (554 nm) exciting electrons from the HOMO to the LUMO of the dye. After 48 hours illumination the absorbance of rhodamine solution containing LN powder had not detectably changed. This can be explained by the conduction band edge of lithium niobate being above the potential of the LUMO of rhodamine b (Figure 6.6). This meant transfer of electrons from the LUMO to the conduction band of LN powder was energetically unfavourable. As a result catalysed photo reactions of rhodamine b could not take place over LN powder. After 48 hours illumination by the fluorescent light the absorbance of solution containing BT powder had decreased by 4 %. The conduction band potential of barium titanate is below that of the LUMO of rhodamine b. The decrease in absorbance can be attributed to transfer of electrons from the dye to the conduction band of BT powder driving catalysed photo reactions (Figure 6.6). As barium titanate's conduction band edge allows electrons to reduce oxygen to form the superoxide anion radical the pathway of catalysed photo reactions is likely similar to the mechanism proposed for reactions over titanium dioxide (Equations 6.7 to 6.11).

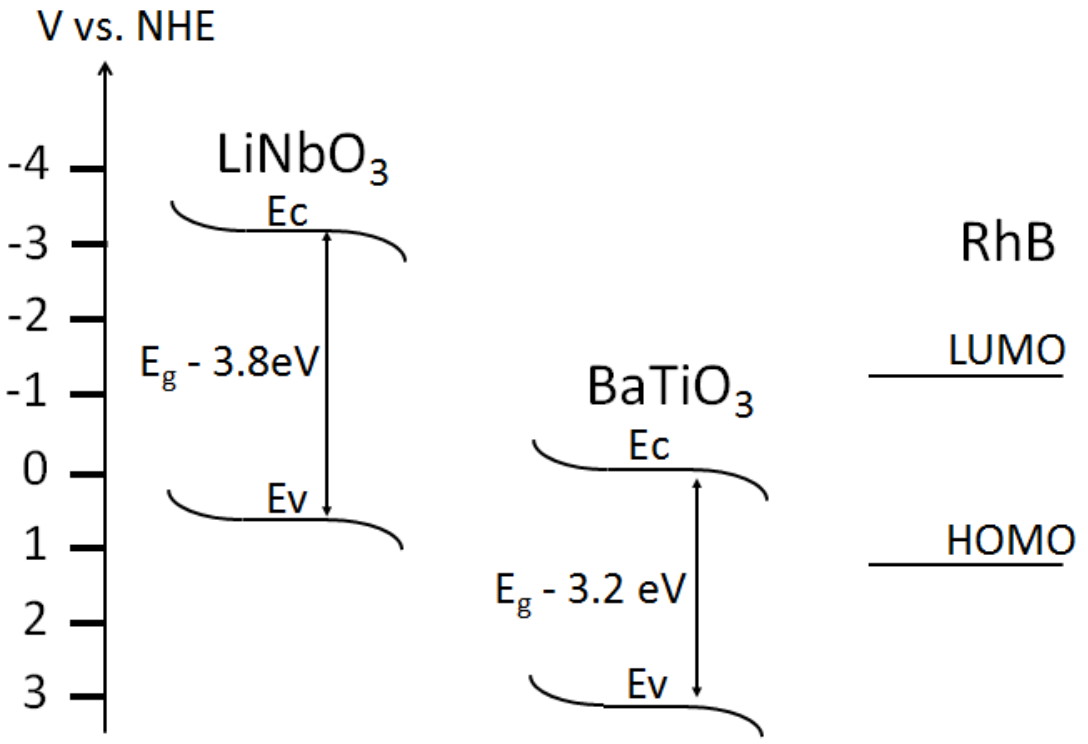

Figure 6.6 The band edges of barium titanate, lithium niobate and the LUMO and HOMO of rhodamine b versus NHE. The value of the HOMO and LUMO of rhodamine b is taken from ref.[173]

6.3.3 Desorption of dye under super band gap illumination

In PCO reactions water is oxidised by hole carriers to form the hydroxyl radical. In aqueous dye solutions water is present in significantly greater concentration than dissolved dye. This means that PCO reactions over semiconductor systems such as titanium dioxide typically follow pseudo first-order kinetics as the concentration of water decreases at a far slower rate than the concentration of dye ions[164; 174; 175]. As discussed in the previous section the photocatalytic degradation of dye molecules over BT powder takes place via a similar PCO mechanism to reactions over titanium dioxide and photocatalytic dye degradation reactions over lithium niobate powders likely take place via a modified PCO mechanism. It would be expected that as reactions over both barium titanate and lithium niobate powders consume water molecules that decolourisation of acid black 1 or rhodamine b solutions would follow pseudo

first-order kinetics. In experiments the rate of reactions was shown to increase gradually for the first 10-20 min of UV illumination (Figure 6.1 & Figure 6.2). After this initial period reactions then appeared to follow pseudo-first order kinetics as was expected. The period in which reaction rates gradually increased may be explained by the effect of internal screening of the surface charge at C+ and C- domains by photogenerated carriers. When the ferroelectric powders were illuminated by super band gap light excited electron and holes carriers that did not undergo recombination migrated to the interface of C+ and C- domains respectively under the action of internal depolarisation fields. Some of these carriers were transferred to adsorbed species to drive photocatalytic reactions. Carriers that were not transferred to reactants contributed to internal screening of the surface charge. This decreased electrostatic interactions between ionic species adsorbed in the double layer and the surface charge. As a result dye ions were desorbed from the double layer (Figure 6.7).

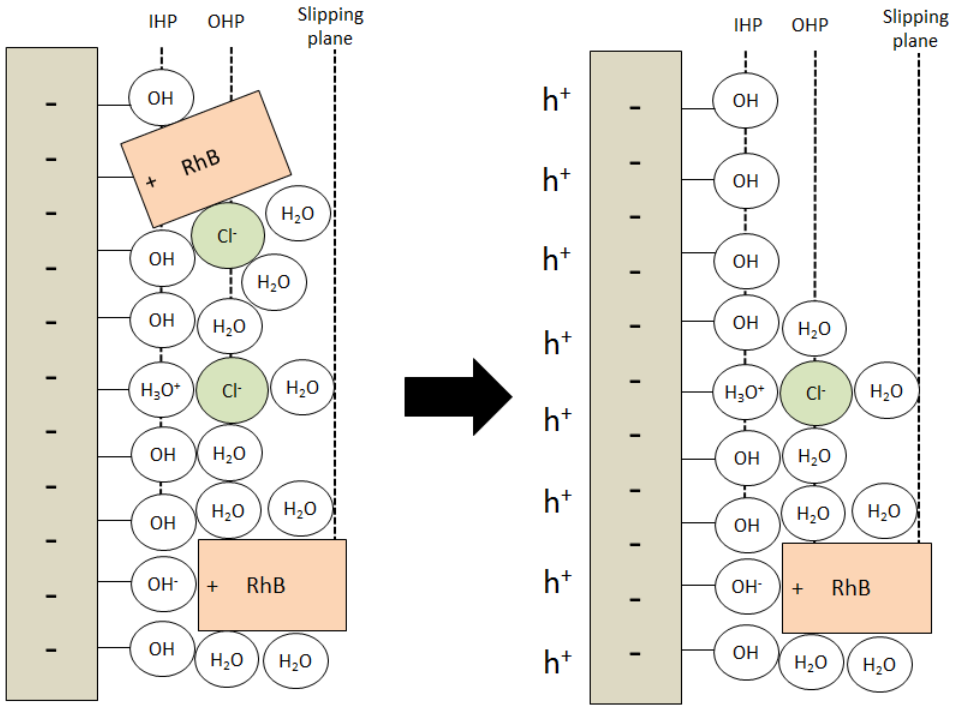

Figure 6.7 The effect of increased internal screening upon adsorption of ionic species in the double layer at the interface between a C- ferroelectric domain and rhodamine b solution

Desorption of dye ions from the powder caused the concentration of dye ion solution to increase. As the absorbance of the dye solutions showed a net decrease under UV illumination this indicated the rate of photocatalytic degradation of dye molecules exceed the rate at which dye molecules were desorbed from the double layer of the powders. As after 10-20 min illumination reactions began to follow pseudo-first order kinetics this suggested adsorption/desorption of dye ions from the powder had reached equilibrium by this point. The desorption of dye as a result of internal screening under UV illumination showed evidence that the ferroelectric surface charge had increased the retention of ionic species in the double layer, as discussed in Chapter 5. However, it also suggests that increased internal screening under high intensity super band gap illumination causes the surface charge to be largely of fully internally screened. This decreases or fully cancels the effect of electrostatic interactions between ionic species in solution and the ferroelectric surface charge.

6.3.4 Photocatalytic activity of ferroelectric powders under UV illumination

A limited amount of data was collected in experiments, however, the measurements of photocatalytic decolourisation of solutions of rhodamine b or acid black 1 over powders of BT, SLN, LN, MgLN or FeLN were found to be repeatable to two significant figures. This showed the results to have a high degree of precision, allowing discussion comparing the photocatalytic activities of the different powders. Under UV illumination reactions of acid black 1 or rhodamine b solution were shown to proceed at a greater rate over BT powder than LN powder (Table 6.1). The band gap of barium titanate is reported to be narrower (3.2 eV) than that of lithium niobate (3.7 eV). This meant a greater proportion of photons emitted by the UV lamp could excite carriers in BT powder, increasing the rate of carrier formation (Figure 6.4). It was shown in Chapter 5 that although the surface area of BT powder (0.7 m^2 g^{-1}) and LN powder (0.6 m^2 g^{-1}) were comparable that BT powder adsorbed more

rhodamine b ions than LN powder. This was attributed to the different surface charge of the materials, the different isoelectric points of the materials but may also indicate the composition and morphology of BT powder produced a larger number of active surface sites than LN powder. The quantity of dye ions and oxygen or hydroxyl species reactants adsorbed at the surface of BT powder would be expected to be greater that at the surface of LN powder if this is the case. This may have increased the rate at which excited carriers were transferred to form the superoxide anion radical or hydroxyl radical and so also the rate at which dye ions in the double layer were decolourised. As was discussed in Chapter 4 the estimated polarisation of particles of LN powder (close to 78 μC cm^{-2}) was greater than that estimated for particles of BT powder (21.34-24.02 μC cm^{-2}). As the rate of reactions was higher over BT powder than LN powder this suggests the powders other properties e.g. the rate of carrier formation and the number of active surface sites, were more significant in determining the rate of photocatalytic reactions than the powders polarisation. Alternatively this could be explained if the larger polarisation of LN particles had a detrimental impact on the rate at which dye decolourisation reactions took place.

Comparison of the rate of reactions over SLN and LN powder showed SLN powder decolourised the dye solutions at a faster rate than LN powder (Table 6.1). As was discussed in Chapter 4 the particle sizes of SLN powder were shown to be smaller than the particles of LN powder. The smaller particle size of SLN powder meant the width of the space charge region represented a larger proportion of the total size of the particle in comparison to particles of LN powder. This may have increase the number of carriers formed within the space charge region. This would allow a greater proportion of carriers to be separated by internal depolarisation fields resulting in a reduced rate of recombination. SLN powder was also shown to have a larger surface area (1.4 m^2 g^{-1}) than LN powder (0.6 m^2 g^{-1}) and so had a greater number of active surface sites. This increased the quantity of reactants (oxygen and water or hydroxyl species) adsorbed at the surface. The rate at which the superoxide anion radical and hydroxyl ion were formed by transfer of excited carriers could have been

increased as a result. In Chapter 5 it was discussed that LN powder adsorbed more rhodamine b ions per active surface site than SLN powder. This suggested that the amount of dye adsorbed per surface site was not a primary factor effecting reaction rate over the lithium niobate powders or that a greater amount of dye adsorption reduced the reaction rate. It was suggested in Chapter 4 that size effects that decrease the polarisation of ferroelectric particles would be more significant in particles of SLN powder than LN powder as the particle of SLN powder were smaller than the particle of LN powder. The higher rate of photocatalytic reactions over SLN compared to LN powders was, therefore, either mainly influenced by properties other than the polarisation or the smaller polarisation of SLN powder compared to LN powder increased the rate of reactions.

In comparison to the rate of reactions of acid black 1 and rhodamine b solution over SLN powder the rate of reactions of the dye solutions over FeLN powder were lower and the rate of reactions over MgLN powder were higher (Table 6.1). The trend in reaction rates over the doped materials does not appear to directly relate to the materials surface areas, band gaps, polarisation or the amount of dye adsorbed in the double layer. The surface area of SLN (1.4 m^2 g^{-1}) and MgLN (1.3 m^2 g^{-1}) powder were found to be comparable and the surface area of FeLN (0.8 m^2 g^{-1}) was found to be smaller. If the surface area was principally responsible for reaction rates over the lithium niobate powders then reactions over MgLN powder would have been expected to be slower or comparable to reactions over SLN powder. Adsorption studies in Chapter 5 showed both MgLN and FeLN powders adsorbed more dye ions than SLN powder. This was attributed to difference in the materials polarisation or the effect of doping increasing internal screening or altering the number of active surface sites or surface morphology. If the number of active surface sites or the amount of dye adsorbed by the powders were the main factor controlling reactions rates then both doped materials would have been expected to drive reactions at a faster rate compared to SLN powder. The polarisation of the bulk materials of lithium niobate was measured to be 78 µC cm^{-2} for SLN, 72 for FeLN µC cm^{-2} and 65 µC cm^{-2} for MgLN. As the powders had comparable sizes

the size effects were assumed to be similar in all three powders as discussed in Chapter 4. The trend in the size of the polarisation of the particles of the powders was, therefore, assumed to reflect size of the polarisation measured for the bulk materials. The rate of reactions in this case did not correlate with the polarisation of the powders as particles of both MgLN and FeLN powders had a smaller polarisation than particles of SLN powder. The band gap of magnesium doped material (4 eV) is reported to be wider than that of undoped material (3.7 eV) and the band gap of iron doped material is reported to be similar to that of undoped material (3.7 eV). Under UV illumination the lamp emitted a similar quantity of photons able to excite carriers in SLN or FeLN powders and fewer photons able to excite carriers in MgLN powder (Figure 6.4). The rate of carrier formation of the powders, therefore, does not appear to relate to the trend in reaction rates over the powders.

The difference in reactivity of the doped lithium niobate powders may instead be attributed to the effect doping had upon the majority carrier type. In comparison to undoped SLN powder doping with magnesium is reported to increase the p-type character; this increased the ratio of carriers excited by super band gap illumination that were holes and so increased the rate of formation of the hydroxyl radical. Doping with iron is reported to increase the n-type character; this caused a greater proportion of carriers formed under super band gap illumination to be electrons and so increased the rate of formation of the superoxide anion radical. As the concentration of adsorbed oxygen was significantly less than that of water molecules in the dye solutions the rate at which hole carriers were transferred to drive formation of the hydroxyl radical would be expected to be faster than the rate at which electron carriers were transferred to form the superoxide anion radical. Compared to undoped material the p-type character of MgLN powder may have increased the rate at which reactive species were formed and the n-type character of FeLN powder may have decreased the rate at which reactive species were formed. The superoxide anion radical and hydroxyl radical also have different oxidation potentials, +0.33 V vs. NHE in the case of the superoxide anion radical and +2.8 V vs. NHE in the case of the hydroxyl radical. The different oxidation

potentials of these species may alter the rate at which they react with dye molecules and the bonds with which they react in the dye molecules. Spatially distinct reduction and oxidation at the surface of ferroelectric materials meant that the majority carrier type determined if reactions occur primarily at C+ or C- domains. When hole carriers are the majority carrier reactions occur primarily at C- domains and when electrons are the majority carrier reactions occur at C+ domains. The different charges at these surfaces may affect the orientation in which reactive species formed by excited carriers are adsorbed (Figure 6.9). At positive domains the superoxide anion radical would be expected to be adsorbed with the activated oxygen atom toward the surface. At C- domains the hydroxyl radical would be expected to be adsorbed with the reactive oxygen atom positioned away from the surface. The different orientations of the activated atoms could affect the rate at which the radical species react with dye ions in the double layer.

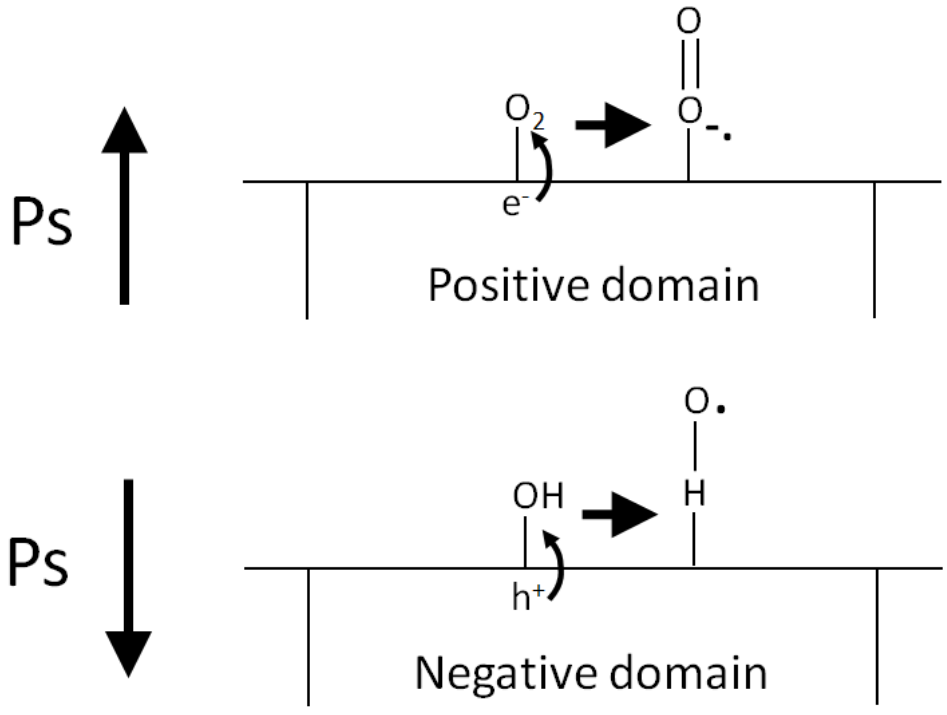

Figure 6.8 Possible orientation of the superoxide anion radical adsorbed at C+ domains and of the hydroxyl radical formed at C- domains

The increased reactivity of MgLN powder and decreased reactivity of FeLN powder in comparison to SLN powder suggested dye decolourisation reactions over lithium niobate to be oxidation led. This may be explained by the faster rate at which oxidation reactions formed the hydroxyl radical compared to reduction reactions forming the super oxide radical, the different orientation in which the reactive species formed by reduction and oxidation reactions are adsorbed affecting the rate at which they react with dye molecules, difference in the pathway by which hydroxyl radical and superoxide anion radical decolourise dye molecules or a combination of these factors.

6.3.5 Structural selectivity of photocatalytic dye degradation reactions over ferroelectric powders

The rate of dye decolourisation reactions over semiconductor systems has been suggested to be related to the quantity of dye adsorbed at the photocatalysts surface. As different dye molecules have different zeta potentials the electrostatic interactions with the surface of the semiconductor or the charge of the inner Helmholtz layer are also different. This results in dye ions being adsorbed in different quantities at the surface of a photocatalyst. Consequently reactions are structurally selective i.e. the rate of decolourisation over of different dye solutions are typically dissimilar under otherwise identical experimental conditions[153; 176-179]. Reactions over ferroelectric materials would also be expected to be structurally selective as dyes with different zeta potentials are adsorbed in different quantities at C+ and C- domains as discussed in Chapter 5. In the previous section it was discussed that spatially separated redox reactions mean the location at which dye ions are adsorbed determines whether they react with the superoxide anion radical formed at C+ domains or the hydroxyl radical formed at C- domains. This also can affect the rate of reactions.

In experiments the rate of reaction of acid black 1 solution over BT powder was lower than the rate of reaction of rhodamine b solution (Table 6.1). This was as would be expected. The negative acid black 1 ion and positive rhodamine b ion

were adsorbed in different total quantities and the opposite charge meant they were adsorbed at different domains. Comparison of reaction rates over lithium niobate powder showed LN, SLN or MgLN powders to decolourise solutions of acid black 1 and rhodamine b at similar rates (Table 6.1). This is not consistent with expectations or the rate of reactions of the dye solutions over BT powder. The similar rates may be explained by the location of reactions taking place at the surface. It was discussed in in the literature review that investigation of photochemical reduction of silver ions at the surface of periodically poled lithium niobate showed the location of reactions was dependent upon the concentration of silver ions in aqueous solution. When a high concentration silver ion solution was used the high coverage of silver ions at the surface meant that as electrons were able to immediately reduce an available silver ion after migrating to the surface. The concentration of electrons was highest toward the domain boundary as this is where the internal electric field had been calculated to be greatest in lithium niobate. As a result silver deposition occurred predominantly at the boundary of C+ domains. When a low concentration silver ion solution was used the surface coverage of silver ions was lower. This meant carriers migrating to the surface were less likely to immediately reduce a silver ion. Instead carriers migrated to the sites where silver ions were adsorbed to drive photochemical reduction to form deposits. This resulted in deposition reflecting the distribution of silver ions i.e. evenly across the C+ domains surface. In dye decolourisation experiments as water and hydroxide ions are readily available in the double layer at the surface of the lithium niobate powders hole carriers driven to the surface by depolarisation fields at the boundaries of negative domains readily drove formation of the hydroxyl radical (Figure 6.9). Formation of hydroxyl radicals close to the domain boundary may have allowed these species to react with acid black 1 or rhodamine b molecules adsorbed in the double layer at C+ or C- domains at a similar rate. This may explain the reduced structural selectivity of reactions of over MgLN, SLN or LN powders.

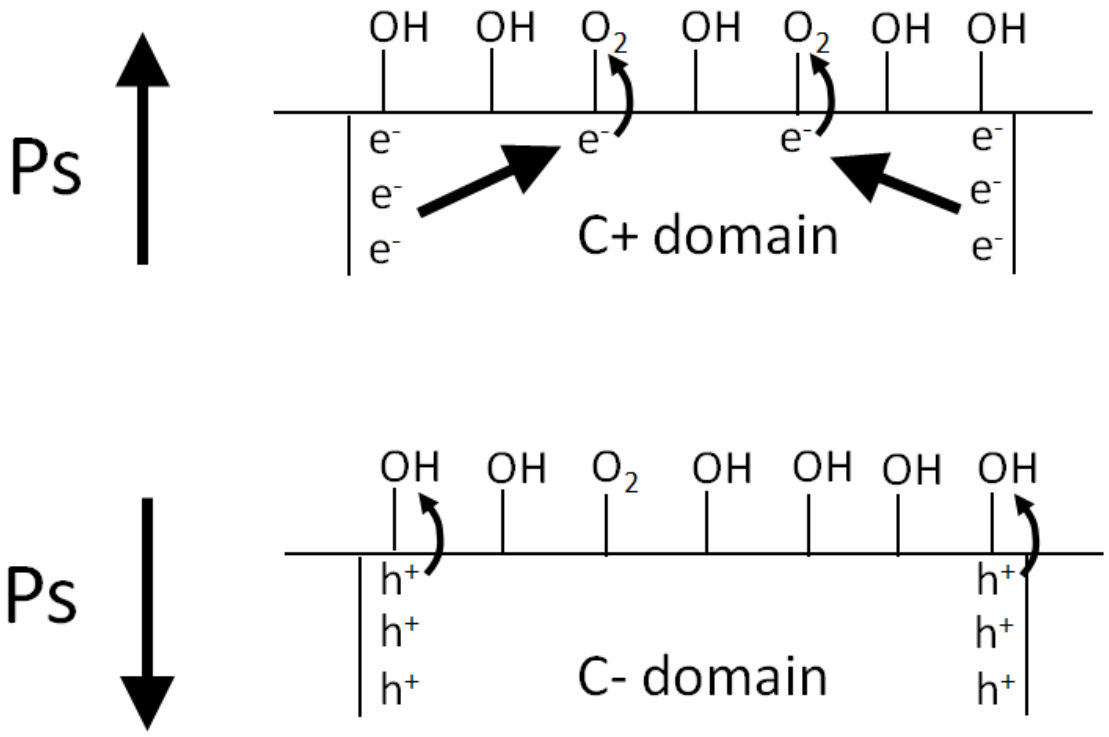

Figure 6.9 The possible location of photochemical reduction and oxidation reactions of PCO mechanisms at the C+ and C- domains of lithium niobate

Reactions over FeLN powder unlike MgLN or SLN powders did not decolourise the dye solutions at a similar rate. Reactions over FeLN powder decolourised acid black 1 solution at a greater rate than rhodamine b solution (Table 6.1). As discussed reactions over FeLN powder are reduction led due to its n-type character. As the concentration of dissolved oxygen in solutions was low this meant coverage of oxygen at the surface was also low. At C+ domains electron carriers accumulating at the domain boundary did not readily take part in reactions as a result. Formation of the superoxide anion radical would be expected to occur when carriers migrated to the location of adsorbed oxygen atoms. This would cause formation of the superoxide anion radical to reflect the distribution of oxygen atoms adsorbed in the double layer i.e. across the domains surface (Figure 6.9). This meant as the superoxide anion radical was formed across the C+ domains reactions with dye ions adsorbed at C+ domains occurred at a faster rate than dye ions adsorbed mainly at C- domains. This may explain the greater rate of reactions of the negative acid black 1 ions which

would be expected to be adsorbed mainly at C+ domains than positively charged rhodamine b ions adsorbed at C- domains.

6.4 Summary and conclusions

Under super band gap illumination SLN, LN, MgLN, FeLN or BT powders were shown to drive photocatalytic decolourisation of solutions of acid black 1 or rhodamine b. The reaction kinetics suggested internal screening of the powders surface charge resulted in desorption of dye from the double layer under super band gap illumination. This provided further evidence that the surface charge increases adsorption of ionic species. However, this result also showed that under high intensity of super band gap illumination the surface charge is largely or fully internally screened. As a result electrostatic interactions between ionic species and the surface charge are diminished. Comparison of the rate of reactions over the powders showed that neither the polarisation nor adsorption of dye showed a clear correlation with the rate of reactions. Reactions over SLN, FeLN or MgLN powder showed that doping affects the reaction rate probably due to the effect this had upon the majority carrier type. Reactions over LN, SLN or MgLN powder were also found to decolourise the dye solutions at similar rates. This was attributed to the hydroxyl radical being formed at boundaries of C- domains. The hydroxyl radical may, therefore, react with species adsorbed in the double layer at C+ or C- domains at similar rates. As factors other than the materials polarisation e.g. surface area contributed to differences in the powders photocatalytic activates the role of the polarisation in determining the rate of photocatalytic reactions was not established. Repeating dye decolourisation reactions using single crystal samples may more clearly demonstrate the effect of the polarisation orientation upon the rate of reactions. Using single crystal samples allows the C+ or C- domains to be exposed to the dye solution separately and so the role of the polarisation could be studied more systematically.

7 Photocatalytic properties of lithium niobate and barium titanate powders after deposition of metal nanoparticles at the surface

7.1 Introduction

The photocatalytic properties of semiconductor materials have been shown to be altered after deposition of noble metal nanoparticles at the surface[100-103]. The resulting systems drive dye decolourisation reactions at increased rates and have greater sensitivity to visible spectrum light compared to the raw semiconductor. The changes are attributed to the formation of a Schottky barrier at the interface. This results in electrons being transferred from the semiconductor conduction band to the metal particle. Trapping electrons in this manner reduces the rate of carrier recombination in the semiconductor allowing a larger proportion of excited carriers to drive redox reactions of adsorbed species[106]. Noble metal nanoparticles can also adsorb visible light photons to produce a localised surface plasmon resonance (LSPR) i.e. photons interact with metal particles free conduction electrons causing collective excitation and oscillation and a strong enhancement of local electromagnetic fields[107]. LSPR has been shown to excite carriers in the semiconductor host material[108] and has been proposed to increase the rate of transfer of electrons from the conduction band to metal particles[103].

At the surface of ferroelectric materials photochemical reduction of metal particles occurs selectively at C+ domains. The action of internal depolarisation fields produces accumulation of electron density in the space charge region at the C+ domains. This property may cause metal particles to trap a greater number of excited electrons at the surface of ferroelectrics than at the surface of non-polar semiconductor materials. In this chapter ferroelectric-metal systems were prepared through photochemical deposition of copper or iron particles or silver noble metal particles at the surface of BT, LN or SLN powders. The activity of the ferroelectric-metal systems and raw BT or LN powders were compared for driving photocatalytic decolourisation of rhodamine b solutions under UV or simulated solar illumination.

7.2 Photochemical deposition of metal particles at the surface of ferroelectric powders

7.2.1 Results

Suspensions of BT powder in silver nitrate, copper nitrate or iron nitrate solution (2.5 gL^{-1}, 100 mL), LN powder in silver nitrate solution (2.5 gL^{-1}, 100 mL) and SLN powder in silver nitrate solution (2.5 gL^{-1}, 100 mL) were illuminated by UV light for 20 or 30 minutes in order to deposit metal particles on the powders surface. The quantity of metal particles photochemically deposited on the surface of the powders increases with the length of UV illumination. Two durations, 20 minutes or 30 minutes, were used to produce powders of lithium niobate and barium titanate with different loadings of silver particles. The resulting ferroelectric-metal powders are here on referred to by the abbreviations in Table 7.1.

Table 7.1 Preparation of ferroelectric-metal powders by photochemical deposition

Powder	UV exposure (min)	Salt solution	Abbreviation
LN	20	0.01 M $AgNO_3$	Ag:LN-20
SLN	30	0.01 M $AgNO_3$	Ag:SLN-30
BT	20	0.01 M $AgNO_3$	Ag:BT-20
BT	30	0.01 M $AgNO_3$	Ag:BT-30
BT	30	0.01 M $CuSO_4$	Cu:BT-30
BT	30	0.01 M $Fe(NO_3)_3$	Fe:BT-30

After UV illumination in metal salt solution the powders had changed colour. BT powder turned from white to light grey when suspended in silver nitrate solution, light yellow after suspension in iron nitrate solution and light blue after suspension in copper nitrate solution. SEM images of Ag:BT-30, Cu:BT-30 and Fe:BT-30 showed deposits had formed at the surface of the powders (Figure 7.1). The number of deposits and size of deposits differed between faces of the

powder, some showing a small number or no deposits while others showed higher coverage or larger deposits. Some of the deposits at the surface of Ag:BT-30 or Fe:BT-30 formed ordered regions with straight edges. Examples of this are marked by black lines in the right hand side of Figure 7.1. EDX analysis of the deposits at the surface of Ag:BT-30 or Fe:BT-30 could not identify their composition. Silver or iron was not detected but nor were elements other than barium, titanium or oxygen. At the surface of Cu:BT-30 powder EDX detected a loading of 0.05 weight % of copper. The average size of the deposits at the surface of the powders were measured to be 58 nm at the surface of Ag:BT-30, 38 nm for deposits formed at the surface of Fe:BT-30 and 91 nm for deposits formed at the surface of Cu:BT-30.

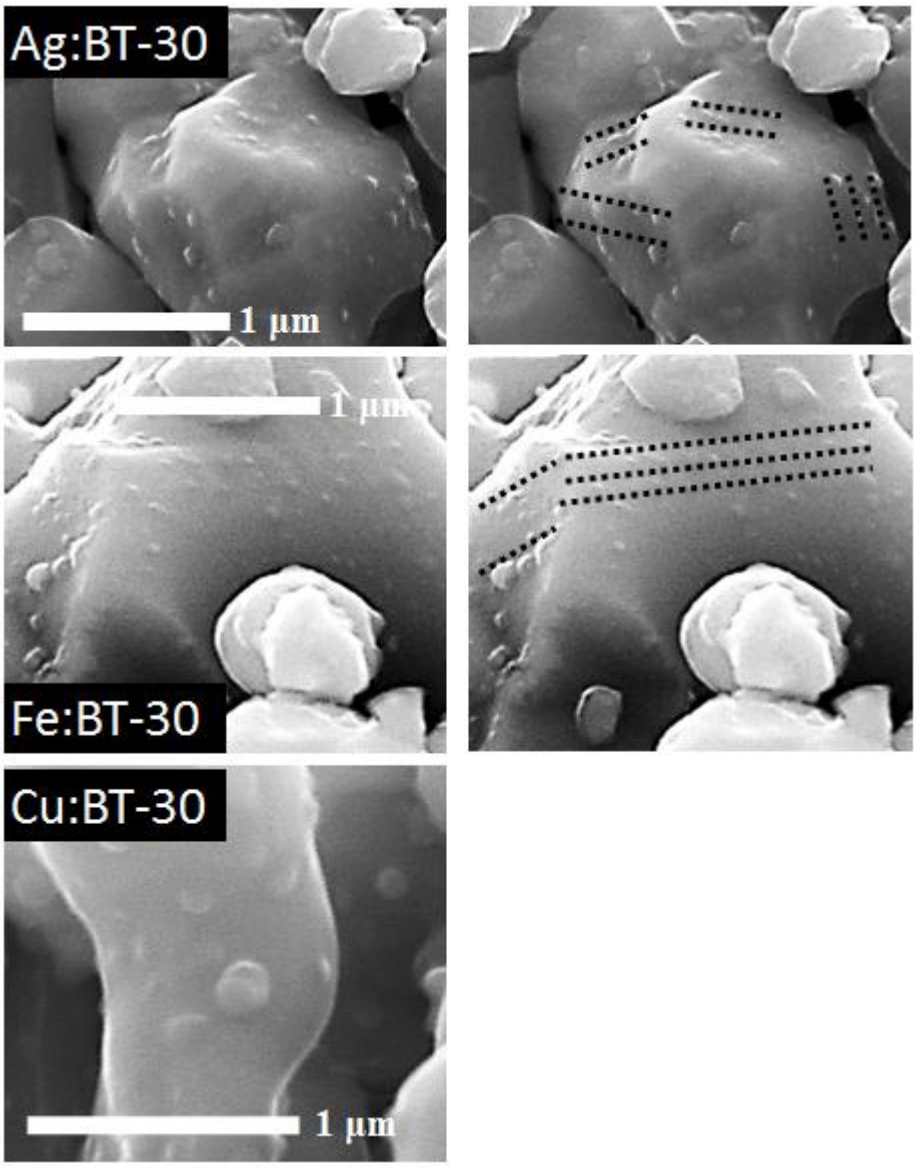

Figure 7.1 SEM images showing deposits at the surface of Ag:BT-30, CuBT-30 and Fe:BT-30 powders after UV illumination in salt solutions

SLN and LN powders turned from white to light grey in colour after UV illumination in silver nitrate solution. SEM analysis of Ag:LN-20 or SLN-30 powders was unable to determine if deposits had formed at the surface as significant charging occurred producing an image with low resolution. This meant change in the surface topography could not be analysed at high magnification. Attempts to reduce charging through carbon coating or use of a high or low accelerating voltage during analysis was unable to sufficiently

improve the image resolution. EDX analysis of the powders surfaces did not detect elements other than niobium or oxygen.

7.2.2 Discussion

The light grey colour of Ag:BT-30 and Ag:BT-20 powders indicated formation of a coating at the surface. The grey colour corresponded to formation of silver metal deposits. As discussed in Chapter 5 XPS analysis of BT powder that had been illuminated in silver nitrate solution detected silver in the metal state at the surface. The grey colour of Ag:BT-30 and Ag:BT-20 powders was, therefore, assumed to indicate the formation of silver metal deposits. EDX analysis of the powders did not detect silver. As the detection threshold of this technique is approximately 0.05 weight % this suggested the loading of silver deposits to be less than 0.05 weight %.

It is reported that photochemical reduction of silver at C+ domains of barium titanate produces regions of deposits with straight edges as a result of discontinuation of reactions at the boundaries of 90^{o} domain walls[21]. Regions of silver deposits with curved edges at the surface of barium titanate are reported to indicate the location of 180^{o} domain walls[21]. The SEM image of Ag:BT-30 powder showed some of the deposits had produced ordered regions with straight edges indicating the location of 90^{o} domains walls (Figure 7.1). Regions of silver deposits with curved edges were not clearly formed the surface of Ag:BT-30 powder. The domain structure of the Ag:BT-30 powder was not as distinctly marked as a result of photochemical reduction of silver in comparison to investigations of silver deposition at the surface of barium titanate samples in the literature[22; 113]. This could be explained by the length of illumination in experiments and the effect this has upon the size of deposits. Powders were illuminated for long exposures of 20 or 30 minutes. This meant that once silver particles had formed they could trap electrons from the conduction band to drive further reduction of silver ions at their surface. This may cause particles to coalesce to form a smaller number of larger deposits (Figure 7.2). If this effect is

significant, as appears to be the case at the surface of the Ag:BT-30 powder, the marking of domain boundaries becomes less apparent.

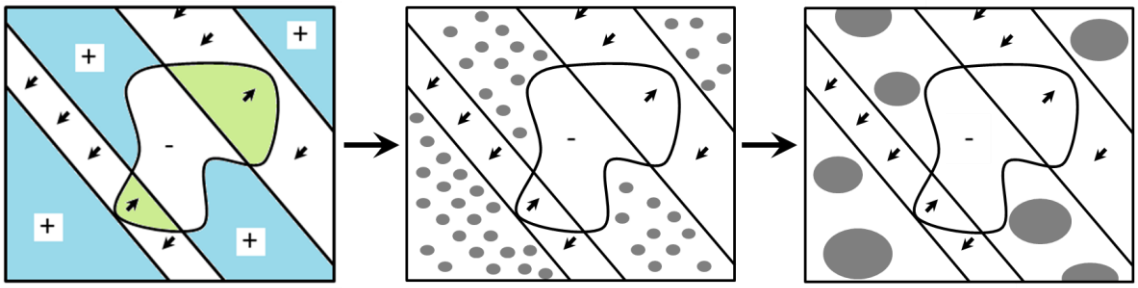

Figure 7.2 Deposition of silver particles at the surface of barium titanate with increasing length of exposure to super band gap light. Straight edged 90^o and curved edged 180^o domain boundaries are shown. With longer illumination time the particles coalesce to form a smaller number of larger deposits

The yellow colour of Fe:BT-30 indicated formation of a coating at the surface of the powder but did not correspond to the colour of iron metal. EDX analysis did not detect elements other than barium, titanium or oxygen at the powders surface. This meant the deposits composition was unknown and also indicated the loading to be below 0.05 weight %. The light yellow colour may correspond to formation of $Fe(OH)_3$ deposits. The SEM image of Fe:BT-30 (Figure 7.1) shows ordered straight edged regions corresponding to the presence of 90^o domain walls. This suggested deposition occurred selectively at C+ or C- domains. In iron nitrate solution metal ions were in the Fe^{3+} oxidation state. This meant oxidation of Fe^{3+} ions by hole carriers to form $Fe(OH)_3$ deposits could not have occurred. The $Fe(OH)_3$ deposits may have formed after Fe^{3+} ions were reduced at C+ domains (Equation 7.1). The iron particles may then have reacted with water to form Fe_2O_3 (Equation 7.2) with subsequent reaction with water forming $Fe(OH)_3$ deposits (Equation 7.3).

$$Fe^{3+} + 3e^- \rightarrow Fe_{(S)} \qquad (7.1)$$

$$2Fe_{(S)} + 3H_2O \rightarrow Fe_2O_3 + 6H^+ + 6e^- \qquad (7.2)$$

$$2Fe_2O_3 + 6H_2O \rightarrow 2Fe(OH)_3 + 6H^+ + 6e^- \qquad (7.3)$$

Cu:BT-30 powder was blue in colour after illumination in copper sulphate solution. This colour change indicated a coating at the powders surface but did not correspond to that of copper metal. EDX analysis detected a loading of 0.05 weight % of copper at the powders surface. In this case the blue colour may indicate formation of $Cu(OH)_2$ deposits. In solution the copper ions were in the Cu^{2+} oxidation state. This meant further oxidation at C- domains could not occur as copper exists only in the Cu^0, Cu^+ or Cu^{2+} state. Deposits may have formed after Cu^{2+} ions were reduced at C+ domains (Equation 7.4). The particles could then have reacted with water molecules to form copper hydroxide (Equation 7.5).

$$\boldsymbol{Cu^{2+} + 2e^- \rightarrow Cu_{(S)}} \qquad (7.4)$$

$$\boldsymbol{Cu_{(S)} + 2H_2O \rightarrow Cu(OH)_2 + 2H^+ + 2e^-} \qquad (7.5)$$

Powders of Ag:SLN-30 and Ag:LN-20 were light grey in colour after UV illumination in silver nitrate solution. As discussed in Chapter 5 XPS analysis confirmed silver in the metal state at the surface of LN powder after illumination with UV light in silver nitrate solution. The grey colour of Ag:LN-20 and Ag:SLN-30 powders was, therefore, taken as an indication of the formation of silver metal deposits at the surface. EDX analysis did not detect silver on either of the powders. This showed the loading of silver deposits to be below the detection threshold of 0.05 weight %. The location at which silver particles had formed was unable to be determined by SEM analysis due to charging at the powders surface. However, as the particles of LN powder were in the ferroelectric phase deposition of silver particles would be expected to have taken place selectively at C+ domains. In Chapter 6 it was discussed that investigation of deposition of silver particles at the surface of periodically poled lithium niobate has shown when photochemical deposition is carried out using a high concentration of silver ions and high intensity of super band gap light that reactions occur preferentially at the boundaries of C+ domains[19]. The high concentration of silver nitrate solution used (0.01 M) and the high intensity of super band gap light emitted by the UV lamp in experiments meant that photochemical reduction

of silver ions may have occurred preferentially at domain boundaries of LN and SLN powders.

7.3 Decolourisation of rhodamine b solution over ferroelectric-metal powders under UV or simulated solar illumination

7.3.1 Results

LN, BT or ferroelectric-metal powders were suspended in solutions of rhodamine b (0.5 g L^{-1}., 200 mL) and illuminated with UV or simulated solar light. The rate of reactions was determined by measuring the change in absorbance of the solutions over time. The decrease in absorbance of the rhodamine b solution after 80 min illumination is shown in Table 7.2.

Table 7.2 Decrease in absorbance of rhodamine b solution over LN, BT and modified BT or LN powders after 80 min UV or simulated solar illumination

Powder	Decrease in rhodamine b solution absorbance (%) under UV illumination	Decrease in rhodamine b solution absorbance (%) under simulated solar illumination	Estimated experimental error
BT	4	2	± 1
Ag: BT-20	16	51	± 1
Ag:BT-30	-	92	± 1
Cu:BT-30	-	27	± 1
Fe:BT-30	-	14	± 1
LN	0	0	± 1
Ag:LN-20	0	1	± 1

Reactions over BT or Ag:BT-20 were compared under UV illumination (Figure 7.3). After 80 min BT powder decolourised the solution by 4 % and Ag:BT-20 powder decolourised the solution by 16 %. The rate of reactions over BT, Ag:BT-20 or Ag:BT-30 powder was compared under simulated solar illumination (Figure 7.2). After 80 min BT powder decolourised the solution by 2 %, Ag:BT-20 powder decolourised the solution by 51 % and Ag:BT-30 powder decolourised the solution by 92 %. In comparison to BT powder, Ag:BT-20 showed a greater increase in decolourisation of the dye solution under simulated solar illumination than UV illumination (Table 7.2).

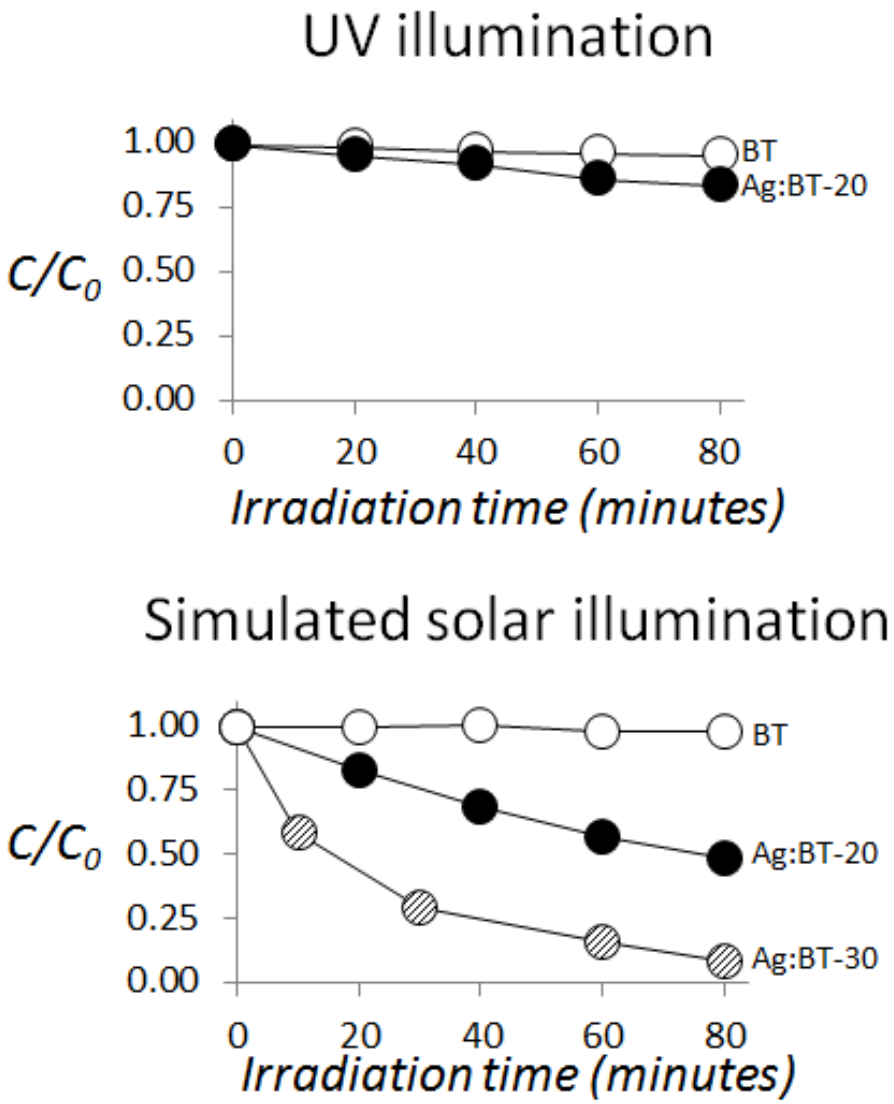

Figure 7.3 Plot of the decolourisation rate of rhodamine b solution BT and Ag:BT-20 powder under UV or simulated solar illumination

The rate of reactions over Cu:BT-30, Fe:BT-30 and BT powder were compared under simulated solar illumination (Figure 7.4). After 80 min illumination Cu:BT-30 powder decolourised the solution by 27 % and Fe:BT-30 powder decolourised the solution by 14 % (Table 7.2).

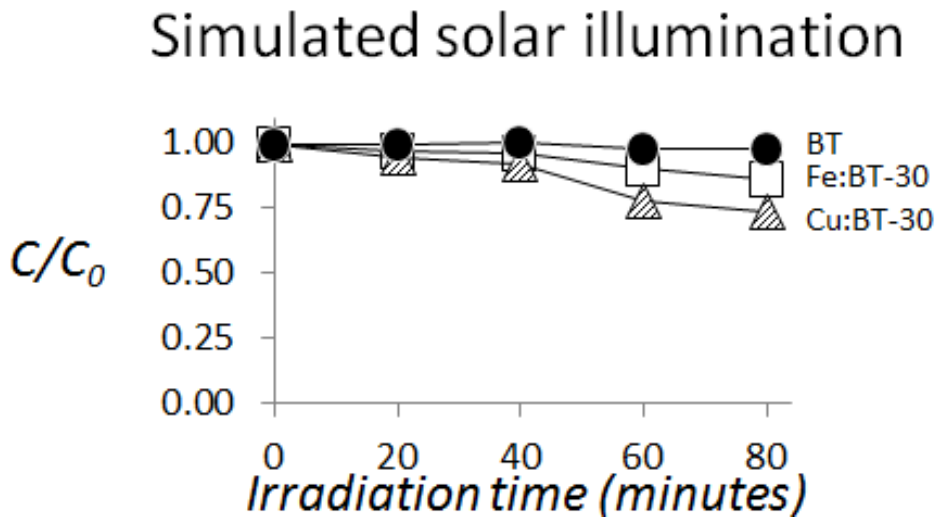

Figure 7.4 Plot of the decolourisation rate of rhodamine b solution Ag:BT-30, Cu:BT-30 and Fe:BT-30 powder under simulated solar illumination

Reactions over LN or Ag:LN-20 powder were compared under UV or simulated solar illumination (Figure 7.5). The plot of change in absorbance is shown on a decreased Y axis scale as the rate of reaction was lower than over silver modified BT powders (Table 7.2). It was shown that under UV or simulated solar illumination the absorbance of the dye solution containing LN powder increased. The increase in absorbance after 80 min was 3 % under UV illumination and 3 % under simulated solar illumination. Under UV illumination Ag:LN-20 powder also showed a net increase in the absorbance of the solution of 1 % after 80 min. Under simulated solar illumination Ag:LN-20 powder decolourised the solution by 1 % after 80 min (Table 7.2).

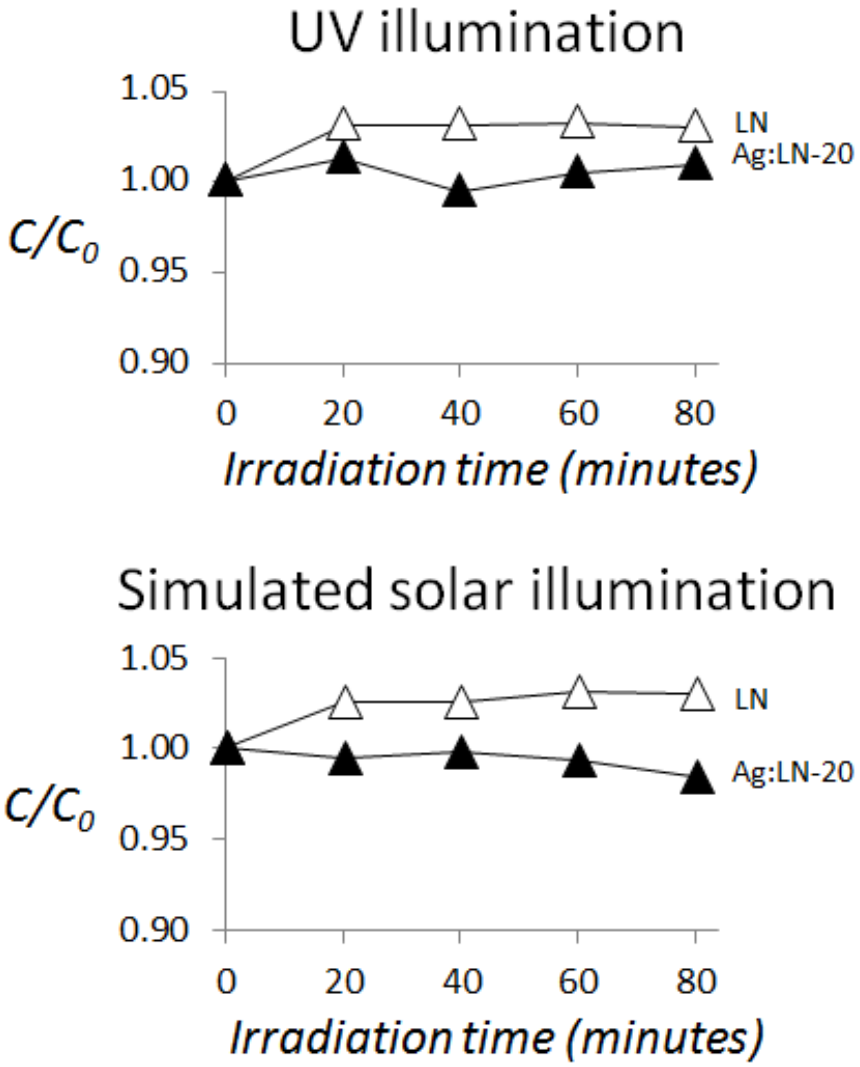

Figure 7.5 Plot of the decolourisation rate of rhodamine b solution LN and Ag:LN-20 powder under UV or simulated solar illumination

Using different conditions to the other experiments suspensions of Ag:SLN-30 or SLN powder suspended in rhodamine b solution (1.5 g L^{-1}, 40 mL) were illuminated for 120 min by simulated solar light (Figure 7.6). The rate of reactions was lower over Ag:SLN-30 powder in comparison to SLN powder. After 120 min the solution was decolourised by 25 % by Ag:SLN-30 powder and by 43 % by SLN powder.

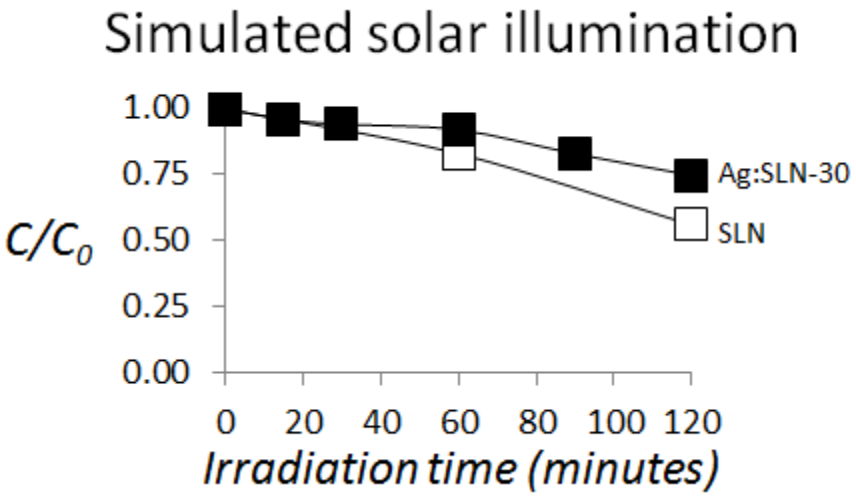

Figure 7.6 Plot of the decolourisation rate of rhodamine b solution SLN and Ag:SLN-30 powder under simulated solar illumination

7.3.2 Discussion

7.3.2.1 Decolourisation reactions over BT and LN powders under UV or simulated solar illumination

In Chapter 6 suspensions of BT (1.5 g L^{-1}, 40 mL) were shown to decolourise rhodamine b solution by 37 % after 60 min UV illumination. Experiments in this Chapter used a lower loading of powder (0.5 g L^{-1}) and larger volume of rhodamine b solution (200 mL). BT powder decolourised the rhodamine b solution by 4 % after 80 min UV illumination (Figure 7.3). The lower loading of powder reduced the number of particles adsorbing super band gap light to produce excited carriers. This decreased the rate of transfer of carriers to reactants to drive decolourisation reactions. The higher volume of solution also meant that per molecule decolourised by BT powder the decrease in concentration in solution was lower. As result the rate of decolourisation over BT powder was decreased using these conditions in comparison to the conditions used in Chapter 6.

Comparison of the rate of reactions over BT powder under UV and simulated solar illumination showed reactions proceeded at a slower rate under simulated solar illumination (Table 7.2). The solar simulator emitted photons of light

equalling or exceeding the band gaps of barium titanate (3.2 eV) and lithium niobate (3.7 eV) (Figure 7.7). The intensity of light emitted that equalled or exceeded the band gap of BT powder was estimated to be 20.5 mW cm^{-2} by the UV lamp and 9.1 mW cm^{-2} by the solar simulator. The slower reaction rate under simulated solar illumination can be attributed to the lower intensity of super band gap light emitted causing a lower rate of carrier excitation in BT powder to drive PCO reactions in comparison to when illuminated by the UV lamp.

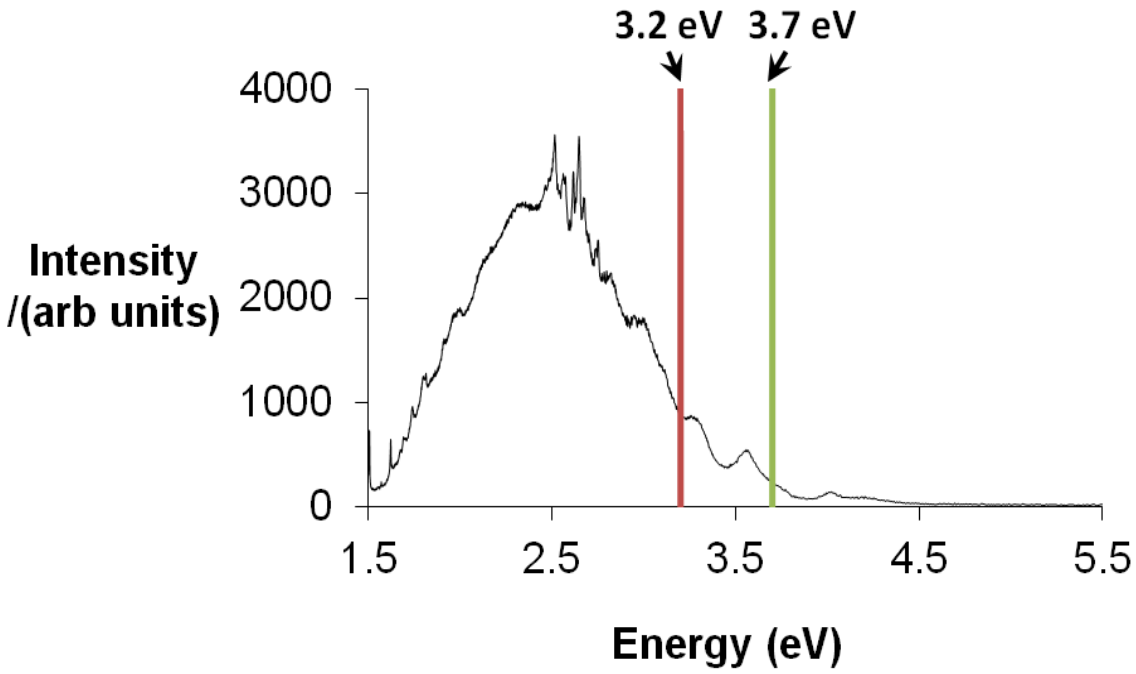

Figure 7.7 The emission spectrum of the solar simulator with the band gap energies of barium titanate (3.2 eV) and lithium niobate (3.7 eV) marked

In Chapter 6 suspensions of LN powder (1.5 g L^{-1}, 40 mL) were shown to decolourise rhodamine b solution under UV illumination. Experiments in this Chapter found that the absorbance of rhodamine b solutions containing LN powder did not detectably decrease under illumination and in fact increased by 3 % after 80 min UV illumination or by 3 % after 80 min simulated solar illumination (Figure 7.5). The increase in absorbance under illumination can be attributed to dye molecules being desorbed from the powders surface as a result of excited carriers increasing internal screening as discussed in Chapter

6. Under UV illumination the increase in absorbance of the solution had become steady after 20 min at 3 % (Figure 7.5). This suggested that either internal screening had completely compensated the surface charge or that the rate of carrier formation and recombination had reached equilibrium at the interface. Under simulated solar illumination desorption increased over the course of 80 min illumination, peaking at 3 %. The intensity of light emitted by the UV lamp and solar simulator exceeding the band gap of LN powder was estimated to be 9.0 mW cm^{-2} and 2.5 mW cm^{-2} respectively. The slower rate of desorption of dye under simulated solar illumination can be explained by the lower rate of carrier formation in LN powder, this caused internal screening to increase more slowly compared to when LN powders was illuminated with UV light. The rhodamine b solution was not decolourised under UV or simulated solar illumination suggesting that although excited carriers screened the surface charge by accumulating at the interface the rate of transfer of carriers to drive photocatalytic reactions was too low to produce a detectable reaction under the conditions used.

7.3.2.2 The effect of deposition of silver nanoparticles upon BT or LN powders photocatalytic activity

Photocatalytic decolourisation of dye over semiconductor powders with silver nanoparticles deposited at the surface has been proposed to take place via a similar mechanism to the PCO mechanism discussed in Chapter 6[106]. The silver particles form a Schottky barrier with the semiconductor (Figure 7.8). This causes trapping of electrons, reducing the recombination of carriers. Reduction of oxygen takes place at the surface of the metal particles (or the semiconductor powder) to form the superoxide anion radical. Hole carriers migrate to the surface and oxidise hydroxide ions to form the hydroxyl radical. The superoxide anion radical or hydroxyl radicals then react with dye molecules to drive decolourisation. Adsorption of visible light photons by the silver particles can also excite a localised surface plasmon resonance (LSPR)[107]. The LSPR

enhances the localised electric fields, exciting carriers in the semiconductor[108] and increasing the rate of trapping of electrons by the metal particles[103].

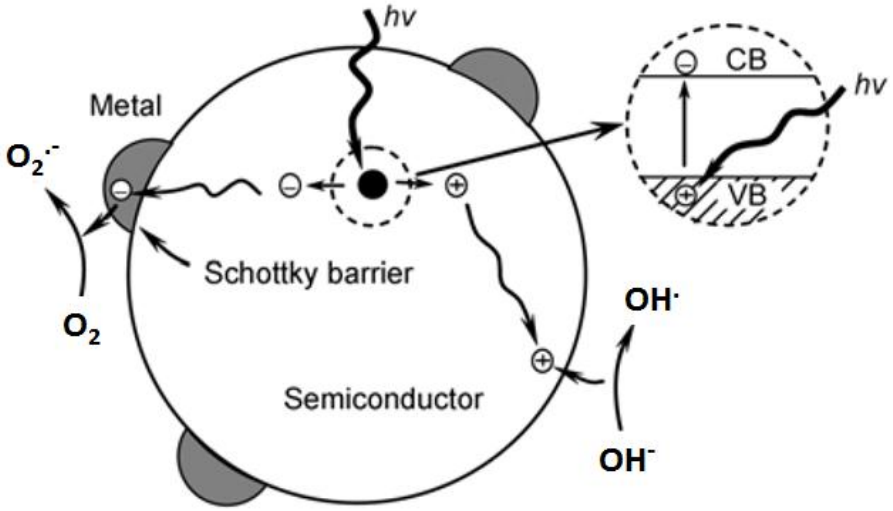

Figure 7.8 Schematic diagram showing reactions over a metal modified semiconductor photocatalyst particle (Source ref. 106)

The Schottky barrier height formed between deposited silver particles and BT powder can be determined using Equation 7.6. The work function of silver is reported to be 4.6 eV[106] and the electron affinity of BT powder is estimated to be 4.2-4.3 eV. The Schottky barrier height is, therefore, calculated to be 0.3-0.4 eV. As the barrier height is positive the silver particles are able to trap electrons from the conduction band of BT powder.

$$\emptyset_{\mathbf{B}} = \emptyset_{\mathbf{M}} - \boldsymbol{\chi} \qquad (7.6)$$

Where $\boldsymbol{\chi}$ is the electron affinity, $\emptyset_{\mathbf{B}}$ is the barrier height and $\emptyset_{\mathbf{M}}$ is the metal barrier height.

In Chapter 6 BT powder was proposed to drive photocatalytic reactions via a PCO mechanism. Decolourisation reactions over silver modified BT powders likely follow the PCO type mechanism suggested to take place over silver modified semiconductor systems.

The effect of silver deposition at the surface of BT powder upon the rate at which the powder decolourised rhodamine b solution was first investigated under UV illumination (Figure 7.3). After 80 min BT powder decolourised

rhodamine b solution by 4 % and Ag:BT-20 powder decolourised rhodamine b solution by 16 % (Table 7.2). The increased reaction rate over Ag:BT-20 powder can be explained by trapping of electrons reducing the rate of carrier recombination. Under simulated solar illumination the rate of reaction over Ag:BT-20 powder was found to be greater than under UV illumination. Ag:BT-20 powder decolourised rhodamine b solution by 51 % after 80 min simulated solar illumination compared to 16 % under UV illumination (Table 7.2). As discussed in the previous section the UV lamp emitted a higher intensity of photons exceeding the band gap of BT powder than the solar simulator. The greater photocatalytic activity of Ag:BT-20 powder under simulated solar light was, therefore, not a result of increased super band gap illumination. Instead this can be attributed to the solar simulator emitting photons able to excite LSPR in the silver particles. The LSPR peak adsorption (λ_{max}) of silver particles at the surface of Ag:BT-20 powder could not be measured directly using UV-Vis analysis. The small size of the metal deposits of less than 100nm and the larger size of the powder of the order of the order of μm meant that light incident to the metal particles was diffracted by the powder. The value of the LSPR λ_{max} of silver particles was instead estimated based upon the average particle size and the refractive index of barium titanate. Silver deposits at the surface of Ag:BT-30 were measured to have an average diameter of 58 nm. Unsupported silver nanoparticles with an average diameter of 60 nm have been shown to have an LSPR λ_{max} at 450nm[180]. The LSPR λ_{max} of metal deposits is known to be dependent upon the local refractive index at the particles surface[181; 107]. As a result when particles are mounted on a support the refractive index of the material causes the LSPR λ_{max} to be red shifted to a longer wavelength. The refractive index of titanium dioxide powder is reported to be 2.49. The LSPR λ_{max} of silver particles was found to be red shifted by 100nm[182]. The refractive index of barium titanate is reported to be 2.42 measured at 600 nm[183], similar to that of titanium dioxide. The red shift of the LSPR λ_{max} of silver at the surface of barium titanate was assumed to also be approximately 100nm. The estimated LSPR λ_{max} for silver particles at the surface of Ag:BT-30 was, therefore, 550 nm. The solar simulator emitted photons continuously between wavelengths of

300-900 nm. This meant photons were emitted at, and around, the estimated LSPR λ_{max} of silver particles (Figure 7.9). The increased reactivity of Ag:BT-20 under simulated solar light compared to under UV illumination suggests that LSPR in silver particles strongly influenced the rate of reactions by increasing electron excitation in the BT powder and the rate at which conduction band electrons in BT powder were trapped by silver deposits.

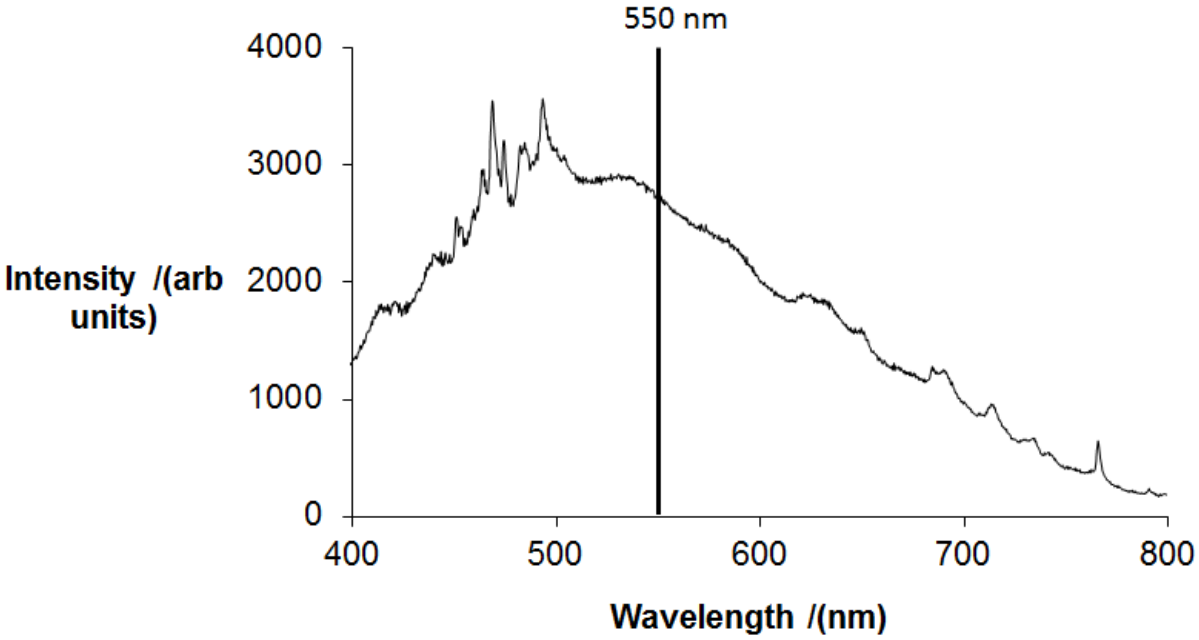

Figure 7.9 Emission spectrum of the solar simulator. The estimated LSPR λ_{max} of silver nanoparticles is marked

The electron affinity of lithium niobate is reported to be 1.1 eV[184]. Using equation 7.7 the Schottky barrier height formed with silver particles is calculated to be 3.5 eV. The positive Schottky barrier height meant that metal particles trapped could trap electrons from the conduction band of lithium niobate powders. As discussed in Chapter 6 LN powder decolourised dye under super band gap illumination via a modified PCO reaction. Reactions over silver modified lithium niobate powders, therefore, likely followed a similar mechanism to that proposed for reactions over silver modified semiconductor systems. The rate of reactions over LN and Ag:LN-20 powder were compared under UV illumination (Figure 7.5). Neither Ag:LN-20 or LN powder detectably decolourised the dye solution and so Ag:LN-20 powder did not show a clear

change in photocatalytic activity in comparison to LN powder. Dye was desorbed from the surface of both LN and Ag:LN-20 powders under UV illumination as a result of internal screening as discussed in Chapter 6. After 80 min illumination the absorbance of rhodamine b solution containing LN powder increased by 3 % and the absorbance of dye solution containing Ag:LN-20 powder increased by 1 %. This showed less dye was desorbed from the surface of Ag:LN-20 powder than LN powder. This can be explained due to fewer dye molecules having been adsorbed in the double layer by Ag:BT-20 powder than LN powder prior to illumination due to silver deposits externally screening the surface charge at C+ domains as discussed in Chapter 6. Internal screening of the surface charge under super band gap illumination caused fewer dye molecules to be desorbed as a result. Under simulated solar illumination after 80 min Ag:LN-20 powder decolourised the dye solution by 1 % and LN powder did not detectably decolourise the dye (Table 7.2). As the LSPR λ_{max} of silver particles in the structure of lithium niobate samples has been reported to be 543nm[185] and the solar simulator emitted light at wavelengths between 200-900 nm continuously (Figure 7.9) the increased rate of reaction over Ag:LN-20 powder compared to LN powder can be attributed to excitation of LSPR in the metal deposits generating carriers in Ag:LN-20 powder and increasing the rate of trapping of electrons by the metal deposits.

The increase in photocatalytic activity of Ag:BT-20 powder in comparison to BT powder was significantly greater than the increase in photocatalytic activity of Ag:LN-20 powder in comparison to LN powder (Table 7.2). This can be explained by several factors. Firstly, silver particles may be less stable to oxidation at the surface of LN powder than BT powder. As silver oxide particles are unable to trap electrons to reduce recombination rates and also do not adsorb photons to excite a LSPR oxidation of silver deposits would decrease the photocatalytic activity of the silver modified powder. Secondly, difference in loading at the surface of the powders may be significant in determining the reaction rate. Investigation of silver nanoparticle deposition at the surface of titanium dioxide powder has shown reaction rates increase with loading up to an optimal value[103; 106]. As the loading of silver at the surface of the powders was

not detected by EDX analysis the difference in loading at the surface of the powder cannot be directly compared. However, it was show in Chapter 6 that the rate of dye decolourisation reactions over BT powder was greater than over LN powder. The greater photocatalytic activity of BT powder may have meant the quantity of silver deposits formed by photochemical reduction reactions was higher at the surface of Ag:BT-20 powder than at the surface of Ag:LN-20 powder. The greater loading may have increased the photocatalytic activity of Ag:BT-20 powder in comparison to Ag:LN-20 powder. Finally when the optimal loading of silver deposits at the surface of titanium dioxide powder is exceeded the powders photocatalytic activity decreases[102]. This is attributed to silver deposits becoming large enough to attract positive hole carriers toward them. This causes silver deposits to become centres for recombination of electrons and hole carriers (Figure 7.10).

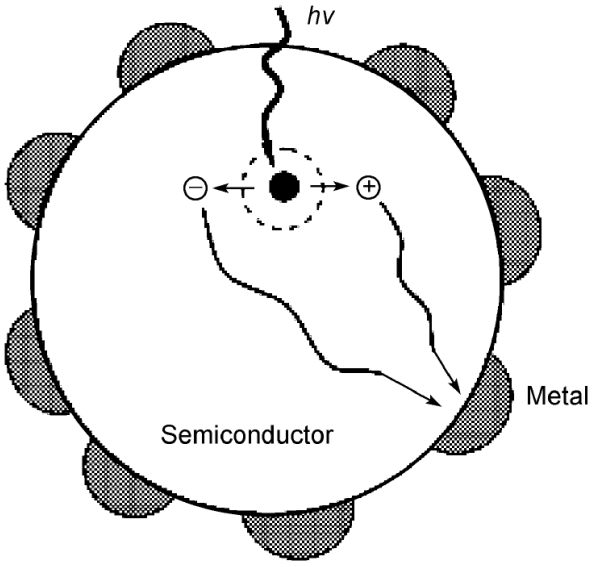

Figure 7.10 Metal particles acting as recombination centres at high loading at a semiconductor surface (Source ref. 106)

The lower photocatalytic activity of Ag:LN-20 powder may be a result of a greater proportion of silver deposits driving carrier recombination than at the surface of Ag:BT-20 powder. Evidence that this may be the case was shown by comparison of the rate of reactions over Ag:SLN:30 powder and SLN powder under simulated solar illumination. It was shown in Chapter 6 that the rate of

photocatalytic dye decolourisation was greater over SLN powder than LN powder. This was attributed to difference in the purity or morphology of the materials. In these experiments the rate of reaction of rhodamine b solution over SLN powder was again greater than over LN powder. After deposition of silver particles on the powders rate of reaction over Ag:LN-20 powder increased compared to over LN powder, however, over Ag:SLN-30 powder the decolourisation of dye solution after 120 min was lower (25 %) than over SLN powder (43 %) (Figure 7.6). This can be explained by the rate of carrier recombination in Ag:SLN-30 powder being higher than in the unmodified SLN powder. This could be a result of the loading of silver deposits at the surface of Ag:SLN-30 being large enough to attract hole carriers to the interface to drive carrier recombination. However, as EDX analysis was unable to detect silver at the surface of Ag:SLN-30 powder this suggested the loading to be less than 0.05 weight %. As the photocatalytic activity of silver modified titanium dioxide powder is reported to begin to decrease at loadings above 1.5-2.0 weight %[102] this meant the loading of silver at the surface of Ag:SLN-30 powder does not appear to be great enough to account for the high rate of carrier recombination. Alternatively carrier recombination in Ag:SLN-30 powder could be explained by silver deposition having occurred at the edge of C+ domains. Particles nucleating at the C+ domain boundary may have continued to grow to bridge the surface of C+ and C- domains (Figure 7.11). Silver deposits bridging C+ and C- domains would drive recombination of electrons trapped by the silver particles at C+ domains with hole carriers accumulating at C- domains. If the high rate of carrier recombination in Ag:SLN-30 powder was a result of silver deposits bridging C+ and C- domains then growth of silver deposits at the domain boundaries of LN powder to causing bridging between C+ and C- domains may also partly account for the lower photocatalytic activity of Ag:LN-20 powder in comparison to Ag:BT-20 powder.

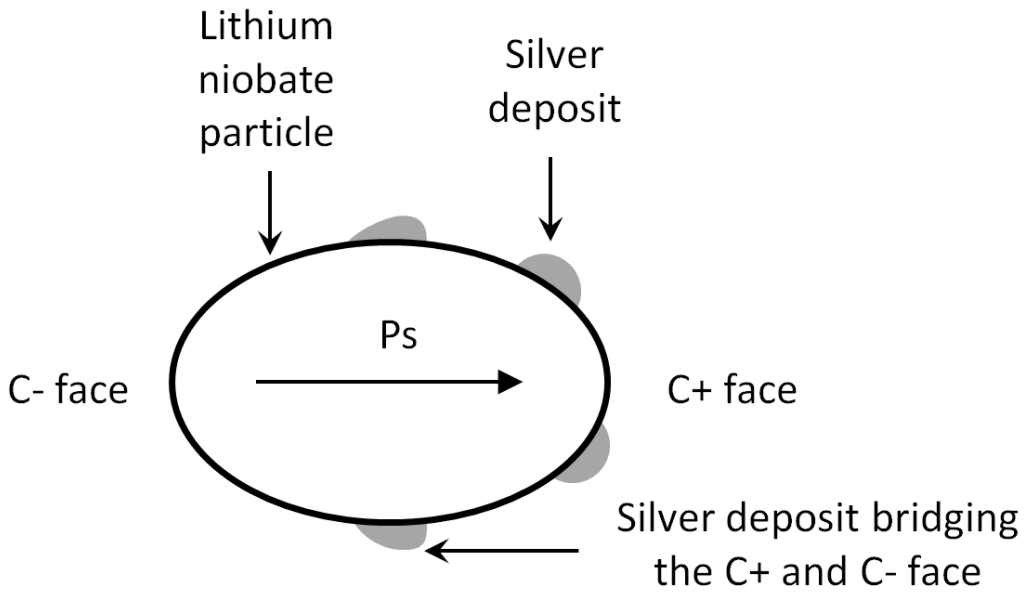

Figure 7.11 Scheme showing the possible growth of silver deposits at the surface of lithium niobate powder. As the deposits continue to grow at the C+ domain this may have caused bridging between C+ and C- domains to allow recombination of electron and hole carriers to occur. This would cause some of the metal deposits to act as recombination centres.

Of the two possibilities proposed to explain the difference in silver deposition on the photocatalytic activity of barium titanate powder in comparison to lithium niobate powder it appears more plausible that a greater proportion of silver deposits bridged C+ and C- domains to drive carrier recombination at the surface of lithium niobate in comparison to barium titanate powders rather than the quantity of silver deposits at the surface of the lithium niobate powders exceeded the optimal loading whereas the quantity of silver deposits at the surface of barium titanate powder did not exceed the value of optimal loading. EDX analysis of the surface of silver modified barium titanate or lithium niobate powders was unable to detect silver on any of the powders. This suggested the loading to be low, less than 0.05 weight % for all of the powders. As the optimal loading of silver deposits for titanium dioxide powder is reported to be between 1-2 weight % this suggests that it is unlikely that a comparatively low loading of silver deposits of less than 0.05 weight % was below the optimal loading value

of deposits for barium titanate powder but was sufficient to exceed the optimal loading value of SLN or LN powders to result in decreased photocatalytic activity. Instead this suggests that the role of silver deposits at the surface of the lithium niobate powders may differ from that of silver deposits at the surface of barium titanate powder in determining photocatalytic activity. The explanation that a greater proportion of silver deposits bridged C+ and C- domains to drive carrier recombination at the surface of lithium niobate powders compared to at the surface of barium titanate powders is more consistent with this observation.

7.3.2.3 Effect of the polarisation on photocatalytic activity of silver modified LN or BT powders

The internal depolarisation fields in ferroelectrics cause electrons to accumulate in the space charge region at C+ domains. It was hypothesised that metal deposits formed at C+ domains may trap a greater proportion of excited electrons than metal particles at the surface of semiconductors as a result. The effect of the accumulation region at C+ domains upon the photocatalytic activity of BT or LN powders modified with silver deposits was considered by comparing the reactions rates from experiments with literature values reporting the change in photocatalytic activity of titanium dioxide powders after modification with silver particles under similar conditions to those used in this work.

In one study titanium dioxide powder with a surface area of 21.5 m^2 g^{-1} was investigated[102]. Loadings of between 0.5-2.0 weight % of silver were deposited at the surface of the powders. Eight 8 W mercury UV lamps were used to illuminate suspensions of powder in 50 mL of aqueous direct red 23 dye solution for 120 min. The plot of the rates of decolourisation of the dye solution over the powders is shown in Figure 7.12. The rate of reactions increased with loading of silver up to 1.5 weight %. The total amount of dye decolourised after silver deposition increased by between approximately 12-20 % compared to the raw titanium dioxide powder.

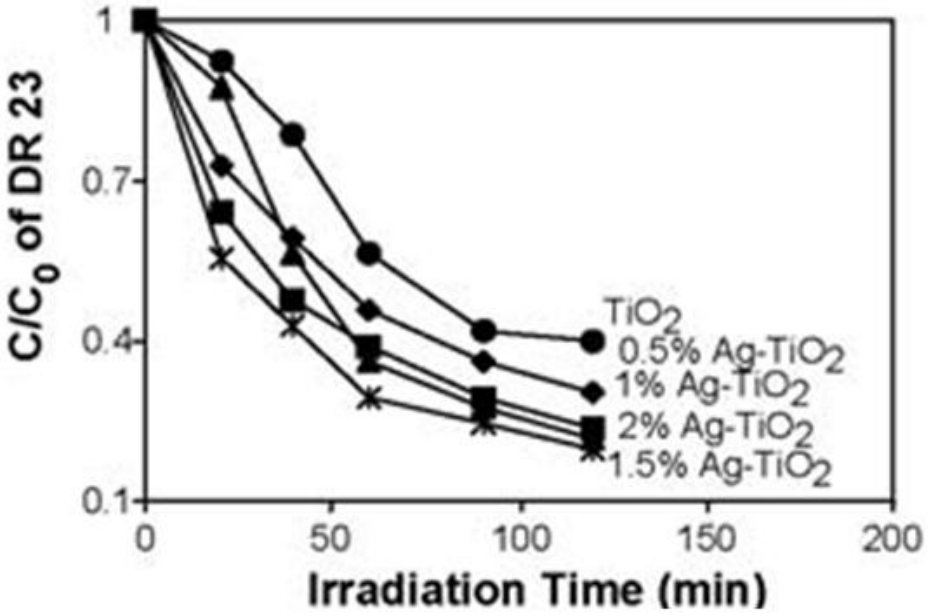

Figure 7.12 Comparison of decolourisation of DR 23 over titanium dioxide and silver modified photocatalysts under UV illumination (Source ref.102)

In another study titanium dioxide powder and silver modified titanium dioxide powder were suspended in rhodamine b solution (1.2 g L-1, 50 mL) and illuminated with a Q-sun solar simulator or natural sunlight[186]. The results showed that after 20 min simulated solar light illumination titanium dioxide decolourised the solution by approximately 65 % and silver modified titanium dioxide (5.0 weight %) decolourised the solution by approximately 95 %. After 90 min illumination by natural sunlight titanium dioxide powder decolourised the dye solution by approximately 65 % and silver modified titanium dioxide (2.0 weight %) decolourised the solution by approximately 80 %.

The loading of silver deposits at the surface of BT:Ag-20 and Ag:BT-30 powders was shown by EDX analysis to be less than 0.05 weight %. This is significantly lower than the loadings deposited at the surface of the titanium dioxide powders in the experiments from the literature described in the previous paragraphs. As photocatalytic activity of titanium dioxide powder was shown to increase with loading of silver particles, the comparatively low loading of silver at the surface of BT might be expected to produce a small increase in photocatalytic activity. Under UV illumination BT powder decolourised the dye solution by 4 % and

Ag:BT-20 decolourised the solution by 16 % (Table 7.2). The increase in photocatalytic was comparable to the reported increase in photocatalytic activity of titanium dioxide powder after silver deposition under UV illumination (Figure 7.12). Under simulated solar illumination BT powder decolourised the dye solution by 2 %, in comparison Ag:BT-20 or Ag:BT-30 powder decolourised the solution by 51 % and 92 % respectively (Table 7.2). The increase in photocatalytic activity of BT powder under simulated solar illumination after silver deposition was greater than the reported increase of photocatalytic activity of titanium dioxide powder under natural sunlight or simulated solar illumination after deposition of silver particles. The apparent similar or greater increase in photocatalytic activity of BT powder after deposition of less than 0.05 weight % of silver particles in comparison to the increase in photocatalytic activity of titanium dioxide powder after deposition of several weight % of silver particles may be a result of several factors. The light sources used in this work may have emitted a higher intensity of super band gap light or light able to excite LSPR in silver deposits than in the experiments investigating silver modified titanium dioxide powders. This could have increased the rate of reactions of the silver modified BT powders in experiments. It is also possible that low loadings of less than 0.05 weight % silver deposition produces a greater increase in photocatalytic activity than at loadings of several weight %. Alternatively the results may show evidence that the accumulation of electrons at C+ domains of BT powder caused silver deposits to trap carriers at a higher rate than at the surface of titanium dioxide powder, producing a large increase in photocatalytic activity at low loading.

Under UV illumination neither Ag:LN-20 powder or LN powder detectably decolourised the rhodamine b solution. Under simulated solar illumination LN powder did not detectably decolourise the dye solution whereas Ag:LN-20 powder decolourised the solution by 1 % after 80 min (Table 7.2). The increase in photocatalytic activity of LN powder after deposition of silver particles was significantly lower than the reported increase in photocatalytic activity of titanium dioxide powder after silver deposition. This suggested that other factors e.g. loading of silver particles, oxidation of silver deposits or silver deposits

bridging C+ and C- domains to drive carrier recombination, had a greater impact on determining the photocatalytic activity of Ag:LN-20 powder than the effect of accumulation of electrons at C+ domains upon increasing the rate at which silver particles trapped carriers.

7.3.2.4 Increased reaction rates over Cu:BT-30 or Fe:BT-30 systems in comparison to BT powder

Under simulated illumination the rate of reactions over Fe:BT-30, Cu:BT-30 and BT powders were compared (Figure 7.4). After 80 min BT powder decolourised the dye solution by 2 %, Fe:BT-30 decolourised the dye solution by 14% and Cu:BT-30 powder decolourised the dye solution by 27 %. As discussed in Section 7.2.2 when BT powder was suspended in copper sulphate solution and illuminated with super band gap light to produce Cu:BT-30 powder the colour of the material had changed from white to blue. This indicated that a surface coating had formed on the powder, however, the blue colour of the Cu:BT-30 powder did not correspond to that of copper metal deposits. Instead this suggested that after copper metal deposits formed on the powders surface they had subsequently undergone oxidation to form copper hydroxide ($Cu(OH)_2$) deposits. Similarly when BT suspended in iron nitrate solution was illuminated with super band gap light in order to produce Fe:BT-30 powder the colour of the material changed from white to yellow. The change indicated formation of a surface coating on the powder that did not correspond to that of iron metal. Instead the yellow colour suggested that after photochemically deposited iron particles had formed they subsequently been oxidised to form iron hydroxide ($Fe(OH)_3$) deposits. The greater rates of decolourisation of the rhodamine b solution over Cu:BT-30 and Fe:BT-30 powders compared to BT powder showed the deposits of metal hydroxides to have increased BT powders photocatalytic activity.

In the case of Cu:BT-30 powder the increased photocatalytic activity compared to BT powder may be a result of conduction band electrons reducing $Cu(OH)_2$ back to copper metal (Equation 7.7) when illuminated with super band gap light

as the reduction potential of copper (-0.2 V vs. NHE) is similar to the conduction band edge of BT (-0.3 V vs. NHE).

$$\boldsymbol{Cu(OH)_2 + 2e^- \rightarrow Cu_{(S)} + 2OH^-} \qquad (7.7)$$

The work function of copper metal is 4.7 eV[156]. Using Equation 7.8 the barrier height formed between BT powder and copper metal is calculated to be 0.4-0.5 eV. As the Schottky barrier height is positive, copper particles can trap electrons from BT powder to reduce carrier recombination. Visible light photons emitted by the solar simulator may also excite a LSPR in copper nanoparticles[187]. The greater photocatalytic activity of Cu:BT-30 powder compared to BT powder can, therefore, be attributed to photocatalytically deposited copper which had oxidised to form $Cu(OH)_2$ deposits being reduced back to copper deposits at the C+ domains when the Cu:BT-30 powder is illuminated under super band gap illumination in dye decolourisation experiments.

In the case of Fe:BT-30 powder in order for the $Fe(OH)_3$ deposits to be reduced to iron metal they would first need to be reduced to $Fe(OH)_2$ (Equation 7.8). As the reduction potential of $Fe(OH)_3$ (-0.6 V vs. NHE) is outside the conduction band edge of barium titanate this reaction was unable to occur.

$$\boldsymbol{Fe(OH)_3 + e^- \rightarrow Fe(OH)_2 + OH^-} \qquad (7.8)$$

A possible explanation for the increased activity of Fe:BT-30 powder in comparison to BT powder may be that some of the iron deposits did not undergo oxidation to form $Fe(OH)_3$. As the work function of iron is 4.5 eV[156] the Schottky barrier height is calculate to be 0.2-0.3 eV using Equation 7.7. The positive barrier height would allow electrons to be trapped from the conduction band of barium titanate by iron metal deposits to reduce the rate of carrier recombination. Alternatively $Fe(OH)_3$ deposits may be increasing the rate of reactions over Fe:BT-30 powder through an unexplained mechanism.

7.4 Summary and conclusions

The work in this chapter aimed to study the effect of the polarisation upon the photocatalytic activity of ferroelectric powders with metal particles deposited at the C+ domains. Silver nanoparticles were photochemically deposited at the surface of BT powder or LN powders. Compared to the raw powder the photocatalytic activity of the silver modified powers was greater. The silver modified LN and BT powders were found to drive reactions at greater rates under simulated solar illumination than UV illumination. This was attributed to visible spectrum light exciting LSPR in the metal particles. Silver modified LN powder showed a smaller increase in activity compared to raw LN powder than the increase in photocatalytic activity of silver modified BT powder in comparison to raw BT powder. This was attributed to a lower loading of silver deposits at the surface of LN powder, silver particles being less stable to oxidation or due to deposition of particles at domain boundaries causing bridging of C+ and C- domains by silver deposits to drive carrier recombination. Comparison with literature values suggested that low loading of silver deposits at the surface of BT powder produced a comparable increase in photocatalytic activity to a higher loading of silver deposition at the surface of titanium dioxide. This could be explained by the formation of accumulation region at C+ domains of BT powder increasing trapping of electrons by metal particles compared to at semiconductors surfaces. In conclusion the significant increase in the rate of dye decolourisation over barium titanate powder after a low loading of metal particles were deposited at the surface suggested that the polarisation may influence the activity of ferroelectric-metal powders as photocatalysts, however, several factors prevented a relationship being demonstrated conclusively. The exact loading of metal particles and the electronic state of the copper and iron particles i.e. whether they had been oxidised, was not established. This meant the influence of these parameters on photocatalytic activity could not be distinguished from the influence of the powders polarisation. Other properties of the powders tested e.g. surface area and band gap may also have been responsible for the differences in the photocatalytic activity between the metal modified powders of LN and BT investigated. A clearer understanding of the

relationship between polarisation and the photocatalytic activity of ferroelectric-metal systems may be possible through further work carrying out similar experiments using thin film samples of barium titanate. XPS and EDX analysis techniques are better suited to investigating the surface of thin films than powders. The use of thing films would allow these methods to more accurately determine the loading as well as their electronic state of deposited metal particles. Accurately determining the loading of metal deposits on barium titanate thin films would allow the relationship between photocatalytic activity and the loading of metal deposits to be investigated using the experimental setup used in this work. A barium titanate thin film sample could also be used to decolourise dye solutions under super band gap illumination when polarised to have a C+, C- or poly domain structure. Photocatalytic deposition of metal particles on the films surface when poled to produce a C+ face could then be carried out and the metal modified thin film sample could also be used to decolourise dye solutions under super band gap illumination when polarised to have a C+, C- or poly domain structure. By comparing the activity of the thin film with and without metal particles on the surface the relationship between the orientation of the thin films polarisation and the extent by which metal deposits increased the films photocatalytic activity could be investigated.

8 Lithium niobate as a photocatalyst for driving solid-liquid and solid-gas phase photochemical reduction of carbon dioxide

8.1 Introduction

Concern as to the consequences of the rising levels of greenhouse gases in the atmosphere, particularly carbon dioxide produced by burning of fossil fuels, has led to a demand for alternative methods of meeting global energy demands. Over the past 30 years use of semiconductors to photochemically reduce carbon dioxide gas to form hydrocarbon has been studied as a potential method of meeting this demand [3; 6; 97; 98]. Photochemical reduction of carbon dioxide produces formic acid, formaldehyde, methanol, carbon monoxide and methane as well as longer chain hydrocarbons as products[188]. These chemical can be stored and used as fuel stock or in industrial processes. Use of these products as fuel stock is carbon neutral, carbon dioxide gas is released by burning the products but carbon dioxide is also consumed as a reactant in formation of the fuel stock. Previously ferroelectric materials such as strontium titanate and lithium niobate have been shown to drive photochemical reduction using solid-liquid phase conditions[189; 190]. In this chapter lithium niobate is investigated as a photocatalyst for driving solid-liquid and solid-gas phase reduction of carbon dioxide.

8.2 Solid-liquid phase photochemical reduction of carbon dioxide over SLN powder

8.2.1 Results

SLN powder was suspended in distilled water (2.0 g L^{-1}, 50 mL). The suspension was bubbled with carbon dioxide gas at a high flow rate to saturate the solution. The suspension was then illuminated with UV light for 45 min while being bubbled with carbon dioxide gas. Gas chromatograph/mass spectroscopy

(GC/MS) was used to analyse liquid samples for the concentration of formic acid and formaldehyde produced. Samples were found to not contain a detectable amount of either chemical.

8.2.2 Discussion

The quantity of formic acid and formaldehyde formed over SLN powder was investigated as these chemicals are soluble in water and so easily recovered. Formic acid and formaldehyde have also been shown to be typical products of photochemical reduction reactions[188]. The reduction potentials for conversion of carbon dioxide to hydrocarbons are shown in Equations 8-1 to 8-4[190].

$$CO_2 + 2H^+ + 2e^- \rightarrow HCOOH \qquad \text{-0.61V vs. NHE} \quad (8.1)$$

$$CO_2 + 4H^+ + 4e^- \rightarrow HCHO \qquad \text{-0.52V vs. NHE} \quad (8.2)$$

$$CO_2 + 6H^+ + 6e^- \rightarrow CH_3OH \qquad \text{-0.38V vs. NHE} \quad (8.3)$$

$$CO_2 + 8H^+ + 8e^- \rightarrow CH_4 \qquad \text{-0.24V vs. NHE} \quad (8.4)$$

SLN powder would be expected to drive reduction of carbon dioxide to form formic acid (Equation 8.1) and formaldehyde (Equation 8.2) as both reactions reduction potential lie within lithium niobate's band edges (Figure 8.1).

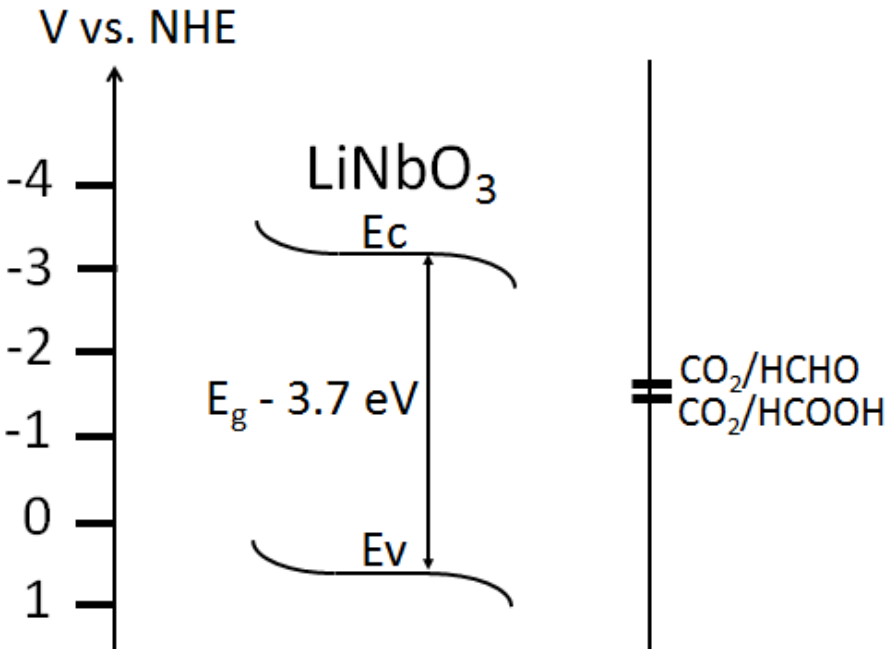

Figure 8.1 The band potentials of lithium niobate and the redox potentials of reduction of carbon dioxide to formic acid or formaldehyde vs. NHE

GC/MS analysis had been calibrated to detect formic acid and formaldehyde down to concentrations of 0.01 ppm. As samples collected from the SLN suspensions were found to not contain either product this suggested the rate of formation of formic acid and formaldehyde was too low to be detected. In Chapter 6 the UV lamp was shown to emit photons with energy equalling or exceeding the band gap of SLN powder. It was also shown that SLN powder is able to drive decolourisation of dye in aqueous suspensions under UV illumination. The low rate of photochemical reduction reactions may, therefore, be a result of the limited availability of dissolved carbon dioxide. The solubility of carbon dioxide gas in aqueous solution is reported to be 0.03 M to 0.06 M at temperatures of 20-35 ^{o}C[191].

8.3 Solid gas phase photochemical reduction of carbon dioxide over SLN powder

8.3.1 Results

A vessel was designed and constructed to house solid-gas phase reactions as described in the Chapter 3. The vessel was used to carry out photochemical reduction of gaseous carbon dioxide over SLN or TiO_2 powder. Distilled water was placed in the reaction chamber along with a stand holding SLN or TiO_2 powder above the water line. The reaction chamber was vented with carbon dioxide and then sealed. Using gas chromatography/ thermal conductivity detection (GC/TCD) samples of gas collected from the vessel were analysed. The composition of gas inside in the vessel after venting was found to be between 10-30 % carbon dioxide by volume after several samples were tested. In separate runs the vessel loaded with SLN or TiO_2 powder was illuminated for 20, 40, 60, 80 or 120 min with UV light. The vessel was opened and liquid samples were collected. GC/MS analysis was used to determine the concentration of formic acid and formaldehyde produced. A plot of the yield in μ mols of formic acid and formaldehyde over SLN or TiO_2 powder is shown in Figure 8.2.

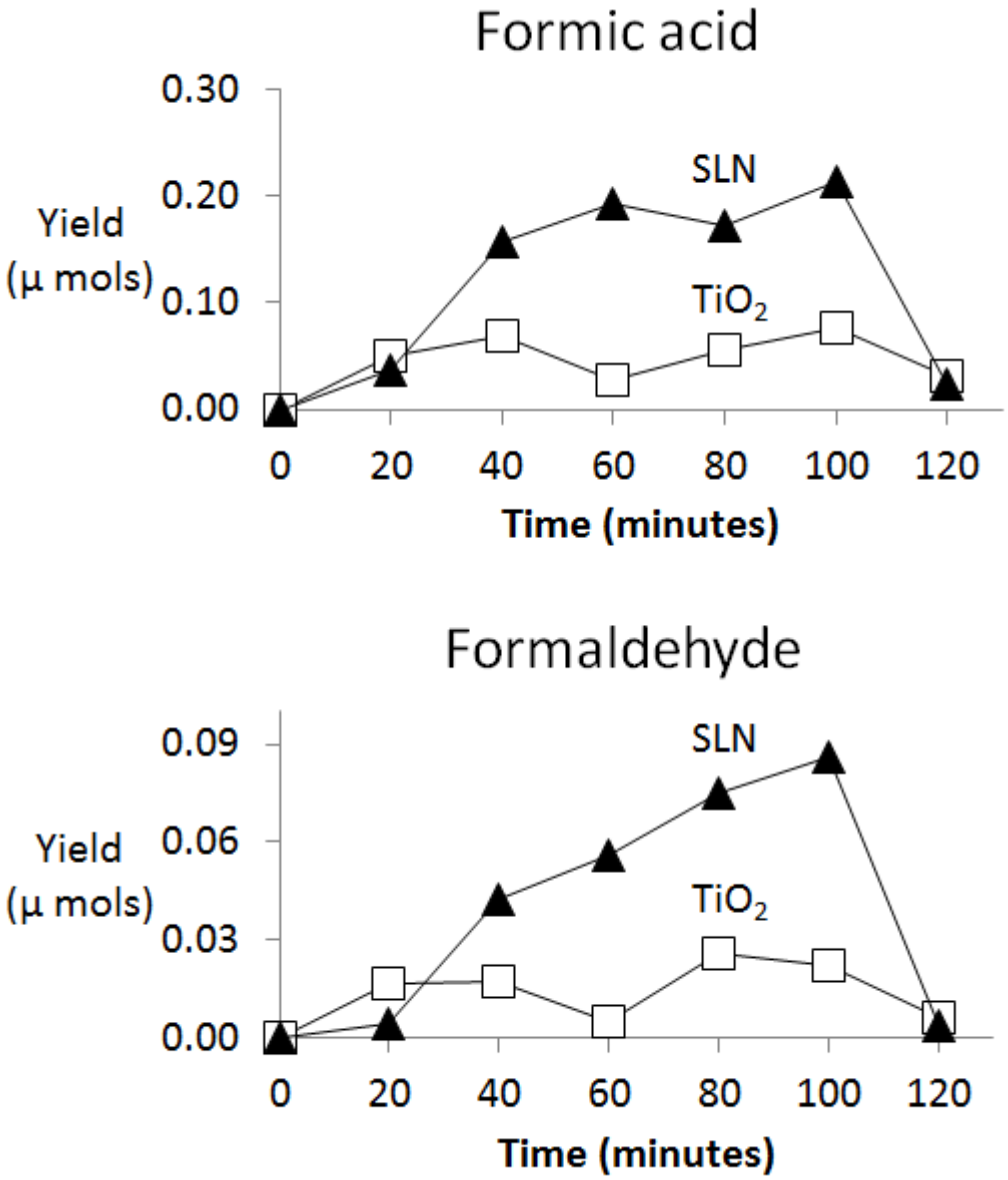

Figure 8.2 Yield of formic acid or formaldehyde produced by photocatalytic solid-gas phase reactions over SLN or TiO_2 powder

The formation of products over SLN powder was shown to initially increase with time before reaching a maximum. The amount of products detected then decreased. Formation of products over TiO_2 powder also fluctuated, shown to increase and decrease. After 120 min illumination the yield of products over SLN or TiO_2 powder had decreased to close to 0. The rate at which formic acid and formaldehyde were produced was shown to be greater over SLN powder than over TiO_2 powder (Figure 8.2).

8.3.2 Discussion

Fluctuations in the quantity of products formed over SLN or TiO_2 powder may be partly explained by inconsistencies in the experimental procedure. To collect liquid samples for analysis the vessel had to be opened. This released the carbon dioxide gas contained in the reaction chamber. Consequently each data point was collected from a separate run rather than removing aliquots from the vessel. Between separate runs the loading of water in the reaction chamber and the surface area of photocatalyst powder used were consistently reproduced. The carbon dioxide venting procedure, however, was found to be inconsistent. GC/TCD analysis of gas samples removed from the vessel showed carbon dioxide loading varied between approximately 10-30%. Different loadings of carbon dioxide may have affected the rate at which products were formed over the photocatalysts. Another cause of the observed fluctuations in the quantity of product may be that formic acid and formaldehyde underwent further photocatalytic reactions over SLN or TiO_2 powders. Photochemical reduction of carbon dioxide is reported to typically produce methanol and methane as products in addition to formic acid and formaldehyde[188]. These products can be formed directly from carbon dioxide by multiple electron reduction as shown in Equations 8.1 to 8.4. Methane and methanol can also be produced via stepwise processes in which formic acid and formaldehyde are consumed as reactants (Equations 8.5 to 8.8)[192].

$$CO_2 + 2H^+ + 2e^- \rightarrow HCOOH \qquad \text{-0.61V vs. NHE} \qquad (8.5)$$

$$HCOOH + 2H^+ + 2e^- \rightarrow HCHO \qquad \text{-0.03V vs. NHE} \qquad (8.6)$$

$$HCHO + 2H^+ + 2e^- \rightarrow CH_3OH \qquad \text{+0.23V vs. NHE} \qquad (8.7)$$

$$CH_3OH + 2H^+ + 2e^- \rightarrow CH_4 \qquad \text{+0.59V vs. NHE} \qquad (8.8)$$

Photocatalytic reduction of carbon dioxide to produce hydrocarbon products has been reported to drive reactions both by direct and stepwise mechanisms. In studies of reactions over titanium dioxide powder the yield of formic acid has

been shown to have reached a maximum after 5 hours UV illumination after which the yield declined[98]. In another study the yield of methane reached a maximum after 4 hours of UV illumination after which the yield decreased [193]. These results indicated products may have been consumed as reactants in subsequent photocatalytic reactions. In other work the yield of methanol, carbon monoxide and methane formed over titanium dioxide powder continued to increase over the course of 20 hours UV illumination, showing evidence these products were not consumed as reactants[194]. The fluctuation in the amount of formic acid and formaldehyde produced over SLN or TiO_2 powder appears to be consistent with products undergoing further photochemical reactions, likely to produce methanol or methane (Equations 8.7 and 8.8).

Samples collected from solid-gas phase reactions over SLN powder after 40 min UV illumination contained a concentration of 1.4 ppm of formic acid. In contrast samples collected from solid-liquid reactions over SLN after 45 min illumination did not contain a detectable amount of formic acid. This showed the concentration of formic acid was below the 0.01 ppm detection threshold of GC/MS analysis in the sample collected from solid-liquid phase reactions, more than 100 times lower than in the sample collected from solid-gas phase reactions. This can be partly attributed to the different volumes of distilled water used in experiments. In solid-gas phase experiments 5 mL of distilled water was placed in the reaction chamber. In solid-liquid phase reactions 50 mL of distilled water was used to suspend SLN powder. As ten times the volume of distilled water was used in solid-liquid phase reactions this meant the same molar yield of product as in solid-gas phase reactions would produce a concentration of formic acid 10 times lower. However, these results still show the molar quantity of formic acid produced in solid-liquid phase reactions was at least 10 times lower than in solid-gas phase reactions over SLN powder after a similar duration of UV illumination. This may be explained by difference in the concentration of carbon dioxide gas present under these conditions. The composition of gas samples collected from the reaction vessel was found to be 10-30% carbon dioxide gas by volume. In comparison the solubility of carbon dioxide in aqueous solution used in solid-liquid phase conditions was

approximately 0.03 M to 0.06 M. The greater concentration of carbon dioxide gas under solid-gas phase conditions may have increased the rate of reactions over SLN powder. Another factor affecting the rate of reaction in solid-gas phase and solid-liquid phase reactions may be the relative amount of super band gap photons adsorbed by the SLN powder. In solid-liquid phase reactions some of the photons emitted by the UV lamp exceeding SLN powders band gap were adsorbed or diffracted by the water rather than being adsorbed by the suspended powder. This may have reduced the rate of carrier excitation compared to under solid-gas phase conditions. In solid-gas phase reactions carbon dioxide gas and water vapour also have higher energy than molecules of liquid water or dissolved carbon dioxide molecules in solid-liquid phase reactions. The higher energy may have increased the rate at which species were adsorbed and desorbed from the double layer at the surface of SLN powder to increase the rate at which excited carriers were transferred to drive reactions.

Comparison of the rate of solid-gas phase reactions over SLN and TiO_2 power showed SLN produced formic acid and formaldehyde at a greater rate than TiO_2 powder (Figure 8.2). As discussed in chapter 6 the UV lamp emitted a lower intensity of photons with energy equalling or exceeding the band gap of lithium niobate (3.7 eV) than barium titanate (3.2 eV). As titanium dioxides band gap is reported to be 3.2 eV[8] the greater rate of reaction over SLN powder was not a result of SLN powder absorbing more super band gap photons than TiO_2 powder to increase the rate of carrier excitation. Instead the faster reaction rate can be partly attributed to the effect of the surface charge of SLN powder. The surface charge affects the mode of adsorption of carbon dioxide molecules. Carbon dioxide is reported to be adsorbed as a bent molecule rather than in its usual linear form at the surface of lithium niobate[195]. Bending of the molecules bonds by the surface charge would be expected to result in the delocalisation of electron density in the carbon dioxide molecules (Figure 8.3). At C+ domains this may increase the withdrawal of electron density from the carbon atom. The rate of transfer of conduction band electrons to the carbon atom of adsorbed molecules may be more thermodynamically favourable at the surface of SLN

powder than at the surface of non-polar TiO_2 powder as a result. This may increase the rate of carrier transfer to drive reactions.

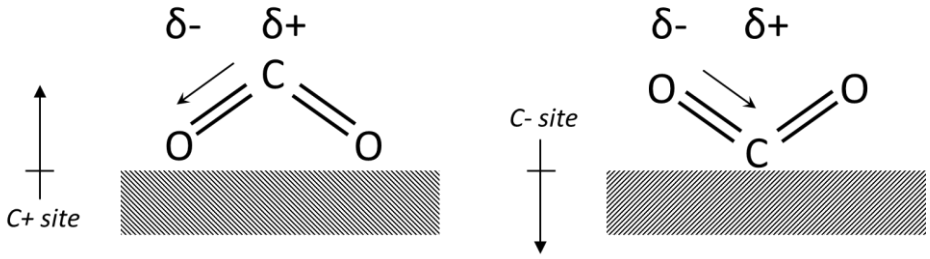

Figure 8.3 Adsorption of carbon dioxide at C+ and C- domains. The arrow shows the possible direction of delocalisation of electron density in the molecules bonds

Lithium niobates band potentials also enable carriers to drive direct reduction of carbon dioxide to the carbon dioxide radical ($CO_2^{\cdot -}$) or oxidation of undissociated water molecules to form H^+ (Figure 8.4). These reactions are outside the band edges of titanium dioxide. Photochemical reduction of carbon dioxide over SLN powder may, therefore, follow a different reaction pathway to reactions over TiO_2 powder. The reaction pathway over SLN powder may favour the formation of formic acid and formaldehyde whereas reactions over TiO_2 powder may favour formation of other products to explain the greater yield or products over SLN powder. Alternatively the reaction pathway over SLN powder may proceed at a greater rate than the reaction pathway over TiO_2 powder.

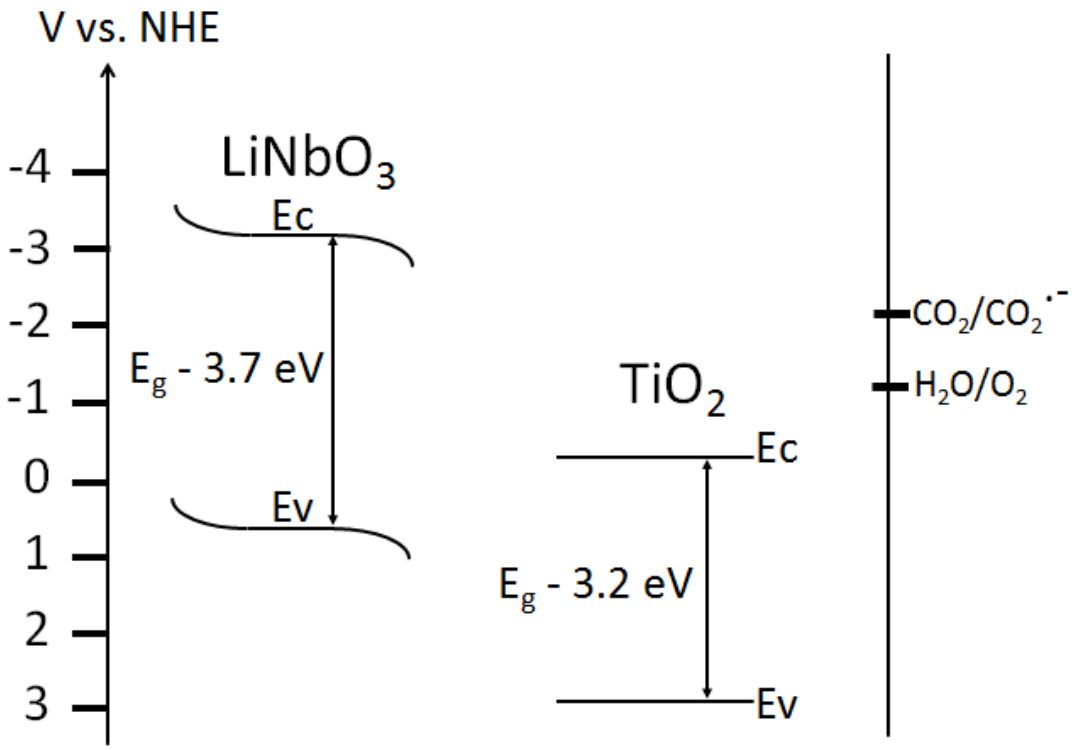

Figure 8.4 The potentials of the reduction of carbon dioxide ($CO_2/CO_2^{\cdot-}$) and oxidation of water in relation to the band potentials of titanium dioxide and lithium niobate

8.4 Summary

SLN powder was investigated as a photocatalyst for driving photochemical reduction of carbon dioxide to hydrocarbon products using solid-liquid phase or solid-gas phase conditions. The rate of formation of formic acid and formaldehyde over SLN powder was greater using solid-gas phase conditions than using solid-liquid phase conditions. This was attributed to a higher concentration of gas being loaded in the reaction vessel than was dissolved in aqueous solutions. It was also shown that under solid-gas phase conditions SLN powder formed formic acid and formaldehyde at a faster rate than over titanium dioxide powder. Two possible causes may be that the surface charge of SLN powder affects the mode of adsorption of carbon dioxide molecules compared to at the surface of non-polar titanium dioxide powder to alter the rate of carrier transfer. The band edges of SLN powder also may allow

photochemical reduction reactions to take place via a different reaction pathway to over titanium dioxide powder.

9 Conclusions and future work

9.1 Conclusions

The aim of this thesis was, through investigation of barium titanate and lithium niobate particulates, to contribute to the understanding of ferroelectric material's photocatalytic properties and to demonstrate their potential application in photocatalytic reactions in which semiconductors are traditionally used. It was hypothesised that the polarisation of ferroelectric powder may increase photocatalytic activity by reducing the rate of carrier recombination. It was also postulated that the surface charge may influence the location and quantity of reactants adsorbed in the double layer.

The first objective was to investigate the effect of the ferroelectric surface charge upon the structure of the double layer by monitoring change in concentration of ionic dye molecules in aqueous solution after powders of barium titanate or lithium niobate were added. Adsorption studies of ionic dye molecules showed the amount of dye adsorbed by LN, SLN, MgLN, FeLN or BT powders did not correspond to their surface charges. This suggested that other properties such as the isoelectric point, surface area or composition were more significant in determining the structure of the double layer formed with an aqueous dye solution. Comparison of dye adsorption by BT and titanium dioxide powders showed BT powder adsorbed more rhodamine b ions per unit surface area than non-polar titanium dioxide powder. This could be explained by the electrostatic interactions between the surface charge of BT powder and the dye ions increasing adsorption in the double layer.

It was also shown that the retention of rhodamine b ions by powders of BT or LN decreased after silver particles were photochemically deposited at the powders surface. As silver particles were formed at positive domains the decrease in dye retention can be attributed to the negatively charged silver deposits externally screening the positive surface potential. This reduced adsorption of chlorine ions from solution in the inner Helmholtz layer and, as a result, fewer solvated rhodamine b ions were adsorbed in the outer Helmholtz

layer. Formation of excited carriers under super band gap illumination drove photocatalytic reactions but also caused carriers to accumulate in the space charge region at the interface, internally screening the surface charge. This caused dye ions that were adsorbed to externally screen the surface charge to be desorbed from the double layer. This was shown when a suspension of LN powder in rhodamine b solution was illuminated with super band gap light. The concentration of dye in solution increased above the starting value showing the rate of desorption exceeded the rate of photocatalytic reactions in this case. It was also observed that when suspensions of SLN, MgLN or FeLN powders were illuminated with super band gap light the rate of decolourisation reactions initially increased with time. This was explained by desorption occurring at the same time as photocatalytic reactions until desorption/adsorption of dye in the double layer reached a new equilibrium. The desorption of dye suggested that the surface charge had increased adsorption of dye ions at the surface but that under high intensity super band gap illumination internal screening of the surface charge significantly reduces electrostatic interactions between the surface and adsorbates.

The second objective was to study the properties of lithium niobate and barium titanate as photocatalysts for degradation of dye pollutants under UV illumination. Powders of BT, LN, SLN, MgLN or FeLN were shown to decolourise solutions of acid black 1 or rhodamine b under super band gap illumination. The rate of decolourisation of dye solutions over the ferroelectric powders was found not to correspond with the powders' polarisation. This suggested that the rate of photocatalytic reactions was determined to a greater extent by the materials other properties e.g. the band gap, band edge positions and surface area. SLN powder was found to drive decolourisation reactions at a greater rate than LN powder. This may be a result of the SLN powder having a smaller size, larger surface area and probably a different isoelectric point to LN powder. These differences would affect the number of active surface sites and the amount of dye adsorbed at the powders surface to alter the rate of carrier transfer to drive reactions. The rate of decolourisation of acid black 1 or rhodamine b solutions were shown to be different over BT powder. This is

consistent with work from the literature showing dyes to be decolourised at different rates over semiconductor materials. This is explained by the different zeta potentials affecting the quantities of dye adsorbed in the double layer and the different quantity of dye adsorbed impacting the rate of decolourisation reactions. In the case of reactions over ferroelectric materials reduction and oxidation processes are also spatially distinct with reduction taking place at positive domains and oxidation at C- domains. This means that dyes adsorbed at different domains of BT powder may also undergo either an oxidation or a reduction led pathway which would explain the difference in reaction rate. However, over SLN, LN or MgLN powder the rate of decolourisation of rhodamine b or acid black 1 solution were found to be similar. In the literature the location of photochemical reactions at the surface of periodically poled lithium niobate has been shown to be affected by the intensity of super band gap light. At high intensity the location of reactions reflects the internal electric field which causes carriers to accumulate at domain boundaries. A possible explanation for the similar rate of reactions over LN or SLN powder was that the UV lamp produced a sufficiently high intensity of super band gap light to cause reactions to occur near domain boundaries. This would mean that dyes adsorbed at C+ or C- domains could react with species formed by photogenerated carriers at a similar rate, reducing the effect of the dyes different zeta potentials upon the rate of reactions. It was found that compared to SLN powder, doped FeLN or MgLN powder drove reactions at different rates. This was attributed to the majority carrier type, holes in the case of p-type MgLN powder and electrons in the case of n-type FeLN powder. This altered the reactive species formed by excited carriers, the superoxide anion radical in the case of FeLN powder or the hydroxyl radical in the case of MgLN powder. The rate of formation of the superoxide anion radical may be slower than the rate at which the hydroxyl radical is formed as oxygen is adsorbed in low concentration in aqueous solution whereas water molecules are abundant. The superoxide anion radical and hydroxyl radical also have different oxidation potentials and so may decolourise dye molecules via different pathways. Compared to SLN powder the rate of reactions was greater over MgLN powder and lower over

FeLN powder. This showed reactions over lithium niobate powders may be oxidation led.

The third objective was to investigate changes in the photocatalytic properties of lithium niobate and barium titanate powders for driving dye degradation reactions after photochemical deposition of silver nanoparticles at the surface. Silver nanoparticles were photochemically deposited at the surface of BT or LN powders causing the rate of dye decolourisation reactions to increase under UV or simulated solar illumination compared to the raw powders. This was attributed to the metal particles forming a Schottky barrier at C+ domains, trapping electrons to reduce the rate of carrier recombination. The activity of the silver modified powders was greater under simulated solar illumination than UV illumination. This was explained by the solar simulator emitting photons of visible spectrum light able to excite a LSPR in the silver nanoparticles. This probably enhanced the rate of carrier excitation in the powders and the rate of carrier trapping by the metal particles. Silver modified BT showed a greater increase in reaction rates than silver modified LN powder. This may be a result of difference in loading of silver particles which has been shown to be linked to reaction rate in the literature. Another possibility is that silver deposition occurred at domain boundaries of LN powder as deposition was carried out under high intensity of super band gap light. This may have caused silver deposits to grow at the boundary to cause bridging between C+ and C- domains. This would allow carrier recombination to occur and decrease the systems photocatalytic activity. Silver modified BT powder appears to show a greater increase in reaction rate compared to BT powder than literature values for the increase in reaction rates over titanium dioxide powder after silver deposition. A possible explanation for this may be that the accumulation region by internal depolarisation fields at the C+ domains of BT powder increased the rate at which silver deposits trapped carriers compared to at the surface of non-polar titanium dioxide powders.

The fourth objective was to study the solid-liquid phase and solid-gas phase photochemical reduction of carbon dioxide to form hydrocarbon products over

lithium niobate powder. In experiments it was demonstrated SLN powder drove reduction of carbon dioxide to form formic acid or formaldehyde under solid-gas phase conditions but not using solid-liquid phase conditions. This was attributed to carbon dioxide concentration in aqueous solution being rate limiting whereas solid-gas phase reactions allowed a higher concentration of carbon dioxide gas to be used by venting the vessel with gas. The rate of formation of formic acid and formaldehyde was also found to be greater over SLN powder than over TiO_2 powder. This can be attributed to the band edges of LN allowing reactions to occur via a different pathway to over TiO_2 powder. The surface charge of SLN powder may have also affected the mode of adsorption of carbon dioxide molecules to increase bending of the molecule. This could have caused delocalisation of electron density in the carbon dioxide molecules and affect the rate of carrier transfer from SLN powder to drive reactions.

In conclusion, the surface charge of ferroelectric powders was shown to affect the quantity of dye reactants that were adsorbed. However, as the surface charge of the powders appeared to be significantly internally screened under super band gap illumination this property probably has limited influence upon ferroelectric materials photocatalytic activity unless the photocatalyst is illuminated with low intensity super band gap light. Comparison of barium titanate and lithium niobate powders' photocatalytic activity for driving decolourisation of dyes showed no correlation between the magnitude of the polarisation and the rate of reactions. This suggested the materials other properties e.g. band edge positions and surface area, were more significant in determining photocatalytic activity than spatial separation of reactions and/or decreased carrier recombination as a result of the ferroelectric polarisation. However, investigation of barium titanate and lithium niobate powders properties has highlighted their possible applications for use in place of traditional semiconductor materials for driving photocatalytic reactions. The low structural selectivity of dye decolourisation reactions over lithium niobate powders as a result of reactions taking place at domain boundaries may have application in industrial processes. Industrial dye waste typically contains different types of pollutants. The suitability of semiconductor systems as

photocatalysts for remediation of industrial waste is limited as the structural selectivity of reactions means that different dye pollutants are degraded at different rates. Photocatalytic reactions over lithium niobate may offer a solution by enabling a range of dyes or other types of pollutants to be degraded at similar rates. Silver nanoparticle deposition increased both the photocatalytic activity and visible light sensitivity of barium titanate powder meaning that this system may have suitable properties for real world applications. This also demonstrated that barium titanate and, potentially, other ferroelectric materials modified with silver nanoparticles are a new class of photocatalyst for remediation of dye waste or other reactions. It was also shown the SLN powder drove solid-gas phase reduction of carbon dioxide at a faster rate than reactions over TiO_2 powder. This was explained by the band edges of lithium niobate possibly allowing reactions to follow a different pathway and lithium niobates surface charge having affected the adsorption mode of carbon dioxide to alter the rate of carrier transfer. Lithium niobate may, therefore, be a possible alternative to commonly used semiconductor photocatalysts, such as titanium dioxide, for generation of fuel stock under solid-gas phase conditions.

9.2 Future work

The work undertaken has highlighted several areas that would benefit from further research. These include:

- Investigation of different ferroelectric powders. Powder of barium titanate, lithium niobate and magnesium or iron doped lithium niobate were shown to drive photocatalytic reactions. Different ferroelectric materials, powders with different particle size and powders with different dopants and different quantities of dopant could be investigated to determine the effects upon activity for driving dye decolourisation reactions.
- Optimisation of decolourisation reactions. Investigating the effect of varying the super band gap light intensity, the concentration of dye in solutions, the temperature of experimental conditions, the pH of the dye solution and the loading of powder would allow the optimal conditions for

decolourisation reactions using different ferroelectric powders to be determined and the most significant factors affecting photocatalytic efficiency.

- Structural selectivity of reactions over lithium niobate. The structural selectivity of dye decolourisation reactions of acid black 1 or rhodamine b were shown to be low over lithium niobate powders. Using different dye solutions or reactants it could be investigated if it is generally true that decolourisation reactions over lithium niobate show low structural selectivity. It was proposed that the high intensity of super band gap light caused reactions to occur near domain boundaries resulting in low structural selectivity. Comparing dye decolourisation reactions under high and low intensities of super band gap light could be used to investigate if reactions taking place near domain the boundary has an impact upon the structural selectivity of reactions over lithium niobate.
- Effect of silver deposition on reaction rates. The rate of decolourisation reactions over barium titanate or lithium niobate powder increased after photochemical deposition of silver particles at positive domains. By preparing silver modified powders using different length of deposition the loading of silver can be altered. EDX was unable to detect the loading of silver at the surface of BT or LN powder, other techniques such as XPS may allow the loadings to be determined. The photocatalytic activities of the powders could be compared to determine the optimal loading of silver deposits for driving photocatalytic reactions. It was also proposed that the high intensity of super band gap light used in photochemical deposition of silver may have caused particles to form preferentially near domain boundaries of LN powder. This could have resulted in bridging across C+ and C- domains to allow carrier recombination. Preparing silver modified LN powders using a low intensity of light may allow deposits to be formed across positive domains which may increase the photocatalytic activity of the powder.
- The polarisations effect upon photocatalytic activity. A barium titanate thin film sample could also be used to decolourise dye solutions under

super band gap illumination when polarised to have a C+, C- or poly domain structure. This would more clearly show the effect of the polarisation on reaction rate. Decolourisation reactions could also be carried out using a barium titanate powder with a Curie point close to that of room temperature. Using an isotherm, reactions could be carried out at temperatures above or below the Curie point of the powder. This would show the photocatalytic activity of the powder in the paraelectric and ferroelectric phase.

- Study of the effect of the surface charge upon dye adsorption using a barium titanate thin film sample. The sample could be polarised to have a + domain, C- domain or poly domain structure. Adsorption studies of different ionic dyes in aqueous solution could be carried out under all three conditions using the same sample. In between experiments the film could be cleaned and illuminated with UV light to remove any adsorbed dye molecules. This would show more clearly the effect of the surface charge upon adsorption of dye ions and the structure of the double layer at ferroelectric surfaces.
- Photochemical reduction of carbon dioxide. By producing an experimental setup to allow samples to be collected from solid-gas phase reactions during illumination, reactions over lithium niobate powder or barium titanate powders can be investigated in more detail. In situ gas sampling could be used to determine the rate of formation of products. Samples could be analysed for a range of hydrocarbon products or the change in the concentration of carbon dioxide could be used to determine the total reaction rate over the powders. Powders of barium titanate and lithium niobate modified by silver deposition could also be tested to determine the effect silver loading has upon solid-gas phase reactions of carbon dioxide over these systems.

The proposed further studies of solid-gas phase reactions of carbon dioxide over ferroelectric materials would require development of a new experimental setup as described. The other experiments proposed above could be performed using the experimental setups used to collect the data in this thesis. These

studies were not carried out in this work due restraints on the time available to perform experimental work or, in the case of investigations using thin film or single crystal samples due to these experiments being outside the scope of this thesis which aimed to specifically study the properties of ferroelectric powders.

REFERENCES

1. Mills, A. and Le Hunte, S. (1997), "An overview of semiconductor photocatalysis", *Journal of Photochemistry and Photobiology A: Chemistry,* vol. 108, no. 1, pp. 1-35.

2. Fujishima, A. and Honda, K. (1972), "Electrochemical photolysis of water at a semiconductor electrode", *Nature,* vol. 238, no. 5358, pp. 37-38.

3. Nishimura, A., Komatsu, N., Mitsui, G., Hirota, M. and Hu, E. (2009), "CO2 reforming into fuel using TiO2 photocatalyst and gas separation membrane", *Catalysis Today,* vol. 148, no. 3-4, pp. 341-349.

4. Ni, M., Leung, M. K. H., Leung, D. Y. C. and Sumathy, K. (2007), "A review and recent developments in photocatalytic water-splitting using TiO2 for hydrogen production", *Renewable and Sustainable Energy Reviews,* vol. 11, no. 3, pp. 401-425.

5. Dey, G. R. and Pushpa, K. K. (2006), "Methane generated during photocatalytic redox reaction of alcohols on TiO2 suspension in aqueous solutions", *Research on Chemical Intermediates,* vol. 32, no. 8, pp. 725-736.

6. Kočí, K., Obalová, L. and Lacný, Z. (2008), "Photocatalytic reduction of CO2 over TiO2 based catalysts", *Chemical Papers,* vol. 62, no. 6, pp. 1-9.

7. Wu, C., Zhou, Y. and Zou, Z. (2011), "Research progress in photocatalytic conversion of CO2 to hydrocarbons", *Cuihua Xuebao/Chinese Journal of Catalysis,* vol. 32, no. 10, pp. 1565-1572.

8. Konstantinou, I. K. and Albanis, T. A. (2004), "TiO2-assisted photocatalytic degradation of azo dyes in aqueous solution: Kinetic and mechanistic investigations: A review", *Appl. Catal. B. Environ,* vol. 49, no. 1, pp. 1-14.

9. Hashimoto, K., Irie, H. and Fujishima, A. (2005), "TiO2 photocatalysis: A historical overview and future prospects", *Japanese Journal of Applied Physics, Part 1: Regular Papers and Short Notes and Review Papers,* vol. 44, no. 12, pp. 8269-8285.

10. Vinu, R. and Madras, G. (2010), "Environmental remediation by photocatalysis", *Journal of the Indian Institute of Science,* vol. 90, no. 2, pp. 189-230.

11. Bhatkhande, D. S., Pangarkar, V. G. and Beenackers, A. A. C. M. (2002), "Photocatalytic degradation for environmental applications - A review", *Journal of Chemical Technology and Biotechnology,* vol. 77, no. 1, pp. 102-116.

12. Hoffmann, M. R., Martin, S. T., Choi, W. and Bahnemann, D. W. (1995), "Environmental applications of semiconductor photocatalysis", *Chemical reviews,* vol. 95, no. 1, pp. 69-96.

13. Linsebigler, A. L., Lu, G. and Yates Jr., J. T. (1995), "Photocatalysis on TiO2 surfaces: Principles, mechanisms, and selected results", *Chemical reviews,* vol. 95, no. 3, pp. 735-758.

14. Valasek, J. (1920), *Physics review,* vol. 15, pp. 537-538.

15. Dawber, M., Rabe, K. M. and Scott, J. F. (2005), "Physics of thin-film ferroelectric oxides", *Reviews of Modern Physics,* vol. 77, no. 4, pp. 1083-1130.

16. Polla, D. L. and Francis, L. F. (1996), "Ferroelectric thin films in microelectromechanical systems applications", *MRS Bulletin,* vol. 21, no. 7, pp. 59-65.

17. Scott, J. F. (2000), *Ferroelectric memories,* Springer, New York.

18. Dunn, S., Sharp, S. and Burgess, S. (2009), "The photochemical growth of silver nanoparticles on semiconductor surfaces - Initial nucleation stage", *Nanotechnology,* vol. 20, no. 11.

19. Sun, Y., Eller, B. S. and Nemanich, R. J. (2011), "Photo-induced Ag deposition on periodically poled lithium niobate: Concentration and intensity dependence", *Journal of Applied Physics,* vol. 110, no. 8.

20. Qin, M., Yao, K. and Liang, Y. C. (2009), "Photovoltaic mechanisms in ferroelectric thin films with the effects of the electrodes and interfaces", *Applied Physics Letters,* vol. 95, no. 2.

21. Giocondi, J. L. and Rohrer, G. S. (2001), "Spatial separation of photochemical oxidation and reduction reactions on the surface of ferroelectric BaTiO3", *Journal of Physical Chemistry B,* vol. 105, no. 35, pp. 8275-8277.

22. Giocondi, J. L. and Rohrer, G. S. (2001), "Spatially selective photochemical reduction of silver on the surface of ferroelectric barium titanate", *Chem. Mater.,* vol. 13, no. 2, pp. 241-242.

23. Garra, J., Vohs, J. M. and Bonnell, D. A. (2009), "The effect of ferroelectric polarization on the interaction of water and methanol with the surface of LiNbO3(0 0 0 1)", *Surface Science,* vol. 603, no. 8, pp. 1106-1114.

24. Zhang, Z., Sharma, P., Borca, C. N., Dowben, P. A. and Gruverman, A. (2010), "Polarization-specific adsorption of organic molecules on ferroelectric LiNbO3 surfaces", *Applied Physics Letters,* vol. 97, no. 24.

25. Lines, M. E. A. M. G. (1977), *Principles and Applications of Ferroelectrics and Related Materials,* Oxford: Clarendon Press.

26. Bozorth, R. M. (1993), *Ferromagnetism ,* Wiley-IEEE Press.

27. Tiwari, D. and Dunn, S. (2009), "Photochemistry on a polarisable semi-conductor: What do we understand today?", *Journal of Materials Science,* vol. 44, no. 19, pp. 5063-5079.

28. Huber, J. E., Fleck, N. A., Landis, C. M. and McMeeking, R. M. (1999), "Constitutive model for ferroelectric polycrystals", *Journal of the Mechanics and Physics of Solids,* vol. 47, no. 8, pp. 1663-1697.

29. Dennis, M. D. and Bradt, R. C. (1974), "Thickness of 90° ferroelectric domain walls in (Ba,Pb)TiO3 single crystals", *Journal of Applied Physics,* vol. 45, no. 5, pp. 1931-1933.

30. Foeth, M., Stadelmann, P. and Buffat, P. -. (1999), "Quantitative determination of the thickness of ferroelectric domain walls using weak beam transmission electron microscopy", *Ultramicroscopy,* vol. 75, no. 4, pp. 203-213.

31. Damjanovic, D. (1998), "Ferroelectric, dielectric and piezoelectric properties of ferroelectric thin films and ceramics", *Reports on Progress in Physics,* vol. 61, no. 11, pp. 1267-1324.

32. Glinchuk, M. D., Zaulychny, B. Y. and Stephanovich, V. A. (2005), "Depolarization field and properties of thin ferroelectric films with inclusion of the electrode effect", *Physics of the Solid State,* vol. 47, no. 7, pp. 1331-1339.

33. Eng, L. M. (1999), "Nanoscale domain engineering and characterization of ferroelectric domains", *Nanotechnology,* vol. 10, no. 4, pp. 405-411.

34. Fridkin, V. M. (1980), *Ferroelectric semiconductors,* Consultants Bureau.

35. Fatuzzo, E. and Merz, W. J. (1967), *Ferroelectricity,* Wiley, New York.

36. Tilley, D. R. and Žekš, B. (1984), "Landau theory of phase transitions in thick films", *Solid State Communications,* vol. 49, no. 8, pp. 823-828.

37. Wang, Y. G., Zhong, W. L. and Zhang, P. L. (1994), "Size effects on the Curie temperature of ferroelectric particles", *Solid State Communications,* vol. 92, no. 6, pp. 519-523.

38. Szwarcman, D., Vestler, D. and Markovich, G. (2011), "The size-dependent ferroelectric phase transition in BaTiO3 nanocrystals probed by surface plasmons", *ACS Nano,* vol. 5, no. 1, pp. 507-515.

39. Du, Y. L., Zhang, M. S., Chen, Q., Yuan, Z. R., Yin, Z. and Zhang, Q. A. (2002), "Size effect and evidence of a size-driven phase transition in Bi4Ti3O12 nanocrystals", *Solid State Communications,* vol. 124, no. 3, pp. 113-118.

40. Shih, W. Y., Shih, W. -. and Aksay, I. A. (1994), "Size dependence of the ferroelectric transition of small BaTiO3 particles: Effect of depolarization", *Physical Review B,* vol. 50, no. 21, pp. 15575-15585.

41. Zhong, W. L. (1998), "Particulate ferroelectrics: Finite size effects", *Journal of the Korean Physical Society,* vol. 32, no. SUPPL. 1, pp. S265-S269.

42. Wang, Y. G., Zhong, W. L. and Zhang, P. L. (1994), "Size driven phase transition in ferroelectric particles", *Solid State Communications,* vol. 90, no. 5, pp. 329-332.

43. Asiaie, R., Zhu, W., Akbar, S. A. and Dutta, P. K. (1996), "Characterization of submicron particles of tetragonal BaTiO3", *Chemistry of Materials,* vol. 8, no. 1, pp. 226-234.

44. Hsiang, H. -. and Yen, F. -. (1996), "Effect of crystallite size on the ferroelectric domain growth of ultrafine BaTiO3 powders", *Journal of the American Ceramic Society,* vol. 79, no. 4, pp. 1053-1060.

45. Frey, M. H. and Payne, D. A. (1996), "Grain-size effect on structure and phase transformations for barium titanate", *Physical Review B - Condensed Matter and Materials Physics,* vol. 54, no. 5, pp. 3158-3168.

46. Landis, C. M. and Mcmeeking, R. M. (2000), "Phenomenological constitutive law for ferroelastic switching and a resulting asymptotic crack tip solution", *Journal of Intelligent Material Systems and Structures,* vol. 10, no. 2, pp. 155-163.

47. Hwang, S. C., Lynch, C. S. and McMeeking, R. M. (1995), "Ferroelectric/ferroelastic interactions and a polarization switching model", *Acta Metallurgica Et Materialia,* vol. 43, no. 5, pp. 2073-2084.

48. Jaffe, B., Cook, W. R. and Jaffe, H. (1971), *Piezoelectric ceramics,* Academic press, London.

49. Hvizdoš, P., Reece, M. J., Bushby, A. J., Whatmore, R. W., Zhang, Q. and Algueró, M. (2002), "Depolarisation of PZT thin films by nanoindentation", *Integrated Ferroelectrics,* vol. 50, pp. 199-207.

50. Franke, K., Huelz, H. and Weihnacht, M. (1998), "Stress-induced depolarization in PZT thin films, measured by means of electric force microscopy", *Surface Science,* vol. 416, no. 1-2, pp. 59-67.

51. Algueró, M., Bushby, A. J., Reece, M. J., Poyato, R., Ricote, J., Calzada, M. L. and Pardo, L. (2001), "Stress-induced depolarization of (Pb, La)TiO3 ferroelectric thin films by nanoindentation", *Applied Physics Letters,* vol. 79, no. 23, pp. 3830-3832.

52. Fische, E. T. (2008), *Materials science for engineering students ,* 1st ed, Academic Press.

53. Ibach, H. (2003), *Solid-State Physics: An Introduction to Principles of Materials Science,* 3rd ed, Springer.

54. Dunlap, W. C. (1957), *An introduction to semiconductors,* 1st ed, Wiley, New York.

55. Balkanski, M. and Wallis, F. R. (2000), *Semiconductor physics and applications,* Oxford university press.

56. Shockley, W. (1939), *Physics review,* vol. 56, pp. 317.

57. Van de Krol, R. and Gratzel, M. (2011), *Photoelectrochemical Hydrogen Production,* Springer.

58. Robertson, J. and Chen, C. W. (1999), "Schottky barrier heights of tantalum oxide, barium strontium titanate, lead titanate, and strontium bismuth tantalate", *Applied Physics Letters,* vol. 74, no. 8, pp. 1168-1170.

59. Sadashivan, S., Aggarwal, S., Song, T. K., Ramesh, R., Evans Jr., J. T., Tuttle, B. A., Warren, W. L. and Dimos, D. (1998), "Evaluation of imprint in fully integrated (La,Sr)CoO3/Pb(Nb,Zr,Ti)O3/(La,Sr)CoO3 ferroelectric capacitors", *Journal of Applied Physics,* vol. 83, no. 4, pp. 2165-2171.

60. Park, B. H., Hyun, S. J., Moon, C. R., Choe, B. -., Lee, J., Kim, C. Y., Jo, W. and Noh, T. W. (1998), "Imprint failures and asymmetric electrical properties induced by thermal processes in epitaxial Bi 4Ti 3O 12 thin films", *Journal of Applied Physics,* vol. 84, no. 8, pp. 4428-4435.

61. Pintilie, L., Lisca, M. and Alexe, M. (2005), "Lead-based ferroelectric compounds: Insulators or semiconductors?", *Integrated Ferroelectrics,* Vol. 73, pp. 37.

62. Boerasu, I., Vasilevskiy, M. I., Pereira, M., Costa, M. F. and Gomes, M. J. M. (2002), "Optical properties of PZT 65/35 thin films deposited by sol-gel", *Ferroelectrics,* Vol. 268, pp. 187.

63. Boerasu, I., Pintilie, L., Pereira, M., Vasilevskiy, M. I. and Gomes, M. J. M. (2003), "Competition between ferroelectric and semiconductor properties in Pb(Zr0.65Ti0.35)O3 thin films deposited by sol-gel", *Journal of Applied Physics,* vol. 93, no. 8, pp. 4776-4783.

64. Pintilie, L. and Pintilie, I. (2001), "Ferroelectrics: New wide-gap materials for UV detection", *Materials Science and Engineering B: Solid-State Materials for Advanced Technology,* vol. 80, no. 1-3, pp. 388-391.

65. Pintilie, L., Lisca, M. and Alexe, M. (2006), "Epitaxial-quality PZT: Insulator or semiconductor?", *Journal of Optoelectronics and Advanced Materials,* vol. 8, no. 1, pp. 7-12.

66. Naik, R. (2000), *Phys. Rev. B,* vol. 61, no. 17, pp. 11367-11372.

67. Hanson, J. N., Rodriguez, B. J., Nemanich, R. J. and Gruverman, A. (2006), "Fabrication of metallic nanowires on a ferroelectric template via photochemical reaction", *Nanotechnology,* vol. 17, no. 19, pp. 4946-4949.

68. Gruverman, A. (2004), *Nanoscale Characterisation of Ferroelectric Materials: Scanning Probe Microscopy Approach ,* 1st ed, Springer.

69. Butt, H. J., Graf, K. and Kappl, M. (2006), *Physics and chemistry of interfaces,* .

70. Bouzigues, C. I., Tabeling, P. and Bocquet, L. (2008), "Nanofluidics in the debye layer at hydrophilic and hydrophobic surfaces", *Physical Review Letters,* vol. 101, no. 11.

71. Stern, O. (1924), *Zeitschrift fur Elecktrochemie,* , no. 30, pp. 508.

72. Parfitt, G. D. (1976), "SURFACE CHEMISTRY OF OXIDES", *Pure and applied chemistry,* vol. 48, pp. 415-416, 417, 418.

73. Yun, Y., Kampschulte, L., Li, M., Liao, D. and Altman, E. I. (2007), "Effect of ferroelectric poling on the adsorption of 2-propanol on LiNbO3(0001)", *Journal of Physical Chemistry C,* vol. 111, no. 37, pp. 13951-13956.

74. Li, D., Zhao, M. H., Garra, J., Kolpak, A. M., Rappe, A. M., Bonnell, D. A. and Vohs, J. M. (2008), "Direct in situ determination of the polarization dependence of physisorption on ferroelectric surfaces", *Nat. Mater.,* vol. 7, no. 6, pp. 473-477.

75. Zhao, M. H., Bonnell, D. A. and Vohs, J. M. (2008), "Effect of ferroelectric polarization on the adsorption and reaction of ethanol on BaTiO3", *Surface Science,* vol. 602, no. 17, pp. 2849-2855.

76. Ramos-Moore, E., Lederman, D. and Cabrera, A. L. (2011), "Modification of ferroelectric hysteresis in Pb(Nb,Zr,Ti)O3 thin films induced by CO2 adsorption", *Applied Surface Science,* vol. 258, no. 3, pp. 1181-1183.

77. Pacchioni, G. (1993), "Physisorbed and chemisorbed CO2 at surface and step sites of the MgO(100) surface", *Surface Science,* vol. 281, no. 1-2, pp. 207-219.

78. Pacchioni, G., Ricart, J. M. and Illas, F. (1994), "Ab initio cluster model calculations on the chemisorption of CO2 and SO2 probe molecules on MgO and CaO (100) surfaces. A theoretical measure of oxide basicity", *Journal of the American Chemical Society,* vol. 116, no. 22, pp. 10152-10158.

79. Habicht, S., Nemanich, R. J. and Gruverman, A. (2008), "Physical adsorption on ferroelectric surfaces: photoinduced and thermal effects", *Nanotechnology,* vol. 19.

80. Zhang, Z., Sharma, P., Borca, C. N., Dowben, P. A. and Gruverman, A. (2010), "Polarization-specific adsorption of organic molecules on ferroelectric LiNbO3 surfaces", *Applied Physics Letters,* vol. 97, no. 24.

81. Dunn, S., Cullen, D., Abad-Garcia, E., Bertoni, C., Carter, R., Howorth, D. and Whatmore, R. W. (2004), "Using the surface spontaneous depolarization field of ferroelectrics to direct the assembly of virus particles", *Applied Physics Letters,* vol. 85, no. 16, pp. 3537-3539.

82. Outhwaite, C. W., Lamperski, S. and Bhuiyan, L. B. (2011), "Influence of electrode polarization on the capacitance of an electric double layer at and around zero surface charge", *Molecular Physics,* vol. 109, no. 1, pp. 21-26.

83. Lamperski, S. and Bhuiyan, L. B. (2003), "Counterion layering at high surface charge in an electric double layer. Effect of local concentration approximation", *Journal of Electroanalytical Chemistry,* vol. 540, pp. 79-87.

84. Lohmann, F. and Naturforsch, Z. (1967), "1967. 22A. ", , no. 22A.

85. Goodeve, C. F. and Kitchener, J. A. (1938), *Trans Farady Soc.,* , no. 34, pp. 902.

86. Kato, S. and Mashio, F. (1956), *Abtr. Book Annu. Meet. Chemical Society of Japan,* , pp. 223.

87. Fujishima, A., Zhang, X. and Tryk, D. A. (2008), "TiO2 photocatalysis and related surface phenomena", *Surface Science Reports,* vol. 63, no. 12, pp. 515-582.

88. Gaya, U. I. and Abdullah, A. H. (2008), "Heterogeneous photocatalytic degradation of organic contaminants over titanium dioxide: A review of fundamentals, progress and problems", *Journal of Photochemistry and Photobiology C: Photochemistry Reviews,* vol. 9, no. 1, pp. 1-12.

89. Sunada, K., Watanabe, T. and Hashimoto, K. (2003), "Studies on photokilling of bacteria on TiO2 thin film", *Journal of Photochemistry and Photobiology A: Chemistry,* vol. 156, no. 1-3, pp. 227-233.

90. Henglein, A. (1989), "Small-particle research: Physicochemical properties of extremely small colloidal metal and semiconductor particles", *Chemical reviews,* vol. 89, no. 8, pp. 1861-1873.

91. Ireland, J. C., Klostermann, P., Rice, E. W. and Clark, R. M. (1993), "Inactivation of Escherichia coli by titanium dioxide photocatalytic oxidation", *Applied and Environmental Microbiology,* vol. 59, no. 5, pp. 1668-1670.

92. Ollis, D. F. (2000), "Photocatalytic purification and remediation of contaminated air and water", *Comptes Rendus de l'Academie des Sciences - Series IIc: Chemistry,* vol. 3, no. 6, pp. 405-411.

93. Jackson, N. B., Wang, C. M., Luo, Z., Schwitzgebel, J., Ekerdt, J. G., Brock, J. R. and Heller, A. (1991), "Attachment of TiO2 powders to hollow glass microbeads. Activity of the TiO2-coated beads in the photoassisted oxidation of ethanol to acetaldehyde", *Journal of the Electrochemical Society,* vol. 138, no. 12, pp. 3660-3664.

94. Bard, A. J. and Fox, M. A. (1995), "Artificial Photosynthesis: Solar Splitting of Water to Hydrogen and Oxygen", *Accounts of Chemical Research,* vol. 28, no. 3, pp. 141-145.

95. Fujishima, A., Zhang, X. and Tryk, D. A. (2008), "TiO2 photocatalysis and related surface phenomena", *Surface Science Reports,* vol. 63, no. 12, pp. 515-582.

96. Khan, S. U. M., Al-Shahry, M. and Ingler Jr., W. B. (2002), "Efficient photochemical water splitting by a chemically modified n-TiO2", *Science,* vol. 297, no. 5590, pp. 2243-2245.

97. Dey, G. R., Belapurkar, A. D. and Kishore, K. (2004), "Photo-catalytic reduction of carbon dioxide to methane using TiO2 as suspension in water", *Journal of Photochemistry and Photobiology A: Chemistry,* vol. 163, no. 3, pp. 503-508.

98. Kaneco, S., Kurimoto, H., Shimizu, Y., Ohta, K. and Mizuno, T. (1999), "Photocatalytic reduction of CO2 using TiO2 powders in supercritical fluid CO2", *Energy,* vol. 24, no. 1, pp. 21-30.

99. Garrett, C. G. and Brattain, W. H. (1955), "Physical Theory of Semiconductor Surfaces", *Physical Review,* vol. 99, no. 2, pp. 376-387.

100. Li, F. B. and Li, X. Z. (2002), "The enhancement of photodegradation efficiency using Pt-TiO2 catalyst", *Chemosphere,* vol. 48, no. 10, pp. 1103-1111.

101. Sakthivel, S., Shankar, M. V., Palanichamy, M., Arabindoo, B., Bahnemann, D. W. and Murugesan, V. (2004), "Enhancement of photocatalytic activity by metal deposition: Characterisation and photonic efficiency of Pt, Au and Pd deposited on TiO 2 catalyst", *Water research,* vol. 38, no. 13, pp. 3001-3008.

102. Sobana, N., Muruganadham, M. and Swaminathan, M. (2006), "Nano-Ag particles doped TiO2 for efficient photodegradation of Direct azo dyes", *Journal of Molecular Catalysis A: Chemical,* vol. 258, no. 1-2, pp. 124-132.

103. Sung-Suh, H. M., Choi, J. R., Hah, H. J., Koo, S. M. and Bae, Y. C. (2004), "Comparison of Ag deposition effects on the photocatalytic activity of nanoparticulate TiO2 under visible and UV light irradiation", *Journal of Photochemistry and Photobiology A: Chemistry,* vol. 163, no. 1-2, pp. 37-44.

104. Rupa, A. V., Manikandan, D., Divakar, D. and Sivakumar, T. (2007), "Effect of deposition of Ag on TiO2 nanoparticles on the photodegradation of Reactive Yellow-17", *Journal of hazardous materials,* vol. 147, no. 3, pp. 906-913.

105. Sökmen, M., Allen, D. W., Akkaş, F., Kartal, N. and Acar, F. (2001), "Photo-degradation of some dyes using Ag-loaded titaniumdioxide", *Water, air, and soil pollution,* vol. 132, no. 1-2, pp. 153-163.

106. Meng, F., Lu, F., Sun, Z. and Lü, J. (2010), "A mechanism for enhanced photocatalytic activity of nano-size silver particle modified titanium dioxide thin films", *Science China Technological Sciences,* vol. 53, no. 11, pp. 3027-3032.

107. Willets, K.A. and Van Duyne, R.P., (2007), *Localized surface plasmon resonance spectroscopy and sensing*.

108. Zhao, G., Kozuka, H. and Yoko, T. (1996), "Sol-gel preparation and photoelectrochemical properties of TiO2 films containing Au and Ag metal particles", *Thin Solid Films,* vol. 277, no. 1-2, pp. 147-154.

109. Morrison, S. R. (1980), "Electochemistry at Semiconductor and Oxidized Metal Electrodes", .

110. Trasatti, S. (1974), "The concept of absolute electrode potential an attempt at a calculation", *Journal of Electroanalytical Chemistry,* vol. 52, no. 3, pp. 313-329.

111. Ryu, J. and Choi, W. (2008), "Substrate-specific photocatalytic activities of TiO2 and multiactivity test for water treatment application", *Environmental Science and Technology,* vol. 42, no. 1, pp. 294-300.

112. Kiriakidou, F., Kondarides, D. I. and Verykios, X. E. (1999), "The effect of operational parameters and TiO2-doping on the photocatalytic degradation of azo-dyes", *Catalysis Today,* vol. 54, no. 1, pp. 119-130.

113. Giocondi, J. L. and Rohrer, G. S. (2001), "Photochemical reduction and oxidation reactions on barium titanate surfaces", *Materials Research Society Symposium - Proceedings,* Vol. 654, pp. AA7.4.1.

114. Forsbergh Jr., P. W. (1949), "Domain structures and phase transitions in barium titanate", *Physical Review,* vol. 76, no. 8, pp. 1187-1201.

115. Hu, Y. H., Chan, H. M., Zhang, X. W. and Harmer, M. P. (1986), "SCANNING ELECTRON MICROSCOPY AND TRANSMISSION ELECTRON MICROSCOPY STUDY OF FERROELECTRIC DOMAINS IN DOPED BaTiO//3.", *Journal of the American Ceramic Society,* vol. 69, no. 8, pp. 594-602.

116. Giocondi, J. L. and Rohrer, G. S. (2008), "The influence of the dipolar field effect on the photochemical reactivity of Sr2Nb2O7 and BaTiO3 microcrystals", *Topics in Catalysis,* vol. 49, no. 1-2, pp. 18-23.

117. Jones, P. M. and Dunn, S. (2009), "Interaction of Stern layer and domain structure on photochemistry of lead-zirconate-titanate", *Journal of Physics D: Applied Physics,* vol. 42, no. 6.

118. Jones, P. M., Gallardo, D. E. and Dunn, S. (2008), "Photochemical investigation of a polarizable semiconductor, lead-zirconate-titanate", *Chemistry of Materials,* vol. 20, no. 18, pp. 5901-5906.

119. Jones, P. M. and Dunn, S. (2007), "Photo-reduction of silver salts on highly heterogeneous lead zirconate titanate", *Nanotechnology,* vol. 18, no. 18.

120. Dunn, S., Tiwari, D., Jones, P. M. and Gallardo, D. E. (2007), "Insights into the relationship between inherent materials properties of PZT and photochemistry for the development of nanostructured silver", *Journal of Materials Chemistry,* vol. 17, no. 42, pp. 4460-4463.

121. Kalinin, S. V., Bonnell, D. A., Alvarez, T., Lei, X., Hu, Z., Ferris, J. H., Zhang, Q. and Dunn, S. (2002), "Atomic Polarization and Local Reactivity

on Ferroelectric Surfaces: A New Route toward Complex Nanostructures", *Nano Lett.,* vol. 2, no. 6, pp. 589-593.

122. Kohno, M., Kaneko, T., Ogura, S., Sato, K. and Inoue, Y. (1998), "Dispersion of ruthenium oxide on barium titanates (Ba 6Ti 17O 40, Ba 4Ti 13O 30, BaTi 4O 9 and Ba 2Ti 9O 20) and photocatalytic activity for water decomposition", *Journal of the Chemical Society - Faraday Transactions,* vol. 94, no. 1, pp. 89-94.

123. Inoue, Y., Kubokawa, T. and Sato, K. (1991), "Photocatalytic activity of alkali-metal titanates combined with Ru in the decomposition of water", *Journal of Physical Chemistry,* vol. 95, no. 10, pp. 4059-4063.

124. Grey, I. E., Madsen, I. C., Watts, J. A., Bursill, L. A. and Kwiatkowska, J. (1985), "New cesium titanate layer structures", *Journal of Solid State Chemistry,* vol. 58, no. 3, pp. 350-356.

125. Ohara, K., Ohsawa, T., Koinuma, H. and Matsumoto, Y. (2006), "Photochemical approach to analysis of ferroelectric transition in Ba xSr1-xTiO3 epitaxial films", *Japanese Journal of Applied Physics, Part 2: Letters,* vol. 45, no. 8-11, pp. L339-L342.

126. Bhardwaj, A., Burbure, N. V. and Rohrer, G. S. (2010), "Enhanced photochemical reactivity at the ferroelectric phase transition in Ba1-xSrxTiO3", *Journal of the American Ceramic Society,* vol. 93, no. 12, pp. 4129-4134.

127. Merz, W. J. (1950), "The effect of hydrostatic pressure on the curie point of barium titanate single crystals", *Physical Review,* vol. 78, no. 1, pp. 52-54.

128. Suzuki, K. and Kijima, K. (2005), "Optical band gap of barium titanate nanoparticles prepared by RF-plasma chemical vapor deposition", *Japanese Journal of Applied Physics, Part 1: Regular Papers and Short Notes and Review Papers,* vol. 44, no. 4 A, pp. 2081-2082.

129. Burfoot, J. C. (1967), *Ferroelecrics: An Introduction to the Physical Properties. 1967, London: Company Ltd,* Van Nost. Reinhold.

130. Pepinsky, R., Okaya, Y. and Unterleitner, F. (1960), "X-ray studies of absolute configurations of ferroelectric crystals", *Acta. Cryst,* vol. 13, pp. 1071.

131. Nassau, K., Levinstein, H. J. and Loiacono, G. M. (1966), "Ferroelectric lithium niobate. 2. Preparation of single domain crystals", *Journal of Physics and Chemistry of Solids,* vol. 27, no. 6-7, pp. 989-996.

132. Ganesamoorthy, S., Nakamura, M., Takekawa, S., Kumaragurubaran, S., Terabe, K. and Kitamura, K. (2005), "A comparative study on the domain switching characteristics of near stoichiometric lithium niobate and lithium tantalate single crystals", *Materials Science and Engineering B: Solid-State Materials for Advanced Technology,* vol. 120, no. 1-3, pp. 125-129.

133. A, R. (1978), "Chemistry and physics of lithium niobate", *Current topics in materials science,* vol. 1, pp. 482-601.

134. Cross, L. E. (1993), *Ferroelectric Ceramics-Tutorial Reviews, Theory, Processing and Applications,* 1st ed, Birkhauser Verlag.

135. Kong, Y., Xu, J., Zhang, W. and Zhang, G. (2000), "The site occupation of protons in lithium niobate crystals", *Journal of Physics and Chemistry of Solids,* vol. 61, pp. 1331-1335.

136. Dhar, A. and Mansingh, A. (1990), "Optical properties of reduced lithium niobate single crystals", *Journal of Applied Physics,* vol. 68, no. 11, pp. 5804-5809.

137. Yang, W. -., Rodriguez, B. J., Gruverman, A. and Nemanich, R. J. (2004), "Polarization-dependent electron affinity of LiNbO3 surfaces", *Applied Physics Letters,* vol. 85, no. 12, pp. 2316-2318.

138. Wong, K. K. (2002), *Properties of Lithium Niobate,* 3rd ed, Institution of Engineering and Technology.

139. Orlowski, R. and Krätzig, E. (1978), "Holographic method for the determination of photo-induced electron and hole transport in electro-optic crystals", *Solid State Communications,* vol. 27, no. 12, pp. 1351-1354.

140. Feng, X. (1990), *Science in China, Series A,* vol. 33, no. 1, pp. 108-118.

141. Volk, T. and Wöhlecke, M. (2008), *Lithium Niobate: Defects, Photorefraction and Ferroelectric Switching,* Springer.

142. Xu, J., Zhang, G., Li, F., Zhang, X., Sun, Q., Liu, S., Song, F., Kong, Y., Chen, X., Qiao, H., Yao, J. and Lijuan, Z. (2000), "Enhancement of ultraviolet photorefraction in highly magnesium-doped lithium niobate crystals", *Optics Letters,* vol. 25, no. 2, pp. 129-131.

143. MTI Corporation *, 860 South 19th Street, Richmond, CA 94804, USA;* available at: www.mtixtl.com.

144. Photox Optical Systems88 Carsick Hill RoadSheffield S10 3LXUnited Kingdom.

145. UQG Ltd. The Norman Industrial Estate, 99 - 101 Cambridge Road, Milton, Cambridge, CB24 6AT, England , available at: http://www.uqgoptics.com.

146. del Barrio, M. -., Hu, J., Zhou, P. and Cauchon, N. (2006), "Simultaneous determination of formic acid and formaldehyde in pharmaceutical excipients using headspace GC/MS", *Journal of pharmaceutical and biomedical analysis,* vol. 41, no. 3, pp. 738-743.

147. Yao, S., Zheng, F., Liu, H., Wang, J., Zhang, H., Yan, T., Wu, J., Xia, Z. and Qin, X. (2009), "Synthesis of stoichiometric LiNbO3 nanopowder through a wet chemical method", *Crystal Research and Technology,* vol. 44, no. 11, pp. 1235-1240.

148. Konstantinou, I. K. and Albanis, T. A. (2003), "Photocatalytic transformation of pesticides in aqueous titanium dioxide suspensions using artificial and solar light: Intermediates and degradation pathways", *Applied Catalysis B: Environmental,* vol. 42, no. 4, pp. 319-335.

149. Xu, A., Chai, Y., Nohmi, T. and Hei, T. K. (2009), "Genotoxic responses to titanium dioxide nanoparticles and fullerene in gpt delta transgenic MEF cells", *Particle and Fibre Toxicology,* vol. 6, no. 3.

150. Velegraki, T., Kalogerakis, M., Charalabaki, M. and Poulious, I. (2005), "Semiconductor-assisted photocatalytic degradation of azo dye acid orange 7 in aqueous solution ", *Proceedings of the 9th international conference on environmental science and technology,* .

151. Herrmann, J. -. (2005), "Heterogeneous photocatalysis: State of the art and present applications", *Topics in Catalysis,* vol. 34, no. 1-4, pp. 49-65.

152. Sauer, T., Cesconeto Neto, G., José, H. J. and Moreira, R. F. P. M. (2002), "Kinetics of photocatalytic degradation of reactive dyes in a TiO2 slurry reactor", *Journal of Photochemistry and Photobiology A: Chemistry,* vol. 149, no. 1-3, pp. 147-154.

153. Tanaka, K., Padermpole, K. and Hisanaga, T. (2000), "Photocatalytic degradation of commercial azo dyes", *Water research,* vol. 34, no. 1, pp. 327-333.

154. Daneshvar, N., Salari, D. and Khataee, A. R. (2003), "Photocatalytic degradation of azo dye acid red 14 in water: Investigation of the effect of operational parameters", *Journal of Photochemistry and Photobiology A: Chemistry,* vol. 157, no. 1, pp. 111-116.

155. Huang, J. -., Huang, K. -., Liu, S. -., Wang, A. -. and Yan, C. (2008), "Adsorption of Rhodamine B and methyl orange on a hypercrosslinked

polymeric adsorbent in aqueous solution", *Colloids and Surfaces A: Physicochemical and Engineering Aspects,* vol. 330, no. 1, pp. 55-61.

156. Peter W. Atkins, Julio de Paula (2002), in Julio de Paula (ed.) 7th ed, Oxford University Press, , pp. 1000-1001.

157. Suttiponparnit, K., Jiang, J., Sahu, M., Suvachittanont, S., Charinpanitkul, T. and Biswas, P. (2011), "Role of Surface Area, Primary Particle Size, and Crystal Phase on Titanium Dioxide Nanoparticle Dispersion Properties", *Nanoscale Research Letters,* vol. 6, no. 1, pp. 1-8.

158. Paik, U. and Hackley, V. A. (2000), "Influence of solids concentration on the isoelectric point of aqueous barium titanate", *Journal of the American Ceramic Society,* vol. 83, no. 10, pp. 2381-2384.

159. Magdassi, S., Bassa, A., Vinetsky, Y. and Kamyshny, A. (2003), "Silver nanoparticles as pigments for water-based ink-jet inks", *Chemistry of Materials,* vol. 15, no. 11, pp. 2208-2217.

160. Römer, I., White, T. A., Baalousha, M., Chipman, K., Viant, M. R. and Lead, J. R. (2011), "Aggregation and dispersion of silver nanoparticles in exposure media for aquatic toxicity tests", *Journal of Chromatography A,* vol. 1218, no. 27, pp. 4226-4233.

161. Sadowski, Z. and Maliszewska, I. H. (2008), "Synthesis of silver nanoparticles using microorganisms", *Materials Science-Poland,* vol. 26, no. 2, pp. 419-424.

162. Hu, C., Tang, Y., Yu, J. C. and Wong, P. K. (2003), "Photocatalytic degradation of cationic blue X-GRL adsorbed on TiO2/SiO2 photocatalyst", *Applied Catalysis B: Environmental,* vol. 40, no. 2, pp. 131-140.

163. Gomes da Silva, C. and Faria, J. L. (2003), "Photochemical and photocatalytic degradation of an azo dye in aqueous solution by UV irradiation", *Journal of Photochemistry and Photobiology A: Chemistry,* vol. 155, no. 1-3, pp. 133-143.

164. Muruganandham, M. and Swaminathan, M. (2006), "Photocatalytic decolourisation and degradation of Reactive Orange 4 by TiO2-UV process", *Dyes and Pigments,* vol. 68, no. 2-3, pp. 133-142.

165. Houas, A., Lachheb, H., Ksibi, M., Elaloui, E., Guillard, C. and Herrmann, J. -. (2001), "Photocatalytic degradation pathway of methylene blue in water", *Appl. Catal. B. Environ,* vol. 31, no. 2, pp. 145-157.

166. Prevot, A. B., Baiocchi, C., Brussino, M. C., Pramauro, E., Savarino, P., Augugliaro, V., Marci, G. and Palmisano, L. (2001), "Photocatalytic degradation of Acid Blue 80 in aqueous solutions containing TiO2

suspensions", *Environmental Science and Technology,* vol. 35, no. 5, pp. 971-976.

167. Daneshvar, N., Salari, D. and Khataee, A. R. (2004), "Photocatalytic degradation of azo dye acid red 14 in water on ZnO as an alternative catalyst to TiO2", *Journal of Photochemistry and Photobiology A: Chemistry,* vol. 162, no. 2-3, pp. 317-322.

168. Xu, C., Cao, L., Su, G., Liu, W., Liu, H., Yu, Y. and Qu, X. (2010), "Preparation of ZnO/Cu2O compound photocatalyst and application in treating organic dyes", *Journal of hazardous materials,* vol. 176, no. 1-3, pp. 807-813.

169. Cheng, H. and Selloni, A. (2010), "Hydroxide ions at the water/anatase TiO2(101) interface: Structure and electronic states from first principles molecular dynamics", *Langmuir,* vol. 26, no. 13, pp. 11518-11525.

170. Cardona, M. (1965), *Physics review A,* vol. 140, pp. 651.

171. Heywangm, W. (1961), "Barium titanate as a PTC thermistor", *Solid-State Electronics,* .

172. Clark, M. G., Disalvo, F. J., Glass, A. M. and Peterson, G. E. (1973), "Electronic structure and optical index damage of iron-doped lithium niobate", *The Journal of chemical physics,* , pp. 6209-6219.

173. P, R., C, S., N, M., P, M. and S, C. (2008), "Photoelectrochemical Characteristic of ZnO Dye-sensitized Solar Cell with Platinum Nanoparticle as a Counterelectrode", *journal of natural science,* vol. 7, no. 1, pp. 177-178-183.

174. Vaithiyanathan, R. and Sivakumar, T. (2011), "Studies on photocatalytic activity of the synthesised TiO2 and Ag/TiO2 photocatalysts under UV and sunlight irradiations", *Water Science and Technology,* vol. 63, no. 3, pp. 377-384.

175. Shama, G. and Drott, D. W. (1997), "Photocatalytically induced dye decolourisation in an unsupported thin film reactor", *Chemical Engineering Communications,* vol. 158, pp. 107-122.

176. Kansal, S. K., Singh, M. and Sud, D. (2007), "Studies on photodegradation of two commercial dyes in aqueous phase using different photocatalysts", *Journal of hazardous materials,* vol. 141, no. 3, pp. 581-590.

177. Arslan, I. and Balcioglu, I. A. (1999), "Degradation of commercial reactive dyestuffs by heterogenous and homogenous advanced oxidation

processes: a comparative study", *Dyes and Pigments,* vol. 43, no. 2, pp. 95-108.

178. Tang, W. Z. and An, H. (1995), "UV/TiO2 photocatalytic oxidation of commercial dyes in aqueous solutions", *Chemosphere,* vol. 31, no. 9, pp. 4157-4170.

179. Lachheb, H., Puzenat, E., Houas, A., Ksibi, M., Elaloui, E., Guillard, C. and Herrmann, J. -. (2002), "Photocatalytic degradation of various types of dyes (Alizarin S, Crocein Orange G, Methyl Red, Congo Red, Methylene Blue) in water by UV-irradiated titania", *Applied Catalysis B: Environmental,* vol. 39, no. 1, pp. 75-90.

180. Oldenburg, S. (2011)*, Silver Nanoparticles: Properties and Applications*, available at: http://www.sigmaaldrich.com/materials-science/nanomaterials/silver-nanoparticles.html.

181. Hall, W. P., Ngatia, S. N. and Van Duyne, R. P. (2011), "LSPR biosensor signal enhancement using nanoparticle-antibody conjugates", *Journal of Physical Chemistry C,* vol. 115, no. 5, pp. 1410-1414.

182. Lundstrom, J. M., Rinehart, L. F., Pate, R. C., Smith, T. L., Krogh, M. L. and Huebner, W. (1999), "Measurement of the dielectric strength of titanium dioxide ceramics", *Digest of Technical Papers-IEEE International Pulsed Power Conference,* Vol. 2, pp. 1489.

183. Gorachand, G. (1952), "Handbook of Refractive Index and Dispersion of Water for Scientists and Engineers", .

184. Yang, W. -., Rodriguez, B. J., Gruverman, A. and Nemanich, R. J. (2004), "Polarization-dependent electron affinity of LiNbO3 surfaces", *Applied Physics Letters,* vol. 85, no. 12, pp. 2316-2318.

185. Milz, S., Rensberg, J., Ronning, C. and Wesch, W. (2011), "Correlation between damage evolution, cluster formation and optical propertiesof silver implanted lithium niobate", *Nuclear Instruments and Methods in Physics Research B,* .

186. Seery, M. K., George, R., Floris, P. and Pillai, S. C. (2007), "Silver doped titanium dioxide nanomaterials for enhanced visible light photocatalysis", *Journal of Photochemistry and Photobiology A: Chemistry,* vol. 189, no. 2-3, pp. 258-263.

187. Chan, G. H., Zhao, J., Hicks, E. M., Schatz, G. C. and Van Duyne, R. P. (2007), "Plasmonic properties of copper nanoparticles fabricated by nanosphere lithography", *Nano Letters,* vol. 7, no. 7, pp. 1947-1952.

188. Yoneyama, H. (1997), "Photoreduction of carbon dioxide on quantized semiconductor nanoparticles in solution", *Catalysis Today,* vol. 39, no. 3, pp. 169-175.

189. M.Ulman, A. H. A. T., A.Mackor. (1982), "Photoreduction of carbon dioxide to formic acid, formaldehyde, methanol, acetaldehyde and ethanol using aqueous suspensions of strontium titanate with transition metal additives", *International journal of solar energy,* vol. 1, pp. 213-222.

190. Ulman, M., Tinnemans, A. H. A., Mackor, A., Aurian-Blajeni, B. and Halmann, M. (1982), "PHOTOREDUCTION OF CARBON DIOXIDE TO FORMIC ACID, FORMALDEHYDE, METHANOL, ACETALDEHYDE AND ETHANOL USING AQUEOUS SUSPENSIONS OF STRONTIUM TITANATE WITH TRANSITION METAL ADDITIVES.", *International Journal of Solar Energy,* vol. 1, no. 3, pp. 213-222.

191. Carroll, J. J. and Mather, A. E. (1992), "The system carbon dioxide-water and the Krichevsky-Kasarnovsky equation", *Journal of Solution Chemistry,* vol. 21, no. 7, pp. 607-621.

192. Aurian-Blajeni, B., Halmann, M. and Manassen, J. (1980), "Photoreduction of carbon dioxide and water into formaldehyde and methanol on semiconductor materials", *Solar Energy,* vol. 25, no. 2, pp. 165-170.

193. Kaneco, S., Shimizu, Y., Ohta, K. and Mizuno, T. (1998), "Photocatalytic reduction of high pressure carbon dioxide using tio2 powders with a positive hole scavenger", *Journal of Photochemistry and Photobiology A: Chemistry,* vol. 115, no. 3, pp. 223-226.

194. Kočí, K., Obalová, L., Matějová, L., Plachá, D., Lacný, Z., Jirkovský, J. and Šolcová, O. (2009), "Effect of TiO2 particle size on the photocatalytic reduction of CO2", *Applied Catalysis B: Environmental,* vol. 89, no. 3-4, pp. 494-502.

195. Cabrera, A. L., Vargas, F. and Albers, J. J. (1995), "Adsorption of carbon dioxide by ferroelectric lithium niobate", *Surface Science,* vol. 336, no. 3, pp. 280-286.

Appendix A – Publications

1. Stock. M, Dunn. S (2011) ***LiNbO3-A New Material for Artificial Photosynthesis***
   IEEE TRANSACTIONS ON ULTRASONICS FERROELECTRICS AND FREQUENCY CONTROL vol. 58, (9) 1988-1993.

2. Stock. M, Dunn. S (2011) ***LiNbO(3)-A Polar Material for Solid-Gas Artificial Photosynthesis***
   FERROELECTRICS vol. vol. 419, (1) 9-13

3. Armani. F, Gougis. M, Impey. SA, James. A.C, Lawson. K, Lihrmann. L, Stock. M, Dunn. S. (2010) ***Nanostructured TiO2 - morphological and structural changes***
   MATERIALS LETTERS vol. 64, (2) 140-143.

Appendix B – Conferences

Presentations

1. ***Using Lithium Niobate for Artificial Photosynthesis and the Role of the Ferroelectric Polarisation in Photocatalytic Reactions***

   EMF 2011 European Meeting on Ferroelectricity, Bordeaux, June 26-July 2 2011

2. ***Lithium Niobate as a New Photocatalyst Material for Artificial Photosynthesis Reactions***

   IOP Dielectrics 2011, Canterbury, Kent 13-15th April 2011